1,2,5-TELLURADIAZOLES

SYNTHESIS, STRUCTURAL CHARACTERIZATION, SPECTROSCOPIC STUDIES AND COMPUTATIONAL INVESTIGATIONS OF 1,2,5-TELLURADIAZOLES AND THEIR SUPRAMOLECULAR ASSEMBLIES

BY

ANTHONY F. COZZOLINO, B.SC.

A THESIS

SUBMITTED TO THE SCHOOL OF GRADUATE STUDIES

IN PARTIAL FULFILLMENT OF THE REQUIREMENTS

FOR THE DEGREE

DOCTORATE OF PHILOSOPHY

MCMASTER UNIVERSITY

Ph.D (2009) McMaster University

(Chemistry) Hamilton, ON

TITLE: Synthesis, Structural Characterization, Spectroscopic Studies and Computational Investigations of 1,2,5-Telluradiazoles and their Supramolecular Assemblies.

AUTHOR: Anthony F. Cozzolino

SUPERVISOR: Professor Ignacio Vargas-Baca

NUMBER OF PAGES: xxxiv, 241

ABSTRACT

The use of Te-N-C heterocycles as supramolecular building blocks was investigated. The propensity of the heavy main-group elements to engage in secondary bonding interactions motivated a survey of the literature that identified the supramolecular association patterns that are most frequent in the crystal structures of tellurium compounds. A notation was proposed to classify those supramolecular synthons. The shortest Te-N secondary bonding distances are observed in the crystals of 1,2,5-chalcogenadiazoles which assemble the virtual four-membered ring $[Te\text{-}N]_2$. Detailed computational investigations (DFT) established that the Te-N secondary bonding interactions are stabilized by a combination of electrostatic and Lewis acid-base covalent contributions. The study also indicated that the $[Te\text{-}N]_2$ supramolecular synthon meets the requirements of strength, directionality and reversibility that are necessary in supramolecular chemistry. A general method was developed for the synthesis of a wide variety of telluradiazoles. These compounds were used in experiments that probed the ability of steric effects to disrupt the self-assembly and select dimers instead of ribbon polymers. Derivatives resulting from the addition of Lewis acids and bases were also investigated. Photoelectron spectroscopy confirmed the details of the calculated electronic structures of benzo-2,1,3-chalcogenadiazoles and mass spectrometry provided evidence of the association of these molecules in gas phase. A molecular mechanics method was parameterized to reproduce the structural features of the $[Te\text{-}N]_2$ supramolecular synthon and, using this information, envision new supramolecular architectures based on 1,2,5-telluradiazoles. The use of the $[Te\text{-}N]_2$ supramolecular synthon in the design and function of materials with properties such as thermochromism and nonlinear optical responses was demonstrated. Preliminary findings also highlighted the potential use of this approach in molecular materials that conduct electricity.

ACKNOWLEDGEMENTS

I thank my supervisor, Dr. Ignacio Vargas-Baca, for his guidance during both my thesis project and the preparation of this manuscript.

I express my gratitude towards my supervisory committee members, Dr. A. Adronov and Dr. G. J. Schrobilgen for their helpful suggestions and guidance.

I thank the optical spectroscopy facility, the NMR spectroscopy facility, the mass spectrometry facility and the X-ray diffraction facility.

I thank both present and former lab group members for their technical expertise and making the lab environment an enjoyable place to work.

I thank my funding sources: Ontario Graduate Scholarship (OGS) program, Natural Science and Engineering Research Council of Canada (NSERC), McMaster University, American Chemical Society Petroleum Research Fund (ACS PRF), the Canada Foundation for Innovation (CFI) and the Ontario Innovation Trust (OIT).

I thank McMaster's Bio-molecular Interactions Initiative and the facilities of the Shared Hierarchical Academic Research Computing Network (SHARCNET:www.sharcnet.ca) for CPU time.

TABLE OF CONTENTS

LIST OF FIGURES

LIST OF SCHEMES

LIST OF TABLES

LIST OF COMPOUNDS

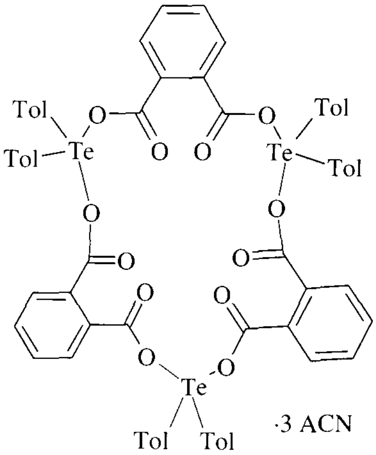

1

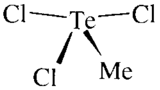

2

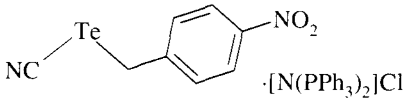

3

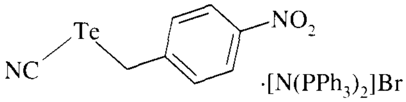

4

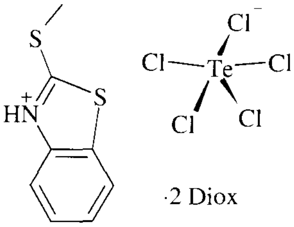

5

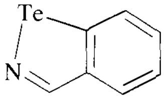

6

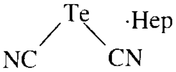

7

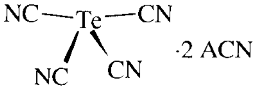

8

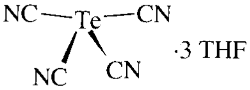

9

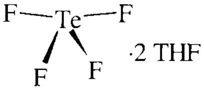

10

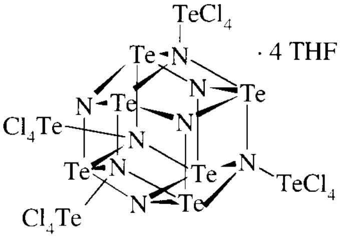

11

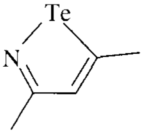

12

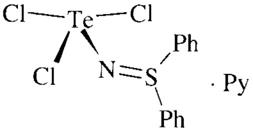

13

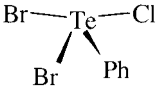

14

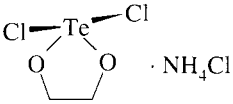

15

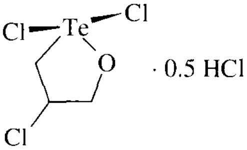

16

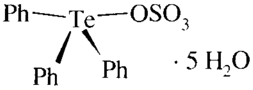

17

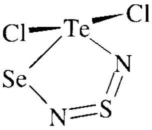

18

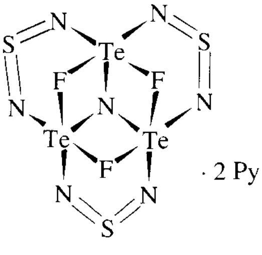

19

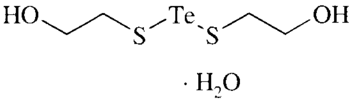

20

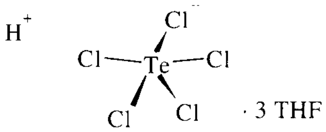

21

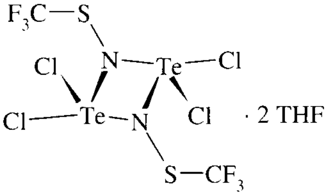

22

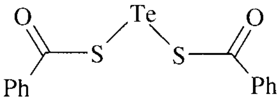

23

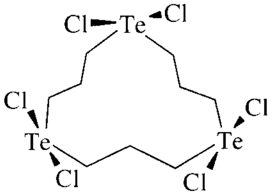

24

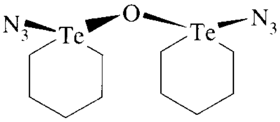

25

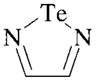

26

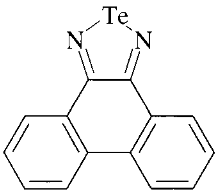

27

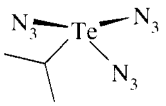

28

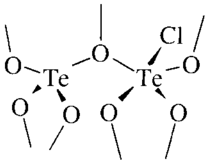

29

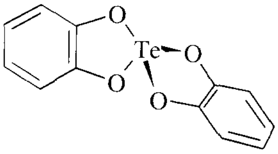

30

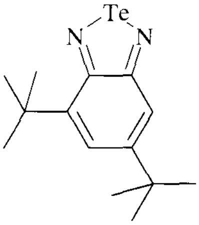

31

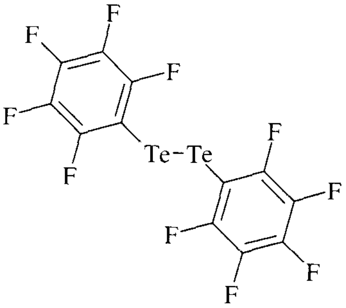

32

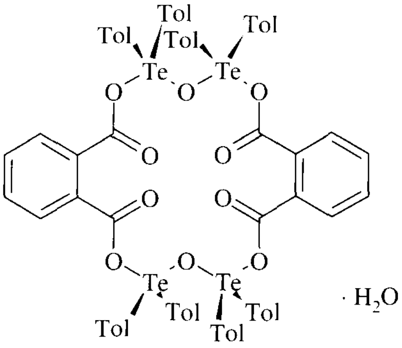

33

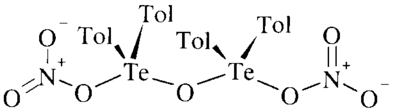

34

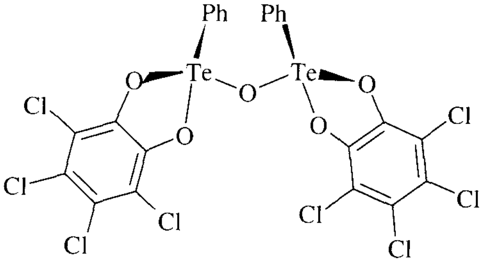

35

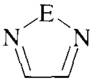

36 E = S
37 E = Se

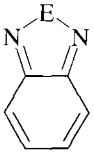

38 E = S
39 E = Se
40 E = Te

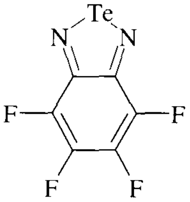

41

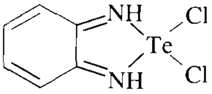

42

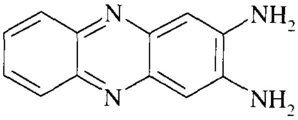

43

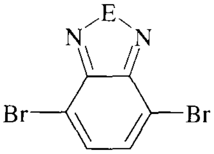

44 E = S
45 E = Se
46 E = Te

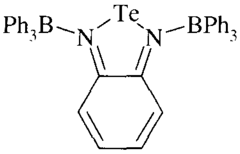

47

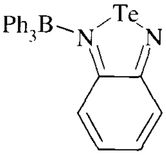

48

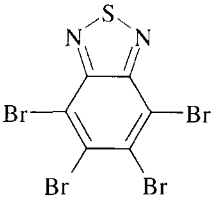

49

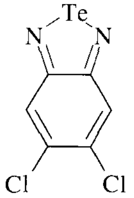

50

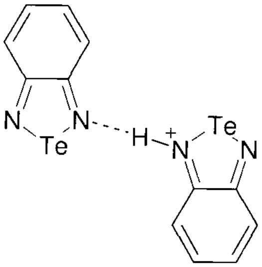

51

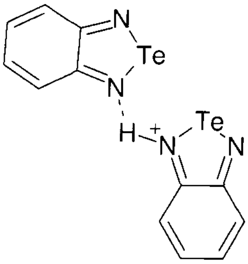

52

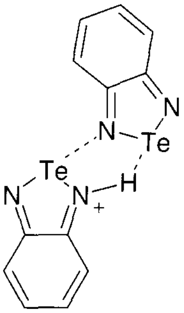

53

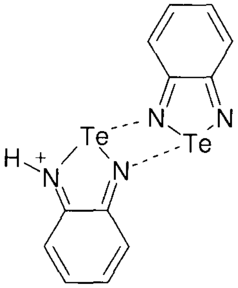

54

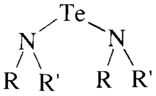

55 R=R'=H
56 R=R'=Me_3Si
57 R=Me_3Si R'=^tBu
58 R=R'=Me

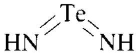

59

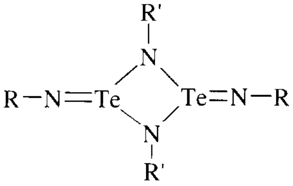

60 $R_{(cis)}$=R'= ^tBu
61 $R_{(trans)}$=PPh_2NSiMe_3, R'= ^tBu
62 $R_{(trans)}$=PPh_2NSiMe_3, R'= ^tOct

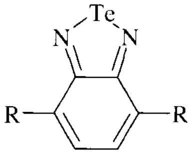

63 R=F
64 R=Cl
65 R=I
66 R=Me

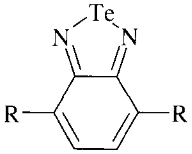

67 R=Et
68 R=^iPr
69 R=^tBu
70 R=Me_3Si

71 R= 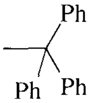

72 R= 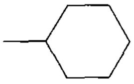

73 R= 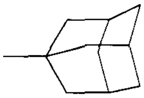

74 R= 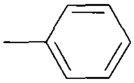

75 R=

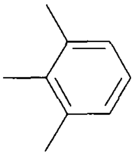

76 R=

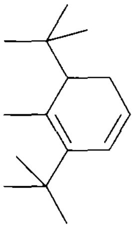

77 R=

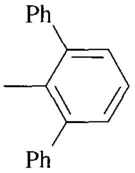

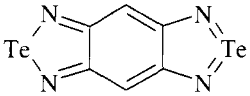

78

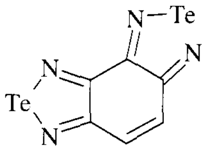

79

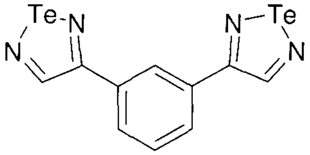

80

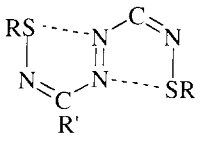

Z,E,Z

81

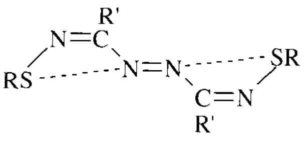

Z,E,Z

82

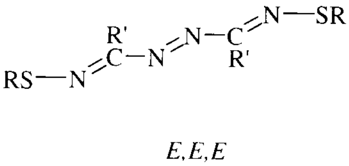

83

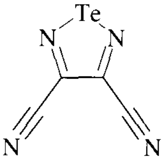

84

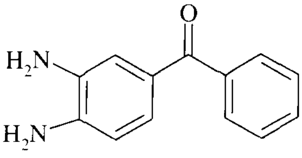

85

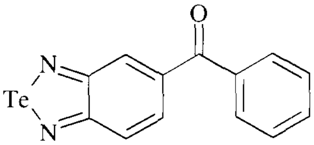

86

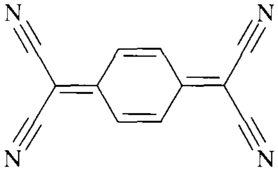

87

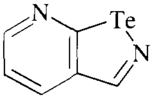

88

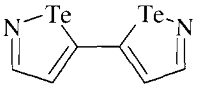

89

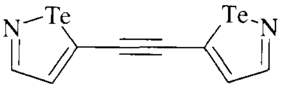

90

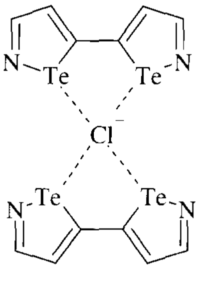

91

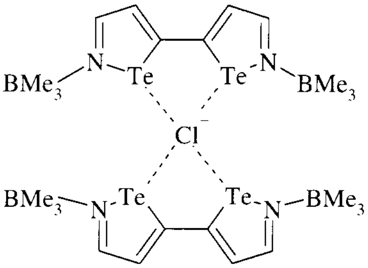

92

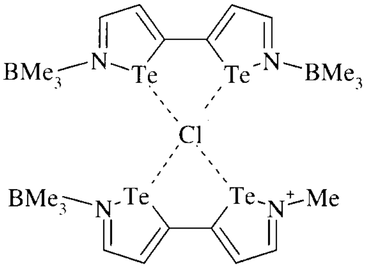

93

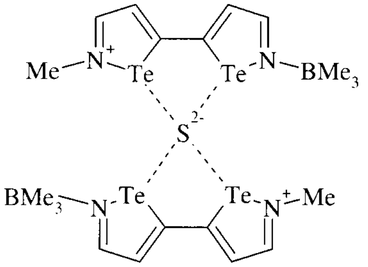

94

LIST OF ABBREVIATIONS AND SYMBOLS

Å	angstrom
a, b, c, α, β, γ	unit cell parameters (in crystallography)
a.u.	arbitrary units
ADF	Amsterdam Density Functional software
ACN	acetonitrile
AIM	atoms in molecules, Bader's theory of
AIP	adiabatic ionization potential
au	atomic units
AU	absorbance units
B3LYP	hybrid exchange correlation functional, Becke 3 term with Lee, Yang, Parr exchange
BCP	bond critical point
BP86	GGA exchange correlation functional, Becke exchange and Perdew correlation
CI	chemical ionization (in mass spectrometry)
cm^{-1}	wavenumber
CSD	Cambridge Structural Database
D	donor atom with an SBI
DFT	density functional theory
Diox	dioxane
DMSO	dimethyl sulphoxide
E	a variable element within a structure, the acceptor element within an SBI
e	electrons (in crystallography)
EI	electron impact (in mass spectrometry)
ELF	electron localization function
Et	ethyl
FT	Fourier transform
FWHM	full width at half maximum
GGA	generalized gradient approximation
GUI	graphical user interface
Hep	heptane
HF	Hartree-Fock
HOMO	highest occupied molecular orbital
iPr	isopropyl
IR	infrared
IUPAC	International Union of Pure and Applied Chemistry
KSMO	Kohn-Sham molecular orbitals
LDI	laser desorption/ionization (in mass spectrometry)
LUMO	lowest unoccupied molecular orbital
MALDI	matrix-assisted laser desorption/ionization

Me	methyl
MO	molecular orbital
MS	mass spectrometry
NBO	Natural Bond Orbital
nBu	butyl
NLO	nonlinear optical
nm	nanometre
NMR	nuclear magnetic resonance
PES	potential energy surface
PMT	photomultiplier tube
ppm	parts per million
PW	pulse width (in NMR spectroscopy)
PW91	GGA exchange correlation functional, Perdew and Wang
Py	pyridine
QTAIM	quantum theory of atoms in molecules
R_1	unweighted residual factor (in crystallography)
RCP	ring critical point
r_{vdW}	van der Waals radii
SAOP	statistical average of orbital potentials
SBI	secondary bonding interaction
SDK	software development kit
SF	spectral frequency (in NMR)
SHG	second harmonic generation
SOMO	single occupied molecular orbital
SW	sweep width (in NMR)
T	temperature
^{t}Bu	tertiary butyl
TCNQ	7,7,8,8-tetracyanoquinodimethane
TD	time domain (in NMR)
TDDFT	time dependant DFT
THF	tetrahydrofuran
TOF	time-of-flight (in mass spectrometry)
Tol	Toluene
TZP	triple-ζ with one polarization function (basis set)
UPS	ultraviolet photoelectron spectroscopy
UV-vis	ultraviolet and visible region
V	unit cell volume (in crystallography)
VDD	Voronoi deformation density
VIP	vertical ionization potential
wR_2	weighted residual factor (in crystallography)
Z	molecules per unit cell (in crystallography)
ZORA	zeroth-order regular approximation
δ	chemical shift, ppm (parts per million)
λ	wavelength

μ	linear absorption coefficient (in crystallography)
ρ	density of a material (in crystallography)

1 Introduction. A Survey of Te-Centered Supramolecular Synthons

1.1 Supramolecular Chemistry

IUPAC defines supramolecular chemistry as "*a field of chemistry related to species of greater complexity than molecules, that are held together and organized by means of intermolecular interactions. The objects of supramolecular chemistry are supermolecules and other polymolecular entities that result from the spontaneous association of a large number of components into a specific phase (membranes, vesicles, micelles, solid-state structures etc.)*".[1] Supramolecular chemistry encompasses a growing number of important subfields that include: molecular host-guest chemistry; solid-state inclusion chemistry; crystal engineering; supramolecular devices; self-assembly; soft/smart materials; and aspects of nanochemistry and biological chemistry. Each subfield emphasizes, to a different extent, the new structure that results from the formation of the intermolecular interactions and the properties that result from the formation of the intermolecular interactions.

1.2 Intermolecular Interactions

The idea of intermolecular interactions was first introduced in order to reconcile the ideal gas law with the behaviour of real gases. Dutch physicist J. D. van der Waals proposed corrections to the ideal gas law to account for the finite size of atoms and the attractive forces that occur between molecules.[2] As a result intermolecular forces are often referred to as 'van der Waals forces' but there is ambiguity in the use of this term. From the original proposal, it is clear that the term 'van der Waals forces' encompasses all intermolecular forces. It is, however, most frequently used to describe interactions arising from dipole-dipole, dipole-induced dipole or dispersion forces. For the sake of accuracy, this thesis will make reference to specific interaction types.

Intermolecular interactions can be classified within the following types: ion-ion interactions, ion-permanent dipole interactions, dipole-dipole interactions, hydrogen bonding, cation-π interactions, anion-π interactions, π-π interactions, ion-induced dipole interactions, dipole-induced dipole interactions, closed shell interactions and dispersion interactions.[3] Table 1.1 gives energy ranges and radial dependencies of the interaction types that are best understood.

Table 1.1 Intermolecular interaction energies and their radial dependencies.[3,4]

Interaction type	Energy range (kJ/mol)	Radial dependency
ion-ion	100-350	r^{-1}
ion-permanent dipole	50-200	r^{-2} (r^{-4})†
permanent dipole- permanent dipole	5-50	r^{-3} (r^{-6})†
hydrogen bond	4-60 (up to 120)	~r^{-2}

†rotating case

In order to identify the presence of intermolecular interactions from structural data, supramolecular chemists define a cutoff distance, beyond which intermolecular contacts are not regarded as the result of an attractive interaction. This arbitrary cutoff is meant to define the region of space occupied by the isolated atom or molecule but is in conflict with the radial decay of electron density which only approaches zero at an infinite distance from the nucleus. In choosing the cutoff distances it is assumed that the balance of external electron density is too small to influence the formation of the supramolecular structure. The most widely used cutoff distances are the set of van der Waals radii (r_{vdW})

proposed by Bondi[5] based on the careful consideration of X-ray diffraction data, gas kinetic collision cross sections, critical densities, and properties of the liquid state.

1.2.1 Closed-Shell Interactions

These are attractive intermolecular interactions characterized by contact distances between two atoms that are shorter than the sum of the van der Waals radii yet longer than a single or hypervalent bond. These interactions occur between atoms that have already filled their primary valencies and are not expected to form any additional strong interactions on the basis of Lewis octet theory. These closed-shell interactions include metallophilic interactions and secondary bonding interactions (SBIs).[6] Metallophilic interactions are frequently observed between d^{10} metal ions. The best known example is the aurophilic (Au-Au) interaction which is thought to be stabilized by significant relativistic contributions.[6] Secondary bonding interactions are a pervasive feature in the structures of compounds of heavy main-group elements.[7]

1.2.2 Secondary Bonding Interactions

The term secondary bonding interaction was proposed by Alcock in 1972[8] to denote contacts between p-block elements that are shorter than the sum of r_{vdW} yet longer than the typical single or hypervalent bond. Although "secondary bonding" is the most appropriate description, other names have been used in literature to denote this phenomenon, including: soft-soft interactions,[9] closed-shell interactions,[6] nonbonding interactions,[10] σ-hole interactions,[11] semibonding interactions,[12] halogen bonds,[13] noncovalent interactions[14] and weakly-bonding interactions.[15,16] Moreover, in the early literature this phenomenon was not always recognized and many short contact distances were merely attributed to 'packing effects' if not completely overlooked.

Alcock[8] proposed a bonding description for SBIs (Figure 1.1) based on empirical observations. First, the central atom in the secondary bond is typically a heavy element (E) attached to a more electronegative atom (A). Second, the other atom (D) participating in the SBI has at least one lone pair of electrons. Third, there are geometric features of the arrangements, for example the secondary bond axis (E--D) is collinear with that of the covalent (primary) bond (A-E), which cannot be explained by electrostatic arguments alone. Alcock reasoned that there must be a covalent contribution to the secondary bond that results from the donation of electrons from D[†] into the A-E σ* molecular orbital.

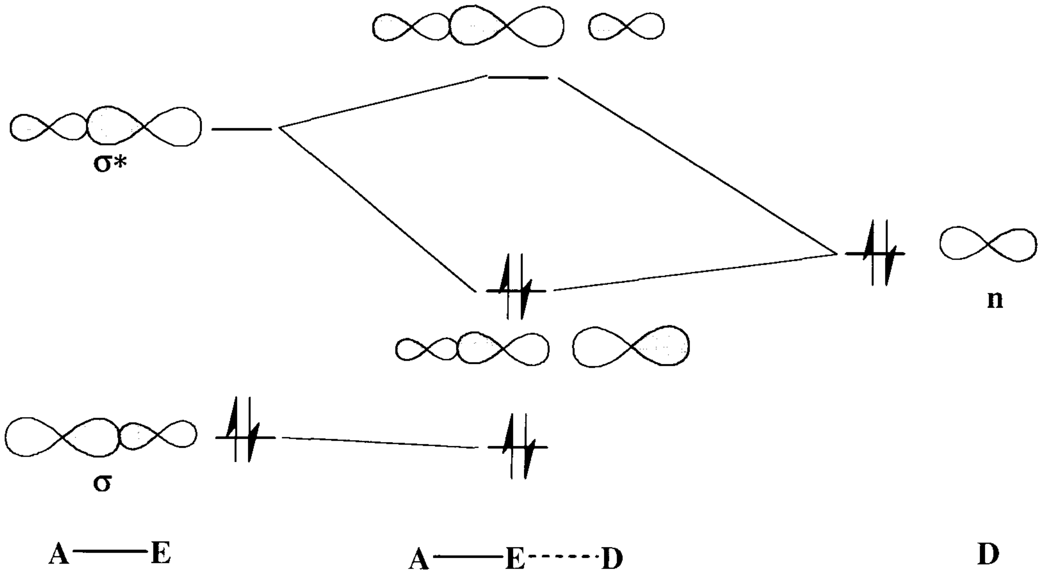

Figure 1.1 Molecular orbital diagram illustrating an SBI between A-E and D.

[†] Although the symbol D is frequently used to denote a deuterium atom, in the context of supramolecular chemistry and specifically secondary bonding interactions D denotes a donor atom (see for example reference 17 or 18).

A more complete bonding description of secondary bonding interactions requires the inclusion of covalent, electrostatic and dispersion contributions. As in Alcock's description, the attractive covalent contribution results from the mixing of occupied and unoccupied orbitals leading to a more energetically favourable state. This attractive covalent contribution gives directionality to the SBI. A repulsive contribution (Pauli repulsion) results from the mixing of occupied orbitals. The electrostatic (or Coulombic) contribution is attractive as the interacting regions usually have opposite partial charges. It has been proposed that some of the directional nature of the SBI could be attributed to the electrostatic component.[11,13,19] The dispersion force is always attractive and arises when the electrons in two molecules become instantaneously correlated. The strength of the dispersion force increases as the electron clouds of the molecules become more polarizable, as it does with the heavy elements involved in the SBIs.[3,4]

Secondary bonding interactions are frequently observed in the solid state and their presence can explain unusual features of the lattice. Despite this, there have been very few attempts to systematically use SBIs as design elements for supramolecular chemistry. There are, however, some notable examples: SBIs involving pnictogens[20] have been used as links between ribbon polymers;[21] SBIs involving chalcogens[22] have been used to construct supramolecular tubes;[10,23-25] and SBIs involving halogens are important structural design elements in the noncentrosymmetric lattice of a material that is capable of second harmonic generation (SHG),[26] are used to resolve a racemic perfluoroalkyl bromide,[27] and are used to separate mixtures of diiodoperfluoroalkanes.[28]

1.3 Supramolecular Synthons

Desiraju[29] defined a supramolecular synthon as "*a structural unit within a supermolecule which can be formed and/or assembled by known or conceivable synthetic operations involving intermolecular interactions.*" This concept has been used for the rational design of hydrogen bonded architectures and examples of various hydrogen bonded supramolecular synthons are given in Figure 1.2. Identification of systems that contain the basic single hydrogen bonded supramolecular synthon (Figure 1.2a) helps to rationalize properties that lead to structural features, such as distance and angle, in the absence of other competing or supplemental interactions. Figures 1.2b and 1.2c highlight the supramolecular synthons that are observed in DNA base pairs and have been used as templates for the design of new supramolecular systems.[30] Figure 1.2d portrays a supramolecular synthon with four hydrogen bonds that leads to materials such as supramolecular polymers.[31] Figures 1.2 b-d demonstrate the use of multiple points of attachment to strengthen the supramolecular synthon. The supramolecular structures of both biological systems and small molecules can be probed to identify promising supramolecular synthons assembled by hydrogen bonds. Starbuck[29] proposed that a similar approach should lead to the rational design of SBI supramolecular systems. A key step in this direction would therefore be the identification of the most efficient supramolecular synthons. This could be achieved, in principle, by careful examination of data already compiled in databases such as the Cambridge Crystallographic Database (CSD).[32]

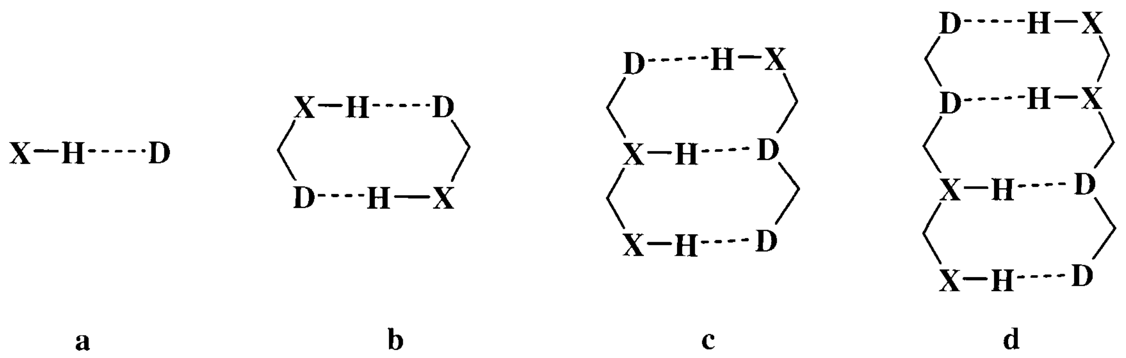

Figure 1.2 Examples of supramolecular synthons assembled by hydrogen bonds.

This overview of strong supramolecular synthons will focus on tellurium-centred secondary bonding interactions. Tellurium is an ideal candidate as it can form bonds with most main-group elements[33] and both the geometries of Te(II) and Te(IV) centres have open sites available for more than one SBI. In addition to this, Haiduc and Zukerman-Schpector[22,34] have reviewed systems containing tellurium-centered SBIs clearly identifying them as promising design elements that can lead to a variety of supramolecular architectures. The current overview does not attempt to duplicate their findings, which emphasize the molecular building blocks and supramolecular structures, but rather extend them by identifying the most promising (short and presumably strong with multiple points of attachment) supramolecular synthons within the structures contained in the CSD.

1.3.1 Identification of SBI Supramolecular Synthons

Efficient supramolecular synthons should be strong and directional. While the strength of an SBI cannot be determined quantitatively from structural data, comparison of interatomic distances does permit an assessment of the relative strengths of the SBIs. While SBIs close to the sum of r_{vdW} would be stabilized primarily by the dispersion contribution, shorter SBIs would also have important covalent and electrostatic components. In order to focus on the strongest supramolecular synthons a cutoff below the sum of r_{vdW} was used. Recent work by Rowland and Taylor,[35] as well as Dance[36] indicates that the statistical maximum in the distribution of interatomic contacts that are primarily dispersive in origin appears at 0.3-0.4 Å (approximately 10%) above the sum of r_{vdW}. Assuming a normal distribution around this maximum, the sum of r_{vdW} would be located $(2 \ln 2)^{1/2}$ times the standard deviation (σ) from the maximum. In order to ensure that the majority of dispersion-dominated contacts are removed, the dataset was cut at 2σ, or 93% of the sum of r_{vdW}.

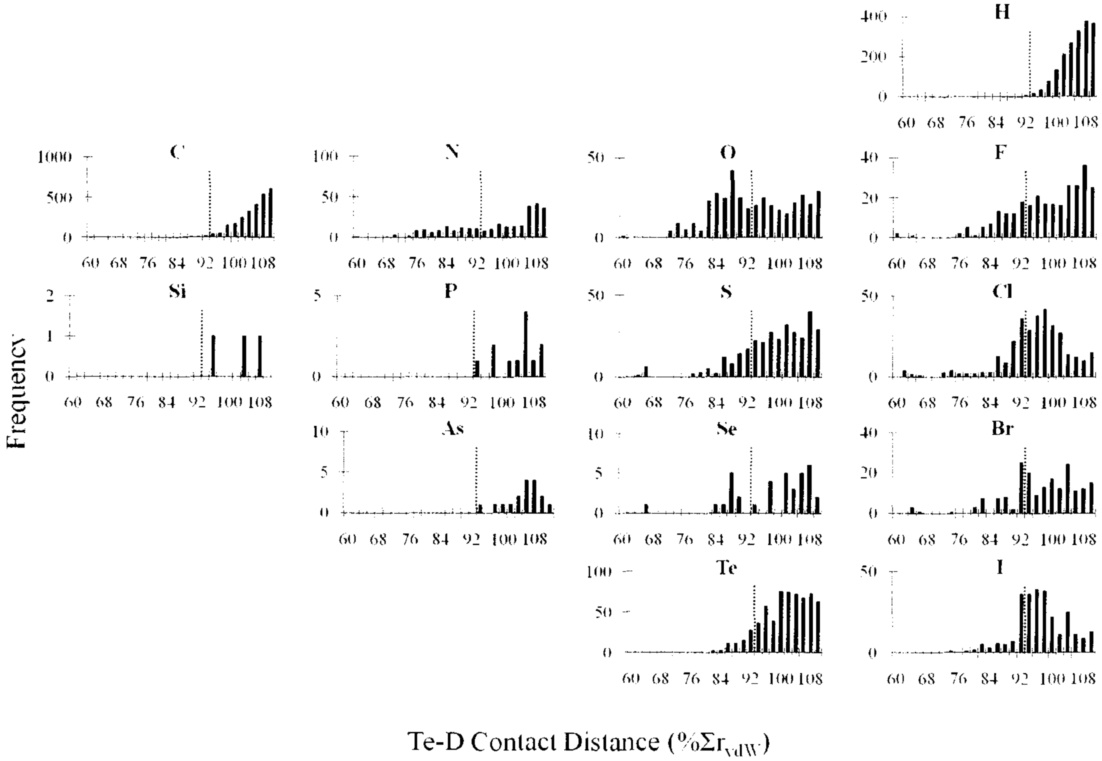

Figure 1.3 Distribution histograms of Te contact distances scaled to the sum of Bondi's van der Waals radii. The dotted line denotes the 93% cutoff.

A search of the Cambridge Structural Database (version 5.9, November 2007 containing 423 752 structures)[32] revealed 1127 structures that contained intermolecular contacts (less than the sum of the van der Waals radii plus 10%) between Te and H, C, Si or D where D is N, O, F, P, S, Cl, As, Se, Br, Sb, Te, I.[37] Histograms have been made for the 1841 Te-H, 2599 Te-C, 3 Te-Si and 2752 Te-D intermolecular contacts and are displayed in Figure 1.3. Some important observations can be made from this initial classification. The systems in which the contact atom does not typically have lone pairs (e.g., Si, C and H) display a continuous increase in frequency of contact vs. distance. For hydrogen, an atom that always is positioned on the periphery of the molecule, the number of contacts begins to increase approximately with the cube of the distance. This is expected for a random spatial distribution of contacts, as should be observed in the system which has the weakest dispersion contribution.[35] Tellurium-silicon intermolecular contacts occur with much less frequency at distances close to the sum of r_{vdW} because Si is usually an internal atom with a saturated tetrahedral coordination geometry. The Te-C intermolecular distance histogram displays a profile similar to that of Te-H. Unlike Si, C often is found sp^2 hybridized, allowing it to be located at the periphery of the molecule. If the contacts were simply the result of random spatial arrangement, the same cubic increase in the frequency of interactions with distance as seen for Te-H would be observed. The increase occurs at a slower rate, which probably results from a stronger dispersion contribution as well as the ability of Te to form SBIs with the π-system.[38, 34] The histograms of the Te-D interactions appear to follow the general trend where the more electronegative donors have a greater proportion of short interactions. It is these short, and presumably strong, interactions that are the most likely to yield promising supramolecular synthons. The 93% cutoff effectively eliminates H, C, Si, P and As interactions altogether as design elements for useful supramolecular synthons.

1.4 A Hierarchical Classification of Supramolecular Structure

In order to organize the structures, this review uses a hierarchical classification similar to that used in the description of protein structures and host-guest aggregates.[39,40] In this system the individual molecules (*tectons*[41] or building blocks) constitute the *primary* (1°) *structure.* The *secondary* (2°) *structure* is that built through the association of molecules in the most elementary form, in other words the supramolecular synthon. The next level of complexity, created by the expansion of the network of supramolecular synthons, constitutes the *tertiary* (3°) *structure* which can encompass dimers, ribbon polymers, helices, 2D- and 3D-networks. This survey of SBI supramolecular synthons is therefore focused on the secondary structure.

1.5 Tellurium-Based Supramolecular Synthons

1.5.1 Classification and Notation

In order to facilitate the classification and comparison of structures that originate from dissimilar building blocks, the following notation will be used to identify SBI supramolecular synthons. The label $[\text{E-m-D}]_n$ denotes in square brackets the fragments of the building blocks that comprise the supramolecular synthon. E and D are the elements that engage in SBIs; in this chapter E is always Te. A dash indicates a covalent link between E and D while no dash implies that the atoms belong to different molecules. Bridging atoms linking E and D are not explicitly identified, only how many (m). The subscript n is the number of times the building blocks are repeated in the structure of the supramolecular synthon. The subscript is removed when n = 1. This notation is applied in Figure 1.4 to the supramolecular synthons most frequently found assembled by short Te-D SBIs in the CSD. The first example, [Te-m-D], corresponds to an intramolecular SBI. Such virtual rings are a prominent feature in the structures of p-block elements,[16,42] however, this case is omitted in this survey because it is an intramolecular phenomenon.

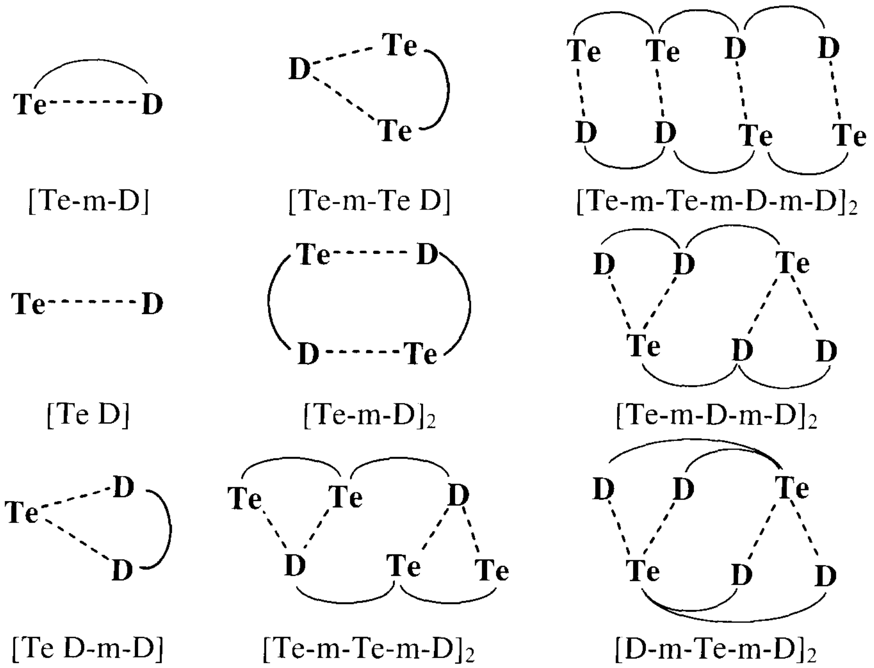
[Te-m-D] [Te-m-Te D] [Te-m-Te-m-D-m-D]$_2$

[Te D] [Te-m-D]$_2$ [Te-m-D-m-D]$_2$

[Te D-m-D] [Te-m-Te-m-D]$_2$ [D-m-Te-m-D]$_2$

Figure 1.4 Te-centered SBI supramolecular synthons.

1.5.2 Supramolecular Synthons with One Point of Attachment

1.5.2.1 [Te D]

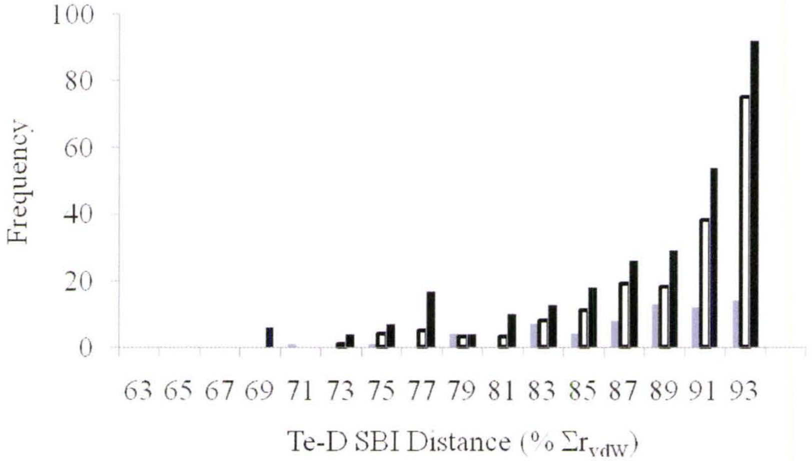

Figure 1.5 Histogram for the distribution of Te-D interaction distances in [Te D] (■),[Te-m-D]$_2$ (□) and all other supramolecular synthons (▨).

The most abundant (52%) supramolecular synthon is [Te D]. Figure 1.5 shows the distribution of the Te-D SBI distances in the [Te D] supramolecular synthons compared with the Te-D SBI distances on the other supramolecular synthons. Table 1.2 highlights the variety of tertiary structures which can be assembled by strong [Te D] supramolecular synthons. The most basic structure types that are formed are solvent or ion 1:1 adducts. Examples of 1:1 adducts with pyridine or THF are the diphenylsulfiminato-trichloro-tellurium(IV) pyridine solvate (**13**)[43] and tetrafluoro-bis(tetrahydrofuran)-tellurium (**10**)[44] while bis(triphenylphosphine)-iminium chloro-cyano-4-nitrobenzyl-tellurium(II) (**3**)[45] and bis(triphenylphosphine)-iminium bromo-cyano-4-nitrobenzyl-tellurium(II) (**4**)[45] are examples of a chloride and a bromide 1:1 adduct, respectively. A ribbon polymer is formed by phenyl-tellurium bromide chloride (**14**)[46] while a helical polymer is formed by 3,5-dimethyl-1,2-tellurazole (**12**).[47] Examples of 2D arrays are catena-((μ_2-chloro)-dichloro-methyl-tellurium(IV)) (**2**)[48] and catena-(4,4-bis(μ_2-chloro)-4-chloro-1-thia-3-selena-2,5-diaza-4-telluracyclopentadienyl) (**18**)[49] while a solvent capped 2D array is formed by catena-((μ_2-cyano)-bis(acetonitrile)-tricyano-tellurium(IV)) (**8**).[44] The [Te D] supramolecular synthons have also been observed to direct the formation of the entire 3D lattice of the crystal, for example dicyano-tellurium heptane solvate (**7**)[50] is able to form a 3D lattice due to its bifunctional primary structure which participates in the formation of ribbon polymers in two different directions.

Table 1.2 A-Te--D SBIs for which the Te-D distance is shorter than 80% of the sum of r_{vdW} in the [Te D]$_2$ supramolecular synthon .

	Reference	Primary Structure	D	A	d_{SBI} (Å)	% Σr_{vdW}	a_{SBI} (°)	Donor	Tertiary structure
1	51	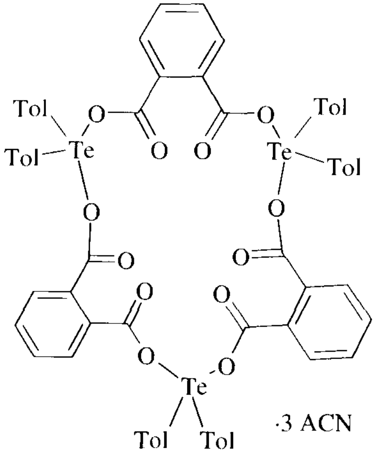	N	C	2.793	77	161.9	ACN	1:1 adduct
2	48	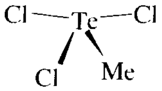	Cl	Cl	2.814	74	171.3		polymer
3	45	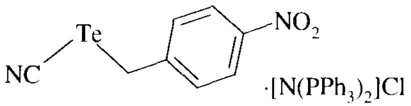	Cl	CN	2.924	77	167.9	Cl^-	1:1 adduct
4	45	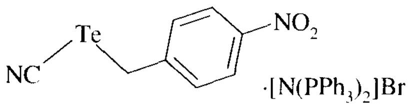	Br	CN	3.100	79	167.6	Br^-	1:1 adduct

	Reference	Primary Structure	D	A	d_{SBI} (Å)	% Σr_{vdW}	a_{SBI} (°)	Donor	Tertiary structure
5	52	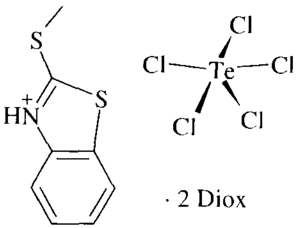	O	Cl	2.765	77	179.7	Diox	1:1 adduct
6	53	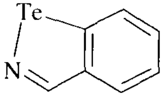	N	N	2.456	68	165		helical polymer
			N	N	2.465	68	165.7		
			N	N	2.488	69	166.7		
7	50	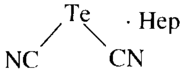	N	CN	2.745	76	163.2		3D network
			N	CN	2.758	76	163.9		
8	44	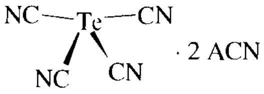	N	CN	2.601	72	158.5		2D network
			N	CN	2.727	76	145.0	ACN	1:1 adduct
			N	CN	2.866	79	136.1	ACN	1:1 adduct
9	44	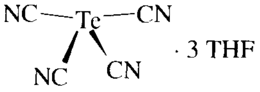	N	CN	2.567	71	148.9		polymer
			O	CN	2.701	75	147.1	THF	1:1 adduct
			O	CN	2.715	76	138.8	THF	1:1 adduct
			O	CN	2.774	77	140.7	THF	1:1 adduct
10	44	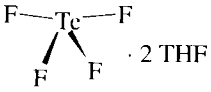	O	F	2.448	68	138.8	THF	1:1 adduct
			O	F	2.696	75	140.7	THF	1:1 adduct

	Reference	Primary Structure	D	A	d_{SBI} (Å)	% Σr_{vdW}	a_{SBI} (°)	Donor	Tertiary structure
11	54	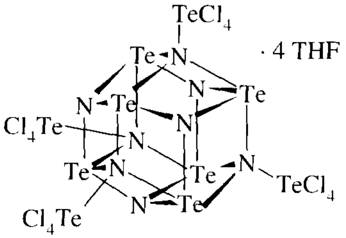	O	N	2.695	75	172.6	THF	1:1 adduct
			O	N	2.715	76	172.6	THF	1:1 adduct
			O	N	2.717	76	172.2	THF	1:1 adduct
			O	N	2.726	76	172.8	THF	1:1 adduct
12	47	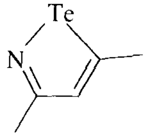	N	N	2.640	73	167.4		helical polymer
			N	N	2.659	74	168.3		
			N	N	2.7.00	75	166.4		
			N	N	2.741	76	168.9		
			N	N	2.744	76	167.0		
			N	N	2.774	77	173.3		
13	43	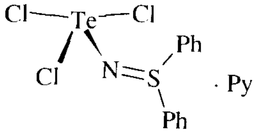	N	Cl	2.426	67	177.5	Py	1:1 adduct
14	46	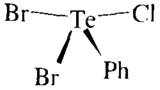	Cl	Br	2.811	74	175.0		polymer
15	55	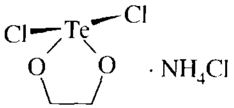	Cl	O	2.723	71	159	Cl$^-$	1:1 adduct
16	56	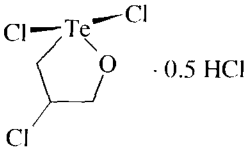	Cl	O	2.918	77	168.4		dimer

	Reference	Primary Structure	D	A	d_{SBI} (Å)	% Σr_{vdW}	a_{SBI} (°)	Donor	Tertiary structure
17	54	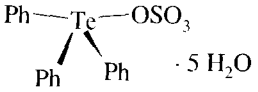	O	C	2.797	78	173.2	H_2O	1:1 adduct
18	49	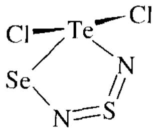	Cl	N	2.933	77	159.7		polymer
19	57	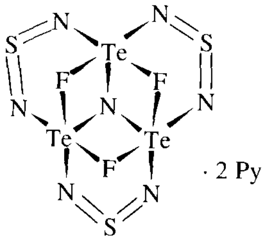	N	N	2.677	74	162.4	Py	1:1 adduct
			N	N	2.852	79	155.4	Py	1:1 adduct
20	58	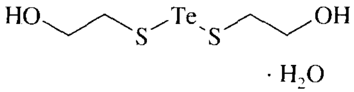	O	S	2.495	70	133.0	H_2O	1:1 adduct
			O	S	2.666	74	134.4	H_2O	1:1 adduct
21	24	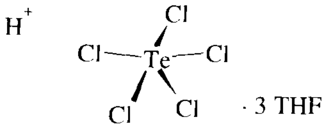	O	Cl	2.593	72	180.0	THF	1:1 adduct
22	59	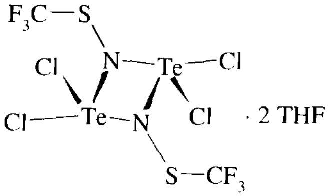	O	Cl	2.448	68	177.9	THF	1:1 adduct

In order to identify any important trends the distances were compared with various factors. First considered was the tellurium environment prior to SBI formation. Figure 1.6 displays a histogram of Te-D SBI distances in [Te D] for the coordination numbers with more than 20 examples. There appears to be no meaningful effect of coordination number on the length of the SBI. The predominant oxidation state of Te when it has a coordination number of 2 is Te(II) (and Te(I) in ditellurides) and Te(IV) when it has a coordination number of 4 and disphenoidal geometry; thus there is no apparent correlation between SBI distance in the [Te D] supramolecular synthon with Te oxidation state either.

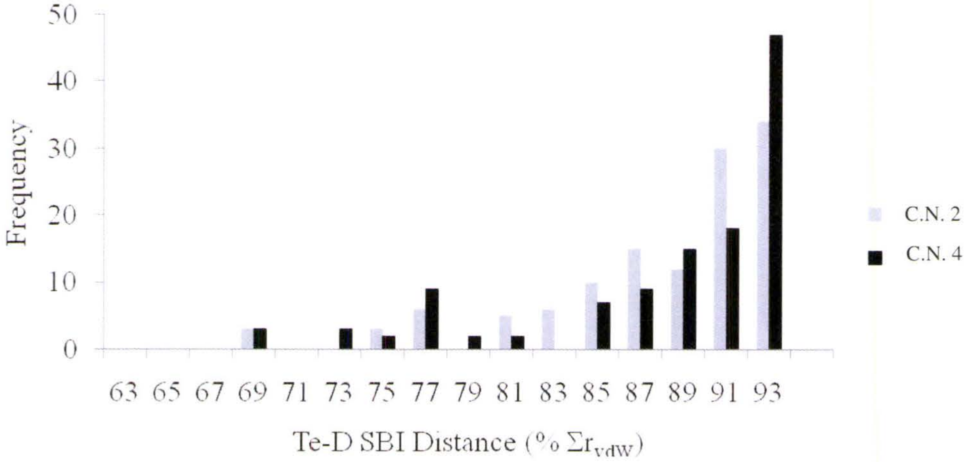

Figure 1.6 Distribution of Te-D interaction distances in the [Te D] supramolecular synthons with different tellurium coordination numbers.

A closer look at the shortest SBIs (<80% Σr_{vdW}) found for the [Te D] supramolecular synthon (Table 1.2) reveals that they primarily involve O, N or Cl as either donor (D) or acceptor (A) in A-Te--D. The pseudohalogen group CN is also involved in these shorter interactions. This is consistent with Alcock's bonding description. As the electronegativity of A increases, the Te contribution to the Te-A σ^*

orbital increases, facilitating overlap with the lone pair orbital of D. In addition, the energy of the acceptor orbital decreases as the Te-A bond is weakened by an increasing Te-A electronegativity difference and leads to a stronger orbital interaction with the lone pair. The electrostatic component of the interaction is also enhanced by increasing the polarization of the Te-A bond.

1.5.3 Supramolecular Synthons with Two Points of Attachment

1.5.3.1 [Te D-m-D]

There are nine structures that contain the [Te D-m-D] supramolecular synthon with Te-D SBIs as short as 70% of the sum of r_{vdW}. This is the simplest supramolecular synthon that contains multiple points of attachment and it highlights the ability of tellurium to form more than one SBI at a time. Five of these structures are assembled in a head to tail fashion as depicted in Scheme 1.1a. The remaining examples are a special case in which the Te atom also acts as the donor (Scheme 1.1b). Seven of the examples form an infinite 1D supramolecular polymer arranged by either motif while one dimerizes according to the arrangement in Scheme 1.1b. Generally this synthon displays one SBI longer than the other; the notable exceptions are bis(thiobenzoato-S)-tellurium(II) (**23**)[60] which has two equal Te-S SBIs (88% Σr_{vdW}) and 1,1,5,5,9,9-hexachlorotritelluracyclododecane dimethylformamide sesquihydrate (**24**)[61] which has two similar Te-Cl SBIs (88 and 91% Σr_{vdW}).

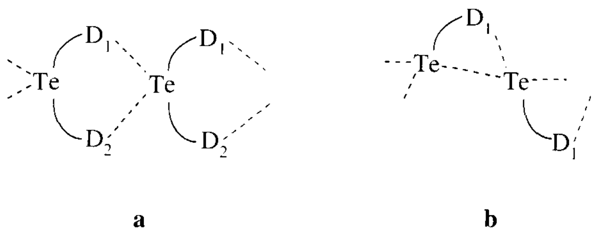

Scheme 1.1 Supramolecular synthons assembled by a D-m-Te-m-D molecule, a) [Te D-m-D], b) [Te Te-D].

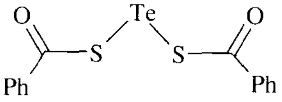

23

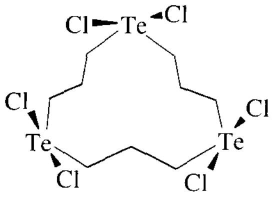

24

1.5.3.2 [Te-m-Te D]

There are four crystal structures that contain the [Te-m-Te D] supramolecular synthon with Te-D SBIs as short as 82% of the sum of r_{vdW}. Three of the examples display the [Te-m-Te D] supramolecular synthon capping open tellurium sites limiting the tertiary structure to capped monomers or dimers. Compound (μ_2-oxo)-bis((azido)-(pentane-1,5-diyl))-di-tellurium(IV) **25**[62] associates to form a ribbon polymer tertiary structure (Scheme 1.2) through $[Te\text{-}1\text{-}Te\ N]_2$.

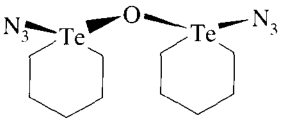

25

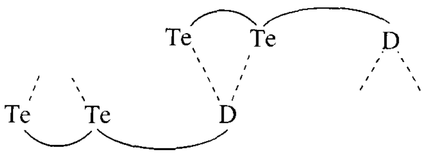

Scheme 1.2 Ribbon polymer structure based on $[Te\text{-}m\text{-}Te\ D]_2$.

1.5.3.3 [Te-m-D]$_2$

After the [Te D] supramolecular synthon, [Te-m-D]$_2$ is the second most prevalent (34%) in the CSD. Like [Te D-m-D] and [Te-m-Te D], there are two points of attachment. The [Te-m-D]$_2$ supramolecular synthon represents virtual heterocycles with m ranging from 0 to 6 (4- to 16-membered virtual rings). The most common value of m is 0 (114 of 148). While [Te-m-D]$_2$ has a distribution of distances similar to that of [Te D] (Figure 1.5), it is inherently stronger as there are twice as many bonds per supramolecular synthon. Following the trends observed for [Te D], the shortest SBIs are observed when N, O, F or Cl donate electrons into Te-X bonds where X is also N, O, F or Cl. There are seven crystal structures that contain the [Te-m-D]$_2$ supramolecular synthon with Te-D SBIs shorter that 80% of the sum of r_{vdW} (Table 1.1) and in each case it is the virtual four-membered heterocycle that is formed. Three of the crystal structures, 1,2,5-telluradiazole (**26**),[63] phenanthro(9,10-c)-1,2,5-telluradiazole (**27**)[64] and 4,6-di-t-butylbenzo-2,1,3-telluradiazole (**31**),[65] have a 1,2,5-telluradiazole heterocycle that forms [Te-N]$_2$ with short Te-N SBIs; this is consistent with short Te-N SBIs in [Te D] (Table 1.2) formed by 1,2-tellurazole heterocycles, 1,2-benzoisotellurazole (**6**)[53] and (**12**).[47]

Table 1.3 A-Te--D SBIs for which the Te-D distance is shorter than 80% of the sum of r_{vdW} in the [Te-m-D]$_2$ supramolecular synthon.

	Reference	Primary Structure	D	A	d_{SBI} (Å)	% Σr_{vdW}	a_{SBI} (°)	Tertiary structure
26	63	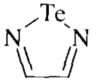	N	N	2.764	77	151.9	polymer
27	64	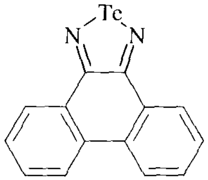	N	N	2.825	78	150.9	polymer
			N	N	2.842	79	151.2	
28	66	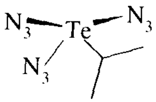	N	N	2.852	79	146.7	dimer
15	55		O	O	2.764	77	145.4	dimer
29	67	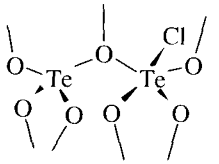	O	O	2.692	75	171.4	dimer
30	68	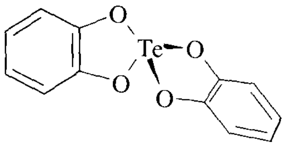	O	O	2.644	74	153.7	polymer
			O	O	3.285	92	138.4	
31	65	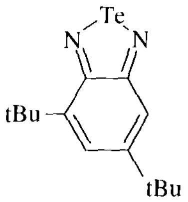	N	N	2.629	73	155.7	dimer

Figure 1.7 shows the histograms of SBI distances for the $[\text{Te-m-D}]_2$ supramolecular synthon classified according to the coordination number prior to SBI formation. Despite having significantly fewer occurrences, two-coordinate Te participates in more SBIs at distances shorter than 80% of the sum of r_{vdW}. This appears to be consistent with the implications of Bent's rule which states that "*Atomic s-character concentrates in orbitals directed toward electropositive substituents.*"[69] Thus, in a Te(IV) structure, the two most electronegative atoms will participate in the linear 3c-4e hypervalent bond as the high p-character will minimize the electron density on the central atom and maximize the electron density on the more electronegative peripheral atoms. The implications for SBI formation are illustrated with the following examples. If there are two N atoms in a structure where Te has a coordination number of 2, such as **26**, then they will necessarily bond to give a bent geometry that leaves the site opposite to the Te-N bond vacant and available to form SBIs. Even if there is only one electronegative atom (e.g., **6**) short SBIs can still form. Alternativly, in a system with a hypervalent bond, such as those observed in Te(IV) structures with disphenoidal geometries, the two most electronegative atoms, according to Bent's rule, will occupy positions that are opposite one another and have the least s-character (the hypervalent bond). Thus the potential SBI sites will be located opposite to the two least electronegative atoms which are positioned in the bent geometry. This means that there must be at least three Te-A bonds where A is N, O, F, CN or Cl (e.g., **28**) in order to ensure the optimal (A-Te--D collinear) geometry for strong Te-D SBI formation.

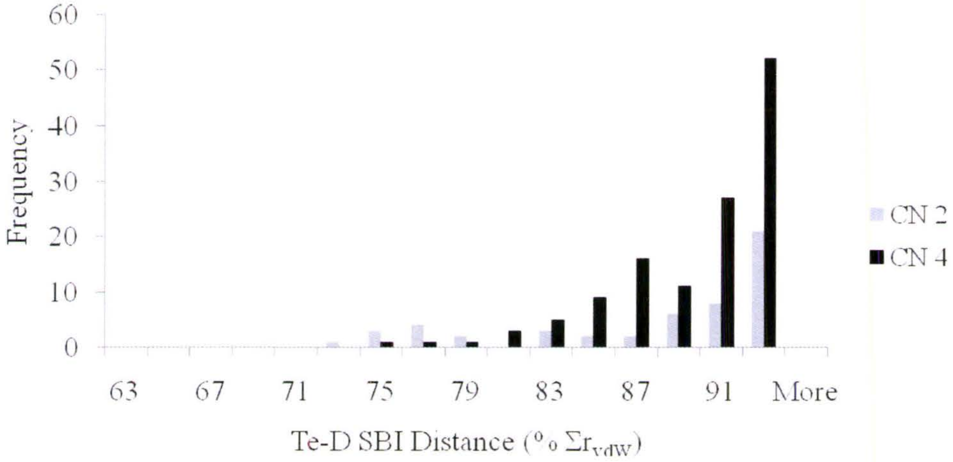

Figure 1.7 Distribution of Te-D interaction distances in [Te-m-D]$_2$ supramolecular synthons with coordination numbers 2 and 4 for Te before SBI formation.

The tertiary structures constructed by the [Te-m-D]$_2$ supramolecular synthons are more limited than those observed with [Te D]. This is probably due to a reduction in the number of degrees of freedom. The [Te-m-D]$_2$ supramolecular synthon leads predominantly to isolated dimers or 1D polymers. The 1D polymers can be divided into two categories as illustrated in Scheme 1.3, those in which a single tellurium center is part of two supramolecular synthons and those where two tellurium atoms are necessary for the formation of two supramolecular synthons. The latter case is more closely related to that of discrete dimers. Another interesting example is the cyclic trimer constructed by bis(pentafluorophenyl)-di-tellurium(I) (**44**) that forms a virtual 6-membered triangular prism with the [Te-D]$_3$ supramolecular synthon (Scheme 1.4).[70]

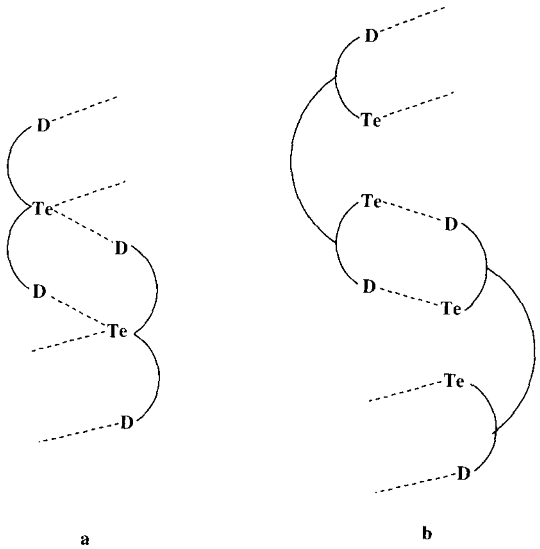

Scheme 1.3 Polymeric arrangements based on [Te-m-D]$_2$.

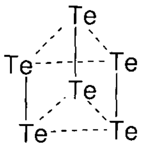

Scheme 1.4 [Te-D]$_3$ supramolecular synthon.

1.5.4 Supramolecular Synthons with Four Points of Attachment

1.5.4.1 [Te-m-Te-m-D]$_2$

This supramolecular synthon can also be regarded as two [Te-m-Te D] supramolecular synthons working cooperatively or a [Te-m-D]$_2$ supramolecular synthon with two peripheral SBIs. There are six examples of the [Te-m-Te-m-D]$_2$ supramolecular synthon, and these lead to isolated dimer or ribbon polymer tertiary structures. The shortest Te-D SBI distance (C-Te--O) is 82% of the sum of r_{vdW} and is found in the [Te-1-Te-5-O]$_2$ supramolecular synthon between bis((μ_2-phthalato-O,O')-(μ_2-oxo)-tetrakis(p-tolyl)-di-tellurium) p-xylene solvate (**33**).[51] Five of the molecules which associate to form [Te-m-Te-m-D]$_2$ have a μ_2-oxo bridged bistellurium(IV) motif (Scheme 1.5) in their primary structure.

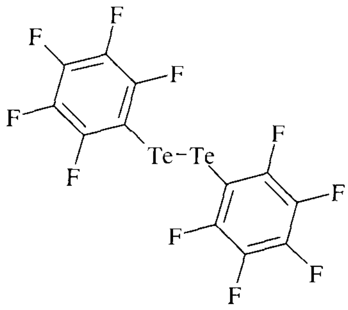

32

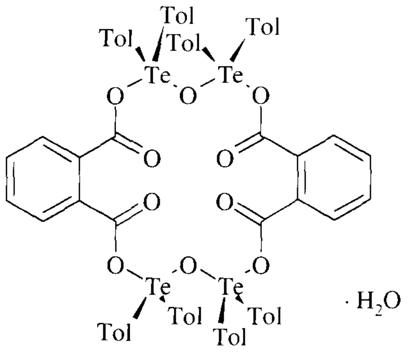

33

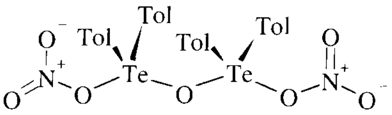

34

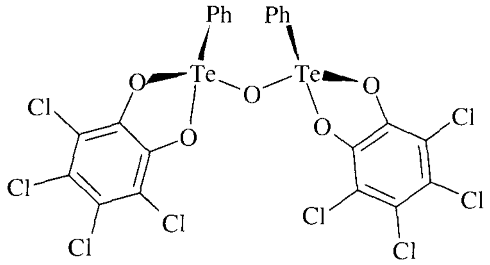

35

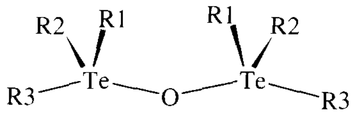

Scheme 1.5 General structure of μ_2-oxo bridged bistellurium(IV) compound.

1.5.4.2 [Te-m-Te-m-D-m-D]$_2$

This supramolecular synthon has been observed in four crystal structures with the shortest Te-D SBI distance (C-Te--O) at 78% of the sum of r_{vdW} between (μ_2-oxo)-bis(butane-1,4-diyl)-(dinitrato-O)-di-tellurium (**34**) in [Te-1-Te-2-O-1-O]$_2$.[71] Three of the crystals contain a μ_2-oxo bridged bistellurium(IV) motif (Scheme 1.5) within their primary structure and all three structures participate in the [Te-1-Te-2-O-1-O]$_2$ supramolecular synthon. [Te-m-Te-m-D-m-D]$_2$ can be viewed as a [Te-m-D]$_2$ supramolecular synthon with two peripheral [Te D] supramolecular synthons. In the known structures this supramolecular synthons generates tertiary structures of either dimers or ribbon polymers.

1.5.4.3 [Te-m-D-m-D]$_2$ or [D-m-Te-m-D]$_2$

This supramolecular synthon arises from a [Te-D]$_2$ supramolecular synthon with two additional peripheral SBIs or two [Te D-m-D] supramolecular synthons. It is observed in four crystal structures, three of which contain the [D-m-Te-m-D]$_2$ supramolecular synthon. In the known structures these supramolecular synthons only form dimers. The shortest SBI distance, 83% of the sum of r_{vdW} (O-Te--O), are observed in (μ_2-oxo)-bis((tetrachlorocatecholato-O,O')-phenyl-tellurium(IV)) tetrahydrofuran solvate (**35**) in the [Te-O-2-Cl]$_2$ supramolecular synthon.[72]

1.6 Summary

This survey of tellurium containing structures in the Cambridge structural database shows that tellurium centred SBIs appear to have an important role in the organization of the supramolecular structure in the solid state. Eight different tellurium-centered supramolecular synthons with one to four Te-D SBIs were identified. A detailed examination of the examples available for [Te D] confirmed the previous observations that the shortest SBIs are formed when D = O, N or Cl. Furthermore, the nature of the atom opposite the SBI is very important. The shortest SBIs also occur when O, N, Cl or CN are attached to Te opposite the SBI. Both of these observations are consistent with Alcock's qualitative bonding description. Molecules, such as 1,2,5-telluradiazoles, that have two of O, N, Cl or CN attached to the tellurium (in the equatorial positions for

Te(IV)) formed the shortest SBIs in supramolecular synthons with two points of attachment. Supramolecular synthons with more points of attachment should be inherently stronger than equivalent synthons with less points of attachment. Systems with a primary structure containing μ_2-oxo bridged bis-Te(IV) were found to lead to secondary structures with four points of attachment. The supramolecular synthons with four points of attachment could often be considered as $[\text{Te-m-D}]_2$ supramolecular synthons with two additional SBIs. The strong $[\text{Te-m-D}]_2$ supramolecular synthons can, in principle, be used as templates for the design of efficient supramolecular synthons with four points of attachment. Interestingly, aside from 1:1 adducts with solvents, there is a lack of supramolecular synthons formed by heteromolecular association. It is conceivable that complementary pairs could be developed to take advantage of molecular recognition in the construction of supramolecular structures.

1.7 1,2,5-Chalcogenadiazoles

Of the known tellurium containing supramolecular synthons listed in Section 1.5, the one that appears to maximize the number of SBIs and minimize the SBI distances is the $[\text{Te-m-D}]_2$ supramolecular synthon when D is N or O. The feature in the primary structure that most frequently assembles this supramolecular synthon with SBI distances less than 80% of the sum of r_{vdW} is the 1,2,5-telluradiazole ring. This suggests that structures containing such heterocycles would be convenient building blocks for supramolecular self-assembly.

This is the heaviest member of the family of 1,2,5-chalcogenadiazoles. The lighter analogues have been the subject of many studies because of their many actual and proposed applications, in addition to their sometimes unusual chemistry. In the case of the 1,2,5-chalcogenadiazole ring, the sulphur derivatives (**36**) can be used in antibacterial[73] and antiviral[72-77] agents, insecticides,[74] fungicides,[75] specialized polymers[74-77] and organic LEDs;[76-79] the corresponding selenium compounds (**37**) are also applicable as antibacterials,[76] fungicides,[75,77] and insecticides[74,77,78] in addition to dyes.[79-81]

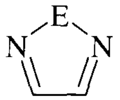

36 E = S
37 E = Se
26 E = Te

1.8 Purpose, Scope and Overview of the Thesis

This thesis documents the initial studies of a research program aimed at the development of supramolecular chemistry based on tellurium-centred SBIs, with the 1,2,5-telluradiazole heterocycle as the key feature of the building blocks. The goals of this project are to:

1. Probe the viability of 1,2,5-telluradiazoles as supramolecular building blocks by examining the resistance of the $[Te-N]_2$ supramolecular synthon to dissociation and/or distortion.

2. Provide an understanding of the molecular features that control the strength of the Te-N SBIs in the $[Te-N]_2$ supramolecular synthon.

3. Establish synthetic methods which can be easily adapted to the synthesis of a wide variety of derivatives of 1,2,5-telluradiazoles.

4. Establish which computational methods are appropriate for the study of the $[Te-N]_2$ supramolecular synthon and its supramolecular assemblies.

5. Identify new supramolecular structures that could be achieved by the use of the $[Te-N]_2$ supramolecular synthon.

6. Establish what properties of a material, if any, could be enabled or controlled by Te-N supramolecular association

Progress in these areas is presented as follows. Chapter 2 provides all of the experimental and computational details pertaining to the following chapters. A computational analysis of the nature of the SBIs in which these molecules participate is presented in Chapter 3. A synthetic method, that is applicable to a variety of 1,2,5-telluradiazoles, is provided in Chapter 4. The control of the $[Te-N]_2$ supramolecular synthon formation between 1,2,5-telluradiazole rings is explored in Chapter 5. Chapter 6 discusses the gas-phase studies of these heterocycles by means of ultraviolet photoelectron spectroscopy and laser desorption/ionization mass spectrometry. Chapter 7 provides the details of the parameterization of a force field for the $[Te-N]_2$ supramolecular synthon as well as its application to the design of new supramolecular structures. Chapter 8 highlights three different supramolecular materials in which the interesting material property arises from the formation of the $[Te-N]_2$ supramolecular synthon. Chapter 9 summarizes the impact of these results and presents an overview of some of the future research avenues suggested by the results of this work.

2 Experimental

2.1 Instrumental Methods

2.1.1 Fourier Transform Raman Spectroscopy

Sample Preparation

Samples were sealed in Pyrex melting point capillaries under a nitrogen atmosphere.

Data Acquisition and Processing

Spectra were recorded at ambient temperature using a Bruker RFS 100 spectrometer equipped with a quartz beam splitter, and a liquid-nitrogen-cooled Ge diode detector. The 1064-nm line of an Nd:YAG laser (350 mW maximum output) was used for excitation of the sample with a spot of ca. 0.2 mm at the sample using 10-300 mW of power and the back-scattered radiation was sampled. The actual usable Stokes range was 100-3500 cm^{-1} with a spectral resolution of 2 cm^{-1}. The Fourier transformations were carried out by using a Blackman-Harris four-term apodization and a zero-filling factor of 4. Acquisitions typically involved 800-2000 scans at 2 cm^{-1} as the samples were generally weakly scattering. A multi-point background correction was applied to the spectra.

2.1.2 Dispersive Raman Spectroscopy

Sample Preparation

Samples were sealed in Pyrex melting point capillaries under a nitrogen atmosphere. In cases of very weak scattering, the sample tube was opened and contents placed on a glass slide immediately prior to acquisition.

Data Acquisition

Spectra were acquired on a Renishaw inVia Raman microscope with the WiRE 3 software package at ambient temperature. The sample was excited with a 785-nm laser source (Renishaw HPNIR785) using 30 mW of power using a 1200 lines/nm grating. Typically 10, 10 second scans were averaged to produce the final spectrum. A multi-point background correction was applied to each spectrum.

2.1.3 Infrared Spectroscopy

Sample Preparation

Samples were prepared in the glove box under nitrogen as either compressed KBr or polyethylene pellets. Samples were transported under nitrogen to the instrument and placed in a nitrogen purged sample housing.

Data Acquisition

IR spectra were recorded at room temperature using a Bio-Rad FTS-40 FT-IR spectrometer. Each spectrum was acquired with a resolution of 4 cm^{-1} in the region of 4000-400 cm^{-1} and the background, which was simultaneously subtracted, was recorded prior to a spectral acquisition. A multi-point background correction was applied to the spectra.

2.1.4 Solution Ultraviolet-Visible Spectroscopy

The ultraviolet-visible (UV-vis) absorption spectra were measured through quartz cuvettes on a Varian Cary 50 spectrometer in dual beam mode by scanning from 200-800 nm with a scan rate of 10 nm/s. The solvent background was manually subtracted.

2.1.5 Solid Ultraviolet-Visible (Diffuse Reflectance) Spectroscopy

The diffuse-reflectance spectra were measured with an illuminated (tungsten-halogen light source) integrating sphere (Ocean Optics ISP-REF Integrating Sphere) attached to a photodiode array spectrophotometer (Ocean Optics SD 2000) and are reported relative to a PTFE standard (Ocean Optics WS-1). Each measurement was an average of 100 scans that were integrated over 3 ms using a boxcar smoothing of 10 points and was corrected for stray light and dark current.

2.1.6 Nuclear Magnetic Resonance Spectroscopy

Sample Preparation

A typical sample was prepared by dissolving 15 mg of compound in 0.7 mL of a deuterated solvent. Benzotelluradiazoles generally were less soluble and were prepared in lower concentration using solvents dried over 4 Å molecular sieves.

Data Acquisition

Low field: A Bruker Avance 200 (200.13 MHz) spectrometer was used to acquire routine low-field NMR spectra at ambient temperature. A 5-mm QNP ('quad') probe was used for ^{1}H, ^{13}C{^{1}H} and ^{19}F spectra operating in locked mode using the deuterium signal from the solvent; typical acquisition parameters are presented in Table 2.1. The ^{1}H and ^{13}C{^{1}H} spectra were referenced to TMS using the deuterated solvent peaks as secondary references. Ambient temperature spectra of $CFCl_3$ were used to reference ^{19}F samples.

High field: A Bruker DRX 500 (500.13 MHz) spectrometer was used to acquire high field nuclear magnetic resonance spectra. A Bruker 5-mm broad band inverse probe was used to acquire ^1H spectra and a 10-mm broad band probe was used to acquire $^{13}C\{^1H\}$ and ^{125}Te spectra. Variable temperature spectra were acquired using either a cold or ambient temperature gas flow with a BV-T 2000 variable temperature controller. In experiments where an accurate temperature measurement was necessary a chemical shift thermometer was employed; methanol for 178-330 K and glycerol for 273-416 K.[82] All samples were run locked to the deuterium signal of the solvent if applicable. The ^1H and $^{13}C\{^1H\}$ spectra were referenced to TMS using the deuterated solvent peaks as secondary references. A 3.73×10^{-4} M solution of Ph_2Te_2 in CH_2Cl_2 (δ 420.36 ppm) previously referenced to Me_2Te (δ 0.0 ppm) was used as an external reference for ^{125}Te samples. Unless otherwise indicated, the spectra were obtained at 303 K. The typical acquisition parameters are presented in Table 2.1.

Table 2.1. Summary of the typical acquisition parameters used for NMR spectroscopy

Acquisition Parameter	^1H	^1H	^{13}C	^{13}C	^{19}F	^{125}Te
B_o (T)	4.7001	11.746	4.7001	11.746	4.7001	11.746
SF [MHz]	200.130	500.130	50.322	125.758	188.310	157.790
TD [K]	16	32	16	32	32	32
SW [kHz]	2.6	6.8	12.5	29.0	39.6	94.3
Hz/pt	0.159	0.207	0.767	0.880	1.207	2.879
PW [μs]	8.15	6.70	4.95	13.50	5.00	9.00
NS	8-64	8-64	1000-100000	1000-50000	64	1000-10000

Data Processing

Data was processed with the XWINNMR software. In all cases the free induction decay (FID) was processed with exponential multiplication and zero-filling before being Fourier transformed. For ^{125}Te NMR, the line broadening parameter was modified as necessary. Chemical exchange data was obtained by modeling the line shapes of exchanging species in the appropriate spectra using the Mexico software.[83]

2.1.7 Photoelectron Spectroscopy

Sample Preparation

The samples were transferred into the sample cell in a glove box with an argon atmosphere. The sample cell was transferred into the spectrometer through an attached port.

Data Acquisition

Photoelectron spectra were recorded with an in-house-built instrument featuring a 36-cm hemispherical analyzer (McPherson), custom-designed sample cells and detection and control electronics. The electron detection and instrument operation are interfaced to a National Instruments PCIe-6259 multi-function data acquisition card and custom software. The samples were ionized with He I radiation (21.21 eV); the $^2E_{1/2}$ ionization of methyl iodide (9.538 eV) was used for calibration of the ionization-energy scale and the Ar $^2P_{3/2}$ ionization (15.759 eV) used as the internal energy scale lock during collection. The instrument resolution (measured using FWHM of the argon $^2P_{3/2}$ peak) was 0.020 eV during data collection. The sample cells were placed in the instrument and collected at the temperature (monitored with a “k”-type thermocouple passed through a vacuum feed-through and attached directly to the sample cell) at which the sample produced sufficient vapour pressure ($\geq 10^{-4}$ Torr) for measurements: 25 °C for both benzo-2,1,3-thiadiazole and benzo-2,1,3-selenadiazole; and 60-90 °C in 10 °C increments for benzo-2,1,3-telluradiazole.

Data Processing

All of the data were intensity corrected with an experimentally determined instrument analyzer sensitivity function that assumes a linear dependence of analyzer transmission (intensity) to the kinetic energy of the electrons within the energy range of these experiments. The ionization bands were fitted to asymmetric Gaussian peaks over a three point baseline with the WinFP software package.[84] The bands were defined by their position, amplitude, half-width for the high binding energy side of the peak, and the half-width for the low binding energy side of the peak. The peak positions and half-widths were reproducible to about ±0.02 eV (3σ level). The fitting procedures used in this work are described in more detail elsewhere.[84]

2.1.8 Electron Impact Mass Spectrometry

Sample Preparation

Samples were introduced into a capillary as a dilute solution. The solution was left to dry before introduction into the mass spectrometer. Samples that were prone to hydrolysis were sealed as a solid in a capillary under nitrogen. The capillary was opened immediately before acquisition.

Data Acquisition

Both low and high resolution electron-impact mass spectrometry was performed on a Micromass GCT (GC-EI/CI Time of Flight) Mass Spectrometer in probe mode. The sample was introduced directly into the ionization chamber in a shortened borosilicate capillary on a probe. The sample was heated by ramp to 300 °C; the temperature range that exhibited the most intense parent ion peaks was used for acquisition. The sample was ionized by a 70 eV electron stream. The positively charged ions were detected by a time-of-flight detector. The final spectrum consisted of the time averaged spectra from regions of the chromatogram where the desired signal was maximized without saturating the detector.

2.1.9 Laser Desorption/Ionization Mass Spectrometry

Sample Preparation

All sample preparation took place in a nitrogen atmosphere glove box. The samples were either sublimed onto a stainless steel plate, deposited on the plate with a coating of low viscosity perfluorinated oil, pressed onto the plate or deposited on the plate as intact crystals. The plate was transferred to spectrometer in a sealed polyethylene bag. An argon filled glove bag was affixed to the spectrometer port to allow for the transfer of the steel plate into the ionization chamber of the spectrometer.

Data Acquisition

The spectrometers used for the measurements were the Micromass TOF-Spec 2/e spectrometer or the Micromass Micro-MX Measurements were performed in *reflectron* mode with low mass bias for the range of 10-2000 m/z. The pulse voltage was set to 1970 and the detector voltage was set to 2350. The instrument was run with a positive polarity and the TOF detector was calibrated using peaks from a mixture of three peptides (Renin Substrate, Substance P and ACTH) and the matrix, α-cyano-4-hyfroxy-cinnamic acid. A linear calibration was determined using the peaks at m/z 172.03, 212.03, 379.09, 1347.74 and 1758.93. The TOF detector was calibrated before each set of samples was run. The laser intensity was increased until sample signal was maximized without saturating the detector.

2.1.10 Elemental Analysis

Elemental analyses were performed either by Guelph Chemical Laboratories Inc. (Guelph, Ontario, Canada) or in house.

The in house samples were run on a Thermo EA1112 CHNS/O analyzer using a pre-packaged Ox/Red quartz reactor for CHNS determinations (Thermo EA 46802015). The samples were combusted using oxygen at 900 °C. He (120 mL/min) was used as a carrier gas to transport the H_2O, NO_2 and CO_2 through a 2 m CHNS/NCS separation column at 75 °C to a thermoconductivity detector. The system was standardized for N, C and H with atropine.

2.1.11 Melting Points

Melting points were measured on a Thomas-Hoover melting point apparatus and reported uncorrected.

2.1.12 Thermogravometric Analysis and Differential Scanning Calorimetry

TGA and DSC were measure at the Brockhouse Institute for Materials Research (BIMR) thermal analysis lab using a simultaneous DTA/DSC/TGA (Netzsch STA 409) instrument with an argon atmosphere. The DSC data was obtained with a heating rate of 15 °C/min over a temperature range of 35 to 300 °C and the TGA data was obtained with a heating rate of 5 °C/min over a temperature range of 35 to 300 °C

2.1.13 Crystallography: Single Crystal

Sample preparation: Samples were handled in either a low-viscosity perfluoropolyether oil using the cryotechnique described by Håkansson[85] or handled at room temperature coated in Paratone-n oil. Crystals were mounted on nylon loops (Hampton, CA) or MiTeGen Micromounts (Ithica, NY) using either a perfluoropolyether glass or Paratone-n oil.

Data Acquisition

Redundant data sets were collected on one of the four following instruments:

1) A P4 Bruker diffractometer upgraded with a Bruker SMART 1K CCD detector and a rotating anode utilizing Mo–Kα radiation (λ= 0.71073 Å, graphite monochromator) equipped with an Oxford cryostream 700 low temperature accessory

2) A SMART APEX II diffractometer utilizing Mo–Kα radiation (λ= 0.71073 Å, graphite monochromator) from a fine-focus sealed X-ray tube with a CCD area detector and equipped with an Oxford cryostream 700 low temperature accessory

3) A STOE IPDS II diffractometer utilizing Mo–Kα radiation (λ= 0.71073 Å, pane graphite monochromator) from a sealed X-ray tube (12 x 0.4 mm long - fine focus) with a 24 cm diameter image plate detector

4) A Bruker SMART 6K CCD area-detector three-circle diffractometer with a Rigaku Rotating Anode (Cu-Kα radiation, λ = 1.54178 Å) with a CCD detector.

The diffractometer and crystal-to-detector distance used for each sample is provided in Table 2.2 and Table 2.3.

Data Treatment

Typically, after a sufficient number of frames were collected the reciprocal lattice was visualized with RLATT[86] or the reciprocal lattice viewer in the APEX 2 software suite.[87] If the data consisted of only one set of reflections a preliminary unit cell and orientation matrix was determined from this raw data. If there were non-overlapping or partially overlapping domains in the data, the cell parameters and orientation matrices were determined using either Gemini[88] or CELL_NOW.[89] The complete dataset was integrated using either SAINT[90] or the integration feature of the APEX 2 software suite. The final cell parameters were obtained by refinement on the positions of the integrated reflections with $I > 10\sigma(I)$. For data that contained multiple domains, the cell parameters were refined separately. If the minor fraction(s) did not have sufficient intensity to provide adequately refined cell parameters then the data was reintegrated holding the unit cell parameters of the minor equal to those of the major fraction. The data was empirically corrected for absorption and other effects using with either TWINABS,[91] SADABS[92] or the absorption correction feature in the APEX 2 software suite. The only exception was for the data collected on the STOE diffractometer which was corrected for absorption and other effects by integration with the STOE X-RED software.[93] The specific details regarding the data treatment for each sample is given in Table 2.2 and Table 2.3. The structures were solved by direct methods using SHELXS[94] and refined by full-matrix least squares on all F^2 data using SHELXL[94] as part of the WinGX software package.[95] The non-H atoms were refined anisotropically, while H atoms were constrained to idealized positions using appropriate riding models. Restraints were only employed when a high degree of twinning affected the behaviour of the thermal parameters. In all cases it was insured that only the minimum number of restraints was employed and the number of restraints was kept below the number of refined parameters. Molecular graphics were produced using either ORTEP-3,[96] Mercury 1.4[97,98] or Mercury 2.2.[99] Crystallographic information files have been included on electronic supplementary information CD.

2.1.14 Crystallography: Powder

Sample Preparation

Samples were placed sealed under nitrogen in a special soda glass capillary tube (bore diameter 0.3 or 0.5 mm). The capillaries were tamped in order to compress the samples in the end of the tube.

Data Acquisition

Data for **46**, α-**41** and β-**41** were acquired on a Bruker SMART 6K CCD area-detector three-circle diffractometer with a Rigaku Rotating Anode (Cu-Kα radiation, $\lambda = 1.54178$ Å) with a CCD detector at ambient temperature. The raw image data was unwarped with SMART[90] and then integrated around χ using GADDS.

Higher spatial resolution data for β-**41** was collected by Dr. Pamela Whitfield at the National Research Council of Canada at 173 K on a Bruker-AXS D8 Advance diffractometer using a primary Goebel mirror with a 0.6 mm exit slit and a Vantec PSD detector. The detector was equipped with radial Soller slits, and was used with a 3° detector window. The Cu-Kα radiation was used, but no Ni filter was necessary because the primary mirror removes the Kβ component.

Table 2.2 Summary of crystallographic details for structures presented in Chapters 4 and 5.

	40·2HCl	**40**	**46**	**46**·DMSO	**43**·HCl·⅓Py	**47**	**48**
Instrument	2	1	1	1	1	3	1
Crystal-to-detector distance (cm)	4.945	4.993	4.999	4.999	4.999	10.0	4.999
Preliminary Orientation	APEX2	Gemini	Gemini	SMART	SMART	STOE X-AREA	SMART
Integration	APEX2	SAINT	SAINT	SAINT	SAINT	STOE X-AREA	SAINT
Absorption	APEX2	TWINABS	SADABS	SADABS	SADABS	STOE X-RED	SADABS

Table 2.3 Summary of crystallographic details for structures presented in Chapter **8**.

	α-**41**	**41**·Py	**84**	**50**	**86**	**39**$_2$·**87**	**40**$_2$·**87**
Instrument	2	2	2	1	2	2	2
Crystal-to-detector distance (cm)	4.982	4.9	4.947	4.994	4.958	4.958	4.958
Preliminary Orientation	CELL_NOW	APEX2	APEX2	CELL_NOW	CELL_NOW	CELL_NOW	CELL_NOW
Integration	APEX2	APEX2	APEX2	APEX2	APEX2	APEX2	APEX2
Absorption	TWINABS	APEX2	APEX2	TWINABS	TWINABS	TWINABS	TWINABS

2.1.15 Second Harmonic Generation

Sample Preparation

Solid samples were carefully ground using an agate mortar to achieve uniform particle size. Sample pellets were pressed by hand between two stainless-steel anvils in a 7-mm die. The thickness and position of the pellet within the die was controlled carefully by a 1.2 mm spacer. The casting die was also used as the pellet holder in the experiment. Excess pressure was avoided to maintain the particle size and reduce preferential orientation.

Instrumentation

A custom-built harmonic-light spectrometer[100] was employed for these measurements. The layout of the optics for the modified Kertz-Perry experiment is shown in Figure 2.1. An Nd:YAG laser (Continuum Surelite II^{TM}) was used as the light source. This system delivered IR pulses with a repetition frequency of 10 Hz, a width of 5-7 ns, producing up to 655 mJ of energy at a wavelength of 1064 nm. The combination of an iris, a half-wave achromatic retarder and a polarizer was used to modulate the intensity of the laser (I_ω), which was monitored by a photodiode with a 177 ps rise time (Newport Model 818-BB-30) and a beamsplitter. The intensity of light scattered in the visible was measured with an end-on photomultiplier tube (Oriel 773346) with an operating range of 185-850 nm, a gain above 5×10^5, a responsivity of 3.4×10^4 A/W and a rise time of 15 ns. This detector received light through an assembly consisting of an 850 nm cut-off short-pass filter (CVI); a crown-glass plano-convex lens of diameter 25.4 mm and focal length 50 mm; and an interferential filter (CVI) centered at 532 nm, with a nominal 10 nm FWHM spectral band. The photomultiplier tube (PMT) was normally operated under a 1000 V bias provided by a regulated power supply (Oriel 70705). The PMT output was delivered to a 350 MHz voltage amplifier (Oriel 70723). The responses of the two detectors were independently calibrated with a power meter (Melles Griot 13PEM001). The response of each detector was kept within its calibration range by means of neutral density filters (CVI) and measured with a boxcar integrator (Stanford Research 250). The boxcar integrator output was acquired with a digital oscilloscope card (National Instruments NI 5112 PCI) installed in a PC and controlled with custom LabView Virtual Instrument software.

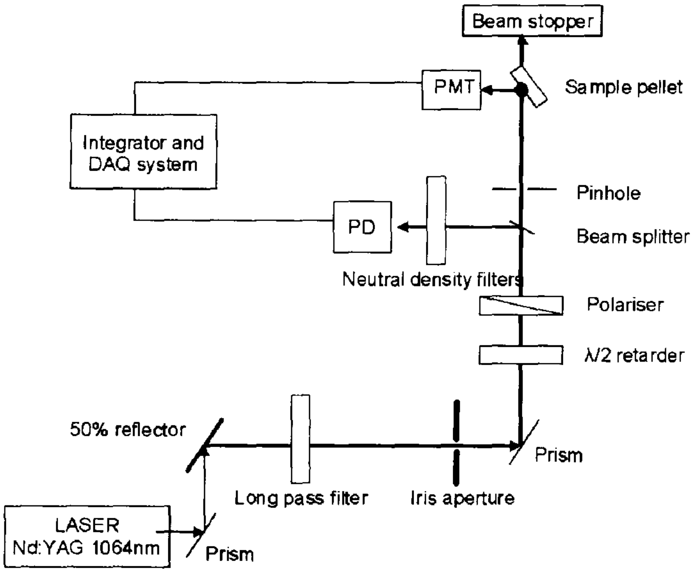

Figure 2.1 Schematic of the Kertz-Perry SHG experiment.

Data Processing

The averaged intensity of the signal ($I_{2\omega}$) was fitted to eq 2.1 where I_{ω} is the averaged intensity of the pump measured at the reference photodiode, and $d_{eff} = ½\, \chi^{(2)}$. The calibration factor, K, was determined with standard samples of KDP.

$$I_{2\omega} = K\, d_{eff}^2\, I_{\omega}^2 \qquad 2.1$$

2.2 Materials and Methods

All materials are reagent grade unless otherwise indicated. Acetone (Caledon), benzene (Caledon), benzo-2,1,3-thiadiazole (Aldrich) (**38**), boron trifluoride diethyl etherate (Aldrich), bromine (Aldrich), chlorine (Aldrich, ≥ 99.5%), cobaltous chloride hexahydrate (Anachemica), 3,4-diaminobenzophenone (Aldrich) (**85**), diaminomaleonitrile (Aldrich), 5,6,-dichloro-1,2-diaminobenzene (Aldrich), ethanol (Commercial Alcohols Inc., anhydrous), hydrobromic acid (Fisher, 47-49%), magnesium turnings (EM Science), pyrazine (Aldrich), selenium(IV) oxide (Alfa-Aesar), sodium borohydride (Aldrich), tellurium (CERAC, 200 mesh, 99.5%), 7,7,8,8-tetracyanoquinodimethane (Aldrich) (**87**) and 3,4,5,6-tetrafluoro-1,2-diaminobenzene (Butt Park Ltd.) were used without any further purification. 1,2-Diaminobenzene (Aldrich) was purified according to literature procedure.[101] Bromobenzene (Aldrich), diethyl ether (Caledon), dimethyl sulphoxide (Caledon), pentane (Caledon), pyridine (Fisher) and triethylamine (Anachemica) were dried according to literature procedure[101] and stored over type 4Å molecular sieves. Acetonitrile (Caledon, HPLC grade), dichloromethane (Caledon, HPLC grade), tetrahydrofuran (Caledon, HPLC grade) and toluene (Caledon, HPLC grade) were purified on an IT solvent purification system and stored over type 4Å molecular sieves.

$TeCl_4$,[102] benzo-2,1,3-selenadiazole (**39**),[103] 4,7-dibromobenzo-2,1,3-thiadiazole (**44**),[104] 3,6-dibromo-1,2-phenylenediamine,[105] 4,5,6,7-tetrabromobenzo-2,1,3-

thiadiazole,[106] triphenyl borane,[107] and *N*-(triphenylboryl)pyrazine[108] were prepared according to established literature procedures.

The manipulation of air-sensitive materials was performed under an atmosphere of dry argon or nitrogen with standard Schlenk and glovebox techniques.

2.2.1 Syntheses

2.2.1.1 Telluradiazoles

The telluradiazoles were prepared using a modification of Zibarev's procedure.[109] The reaction of $TeCl_4$ with the appropriate diamine in pyridine was followed by the addition of a strong base. Two methods are given, the second is an improvement upon the first.

Method 1: In a typical reaction, $TeCl_4$ (5.00g, 18.5 mmol) was dissolved in 275 mL of pyridine. This was added dropwise with stirring to a solution of the diamine (92.8 mmol) in 175 mL of the same solvent. The mixture was stirred for 10 min and an excess of Et_3N (15 mL) was added. Stirring was maintained for 1 h before removing the solvent under vacuum. The residue was first separated from the $Et_3N{\cdot}HCl$ by density. The residue was recrystallized from DMSO and washed with toluene. The product obtained in this way can be further purified by successive steps of recrystallization and/or sublimation.

Method 2: In a typical reaction, $TeCl_4$ (1.00 g, 3.7 mmol) was dissolved in 25 mL of pyridine. This was added dropwise with stirring to a solution of the diamine (3.7 mmol) in 15 mL of the same solvent. The mixture was stirred for 5 min and three equivalents of Et_3N (11.1 mmol, 1.5 mL) were added. Stirring was continued for 10 min.

Toluene was added to the mixture to precipitate the product. The precipitate was washed with 15 mL of toluene three times. The product was recrystallized from pyridine and washed with toluene. The desired product was separated from the $Et_3N{\cdot}HCl$ by density. If an insoluble black impurity persisted it was removed by washing with a mixture of pentane and acetonitrile; the telluradiazole migrated to the upper pentane layer while the black solid sank to the bottom of the acetonitrile layer. The product obtained in this way can be further purified by sublimation under vacuum.

$TeN_2C_6H_4$ (40): Method 1: Yield: 2.3 g (0.0098 mol, 53%). Orange crystals suitable for X-ray diffraction were grown from a DMSO solution. Anal. Calcd. for $TeN_2C_6H_4$: C, 31.10; H, 1.74; N, 12.09; Found: C, 31.36; H, 1.54; N, 12.35. ^1H NMR (200 MHz, d_6-DMSO): δ 7.50, 7.48, 7.47, 7.45, 7.26, 7.24, 7.22, 7.20 (AA'BB', 4H, aryl). $^{13}C\{^1H\}$ NMR (50 MHz, d_6-DMSO): δ 166.58 (aryl, 4°); 128.68, 128.16 (aryl, CH). ^{125}Te NMR (158 MHz, $TeMe_2$): δ 2403. Raman (cm^{-1}): 3061 (26), 3053 (30), 3045 (29), 1511 (28), 1440 (100), 1350 (26), 1343 (31), 1304 (78), 1285 (21), 1203 (18), 1153 (18), 1148 (23), 1132 (27), 982 (21), 938 (20), 799 (27) 702 (25), 691 (71), 593 (18), 545 (42), 472 (24), 299 (52). IR (cm^{-1}): 3067m, 3053m, 3008m, 1508s, 1150m, 1132w, 902w, 778w, 731vs, 702m, 685vs. MS (EI, %): *m/z* 233.9437 (M^+, 10), 129.9121 (M^+-C6H_4N_2, 10).

$TeN_2C_6H_2Br_2$ (46): Method 1: Yield crude 1.1 g (0.0027 mol, 92%); after recrystallization 0.51 g (0.0012 mol, 43%). Orange crystals suitable for X-ray diffraction were grown from a DMSO solution. Anal. Calcd. for $TeN_2C_6H_2Br_2$: C, 18.50; H, 0.52; N, 7.19; Found: C, 18.77; H, 0.69; N, 6.88. ^1H NMR (200 MHz, d_6-DMSO): δ 7.54 (s, 2H, aryl). ^{13}C NMR: The sample was not soluble enough to give a solution NMR spectrum.

^{125}Te NMR (158 MHz, $TeMe_2$): δ 2368. Raman (cm^{-1}): 3047 (29), 3021 (29), 1479 (61), 1371 (100), 1350 (30), 1227 (32), 1077 (33), 830 (26), 725 (28), 701 (41), 662 (65), 577 (29), 554 (34), 325 (42). IR (cm^{-1}): 3063w, 3049w, 3020m, 1860w, 1656w, 1585w, 1476m, 1350w, 1329m, 1163s, 1076m, 921s, 890s, 831s, 725s, 702m, 577m, 549m, 431vs . MS (EI, %): *m/z* 389.7621 (M^+, <1), 265.8798 (M^+-Te, 100)

$TeN_2C_6F_4$ (41): Method 2: Yellow solid; yield after sublimation 0.07 g (0.23 mol, 84%), Mp > 200 °C. Red crystals suitable for X-ray diffraction were grown by sublimation at 130 °C in a sealed tube at 30 mTorr; yellow crystals suitable for X-ray diffraction were grown from a pyridine solution at -24 °C. ^{19}F NMR (188.3 MHz, d_6-DMSO): δ -148.96, -149.00, -149.04, (dd, 2F, aryl); -161.65-161.69, -161.74, (dd, 2F, aryl). Raman (cm^{-1}): 1342 (21), 1331 (25), 683 (77), 631 (8), 456 (8), 446 (12), 333 (14), 312 (12), 250 (9), 221 (100), 162 (8), 106 (9). IR (cm^{-1}): 1677m, 1634m, 1600m, 1519vs, 1460m, 1384m, 1373m, 1339w, 1226w, 1037m, 1016m, 970w, 944s . MS (EI, %): *m/z* 305.9061 (M^+, 30).

$TeN_2C_6H_2Cl_2$ (50): Method 2: Red-purple solid; yield: after recrystallization 0.13 g (0.43 mmol, 76 %). mp > 200 °C. Red-purple crystals suitable for X-ray diffraction were grown from a pyridine solution. ^{1}H NMR (200 MHz, d_6-DMSO): δ 7.86, (s, 2H, aryl). Raman (cm^{-1}): 1487 (10), 1476 (11), 1415 (32), 1349 (13), 1273 (56), 725 (7), 691 (55), 642 (7), 505 (10), 483 (9), 380 (4), 344 (15), 327 (7), 285 (7), 274 (19), 237 (66), 210 (5), 192 (20), 179 (55), 154 (13), 128 (20), 115 (100). IR (cm^{-1}): 1487s, 1478m, 1417s, 1343m, 1270s, 1085vs, 979m, 852s, 84s, 825s, 727vs, 645w, 482m, 452vs. MS (EI, %): *m/z* 301.8645 (M^+, 20).

$TeN_2C_{13}H_9O_1$ (86): Method 2: Orange crystalline solid; yield: after recrystallization 0.23 g (0.48 mol, 86 %), mp > 200 °C. Red/orange crystals suitable for X-ray diffraction were grown by sublimation at 110 °C in a sealed tube at 30 mTorr. ^{1}H NMR (200 MHz, d_6-DMSO): δ 7.86, 7.82, 7.74, 7.72, 7.67, 7.63, 7.60, 7.56 (8H, m). ^{13}C{^{1}H} NMR (50 MHz, d_6-DMSO): δ 132.5 (1C, 3°); 131.1 (1C, 3°), 129.3 (2C, 3°), 128.4 (2C, 3°), 128.1 (1C, 3°), 125.6 (1C, 3°). Raman (cm^{-1}): 1641 (43), 1597 (22), 1488 (16), 1427 (52), 1347 (23), 1326 (33), 1298 (52), 1139 (16), 1115 (17), 1025 (12), 996 (17), 788 (5), 754 (8), 689 (95), 562 (20) 399 (26), 338 (20), 305 (15), 274 (11), 214 (100), 165 (35). IR (cm^{-1}): 3056w, 1642vs, 1595m, 1577w, 1516w, 1493w, 1446m, 1433w, 1329s, 1310m, 1301m, 1238s, 1175w, 1141w, 1117w, 960w, 940w, 890s, 883m, 822m, 805m, 791m, 718vs, 705m, 682m, 630w, 594w, 565w, 509w, 439m. MS (EI, %): *m/z* 337.9678 (M^+, 50). X-ray quality crystals were grown by sublimation under static vacuum at 120 °C.

TeN_4C_4 (84): $TeCl_4$ (0.10 g, 0.37 mmol) was dissolved in 3 mL of pyridine. This was added dropwise with stirring to a solution of the diamine (0.04, 0.4 mmol) in 3 mL of the same solvent. The mixture was stirred for 5 minutes and excess Et_3N (3 mmol, 0.5 mL) was added. Stirring was continued for 10 minutes and the solution was filtered. A yellow solid was precipitated from the filtrate at -20 °C and filtered off. The final product was sublimed under dynamic vacuum (60 mTorr) at 100°C to give a yellow powder. Yield after sublimation 0.06 g (0.3 mmol, 90%). mp 130 °C (dec). Yellow crystals suitable for X-ray diffraction were grown from a pyridine solution at -24 °C. ^{13}C{^{1}H} NMR (50 MHz, d_6-DMSO): δ 141.2 (4°); 119.3 (CN). ^{125}Te NMR (158 MHz, $TeMe_2$): δ

2408. Raman (cm^{-1}): 2224 (56), 1397 (88), 1262 (13), 683 (100), 538 (27) 462 (14), 311 (61). IR (cm^{-1}): 2226m, 1513vs, 1390m, 1264vs, 1106vs, 705vs, 693vs, 576vs. MS (EI, %): *m/z* 233.9181 (M$^+$, 20), 181.9137 (M$^+$-2CN, 20), 129.9027 (Te$^+$, 100). X-ray quality crystals were grown from pyridine at -20 °C.

2.2.1.2 Other Compounds

$TeN_2C_6H_4$·2HCl (40·2HCl): A solution of $TeCl_4$ (0.10 g, 0.37 mmol) in 5 mL of toluene was added dropwise with stirring to a solution of *o*-phenylenediamine (0.20 g, 1.85 mmol) in 5 mL of the same solvent. An orange solid precipitated mixed with the colorless diamine hydrochloride. The solution was decanted from the precipitate. Most of the diamine hydrochloride was removed by suspending the crude product in bromobenzene and, after allowing the mixture to stand for 25 min, skimming off the floating fraction. This procedure afforded 0.18 g of product. However, a small amount of the diamine salt remained as a contaminant. Orange/red crystals suitable for X-ray diffraction were grown by sublimation at 85 °C in a glass tube sealed under vacuum (30 mTorr). M.p. 120 (dec.) ^{1}H NMR (500 MHz, 298 °C, *d*$_6$-DMSO): δ 7.03, 6.67 (AA'BB', 4H, aryl). ^{13}C{^{1}H} NMR (125 MHz, 298 °C, *d*$_6$-DMSO): δ 142.64 (aryl, 4°), 122.73, 120.41 (aryl, CH). IR (cm^{-1}): 3408m, 3334w, 3255w, 2920vs (broad), 2853vs (broad), 2607s, 1626s, 1537s, 1528s, 1513m, 1496vs, 1366w, 1318w, 1295w, 1167vs, 1136vs, 1095vs (broad), 844s, 763vs, 673w, 651w, 630w, 611w, 529w, 473m, 451s. HRMS (EI, %): *m/z* 233.9441 (M$^+$-2HCl, 50), 129.9118 (M$^+$-$C_6H_6N_2Cl_2$, 100).

$C_{12}H_{10}N_4$ (43): The solvent was removed from the reaction of **40**·2HCl which was contaminated with 1,2-diaminobenzene hydrochloride. The product was dissolved in

DMSO (1 mL) and heated at 60 °C overnight. The reaction mixture was added to water and neutralized. The final product precipitated and was separated by filtration giving the final product in 94% yield with respect to the diamine starting material. The final product was stored under nitrogen away from light. X-ray quality crystals of the hydrochloride salt were grown from the reaction mixture dissolved in pyridine. The identity of the product was confirmed by NMR:[110] ^{1}H NMR (200 MHz, 298 °C, d_6-DMSO): δ 7.52 (m, 2H, aryl), 7.87 (m, 2H, aryl), 6.91 (s, 2H, aryl), 6.24 (s, 4H, NH_2).

$TeN_2C_6H_4 \cdot B(C_6H_5)_3$ (48): A solution of BPh_3 (0.021g, 0.087 mmol) in 5 mL toluene was added to a suspension of **40** (0.020g, 0.087 mmol) in 5 mL toluene. The mixture was heated until dissolved. After cooling, the volume was reduced. The crystals were filtered to give a yield of 0.028g (68%); mp. 184-186°C X-ray quality crystals of **48** were obtained by recrystallization from a saturated toluene solution. Anal Calcd. for $Te_1N_2B_1C_{24}H_{19}$: N, 5.91%; C, 60.79%; H, 4.04%. Found: N, 6.30%; C, 59.73%; H, 3.92%. Raman (cm^{-1}): 1585 (8), 1514 (18), 1436 (87), 1358 (7), 1312 (100), 1159 (17), 1026 (8), 825 (16), 719 (22), 589 (14), 554 (31), 344 (10), 310 (41), 235 (21). IR (cm^{-1}): 3059m, 3036m, 3005m, 2992m, 1586m, 1516m, 1486m, 1428s, 1351m, 1307w, 1261m, 1159s, 1139m, 1115w, 1068w, 1031m, 998m, 925w, 911m, 872w, 860m, 820m, 796w, 753s, 746vs, 741vs, 706vs, 640s, 618m, 609m, 584s, 548w, 480m. ^{1}H NMR (500 MHz, d_6-benzene): δ 6.950, 6.240 (broad, 4H, **40** aryl), 7.715, 7.702 (d, 6H, BPh_3 aryl), 7.315,7.302, 7.287 (dd, 6H, BPh_3 aryl), 7.270,7.256,7.241 (t, 3H, BPh_3 aryl). ^{1}H NMR (500 MHz, d_6-benzene 333K): δ 7.043, 7.035, 7.030, 7.024, 6.330, 6.325, 6.316, 6.311 (4H, **40** aryl), 7.642, 7.628 (d, 6H, BPh_3 aryl), 7.268, 7.255, 7.240, 7.220 (multiplet, 9H,

BPh_3 aryl). ^1H NMR (500 MHz, d_8-toluene): δ 7.000, 6.270 (broad, 4H, **40** aryl), 7.600,7.597, 7.585, 7.582 (dd, 6H, BPh_3 aryl), 7.248, 7.236, 7.222, 7.206 (multiplet, 9H, BPh_3 aryl). ^1H NMR (500 MHz, d_8-toluene 333K): δ 7.058, 7.047, 6.378, 6.363 (4H, **40** aryl), 7.542, 7.538, 7.527, 7.523 (dd, 6H, BPh_3 aryl), 7.193, 7.180 (multiplet, 9H, BPh_3 aryl). $^{13}C\{^1H\}$ NMR (250 MHz, d_6-benzene): δ 161.6 (aryl **40**, 4°), 130.1, 126.1 (aryl **40**, CH), 154.1 (aryl BPh_3, 4°), 135.0, 128.3, 126.7 (aryl BPh_3, CH). ^{125}Te (158 MHz, d_6-benzene): δ 2203.

$TeN_2C_6H_4 \cdot 2B(C_6H_5)_3$ (47): A solution of BPh_3 (0.041g, 0.17 mmol) in 5 mL toluene was added to a suspension of **40** (0.012g, 0.053 mmol) in 5 mL toluene. The mixture was heated until dissolved. After cooling, the solvent was removed and the resulting oily residue was treated with acetonitrile to precipitate an orange solid. The orange precipitate was filtered and rinsed with acetonitrile to give a yield of 0.012 g (31%); mp. 156-158 °C. X-ray quality crystals of **47** were obtained by recrystallization at -34 °C from a 50:50 (v/v) bromobenzene/acetonitrile mixture. Anal Calcd. for $Te_1N_2B_2C_{42}H_{34}$: N, 3.91%; C, 70.40%; H, 4.79%. Found: N, 3.75%; C, 70.29%; H, 4.75%. Raman (cm^{-1}): 1587 (7), 1516 (20), 1436 (100), 1371 (26), 1305 (80), 1154 (19), 1026 (10), 998 (54), 936 (16), 857 (42), 810 (12), 697 (11), 570 (14), 360 (15), 312 (58), 240 (68). IR (cm^{-1}): 3065m, 3043m, 2995m, 1588m, 1518m, 1488m, 1428s, 1373m, 1307m, 1260m, 1141s, 1114s, 1033m, 998m, 915m, 872s, 803s, 753s, 738vs, 722vs, 701vs, 650s, 620m, 611m, 592s, 526w, 470m. ^1H NMR (500 MHz, d_6-benzene): δ 7.080, 7.072, 7.066, 7.060, 5.949, 5.943, 5.935, 5.929 (AA'BB', 4H, **40** aryl), 7.578, 7.571, 7.565, 7.561 (dd, 12H, BPh_3 aryl), 7.159 (multiplet, 18H, BPh_3 aryl). ^1H NMR (500 MHz, *d*$_8$-toluene): δ 7.075, 7.069, 5.997, 5.990, 5.982, 5.976 (AA'BB', 4H, **40** aryl), 7.527, 7.520, 7.513, 7.506 (dd, 12H, BPh_3 aryl), 7.143 (multiplet, 18H, BPh_3 aryl). $^{13}C\{^1H\}$ NMR (250 MHz, *d*$_6$-benzene): δ 161.4 (aryl **40**, 4°), 130.7, 126.1 (aryl **40**, CH), 153.0 (aryl BPh_3, 4°), 134.9, 128.3, 127.4 (aryl BPh_3, CH). $^{13}C\{^1H\}$ NMR (250 MHz, *d*$_8$-toluene): δ 161.5 (aryl **40**, 4°), 130.6, 126.1 (aryl **40**, CH), 152.8 (aryl BPh_3, 4°), 134.9, 128.3, 127.4 (aryl BPh_3, CH). ^{125}Te (158 MHz, *d*$_6$-benzene): δ 2188.

($SeN_2C_6H_4)_2$·($C_{12}N_4H_4$) (**39**$_2$·**87**): **39** (0.09 g, 0.5 mmol)and **87** (0.05 g, 0.3 mmol) were dissolved in hot acetone. The solution was hot filtered and left open to atmosphere to reduce in volume. Upon evaporation of the solvent red crystals of **39**$_2$·**87** were observed among crystals of **87** and crystals of **39**. Crystals of **39**$_2$·**87** were separated mechanically and stored in a tightly capped vial to prevent degredation by loss of **39** from the crystal in open atmosphere. Raman (cm^{-1}): 2217 (31), 1602 (45), 1452 (100), 1436 (16), 1353 (3), 1304 (4) 1193 (50), 1179 (8), 1124 (2), 975 (2), 946 (6), 753 (5), 706 (10), 599 (9), 586 (7), 556 (6). IR (cm^{-1}): 3071w, 3052w, 2362w, 2335w, 2218s, 1542s, 1508m, 1483w, 1352w, 1297w, 1139m, 1126m, 1112w, 1092w, 975w, 952w, 863m, 842s, 798w, 751vs, 710m, 615w, 595w, 468s.

($TeN_2C_6H_4)_2$·($C_{12}N_4H_4$) (**40**$_2$·**87**): **40** (0.05 g, 0.2 mmol) and **87** (0.02 g, 0.1 mmol) were placed in a glass tube and sealed under vacuum (30 mTorr). The tube was placed in an oven at 120 °C and purple/black crystals of **40**$_2$·**87** grew among crystals of **87** and crystals of **40**. Small amounts of **40**$_2$·**87** were separated mechanically. Raman (cm^{-1}): 2220 (25), 1597 (34), 1448 (100), 1318 (2), 1296 (2), 1202 (31), 1191 (9), 1183 (5), 945 (3), 748 (5), 705 (7), 685 (5), 580 (7). IR (cm^{-1}): 3050m, 2216s, 2194s, 2168m, 1583m, 1549vs, 1507vs, 1434w, 1365w, 1352m, 1333m, 1297w, 1186m, 1139s, 1127s, 1111m, 1091m, 973w, 950w, 899w, 862m, 841s, 773m, 746 vs 696s, 681vs, 579 m, 528w, 475m, 468s.

2.3 Computational Details

2.3.1 DFT Calculations

The structures considered in this study were fully optimized using the ADF DFT package (versions 2002.02 through 2008.01).[111-113] The Adiabatic Local Density Approximation (ALDA) was used for the exchange-correlation kernel[114,115] and the differentiated static LDA expression was used with the Vosko-Wilk-Nusair parametrization.[116] The calculation of model geometries were gradient-corrected with either the exchange and correlation functionals of the gradient correction proposed in 1988 by Becke[117] and Perdew[118] (BP86) or the exchange and correlation functionals of the gradient correction proposed in 1991 by Perdew and Wang (PW91).[118,119] Preliminary geometry optimizations were conducted using a small double-ζ basis set with frozen cores corresponding to the configuration of the preceding noble gas and no polarization functions; the resulting structures were refined using a triple-ξ all-electron basis set with one polarization function and applying the Zeroth Order Regular Approximation (ZORA)[120-124] formalism with the specially adapted basis sets, unless otherwise stated. Symmetry constraints were used when a point group was applicable. Vibrational calculations[125,126] were performed in order to verify that all the computed frequencies were real. This also provided zero-point energies for all minima. However, this contribution was omitted in all potential energy surface plots. Electronic excitations[127,128] and hyperpolarizabilities[114,115] were calculated using time-dependent density functional theory (TDDFT) as implemented within the ADF package;[127] the Statistical Average of different model Potentials for occupied KS Orbitals (SAOP)[129-131] was used for the exchange-correlation potentials in the zeroth-order KS equations. To obtain Kohn-Sham orbital energies to compare with UPS data, single point calculations were performed on the neutral molecules with the exchange correlation functionals BP86, PW91 and SAOP as well as B3LYP[132-134] for hybrid DFT. To obtain vertical ionization energies, the difference, from single point calculations, between neutral species and ionized species in the neutral geometry were performed using both PW91 and B3LYP. NBO analysis was performed with NBO 5.0[135] and AIM analysis was performed with Xaim.[136] Calculation of the gradient of the density, Fukui functionals, electrostatic potentials and charge distribution surfaces was performed with the ADF GUI (version 2008.01).[137] Additional visualization of the computational results was performed using Cerius2 (Accelrys) supplemented by the ADF SDK (SCM) interface, and Molekel[138] and the ADF GUI (version 2008.01)[137]. Optimized structures have been included on electronic supplementary information CD.

2.3.2 Molecular Mechanics Calculations

Model structures were optimized without any constraints using the MMX[139] force field implemented within PCModel (Serena Software, version 9.10.0)[140] with a custom set of parameters for 1,2,5-telluradiazoles described in Chapter **7**.

3 The Nature of the Supramolecular Association of 1,2,5-Chalcogenadiazoles[141]

3.1 Introduction

The survey of the CSD in Chapter 1 indicated that the 1,2,5-telluradiazole heterocycles have the potential to be used as building blocks for supramolecular self-assembly because they associate through the $[Te\text{-}N]_2$ supramolecular synthon with two points of attachment per molecule. As previously discussed, a short interaction distance is not a measure of strength, although it suggests the presence of a strong interaction. In order to corroborate the findings of the CSD survey as well as determine the limitations of this supramolecular synthon, a detailed DFT investigation of the $[E\text{-}N]_2$ ($E = S, Se, Te$) supramolecular synthon constructed with 1,2,5-chalcogenadiazoles was performed. The lighter heterocycles were included to provide a comparison of binding energies. In addition to the self-association to form the $[E\text{-}N]_2$ supramolecular synthon, recent results (Sections 5.2.3 and 8.2, as well as work done by the groups of Ragogna[142-144] and Oakley[145]) have provided examples of heteromolecular supramolecular assembly, as well as examples of very short E-N SBIs in the $[E\text{-}N]_2$ supramolecular synthon upon N-substitution. The reactivity towards the known donors and acceptors will also be evaluated in an effort to understand any competition that may occur with the self-assembly of the 1,2,5-chalcogenadiazoles.

3.2 Results and Discussion

3.2.1 A Detailed Examination of the Bonding in the 1,2,5-Chalcogenadiazole Rings

Models of the three parent 1,2,5-chalcogenadiazoles (**36**, **37** and **26**) were fully optimized using all-electron basis sets. The ZORA was used to account for relativistic effects. Although this is only essential for tellurium, the approach was applied to all molecules to ensure consistency. It is known that the ZORA causes a small mismatch of total energy and gradients that may result in changes to the molecular dimensions when no heavy atoms are present. Test nonrelativistic calculations for all three molecules with the largest basis set available (frozen up to 4p for tellurium) produced structures that were marginally different; less than 0.003 Å in bond lengths and 0.2° in bond angles. The largest deviations were, as expected, in the Te-N distance and the N-Te-N angle which changed by 0.036 Å and 0.4°, respectively. The calculated molecular dimensions using relativistic corrections are listed in Table 3.1. Along the **36**, **37** and **26** series, the C'-C=N angle becomes progressively wider and the N-E-N angle becomes more acute in order for the planar ring to accommodate the larger atoms.

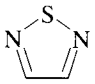

36

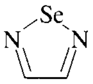

37

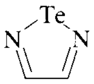

26

The Natural Bonding Orbital (NBO) analysis can be used to further probe the bonding in the 1,2,5-chalcogenadiazole rings. There are two limiting Lewis structures for these heterocycles (Scheme 3.1). Table 3.2 compiles the results of the NBO bond order partitioning applied to **36**, **37** and **26**. According to this analysis, the degree of delocalization decreases from S to Te but in each case the Lewis structure I is the main contributor. These results are consistent with the calculated geometries. At the same time that the E-N bond order decreases from S to Te, the chalcogen lone pair population increases; thus, as the chalcogen becomes heavier its π lone pair is less delocalized into the ring. The NBO analysis also indicates that the E-N bonds are predominantly covalent, but they are increasingly polarized from S to Te. Interestingly, the total lone pair population for nitrogen also decreases from S to Te. This is accompanied by an increase in the N-C bond order and probably results from the N contribution to the N-C π-bond.

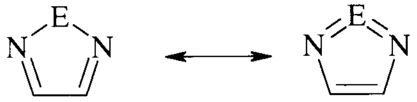

I II

E = S, Se, Te

Scheme 3.1 Possible resonance contributions to 1,2,5-chalcogenadiazole.

Table 3.1 Optimized bond lengths (Å) and angles (°) for the model structures of 1,2,5-chalcogenadiazoles and their dimers.

E	S		Se		Te	
Chain Length	1	2	1	2	1	2
E_1-N_1	1.653	1.658	1.837	1.835	2.053	2.071
E_1-N_2	1.653	1.658	1.837	1.845	2.053	2.064
N_1=C_1	1.331	1.331	1.314	1.317	1.309	1.303
N_2=C_2	1.331	1.332	1.314	1.317	1.309	1.304
C_1-C_2	1.423	1.421	1.440	1.437	1.453	1.456
C_1-H_1	1.089	1.089	1.092	1.093	1.096	1.098
C_2-H_2	1.089	1.089	1.092	1.092	1.096	1.095
$E_1\cdots N_3$		3.199		2.924		2.604
N_1-E_1-N_2	99.2	98.8	93.2	92.2	86.4	83.3
C_1=N_1-E_1	106.1	106.5	105.6	106.7	105.6	108.2
C_2=N_2-E_1	106.1	106.2	105.6	106.3	105.6	108.9
N_1=C_1-C_2	114.3	114.1	117.8	117.3	121.2	120.2
N_2=C_2-C_1	114.3	114.3	117.8	117.5	121.2	119.2
C_1-C_2-H_2	125.8	126.0	123.5	123.5	121.0	120.1
C_2-C_1-H_1	125.8	125.9	123.5	123.5	121.0	121.5

Table 3.2 Natural bond order, percentage of covalent character (in parenthesis), and lone pair populations for 1,2,5-chalcogenadiazoles.

	S	Se	Te
E-N	1.23 (74.6)	1.08 (72.3)	1.06 (62.7)
E (lone pair)	1.50	1.80	1.84
N-C	1.53 (77.2)	1.83 (82.5)	1.88 (82.0)
N (lone pair)	1.20	1.04	1.02
C-C	1.30 (93.2)	1.08 (91.0)	1.04 (93.2)

Topological analysis of the calculated electron density shows seven BCPs and one RCP for each of the monomers; selected topological values are given in Table 3.1. The E-N and C-C BCP densities decrease from S to Te, while the C-N BCP density increases. These trends mirror the NBO bond order and are consistent with the more localized bonding of **26**. The ellipticity values follow the same trend, suggesting that the E-N and C-C bonds lose double bond character as the mass of the chalcogen increases. The values of the Laplacian of the electron density imply that the E-N bond becomes more ionic from S to Te, but given their small magnitudes and the significant electron density at the BCP in each molecule, the appropriate interpretation is that the E-N bond becomes more polar from S to Te.

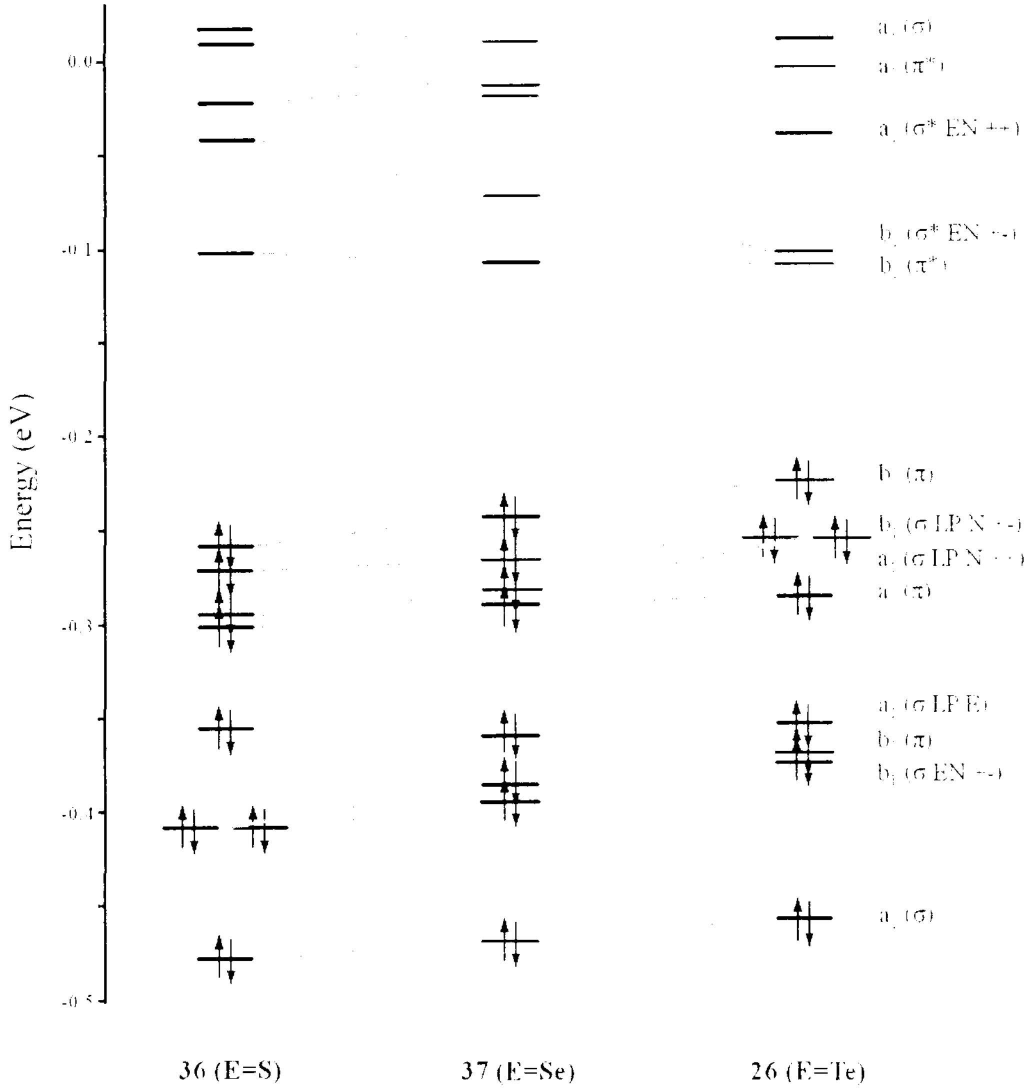

Figure 3.1 Correlation diagram for Kohn-Sham valence orbitals of the 1,2,5-chalcogenadiazoles under C_{2v} symmetry.

Table 3.3 Density (e/Å^3), Laplacian of the density (e/Å^5) and ellipticity values at the critical points for selected bonds in the 1,2,5-chalcogenadiazoles.

	S	Se	Te
ρ			
E-N	0.2262	0.1650	0.1235
N-C	0.3372	0.3485	0.3543
C-C	0.2915	0.2816	0.2757
$\nabla^2\rho$			
E-N	-0.3581	0.0583	0.2178
N-C	-0.8939	-0.9402	-0.9619
C-C	-0.7102	-0.6694	-0.6455
Ellipticity			
E-N	0.2528	0.1600	0.1283
N-C	0.1858	0.1942	0.1924
C-C	0.2093	0.1770	0.1606

Frontier MO theory postulates that the chemistry of the molecule is dominated by the orbitals in the vicinity of the HOMO and the LUMO, and the charges on the molecules. Figure 3.1 shows a correlation diagram for the three 1,2,5-chalcogenadiazoles depicting the effects of the chalcogen on the energy of the Kohn-Sham orbitals. Figure 3.2 displays selected isosurfaces of the Kohn-Sham orbitals of **26**; these orbitals are representative of those calculated for the lighter congeners. The extent to which orbital interactions contribute to the SBI depends on the energy difference and overlap between interaction orbitals. The correlation diagram Figure 3.1 illustrates not only the descent of the σ*E-N acceptor orbitals but also the rise of the nitrogen lone pairs as the mass of the chalcogen increases. Both changes do lead to stronger orbital interactions in the tellurium case.

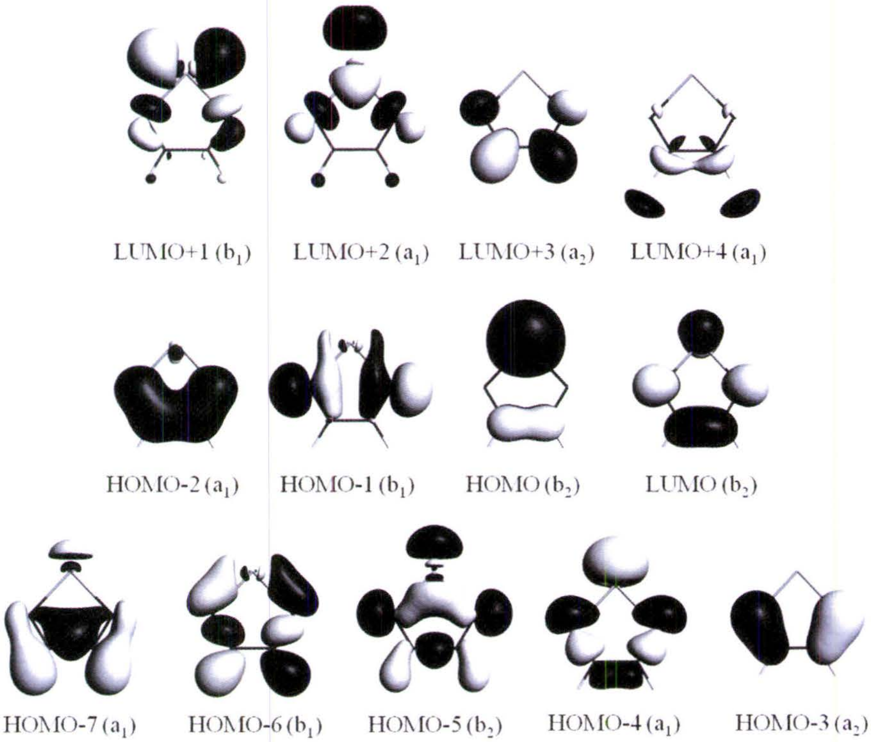

Figure 3.2 Selected Kohn-Sham molecular orbitals of **26** (LUMO+4 to HOMO-7). Isosurfaces plotted at 0.05 au.

The nucleophilic and electrophilic sites of the molecules are more accurately portrayed by the Fukui functions, $f^{+}(r)$ and $f^{-}(r)$, than by the angular wave function alone. The Fukui functions can be visualized by projecting the density changes upon one-electron addition to or removal from the relevant orbital (eqs 3.1 and 3.2) onto the electron density.[146,147] The Fukui function integrated from above, $f^{+}(r)$, maps the electrophilic regions of the molecule and can be approximated using the square of the LUMO, while the Fukui function integrated from below, $f^{-}(r)$, establishes the nucleophilic regions and is approximated with the square of the HOMO. Both Fukui functions, in this case, are confined to the π-system and thus are not applicable to the SBI supramolecular associations which occur in the plane of the molecule. More relevant Fukui functions, obtained from the HOMO-1 and the LUMO+1 (Figure 3.3), identify the nitrogen and tellurium as nucleophilic and electrophilic centres, respectively. The magnitude of the Fukui function that describes the nucleophilic centre suggests that the nucleophilicity is approximately the same for each of **36**, **37** and **26**. The most important difference between the three Fukui functions is in the ionization energy, which can be approximated by the Kohn-Sham orbital energies (Figure 3.1). From this it is apparent that the nucleophilicity of the 1,2,5-chalcogenadiazoles follows the trend **26** > **37** > **36**. Interpretation of the meaning of the $f^+(r)$ is complicated by the differences in the radii of the isosurfaces at the chalcogen atoms. It would, at first, appear that **36** has the largest Fukui function at the chalcogen atom, and thus would be the most electrophilic. This is contrary to what is observed experimentally and what has been previously calculated. The important information that can be obtained from these maps is the location of the electrophilic region. Interpretation of this Fukui function in light of the electron affinity, estimated using the Kohn-Sham orbital energy, provides a much more realistic picture of the importance of each $f^+(r)$ functions. The larger value of the Fukui function of **1a** has little meaning because the orbital is energetically inaccessible. There is a very pronounced energy difference of the LUMO+1 along the series and this better reflects the known trend in the electrophilicities of the chalcogen centres, Te > Se > S.

$$f^+(r) = \rho(r)_{\mathbf{1}^-} - \rho(r)_{\mathbf{1}} \qquad 3.1$$

$$f(r) = \rho(r)_{\mathbf{1}} - \rho(r)_{\mathbf{1}^+} \qquad 3.2$$

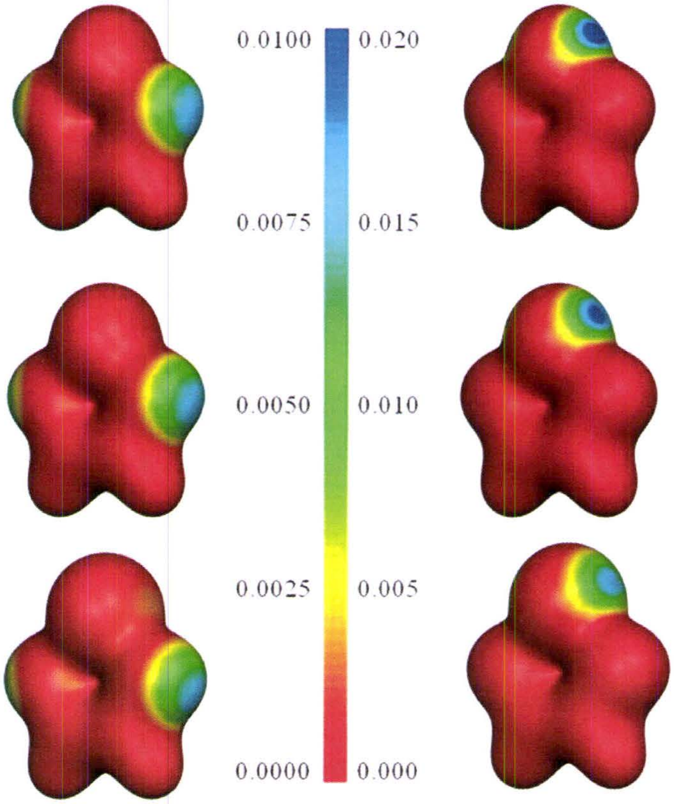

Figure 3.3 HOMO-1^2 and LUMO+1^2 plotted on the electron density isosurface (0.03 e·Å^{-3}) of **36**, **37** and **26**, top to bottom.

The electrostatic contribution to the SBIs can be investigated by considering the charges on the chalcogen and nitrogen atoms in **36**, **37** and **26**. Because Mulliken, AIM and NPA charges are usually strongly dependent on basis set and exchange-correlation functional,[148] this analysis used the density based Hirshfeld and Voronoi deformation density (VDD) charges; the results are summarized in Table 3.4. Consistent with the NBO and AIM analysis, the increasing polarity in the E-N bond leads to an increase in the electron density at the nitrogen and a decrease at the chalcogen from S to Te. Considering the charges in light of the formation of an SBI, this increase in positive charge on the chalcogen from S to Te would be responsible for a larger Coulombic contribution. Considering the charges on the monomer in light of the self-association to form a dimer, the increased charge separation along the E-N bond would lead to a cooperative pairing of larger opposing charges across the E-N SBI resulting in an increased Coulombic component from S to Te.

Table 3.4 Hirshfeld and VDD (in parenthesis) atomic charges for the 1,2,5-chalcogenadiazoles.

	S	Se	Te
E	0.24 (0.24)	0.27 (0.25)	0.34 (0.29)
N	-0.18 (-0.19)	-0.19 (-0.19)	-0.22 (-0.21)

Even in the case of the Hirshfeld and VDD schemes, atomic charges are dependent on the method used to establish atomic boundaries and partition the electron density. This complication can be avoided by examining the deformation density (DD), the difference between the density in the molecule and the density of a promolecule composed of spherically symmetric neutral atoms. Figure 3.4 displays DD isosurfaces for **36**, **37** and **26**. In all cases the regions of space at the chalcogen, opposite to the E-N bonds, are depleted of electron density. This echoes the polarization of electrons towards the more electronegative nitrogen along the E-N bond. It is this depletion that confers the overall positive charge to the chalcogen atom. The σ-hole model emphasizes this contribution to the formation of SBIs.[11,149] In contrast, the regions in which there is increased (localization) of electron density are observed between bonded atoms as well as in those regions of space occupied by the lone pairs of nitrogen and the chalcogen.

Projections of the electrostatic potential onto the electron density (Figure 3.4) are consistent with this analysis. Each of the maps indicates that a positively charged particle would be preferentially attracted to the nitrogen atom at the site of the lone pair. Similarly, a negatively charged particle would be attracted to the chalcogen atom at two spots located opposite to the E-N bond. While the potential at the nitrogen lone pairs is nearly constant, the interactions at the chalcogen would increase significantly from S to Te.

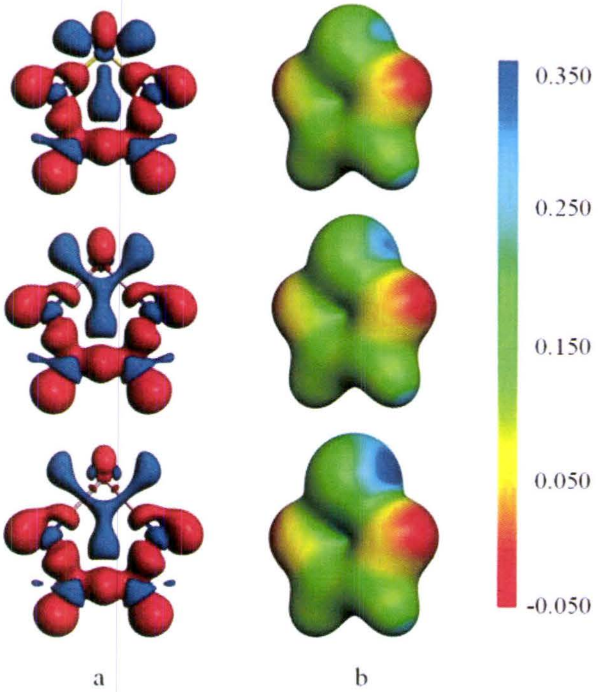

Figure 3.4 Spatial electrostatic analyses of **36**, **37** and **26**. (a) Deformation density isosurfaces plotted at 0.01 e·Å^{-3}, (b) Maps of electrostatic potential projected on the electron density isosurface plotted at 0.03 e·Å^{-3}.

3.2.2 A Detailed Examination of Bonding in the $[E\text{-}N]_2$ (E = S, Se, Te) Supramolecular Synthons

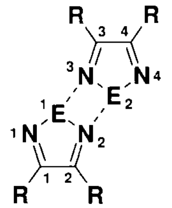

Scheme 3.2 Supramolecular dimer of 1,2,5-chalcogenadiazoles.

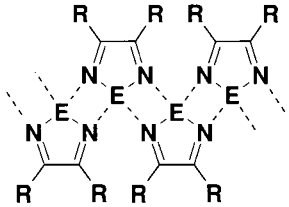

Scheme 3.3 Supramolecular ribbon polymer of 1,2,5-chalcogenadiazoles

A survey of the Cambridge Structural Database (CSD)[150,151] was performed in order to provided the average SBI distances for 1,2,5-chalcogenadiazoles that participate in the $[E\text{-}N]_2$ supramolecular synthon. [63-65,152-172] These values are compared to the sum of the corresponding van der Waals radii[5] in Table 3.5. The two sets of data follow opposite trends, suggesting that the tellurium SBIs are the strongest. In addition to this, it was found that, while the selena- and telluradiazoles are more frequently associated in dimers (Scheme 3.2) and polymers (Scheme 3.3), thiadiazoles most often do not appear to be associated; those that do associate only make dimers (Scheme 3.2).

Table 3.5 SBI distances (Å) in 1,2,5-chalcogenadiazoles.

E	S	Se	Te
$r_{EvdW} + r_{NvdW}$[5]	3.26	3.36	3.54
E···N $_{(Average)}$	3.20	2.95	2.77

The "monomers" from Section 3.2.1 were used to construct models of supramolecular aggregates, beginning with the dimers, which were fully optimized. All three dimers converged to centrosymmetric coplanar structures with the two expected SBIs (Scheme 3.2). These pairs are, in principle, stable because their energies are lower than those of the two isolated molecules and all their vibrational frequencies are real. The minimized structures of the rings in the dimers are compared to those of the isolated molecules in Table 3.1. The E-N SBI distances are in agreement with the average of the experimentally observed distances. The calculated structural modifications of the rings that occur upon supramolecular association are small but significant and are most noticeable in the chalcogen centered dimensions. The largest changes pertain to the telluradiazole case, where the N-Te-N and the Te-N-C angles change as much as 3.1 and 3.2°. In view of the magnitude of these changes, it would not be appropriate to compare the calculated structure of the dimer with that of the experimentally determined polymer; such an analysis is left for models of the polymers themselves (*vide infra*).

The total interaction energy of the self-associated dimers of the heterocycles can be split into three contributions (eq3.3): the reorganization of the structure to adopt the geometry attained in the dimer, the binding of the two fragments, and the zero-point energy correction. These contributions are presented in Table 3.6 for the three chalcogenadiazole rings. The magnitude of the total interaction energy increases in the same order observed for the E-N secondary bond distances: $\mathbf{36}_2$ (-2.82 kJ/mol) < $\mathbf{37}_2$ (-15.54 kJ/mol) < $\mathbf{26}_2$ (-53.85 kJ/mol). The last value is comparable to medium strength hydrogen bonds. These calculations cannot account for London dispersion forces which would probably only provide a small attractive contribution that would not significantly modify the results. Using VT NMR, Tomoda[173] estimated that intramolecular Se-N SBI energies in amino-selenides lie between -31.8 and -79.5 kJ/mol.

$$\Delta E_{\text{Total}} = \Delta E_{\text{Reorganization}} + \Delta E_{\text{Binding}} + \Delta ZPE \qquad 3.3$$

The reorganization energies are modest because all of the structural changes are small; as expected the largest such contribution occurs in the telluradiazole dimer. The calculated reorganization energy for the thiadiazole dimer is very small and negative, this is likely an error due to the mismatch of energy and overlap in the ZORA; the equivalent nonrelativistic calculation afforded a reorganization energy of just +0.01 kJ/mol. In the most straightforward interpretation, the binding energy would be twice the energy of the individual SBIs. A more complete description of the stabilities of the dimers is obtained by plotting the binding energy as a function of the EN distance as the rings are displaced along the direction of the E-N SBI axes; these potential energy curves are displayed in Figure 3.5. This analysis reveals that optimized SBI distances correspond to well defined potential minima and that there is no activation barrier expected for the processes of association and dissociation of these molecular aggregates. Not only is the telluradiazole pair more stable than the selena- and thiadiazole cases, but it is also more difficult to deform by elongation of the SBIs. In the other extreme, the sulphur heterocyclic dimers are very weakly bonded and have shallow potential wells.

Table 3.6 Contributions to the energy of interaction between two 1,2,5-chalcogenadiazoles.

E	Contribution Reorganization	Binding	ZPE
S	-0.08	-5.05	2.39
Se	0.43	-19.56	3.16
Te	4.17	-67.10	4.87
Te[a]	4.12	-65.45	4.95
Te[b]	2.64	-50.67	

[a] Core electrons frozen up to 4p

[b] Core electrons frozen up to 4d

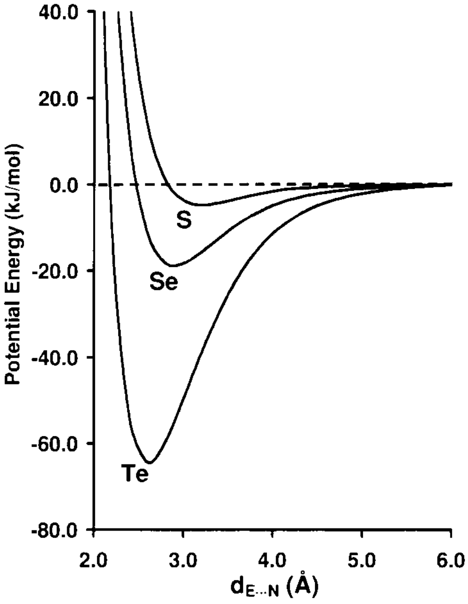

Figure 3.5 Potential energy curves for the in-plane dimerization of the 1,2,5-chalcogenadiazole rings through the $[E\text{-}N]_2$ supramolecular synthon (E = S, Se, Te).

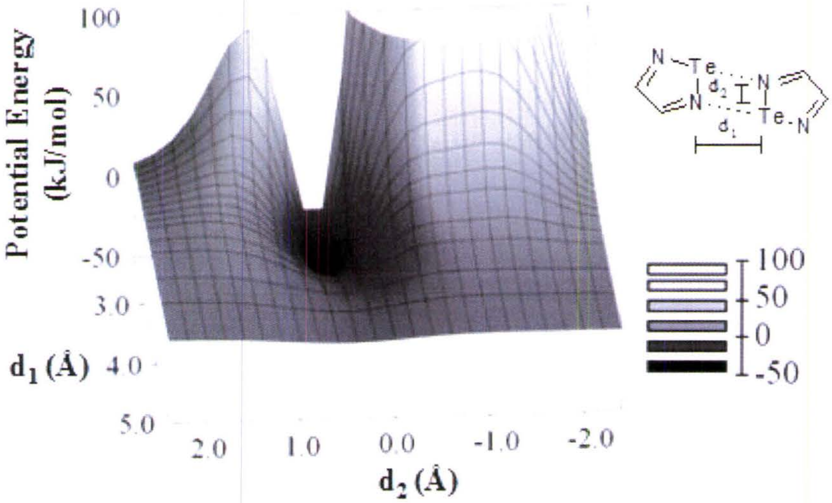

Figure 3.6 Potential energy surface for the in-plane deformation of the $[Te\text{-}N]_2$ supramolecular synthon.

For the case of the most stable dimer, **26_2**, the potential surface was explored in two dimensions with the use of a nonrelativistic basis set and a core frozen up to 4p. The relaxation energy at each point was neglected. Although this underestimated the binding energy by 16 kJ/mol, it was computationally much less expensive than the all-electron relativistic method. The potential surface calculated for the "in-plane" deformation of the dimers is presented in Figure 3.6. The potential well that corresponds to the formation of a stable dimer appears well defined. There are two large potential barriers that prevent the lateral movement of the rings with respect to each other due to repulsion between the lone pairs of nitrogen and tellurium. Similar calculations were performed to evaluate the energetic cost of shifting one ring away from the plane of the other as well as the rotation of one ring about the E-N SBI axis. In both cases, the planar conformation was the most stable and steep slopes would prevent any distortions. The possibility of a face-to-face interaction driven by the molecular dipole moments was considered but the calculations failed to produce a potential energy minimum. These results provide a semiquantitative view of the stability of the telluradiazole pair which, once formed, is a remarkably rigid structure with no competing orientations for molecular association.

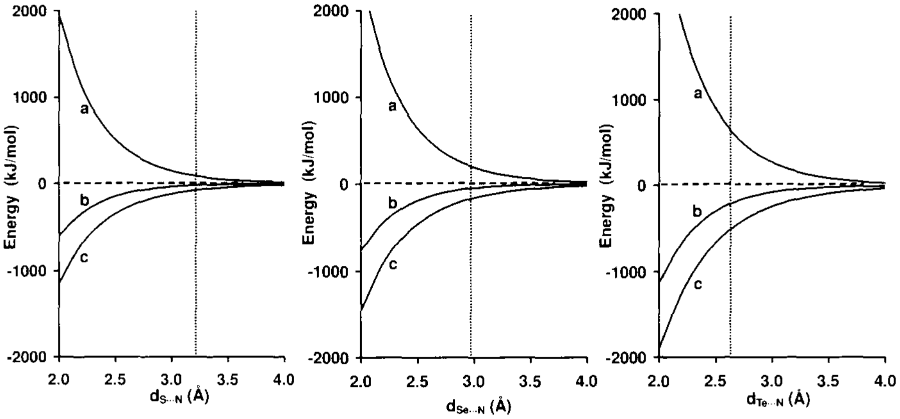

Figure 3.7 Contributions to the binding energy of the 1,2,5-chalcogenadiazole dimers. (a) Pauli repulsion, (b) electrostatic interaction, (c) orbital interaction. The vertical lines are traced at the equilibrium distances.

The position of the minima in the potential surfaces is dictated by the balance of three distance-dependent contributions:[174,175] the Pauli repulsion that arises from the interaction of completely occupied orbitals; the electrostatic that results from the local dipole moments created by differences of atomic electronegativity; and the interaction of empty and occupied orbitals. Figure 3.7 shows graphically the decomposition analysis for the dimers of the three heterocycles. Both the electrostatic and occupied-empty orbital contributions are stabilizing, the latter always being the largest in magnitude. All three interactions are strengthened as the intermolecular separation decreases. The three plots are similar, the main difference being that at any distance, the magnitudes of the interactions increase with the weight of the chalcogen. The Coulombic interactions take place mainly between the negative nitrogen and the positive chalcogen atoms; the difference of electronegativity and the strength of the interactions is greatest in the tellurium molecules. The most important contribution to the stabilization of the dimers results from the interaction between empty and occupied molecular orbitals; in other words, the E-N SBI has a strong donor-acceptor character. The nitrogen atom can donate a lone pair into low-lying empty orbitals which are polarized towards the chalcogen. This interaction is well exemplified by the HOMO-12 of the tellurium dimer (Figure 3.8). This interpretation is consistent with the model of three-center four-electron bonding that has gained increasing acceptance in the interpretation of main-group SBIs.[176-178] The character of these donor-acceptor interactions was confirmed by performing a Constrained-Space Orbital Variation (CSOV)[179-184] analysis in which specific types of monomer virtual orbitals were removed (Table 3.7). The previous discussion is primarily focused on σ-interactions and ignores the intense repulsion that exists between the lone pairs of nitrogen and the chalcogen atom. Studies of the intramolecular "coordination" of chalcogen atoms in diazenes indicated that π-interactions can substantially alleviate such repulsion and in one case are indispensable in the stabilization of a secondary S-N interaction.[185] In the cases of the 1,2,5-chalcogenadiazoles the σ- and π-orbitals are easily distinguished by symmetry. The corresponding extension of the CSOV analysis is presented in Table 3.7. The π-interactions (a_u, b_g) are indeed stabilizing, but their contribution is, in all instances, one order of magnitude smaller than the σ-interactions (a_g, b_u). All of the dimers are stable in calculations where the π virtual orbitals are removed but not when the σ-acceptor orbitals are excluded.

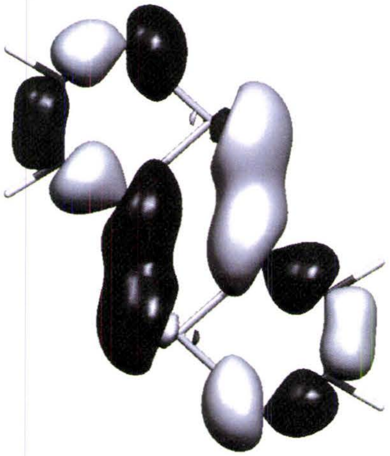

Figure 3.8 Calculated composition of the HOMO-12 (27 b_u) of **26_2**. Isosurface plotted at 0.04 au.

A more detailed picture of the effect of the SBI was obtained by mapping the change of electron density upon dimerization along the E-N SBI axis, as shown in Figure 3.9. The maps show an enhancement of electron density between the two atoms that increases with the size of the chalcogen. Not only is the nitrogen electron cloud polarized towards the SBI, but the vicinity of the chalcogen is also depleted of electron density. This observation is not in contradiction with the donor-acceptor concept but rather highlights both the polarization of and the covalent character of the SBI.

Table 3.7 Contributions to the binding energy (kJ/mol) and CSOV analysis for 1,2,5-chalcogenadiazole dimers in the equilibrium geometries.

	Pauli Repulsion	Electrostatic Interaction	Orbital Interactions				CSOV Analysis		
			σ		π				
			A_g	B_u	A_u	B_g	No virtual	No π	No σ
36_2	28.0	-23.0	-4.0	-5.5	-0.4	-0.2	5.0	-4.5	4.3
37_2	78.9	-62.6	-13.3	-20.0	-1.7	-0.9	16.3	-16.7	13.7
26_2	330.5	-242.0	-63.9	-78.3	-8.9	-4.5	88.5	-51.1	76.4

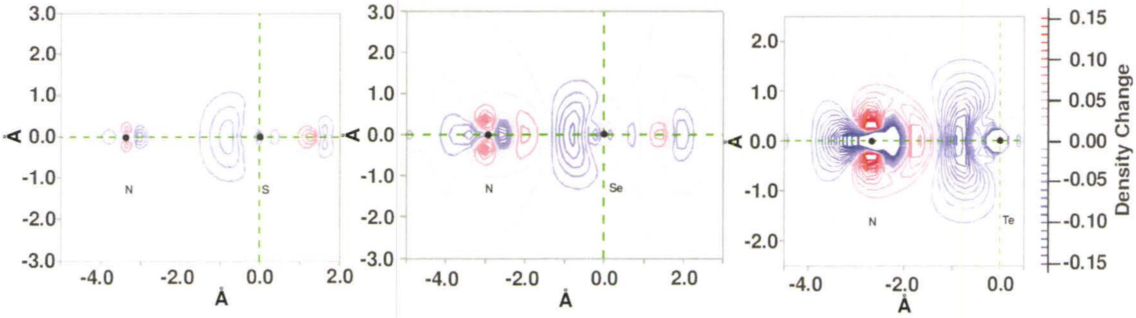

Figure 3.9 Calculated maps of electron density change along the E···N axis for (a) **36**$_2$, (b) **37**$_2$ and (c) **26**$_2$.

NBO methods have been used to evaluate hydrogen bonding[186] and halogen secondary bonding[187] as well as dative bonding between Lewis acid/base pairs.[188,189] In most of these cases the interaction occurs between a heteromolecular pair, thus the transfer of electrons between molecules can be evaluated as the difference in initial and final molecular charge. In the self-associated 1,2,5-calcogenadiazole dimers, the net electron transfer is necessarily zero as the association occurs through a pair of antiparallel secondary bonds. An estimate of the degree of electron transfer can be obtained by evaluating the change in population of the orthogonalized molecular orbitals upon association. Calculated population changes are provided in Table 3.8. The largest changes pertain to the N lone pair orbitals and E-N σ* natural orbitals in the dimers of **36**, **37** and **26**. While the population of the N lone pair that is involved in the SBI decreases, the E-N* populations increase upon SBI formation. These changes become larger as the mass of the chalcogen increases. The population changes in **26** are significantly smaller than those calculated for the formation of H_3N-BH_3 (0.32 electrons)[189] but are larger than those evaluated for the complexes of bromobenzene with neutral donors (0.0029-0.0079 electrons)[187] or in the water dimer H_2O···H-OH (0.0086 electrons).[186] Both the change in the N lone pair populations, and the change in the E-N σ* orbital populations are proportional to the DFT calculated dissociation energy of the SBI dimers (2.82, 15.54 and 53.85 kJ/mol for **36**, **37** and **26**, respectively). Similar correlations are observed in the case of the bromobenzene adducts.[187]

Table 3.8 Change in population (number of electrons) of selected Natural Orbitals upon dimerization of 1,2,5-chalcogenadiazoles.

	S	Se	Te
N Lp	-0.0009	-0.0063	-0.0173
N Lp (SBI)	-0.0017	-0.0179	-0.1134
E-N*	-0.0016	0.0118	0.0690
E-N* (SBI)	0.0022	0.0127	0.0798

The topological analysis of electron density has been extensively used to characterize interactions such as hydrogen bonds.[190] In the case of the $[E\text{-}N]_2$ supramolecular synthon, two bond critical points (BCPs) and one ring critical point (RCP) are observed as local minima between the molecules, as shown in Figure 3.10. The amplification of the region between the two molecules shows the progression from shallow minima in $\mathbf{36}_2$ to the deep minima in $\mathbf{26}_2$. Here the BCPs become less oblong as the density is localized along the Te-N SBI bond path. The density and Laplacian of the density at the BCPs of the SBIs in dimers of **36**, **37** and **26** are given in Table 3.9. The densities at the BCP for the bromobenzene complexes with neutral donor molecules range from 0.0063 to 0.0118 e/Å^3.[187] Mohajeri[11] evaluated the SBIs between a variety of molecules and the donors NH_3, H_2O and HF, and calculated BCP densities that range from 0.0056 e/Å^3 for HF-ClCN to 0.0390 e/Å^3 for H_3N-SeFMe. For hydrogen bonds, this property ranges from 0.002 to 0.04 e/Å^3.[190] The density at the BN BCP in $NH_3{\cdot}BH_3$ is calculated to be significantly larger (0.66 e/Å^3).[188] The Laplacian of the density at a given point describes whether the density is locally depleted (> 0) or locally (< 0) concentrated. The corollary of this is that perfect sharing of electrons will have a large negative value at the BCP while a closed-shell interaction will have a large positive value. Values close to zero are representative of intermediate interactions.[190] In the case of the E-N SBIs in the dimers of **36**, **37** and **26**, the values of the Laplacian of the density are small but positive and similar to the values calculated for BCPs of the above mentioned SBIs with donors NH_3, H_2O and HF (0.0180-0.0972 e/Å^5),[11] the bromobenzene SBIs (0.0191-0.0400 e/Å^5)[187] and those of hydrogen bonds (0.02-0.15 e/Å^5).[190] The value calculated for the B-N bond in $NH_3 \cdot BH_3$ is 12.03 e/Å^5.[188] The small positive values for the Laplacian of the density are indicative of a polarized intermediate interaction involving covalent and electrostatic contributions, rather than a closed-shell electrostatic interaction. The density and the Laplacian of the density at the bond critical points for hydrogen bondsf[191] and halogen SBIs[187] have been shown to correlate well with the respective interaction energies. At the BCP the density and the Laplacian of the density both increase from **36**$_2$ to **26**$_2$ proportionally with the energy of the SBIs. This trend indicates that as the mass of the chalcogen increases the electron density at the BCP increases, but at the same time there is an increase in the local depletion of electron density at the BCP. This indicates that along the series **36**$_2$, **37**$_2$, **26**$_2$ there is an increase in the sharing of electrons which is occurring in an increasingly polarized secondary bond as was depicted by the change in electron density (Figure 3.9).

Table 3.9 Density (ρ) and its Laplacian at the bond critical points of the [E-N]$_2$ supramolecular synthon in the 1,2,5-chalcogenadiazole dimers.

	S	Se	Te
ρ (e/Å^3)	0.90	1.86	4.20
$\nabla^2\rho$ (e/Å^5)	3.10	5.44	10.88

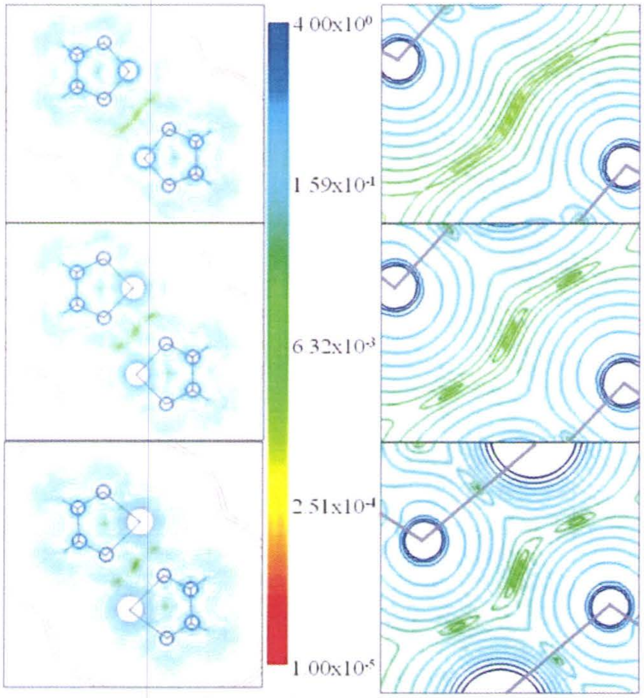

Figure 3.10 Magnitude of the gradient of the density of **36**, **37** and **26** (top to bottom) with an expansion of the [E-N]$_2$ supramolecular synthon.

The progressive increase in electron sharing between the molecules upon dimerization is apparent in the maps of the electron localization function (ELF) displayed in Figure 3.11. The ELF compares the electron density in the molecules to a uniformly dense electron gas. The dimer of **36** shows two nearly independent molecules with very little deformation of electron density with respect to the C_{2v} molecular symmetry. As the mass of the chalcogen increases the region corresponding to the N lone pair becomes increasingly localized along the EN secondary bond path. This is consistent with the presence of an important covalent contribution in the SBI. One additional consequence of the SBI strengthening is the deformation of the chalcogen π lone pair away from the SBI, this indicates that there is a repulsive interaction between filled π orbitals upon SBI formation.

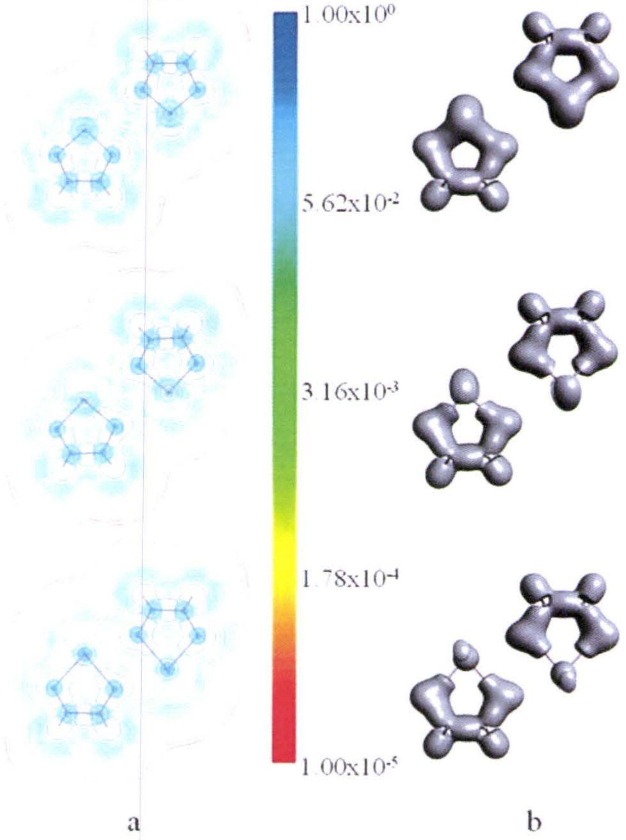

Figure 3.11 ELF for dimers of **36**, **37** and **26**. (a) Contour plot traced at the molecular plane, (b) isosurface plotted at 0.4 e·Å^{-3}.

3.2.3 Models of 1D Polymers of 1,2,5-Telluradiazoles Constructed with the [Te N]$_2$ or [Te-N]$_2$ Supramolecular Synthons

The study of the association of chalcogenadiazoles was extended to consider the infinite one-dimensional arrays observed in the solid state (Scheme 3.3). This analysis was confined to the tellurium heterocycles because they are the most strongly associated and thus have the best potential as supramolecular building blocks. An estimate of the "polymerization energy" was obtained by building model heterocycle chains of increasing length and plotting the association energy as a function of the chain length (Figure 3.12); ZPE corrections were not considered in this case for computational efficiency. The slope of each linear plot corresponds to the association energy per molecule of telluradiazole. The calculated interaction energy per SBI in the polymer $\mathbf{26}_n$ (-29.7 kJ/mol) is less than in the dimer (-31.5 kJ/mol). Here, significant changes to the bond distances and angles were calculated for the central unit of $\mathbf{26}_3$ with respect to the dimer $\mathbf{26}_2$ thus the decrease of the SBI energy primarily results from reorganization. Steric interactions should be more significant for larger molecules. To explore this effect, models of benzo-2,1,3-telluradiazole oligomers, $\mathbf{40}_n$, were optimized. Here the repulsion between the *ortho* hydrogen atoms caused an additional decrease in the SBI association energy. Greater steric interactions would further destabilize the ribbon structure and induce a structural distortion in the molecule or in the chain. The crystal structure of **27** displays a telluradiazole ring puckered to enable the four Te-N SBIs, this leads to a staircase ribbon.[64] While the optimized structure of monomeric **27** is essentially planar, its calculated reorganization energy is only 14.29 kJ/mol; this is easily compensated by the strength of the SBI supramolecular links. Even stronger steric repulsion would prevent formation of a ribbon. In the case of the sterically hindered compound **31** a dimeric structure was observed[65] but an alternative helicoidal chain (Scheme 3.4), analogous to those formed by 3,5-dimethyltellurazole (**12**)[47] and 1,2-benzotellurazole (**6**),[53] is a plausible alternative. This was modeled and found to have approximately the same interaction energy per SBI and presumably the same stability as the discrete dimer. Even stronger steric repulsions, or alternatively much weaker SBIs, would result in monomeric species. Such a situation is observed in the isomorphic crystal structures of the benzothia- and benzoselenadiazole, **38** and **39**,[192-194] in which there are no evident SBIs; instead, each chalcogen atom is positioned at distances longer than the sum of van der Waals radii from the four closest nitrogen atoms of neighbouring molecules. This study, however, predicts a polymeric structure for the tellurium analog **40**.

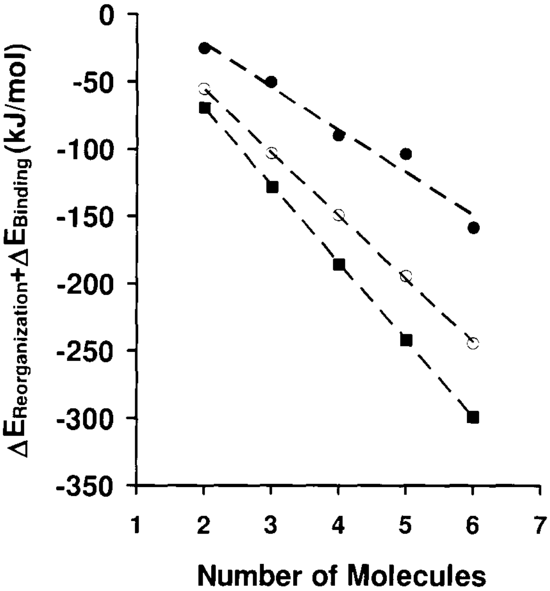

Figure 3.12 Total association energy of model telluradiazole oligomers (n= 2-6). (■) ribbon $\mathbf{26}_n$, -57.4 kJ/mol; (○) ribbon $\mathbf{40}_n$, -46.9 kJ/mol; (●) helicoidal $\mathbf{26}_n$, -31.9 kJ/mol.

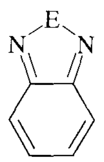

38 E = S
39 E = Se
40 E = Te

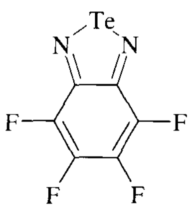

41

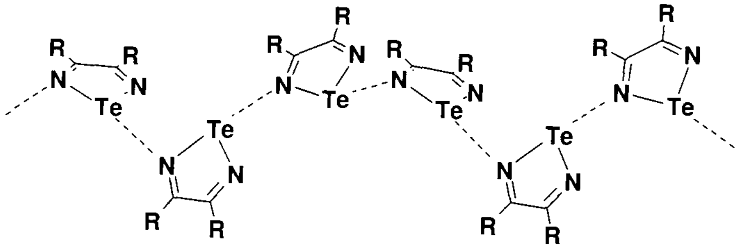

Scheme 3.4 Supramolecular helical polymer 1,2,5-chalcogenadiazoles.

3.2.4 Lewis Basicity of the 1,2,5-Chalcogenadiazoles

Polymer formation provides a clear example of the ambiphilic behaviour of the 1,2,5-chalcogenadiazoles and this behaviour warrants a closer inspection of the Lewis acidic and basic sites on the heterocycles. Chalcogenadiazoles are capable of binding protons and Lewis acids through the nitrogen atoms but they are relatively weak bases.[148,195-200] The geometries of the protonated molecules and the borane adducts of **36**, **37** and **26** were optimized and the corresponding proton affinities and borane binding energies are compiled in Table 3.10. As expected, both the proton and borane affinities increase with the mass of the chalcogen atom. Both the proton affinity and the borane binding energy of **36** are smaller than those for either NH_3 or pyridine (proton: 853.6[201] and 930[201] kJ/mol; borane: 141.0[188] and 149.0[202] kJ/mol for NH_3 and pyridine, respectively), while the basicity of the N in **26** is larger than that of NH_3 with respect to both acids. The lower basicity of **36**, **37** and **26** relative to pyridine is consistent with the ability of pyridine to dissolve these molecules.[203]

Table 3.10 Proton affinity and borane binding energies of the 1,2,5-chalcogenadiazoles (kJ/mol).

Acid	S	Se	Te
H^+	-846.28	-869.62	-903.8
BH_3	-123.29	-132.54	-143.43

Clearly the nitrogen atom is the best donor in a molecule such as **26**, but the chalcogen is another potential nucleophilic site. The energy and equilibrium distance of proton attachment to this and any other point of the molecule can be calculated to generate a proton affinity map (Figure 3.13). There are four significant regions in the map: two regions occupied by the nitrogen lone pairs and two on the tellurium atom above and below the plane of the molecule in the region occupied by the π-lone pair. According to the map, the σ-lone pair of the chalcogen is not available for donation. This is consistent with the HOMO and HOMO-1 Fukui functions and the electrostatic potential maps.

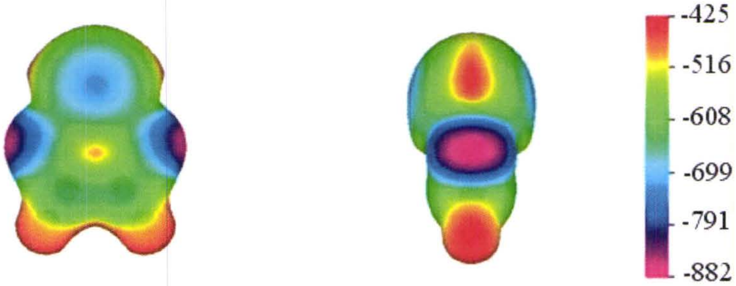

Figure 3.13 Proton affinity map of **26**. Energy in kJ/mol.

N-substitution by either acid causes a significant reorganization of electron density, including increased polarization of the E-N bond. The reorganization of electron density is reflected in the changes to the NBO occupancies (Table 3.11). The E-N(H) bond order in the lighter congeners decreases significantly when compared with the neutral molecules; these weaker bonds would be expected to lead to a lower-lying σ-antibonding orbital. The NBO analysis also suggests that the bond acquires more ionic character when compared with the neutral molecule, but the trend of increasing iconicity from S to Te is still apparent. This means that the bond will be more polarized towards the nitrogen atom resulting in the corresponding antibonding orbital being polarized away from the nitrogen atom, becoming more diffuse in the direction of a potential SBIs.

Table 3.11 Selected natural bond orders (% covalent character) in the *N*-hydro-1,2,5-chalcogenadiazolium cations.

	S	Se	Te
E-N	1.36 (76.1)	1.26 (73.8)	1.22 (63.5)
E-N(H)	1.09 (60.5)	1.05 (56.8)	1.07 (44.0)
E (lone pair)	1.52	1.66	0.69
N (lone pair)	1.03	0.99	0.99
N(H) (lone pair)	0.42	0.16	0.13

The information obtained from the topology of the bond critical points (Table 3.12) is consistent with the NBO analysis. The E-N(H) bond critical point electron density decreases and the Laplacian increases when compared with **1a-c** implying a weaker, more polar bond and subsequently a more diffuse antibonding orbital which is lower in energy. Both the NBO and AIM analysis predict that N-substitution will have important effects on both the electrostatic and covalent contributions in any subsequently formed SBIs.

Table 3.12 Density, ellipticity and Laplacian values at the critical points for selected bonds in the *N*-hydro-1,2,5-chalcogenadiazolium cations.

	S	Se	Te
P			
E-N (e/Å^3)	0.2461	0.1823	0.1359
E-N(H) (e/Å^3)	0.1972	0.148	0.1122
$\nabla^2\rho$			
E-N (e/Å^5)	-0.3751	0.0598	0.2492
E-N(H) (e/Å^5)	-0.2414	0.1191	0.2542
Ellipticity			
E-N	0.3188	0.1785	0.1458
E-N(H)	0.3279	0.2577	0.2205

3.2.5 Lewis Acidity of the 1,2,5-Chalcogenadiazoles

The Lewis acidity of the heterocycles was characterized by the calculation of their affinity for the fluoride anion, following the method based on DFT calculations[204] developed by Christe and Dixon.[205] Approximate pF$^-$ values (eq 3.4) of 1.13, 2.50 and 3.98 for **36**, **37** and **26**, respectively, were found for the attachment of one fluoride anion to the chalcogen. The pF$^-$ value of **26** lies between those of HF and PF$_3$ on the Christe/Dixon scale.

$$pF^- = \frac{F^-\text{affinity (kcal/mol)}}{10} \qquad 3.4$$

This analysis was extended to examine the effect of the binding of BH$_3$ on the acidity of the molecule. The pF$^-$ values are 3.76, 5.07 and 6.43 for **36**·BH$_3$, **37**·BH$_3$ and **26**·BH$_3$, respectively. This is an approximate increase of 2.5 units for each molecule. This appears to agree with the observation made regarding the association of *N*-*tert*-butyl-1,2,5-chalcogenadiazolium (Se and Te) ions with various donors.[142]

As with the proton case, the equilibrium distances and binding energies were combined in a fluoride affinity map for **26** (Figure 3.14). The most Lewis acidic regions on the map are, as expected, opposite the Te-N single bonds. The size of these Lewis acidic regions suggests that the N-Te--F^- angle would be somewhat tolerant of strain. This map is consistent with the LUMO+1 Fukui function, the charge distribution and the electrostatic surface.

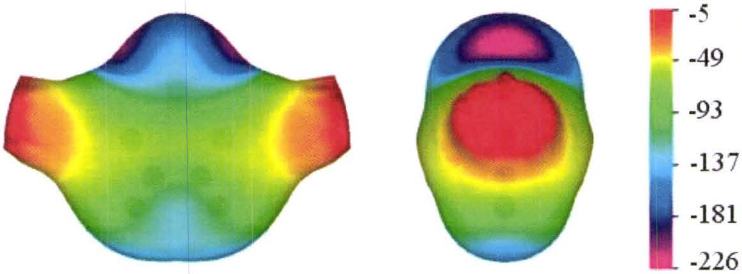

Figure 3.14 Fluoride affinity map of **26**. Energy in kJ/mol.

Experimentally, the Lewis acidity of the site opposite the Te-N bond has been demonstrated by the strong Te-D (D = donor) interactions that occur when, for instance, **26** interacts with solvent molecules. Interactions between substituted benzo-2,1,3-telluradiazoles and either pyridine (Section 8.2) or DMSO[203] (O atom) have been observed in the solid state as well as an intramolecular interaction between Te and one of the aryl rings of BPh_3.[148] The binding energies of model systems, adducts of **36**, **37** and **26** with DMSO, pyridine or benzene, are provided in Table 3.13 where it can be seen that pyridine and DMSO form equally strong interactions while benzene participates in weaker interactions.

Table 3.13 Interaction energy of donor molecules with the 1,2,5-chalcogenadiazoles (kJ/mol).

Donor	S	Se	Te
DMSO	15.3	25.9	39.9
Pyridine	13.9	25.1	41.0
Benzene	5.2	8.6	11.4

AIM and NBO performed on these adducts confirm that there is a strong covalent component in these interactions arising from the mixing of the occupied lone pair (or a pair of π-electrons) from the donor molecule with the low lying $\sigma^*_{E\text{-}N}$ orbitals on the 1,2,5-chalcogenadiazole. This is illustrated by the changes in the occupations of the contributing orbitals or molecules. Table 3.14 summarizes the changes in occupancy for the $\sigma^*_{E\text{-}N}$ orbitals and the donor molecule. The adduct **26**·DMSO is excluded, despite having an optimized geometry, because the NBO program failed to complete due to an irresolvable error. There is a strong correlation between the sum of the $\sigma^*_{E\text{-}N}$ orbital occupancy changes and the interaction energies for pyridine or DMSO as well as the donor molecule population change and the interaction energies for pyridine or DMSO. Despite having almost equal interaction energies with the 1,2,5-chalcogenadiazoles, the extent of donation from pyridine is significantly greater than from DMSO. This would suggest that the covalent contribution to the SBI is more important in pyridine than in DMSO.

Table 3.14 Change in populations (number of electrons) of selected orbitals of the 1,2,5-chalcogenadiazoles or donor molecules upon association.

	Donor	S	Se	Te
ΔEN(A)*[a]	DMSO		0.0156	0.0349
	Pyridine	0.0127	0.0412	0.0696
	Benzene	-0.0003	0.0029	0.0115
ΔEN*	DMSO		0.0081	0.0320
	Pyridine	0.0033	0.0143	0.0492
	Benzene	0.0002	0.0023	0.0105
ΔDonor	DMSO		-0.0383	-0.0759
	Pyridine	-0.0232	-0.0613	-0.1000
	Benzene	0.0002	-0.0062	-0.0191

[a] Antibonding orbital facing the donor

The topological analysis of the electron density revealed bond critical points located between the donor atom and the chalcogen atom for the DMSO and pyridine adducts, and between the C-C bond critical point and the chalcogen atom for the benzene adduct. The densities at the bond critical point for the SBIs increase from S to Te, and also from benzene to DMSO to pyridine. The values of the densities at the critical points are on the same order of magnitude as those calculated for either hydrogen bonds (0.002 to 0.04 au)[191] or halogen SBIs[187] and are approximately an order of magnitude smaller than the E-N bond critical point densities in **36**, **37** and **26** (Table 3.15). The Laplacian is positive in all cases and increases from S to Te. Both the densities and the Laplacian of the densities at the bond critical points increase in magnitude as the SBI becomes stronger, and when plotted against the interaction energies (Figure 3.15), give correlation coefficients of 0.96 and 0.98, respectively. This indicates that, as in the SBIs in the self-associated dimers, the covalent and electrostatic contributions are important and that either is a good measure of the relative interaction strength in these systems.

Table 3.15 AIM bond critical point values for E-D SBIs in 1,2,5-chalcogenadiazole adducts.

	Donor	S	Se	Te
ρ (e/Å^3)	DMSO	0.0134	0.0203	0.0288
	Pyridine	0.0164	0.0268	0.0352
	Benzene	0.0045	0.0072	0.0095
$\nabla^2\rho$ (e/Å^5)	DMSO	0.0469	0.0638	0.0927
	Pyridine	0.0483	0.0670	0.0911
	Benzene	0.0142	0.0206	0.0286

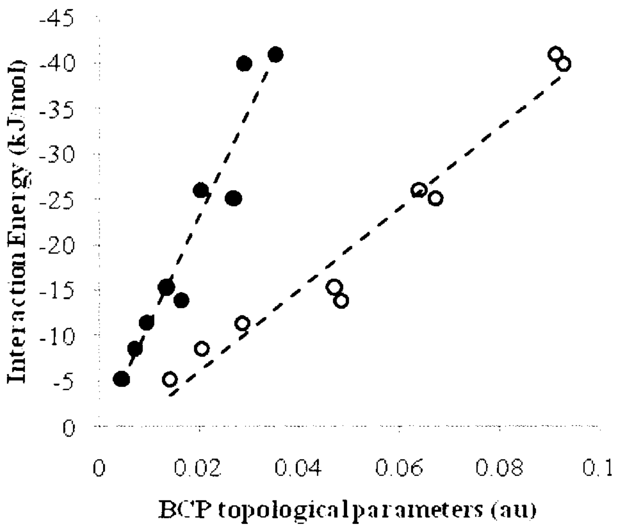

Figure 3.15 Relationship between the density (●) or the Laplacian (○) at the BCP and the interaction energy of the 1,2,5-chalcogenadiazoles with DMSO, pyridine or benzene.

3.2.6 The Effect of C-Substitution on the Dimerization of 1,2,5-Telluradiazoles

The donor-acceptor character of the SBIs does suggest that the self-association strength could be influenced by substituting groups on the carbon atoms (positions 3 and 4) or on a ring fused to those positions. It is, however, not obvious what the effect of electron donating or withdrawing groups should be; thus DFT calculations were used to assess this point. Several mono and disubstituted model 1,2,5-telluradiazoles, and their dimers, with methyl, fluoro, nitro and amino groups were calculated. The mono substituted systems could dimerize in three different geometries (Scheme 3.5). Table 3.16 lists the association energies for the structures considered. In general, the electron donating groups (methyl and amino) have little effect on the strengths of the SBIs. For the monosubstituted rings with electron withdrawing groups, the association energies of the three geometries follows the order I > II > III. Monosubstitution with either the fluoro or nitro group increases the stabilization energy of the supramolecular synthon in I by approximately 20 kJ/mol. The preference for arrangement I is due to the increased polarization of electron density away from Te (

Table 3.17). On the other hand, there is no apparent correlation between secondary bond length and the magnitude of the dimerization energy.

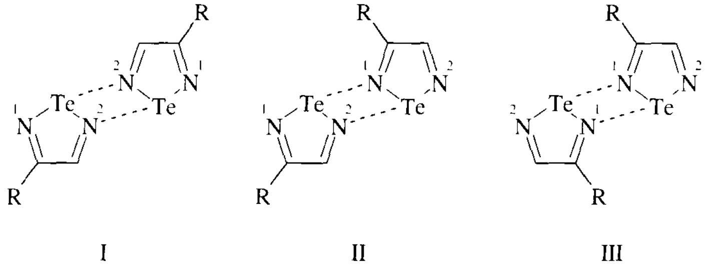

Scheme 3.5 Three possible structures for the dimers of 1,2,5-chalcogenadiazoles functionalized at position 3.

Table 3.16 Dimerization energies and Te-N SBI distances for substituted 1,2,5-telluradiazole dimers.

R1,R2	Geometry	ΔE_{SBI} (kJ/mol)	Te-N (Å)
H,H		-68.2	2.592
H,CH_3	I	-68.8	2.551
H,CH_3	II	-69.0	2.551
H,CH_3	III	-68.6	2.537
CH_3,CH_3		-65.0	2.562
H,NH_2	I	-71.3	2.540
H,NH_2	II	-70.5	2.510
H,NH_2	III	-69.9	2.481
NH_2,NH_2		-67.0	2.507
H,F	I	-87.1	2.612
H,F	II	-75.8	2.572
H,F	III	-64.6	2.587
F,F		-77.2	2.567
H,NO_2	I	-88.1	2.497
H,NO_2	II	-84.1	2.535
H,NO_2	III	-80.7	2.586
NO_2,NO_2		-84.9	2.527

Table 3.17 Hirshfeld and VDD (in parenthesis) atomic charges for substituted 1,2,5-telluradiazole monomers.

R1,R2	Te	N1	N2
H,H	0.29 (0.34)	-0.21 (-0.22)	-0.21 (-0.22)
H,CH_3	0.27 (0.32)	-0.22 (-0.22)	-0.22 (-0.22)
CH_3,CH_3	0.25 (0.30)	-0.23 (-0.23)	-0.23 (-0.23)
H,NH_2	0.26 (0.30)	-0.27 (-0.26)	-0.21 (-0.22)
NH_2,NH_2	0.23 (0.28)	-0.7 (-0.26)	-0.27 (-0.26)
H,F	0.31 (0.37)	-0.22 (-0.23)	-0.20 (-0.21)
F,F	0.34 (0.40)	-0.21 (-0.23)	-0.21 (-0.23)
H,NO_2	0.36 (0.42)	-0.18 (-0.20)	-0.19 (-0.20)
NO_2,NO_2	0.39 (0.46)	-0.17 (-0.19)	-0.17 (-0.19)

3.3 Summary

While previous attempts to apply chalcogen-centered SBIs in supramolecular chemistry have been mostly focused on molecules containing fused sulphur heterocycles and electron-rich functional groups,[162,167] the results of this computational study indicate that the best building blocks should contain the heavier chalcogens. The stability of the $[E\text{-}N]_2$ supramolecular synthon is rooted in the ambiphilic nature of the molecules; their Lewis acidic and basic sites are visualized with maps of electrostatic potential and the Fukui functions. The chalcogen-nitrogen SBI results from both electrostatic and orbital contributions; most prominent is the donation of a lone pair of the nitrogen into the antibonding orbitals of the heavy atom. The thiadiazoles are very weakly bonded and the S···N distance is very long, therefore the SBI in that case is little more than a van der Waals contact. In contrast, the selenium and tellurium heterocycles associate more strongly; the tellurium SBIs being as strong as hydrogen bonds.

The perturbations of molecular geometry and electron density upon supramolecular association together with the possibility of steric interactions imply that the total energy gain due to formation of infinite ribbon chains of heterocycles in the solid state cannot be obtained by simple addition of the SBI energies calculated for the dimers. This is particularly true for telluradiazoles, which have the shortest E···N distances and experience the most significant structural reorganization.

The 1,2,5-chalcogenadiazoles can also engage in heteromolecular association. The Lewis acidity at the chalcogen is maximized by tellurium but it is lower than that of typical Lewis acids such as tricoordinate boron and aluminum. In Section 5.2.3 it will be shown that such Lewis acids disrupt the self-association of these heterocycles. The donor ability of molecules such as DMSO and pyridine towards the 1,2,5-chalcogenadiazoles is calculated to be stronger than one of the SBIs within the $[E\text{-}N]_2$ supramolecular synthon. The interaction with pyridine has similar topology and NBO parameters to the SBIs in the $[E\text{-}N]_2$ supramolecular synthon. The corresponding parameters for DMSO suggest a stronger electrostatic component. Association with such donor molecules should be an important competing interaction with self-association, particularly when the $[E\text{-}N]_2$ supramolecular synthon is weakened, for example by steric repulsion. Chapter 8 will discuss experimental evidence of this in the case of 4,5,6,7-tetrafluorobenzo-2,1,3-telluradiazole.

Perturbations to the electronic structure as a result of Lewis or Brønsted acid N-substitution or the presence of an electron withdrawing group on the periphery of the molecule enhance the strength of the secondary bonding interactions opposite the site of substitution; this is in agreement with experimental investigations of N-substituted rings, this will be discussed in Section 5.2.3.

4 The Products of the Reaction of 1,2-Diaminobenzene with Tellurium Tetrachloride[206, 207]

4.1 Introduction

The DFT analysis presented in Chapter 3 indicated that the $[Te\text{-}N]_2$ supramolecular synthon is both strong and directional, comparable to some hydrogen bonded systems. For these building blocks to be useful in supramolecular chemistry, however, it was necessary to establish a general synthetic method that is applicable to a wide variety of derivatives. To this end, the benzo-2,1,3-telluradiazoles were more desirable as they have additional sites of substitution which can be used to introduce functionality. Previous literature reports described the syntheses of 1,2,5-telluradiazoles starting from the 1,2,5-thia- or 1,2,5-selenadiazoles with magnesium imides as intermediates (eq 4.1).[64,208] Our attempts to apply this method to the synthesis of benzo- and substituted benzo-2,1,3-telluradiazoles did not yield the desired products and, furthermore, attempts to reproduce the synthesis of **26** according to this method failed. Alternative methods have been published for the syntheses of benzo-2,1,3-telluradiazoles, including one in which the benzo-2,1,3-telluradiazole was unexpectedly formed in an attempt to prepare a monomeric tellurium diimide.[65] This method is not applicable to a variety of benzo-2,1,3-telluradiazoles. The direct reaction of $TeCl_4$ with a diamine has been reported and should be a convenient route to substituted benzo-2,1,3-telluradiazoles. These published syntheses use either heat or a base to remove the HCl byproduct.[109,167] These approaches were unsuccessful for the synthesis of **40** because the temperatures required to drive off the HCl led to significant thermal decomposition or because the triethylamine present in the reaction mixture reacted preferentially with $TeCl_4$, yielding an intractable mixture of products.

An alternative approach considered was the solid-state reaction of a diamine with TeO_2 liberating water as a byproduct. The synthesis of benzo-2,1,3-telluradiazole and 4,5-di-methylbenzo-2,1,3-telluradiazole were previously published but it was reported that the reaction yielded the hydrated product (eq 4.5).[209] This reaction has subsequently been utilized to synthesize **40** by using heat to eliminate the water; the yield, however, was only 28%.

For a supramolecular synthesis to be efficient a more convenient, high-yield synthetic method is needed that can be carried out at or below room temperature in order to avoid complications that may arise from thermally sensitive products.

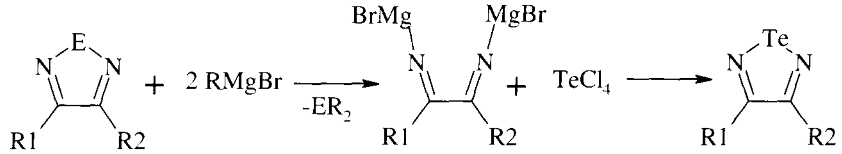

4.1

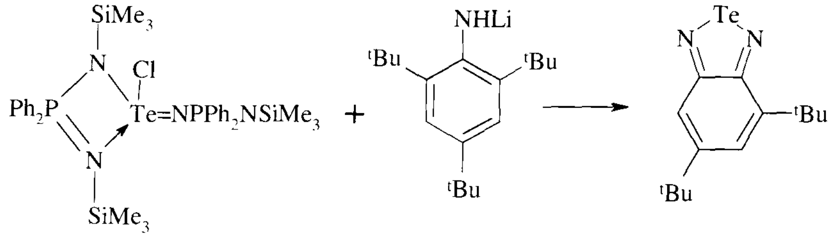

4.2

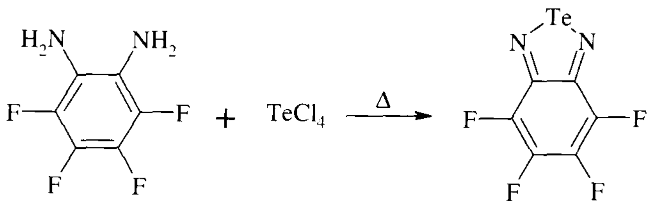

4.3

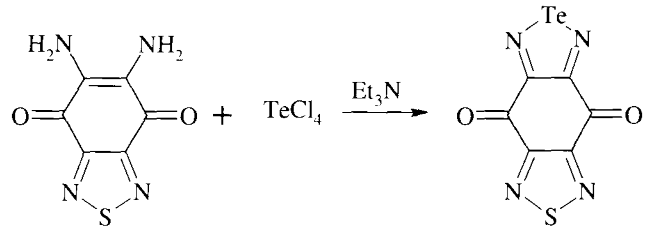

4.4

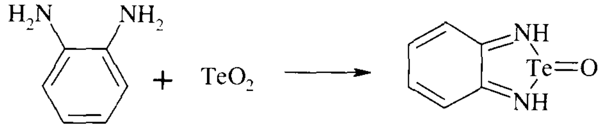

4.5

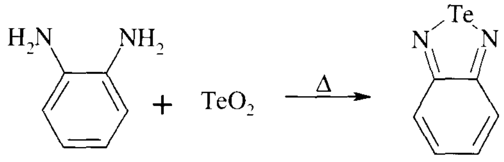

4.6

4.2 Results and Discussion

4.2.1 The Reaction of 1,2-Diaminobenzene with $TeCl_4$

The reaction of $TeCl_4$ with 1,2-diaminobenzene was investigated as a general synthetic method for the synthesis of benzo-2,1,3-telluradiazoles. The reaction was first attempted by adding a toluene solution of $TeCl_4$ to a toluene solution of 1,2-diaminobenzene (eq 4.7). An orange product immediately precipitated that was recovered. NMR spectroscopy in DMSO (30 °C) revealed that the sample consisted of two new products which could not be separated. One product was identified as the hydrochloride salt of 1,2-diaminobenzene and the other product had a splitting pattern consistent with 1,2-disubstitution and, in the IR spectrum, had a vibrational band at 763 cm^{-1} consistent with a Te-N stretch. The EI-MS of this product contained a parent ion at *m/z* 233.9 consistent with **40**, but careful control of the reaction stoichiometry revealed that only two of the four equivalents of HCl were accounted for with the salt of the 1,2-diaminobenzene implying a product with a composition of $TeN_2C_6H_6Cl_2$ (**42**). Attempts to drive off the remaining HCl by dissolution of the reaction mixture in DMSO and heating resulted in the formation of a new product, as determined by NMR, which consumed the starting material, 1,2-diaminobenzene hydrochloride. At 60 °C the reaction proceeded to completion within 12 h. The product was isolated from the neutralized solution and was found to be 1,2-diaminophenazine (**43**). This reaction was also found to proceed slowly at room temperature.

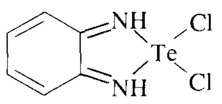

42

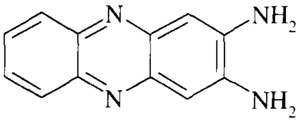

43

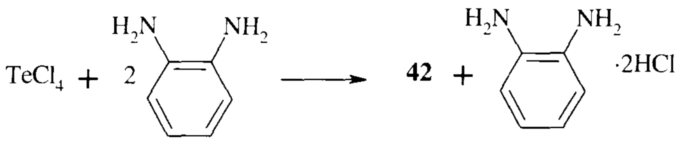

4.7

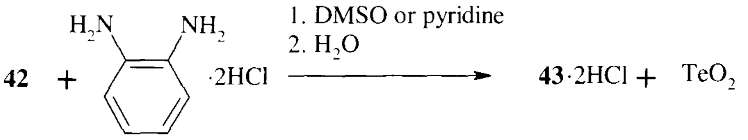

4.8

A base stronger than 1,2-diaminobenzene was required to remove HCl from **42**. Addition of Et_3N to the reaction mixture had no effect as **42** was insoluble, but when the crude product was dissolved in pyridine and followed by treatment with Et_3N or cyclohexylamine, a new solid immediately precipitated which was shown to be **40**. A more efficient route to this product was achieved by mixing a slurry of $TeCl_4$ in pyridine with two equivalents of the appropriate phenylene diamine dissolved in pyridine at room temperature (eq 4.7). This was followed by the addition of four equivalents of triethylamine or cyclohexylamine (eq 4.9). The yield with respect to the diamine was improved by adding equimolar amounts of the diamine and $TeCl_4$.

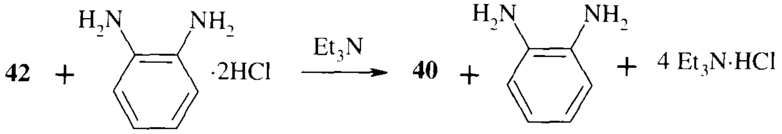

4.9

4.2.2 Formation and Structure of 1,2-Diaminophenazine

Attempts to grow crystals of **42** from pyridine or DMSO solution led to the decomposition product, 1,2-diaminophenazine (**43**). This appeared to result from a cyclic addition (eq 4.8). The identity of this product was determined from the X-ray crystal structure of the HCl salt; the asymmetric unit it shown in Figure 4.1. Although the crystal structure of 1,2-diaminophenazine hydrochloride has been previously reported,[210] the new structure (see Table 4.1 for crystallographic details) is a pseudo-polymorph which contains one molecule of pyridine for every three 1,2-diaminophenazine molecules. The molecules are arranged in helical chains assembled through N(H)-Cl hydrogen bonds. The pyridine molecule fills the voids created between neighbouring chains and the lack of intermolecular interactions with pyridine allows increased thermal motion which is best modelled by a single position.

The formation of this product was followed by NMR spectroscopy and was found to proceed to completion at 60 °C. Neutralization of the DMSO solution liberated the final diamine product in high yield. It is conceivable that the formation of the phenazine proceeds via a hetero-Diels-Alder [4+2] reaction where the '$TeCl_2$' unit in **42** sequesters the diimine[211] which can react with a dienophile, 1,2-diaminobenzene. Without further investigation, it is not possible to determine whether this is a regular or inverse demand Diels-Alder reaction.

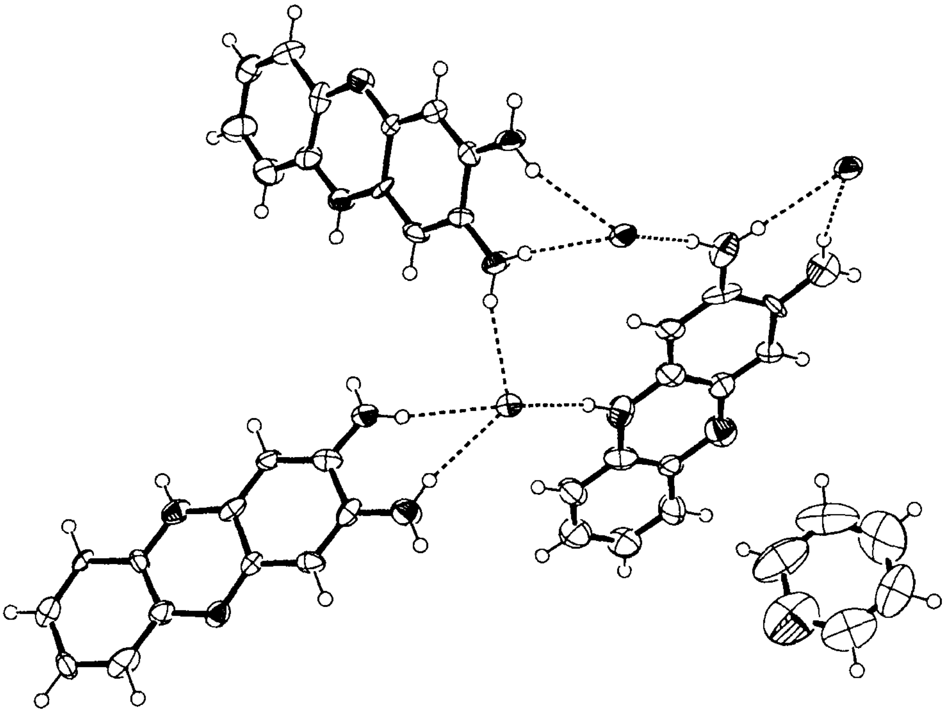

Figure 4.1 ORTEP representation for the asymmetric unit in the crystal structure of **43**. Hydrogen bonds are indicated by dashed lines and thermal ellipsoids are shown at the 50% probability level.

4.2.3 Structure of *N,N'*-Dihydrobenzo-2,1,3-telluradiazolyl Chloride

Slow sublimation of the reaction mixture resulting from eq 4.7 in a sealed tube afforded crystals suitable for X-ray diffraction. Pertinent crystallographic data, and selected bond lengths and angles are provided in Tables 4.1 and 4.2, respectively, for this and other crystal structures discussed in Chapter 4.

Table 4.1 Crystallographic and refinement data for **40**, **42** and **43**.

Compound	**40**	**42**	**43**
Empirical formula	$C_6H_4N_2Te$	$C_6H_6N_2Cl_2Te$	$C_{41}N_{13}H_{38}Cl_3$
Crystal system,	Monoclinic,	Orthorhombic	Triclinic
Space group	C2/c	Pcca	$P\bar{1}$
a [Å]	10.397(5)	11.014(3)	12.600(2)
b [Å]	11.403(6)	4.1788(13)	13.030(2)
c [Å]	22.46(1)	18.816(6)	14.261(2)
α [°]	90.00	90	93.891(9)
β [°]	101.399(9)	90	107.243(9)
γ [°]	90.00	90	115.913(8)
V [Å^3]	2610(2)	866.0(5)	1957.4(5)
Z	16	4	2
ρ(calc.) [g. cm^{-3}]	2.359	2.336	1.159
T [K]	173(2)	293(2)	173(2)
μ [mm^{-1}]	4.457	3.985	0.267
θ range	2.68 – 28.33	2.85 - 24.70	1.54 - 21.97
Limiting indices	$-13 \leq h \leq 13$	$-12 \leq h \leq 11$	$-13 \leq h \leq 13$
	$0 \leq k \leq 15$	$-4 \leq k \leq 3$	$-13 \leq k \leq 13$
	$0 \leq l \leq 29$	$-21 \leq l \leq 22$	$-15 \leq l \leq 14$
Refl. collec./ unique	11312/ 6507	738 / 518	11007 / 4767
R(int.)	0.0552	0.0326	0.1175
No. of parameters	165	55	551
R_1 / wR_2 (I>2σ(I))^a	0.0599/ 0.1672	0.0328 / 0.0599	0.0939 / 0.1900
R_1 / wR_2 for all data^a	0.0687/ 0.1738	0.0588 / 0.0667	0.1961 / 0.2292
Goodness-of-fit on F^2	1.084	0.963	1.046
Larg. diff. peak/ hole [e·Å^{-3}]	1.199/ -1.164	0.602 / -0.659	0.385 / -0.412

^{a} $R_1 = \Sigma ||F_o|-|F_c|| / \Sigma|F_o|$, $wR_2 = \{\Sigma[w(F_o^2-F_c^2)^2] / \Sigma w(F_o^2)^2\}^{1/2}$

Table 4.2 Selected bond lengths (Å) and angles (°) for **40** and **42**.

	40	**42**
Te1-N1	2.015(7)	2.028(5)
Te1-N2	1.988(7)	
Te2-N3	2.007(7)	
Te2-N4	2.001(7)	
N1-C1	1.31(1)	1.321(9)
N2-C6	1.32(1)	
N3-C7	1.33(1)	
N4-C12	1.31(1)	
C1-C6[a]	1.46(1)	1.423(9)
C7-C12	1.48(1)	
N1-Te1-N2	83.7(3)	79.8(2)
N3-Te2-N4	84.0(3)	

[a] C1-C1A for **42**

The structure solution indicates that this is neither a Te(IV) species nor a simple ionic substance. Figure 4.2 portrays the structure of the molecular unit, which occupies a site of C_2 symmetry. The Te-N bond distances are 0.022 Å longer than the average of those observed in **40**. The Cl atoms are located 2.773(2) Å from the tellurium atoms. This distance is significantly shorter than the sum of van der Waals radii (3.81 Å)[5] and is intermediate with respect to the lengths of the terminal (2.311(3) Å) and bridging (2.929(3) Å) bonds of Te_4Cl_{16} units observed in the crystal structure of tellurium tetrachloride.[212] The chalcogen atom environment approximates to square-planar coordination. The plane defined by the Cl1-Te1-Cl1A atoms is rotated by 3.9(3)° from the plane of the heterocycle which causes the Cl atoms to be located 0.167(7) Å above and below this plane. In this respect, the structure resembles that of [(dpp-Bian)TeI_2].[211] The molecules adopt a head-to-tail arrangement along the *c*-axis, with every other molecule rotated by 74.20(8)° relative to its neighbour. These chains stack in the same orientation along the *b*-axis and stack along the *a*-axis with a 180° rotation between adjacent chains. The tellurium atom is also in close contact (3.503(2) Å) with the Cl atoms above and below the molecular plane. The N-H···Cl hydrogen bonds (3.245(6) Å) on each side of the molecule lead to the formation of supramolecular ribbons in the crystal (Figure 4.3).

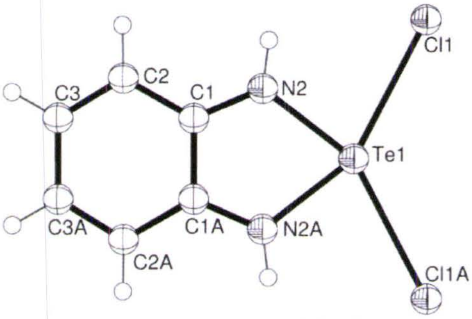

Figure 4.2 Structural unit in the crystal of $C_6H_4(NH)_2TeCl_2$ (**42**).

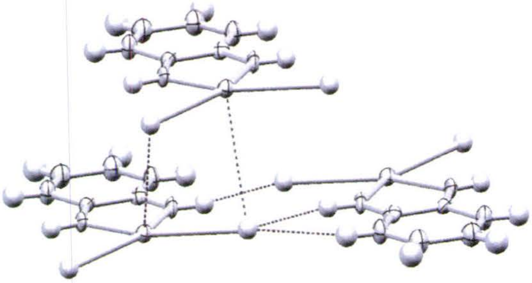

Figure 4.3 Packing in the crystal structure of $C_6H_4(NH)_2TeCl_2$ (**42**).

4.2.4 Structure of Benzo-2,1,3-telluradiazole

Using DFT, reasonable estimations for the stability of polymeric structures were obtained by building short chain models (Section 3.2.3). It was found that the cost of puckering, in order to accommodate the formation of the infinite chains observed in the crystal structure of phenanthrotelluradiazole (**27**), is offset by the very strong binding energy of the $[Te\text{-}N]_2$ supramolecular synthons. On the other hand, H···H steric repulsions between neighbouring molecules would be strong enough to interfere with the formation of the $[E\text{-}N]_2$ synthon in the cases of benzo-2,1,3-thia- (**38**) and benzo-2,1,3-selenadiazole[213] (**39**); the isomorphic crystal structures of these compounds only display very long intermolecular E-N distances and no coplanar association. In contrast, the calculations forecasted the formation of ribbon chains for benzo-2,1,3-telluradiazole (**40**).[214] This appears to be in conflict with the non-associated structure that has been implied for **41**, although actual crystallographic data was not published.[109]

Orange crystals of **40** suitable for X-ray diffraction were grown from a pyridine solution. Although a clean rectangular plate was mounted in the diffractometer, analysis of the scattering data revealed that the sample consisted of multiple crystals. An initial structure was obtained using the data for one component, the remaining components were then integrated separately in order to reach the final solution. An array of infinite ribbon chains, as had been predicted on the basis of the balance of steric repulsions and SBIs, was revealed. The asymmetric unit (Figure 4.4) consists of two molecules of **40** associated through the $[Te\text{-}N]_2$ supramolecular synthon that occupy general positions. The two molecules are almost coplanar (the intermolecular dihedral angle is 2.5(4)°) and are not related by symmetry but their internal dimensions are essentially identical. The Te-N bond distances (average 2.003 Å) are comparable to those observed in the telluradiazoles **26** (2.023(6) Å)[63] and **27** (2.023(6) Å).[64]

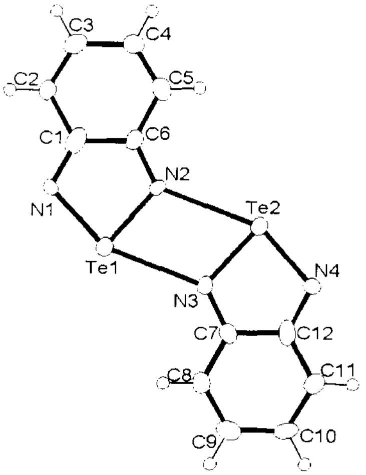

Figure 4.4 ORTEP representation and numbering scheme for the asymmetric unit in the crystal structure of **40**. Thermal ellipsoids are shown at the 50% probability level.

The C-C bond distances within each aromatic ring are unequal; d(C2-C3), d(C4-C5), d(C8-C9) and d(C10-C11) range from 1.32(1) to 1.37(1) Å, while the alternate bond lengths are between 1.40(1) and 1.48(1) Å. The C-N bond distances, 1.31(1)-1.33(1) Å, are typical of double bonds. These features suggest a high degree of double bond localization similar to that observed in the sulfur[192] and selenium[194] analogues. The [Te-N]$_2$ supramolecular synthon is repeated at both ends of the asymmetric unit connecting the molecules, generated by the combination of the C-centering operation and the translation of the unit cell, in order to build the ribbon-polymer chains. Application of the inversion operation to the general and C-centred positions generates parallel ribbons that stack on top of each other at intervals of 3.67(1) and 3.71(1) Å. A c-glide generates another stack of ribbons rotated by 80.59(7)°, completing the crystal structure (Figure 4.5).

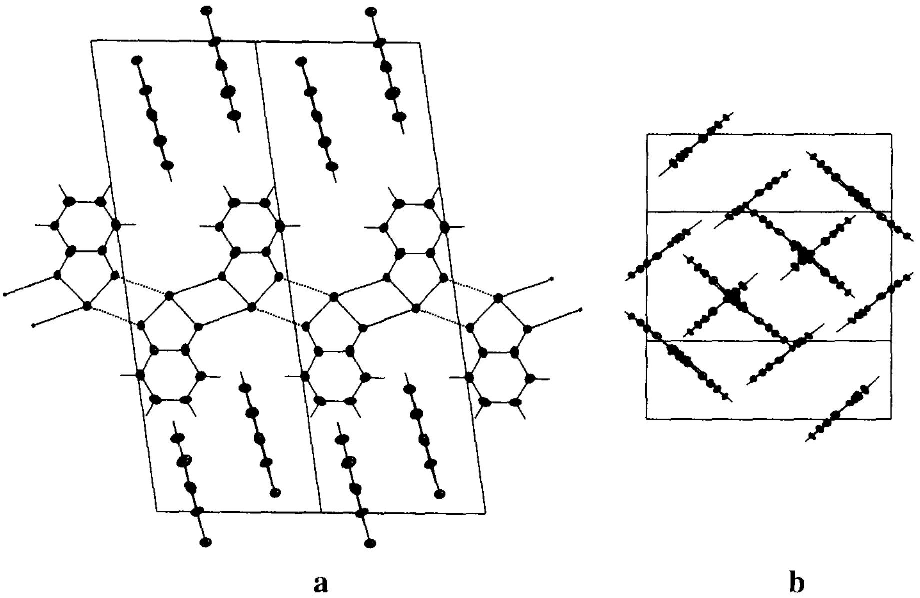

Figure 4.5 Two views of the crystal packing for **40**, (a) along [56-2]; (b) along [10-6]. Thermal ellipsoids are shown at the 50% and 25% probability levels, respectively.

Aside from those in the $[Te\text{-}N]_2$ supramolecular synthon, all the other distances from tellurium to the nearest neighbours are comparable to, or greater than, the sum of van der Waals radii. The average Te-N SBI distance of 2.701(7) Å is comparable to that of **26** (2.764(6))[63] but shorter than the distances observed in **27** (2.825(8) and 2.842(8))[64]. Both **26** and **27** have ribbon-polymer structures but the $[Te\text{-}N]_2$ supramolecular synthon in **27** is elongated to accommodate the steric hindrance between neighbouring phenanthrene rings. The structure of the ribbon polymer of **40** from this crystallographic determination is in excellent agreement with the values that had been estimated from the DFT optimization of a model hexamer chain, both at the intramolecular and supramolecular levels. For example, within the central telluradiazole rings the calculated Te-N distances were 2.054 and 2.055 Å and the Te-N SBI distance calculated at the middle was 2.690 Å. Due to the reorganization of molecular dimensions that takes place upon association, only the dimensions at the center of the model should be compared.

4.2.5 Isomerisation of *N,N'*-Dihydrobenzo-2,1,3-telluradiazolyl Chloride

Two models for $C_6H_4(NH)_2TeCl_2$ were optimized by considering either the experimental near-planar structure or an alternative geometry in which the Cl atoms were positioned above and below the plane of the ring. In the former case the Te-Cl bond was underestimated by 0.163 Å when compared with the experimental Te-Cl bond length, and in the latter the Te-Cl distance was underestimated by 0.154 Å. This study was extended to include all $C_6H_4(NH)_2EX_2$ (E = Se, Te, X = F, Cl, Br, I) molecules. The hypothetical interconversion of the two limiting structures was examined by optimizing the geometries while rotating the EX_2 fragment with respect to the plane of the ring under C_2 point symmetry. The results of these DFT calculations are summarized in Table 4.3 and show that the two geometries are minima on the potential energy surface (Figure 4.6) and that there is a well defined potential barrier for this process. The planar structure, in all cases, is more stable and this is due to the partial delocalization of one chalcogen lone pair into the π-system. The HOMO (33b) is involved in this process and its stabilization is shown in the correlation diagram presented in Figure 4.7. Further stabilization is provided by the HOMO-6 (31b, not shown) which has a similar composition. While the b symmetry of the HOMO is preserved, the energy of this orbital does reach a maximum along the reaction coordinate. The maximum is coincident with the maximum in the potential energy surface and originates in the repulsive interaction between the π lone pair and the E-X bonds. The LUMO and LUMO+1 both have b symmetry but their energy profiles do not correlate with the changes in the energy of the HOMO which rules out the possibility of HOMO-LUMO mixing disguised by the noncrossing rule. The highest occupied orbital of a symmetry is the HOMO-1 throughout the process and is only slightly disturbed by the geometric changes. Overall, this indicates that the isomerisation process is symmetry allowed and therefore can be thermally activated. The disphenoidal TeN_2Cl_2 fragment within the less stable model of $C_6H_4(NH)_2TeCl_2$ features tellurium in oxidation state IV according to the VSEPR model. The isomerisation would therefore imply a formal 2-electron transfer from Te to the π-system. A similar geometric arrangement for the TeN_2Cl_2 fragment has been observed in other tellurium compounds, for example in $Cl_2Te(\mu\text{-}N^tBu)_2Sb[N(H)^tBu]$ where the Te-Cl bond distances are as long as 2.657(3) and 2.695(3) Å.[215]

Table 4.3 Difference of energy, ΔE_1 and conversion barrier, ΔE_2 for isomerisation of $C_6H_4(NH)_2EX_2$ (E = Se, Te; X = F, Cl, Br, I). Energies given in kJ/mol.

	Se		Te	
	ΔE_1	ΔE_2	ΔE_1	ΔE_2
F	-13.4	45.0	-24.5	17.7
Cl	-44.8	18.7	-59.8	5.4
Br	-48.3	12.5	-64.1	3.6
I	-49.8	7.8	-69.6	0.6

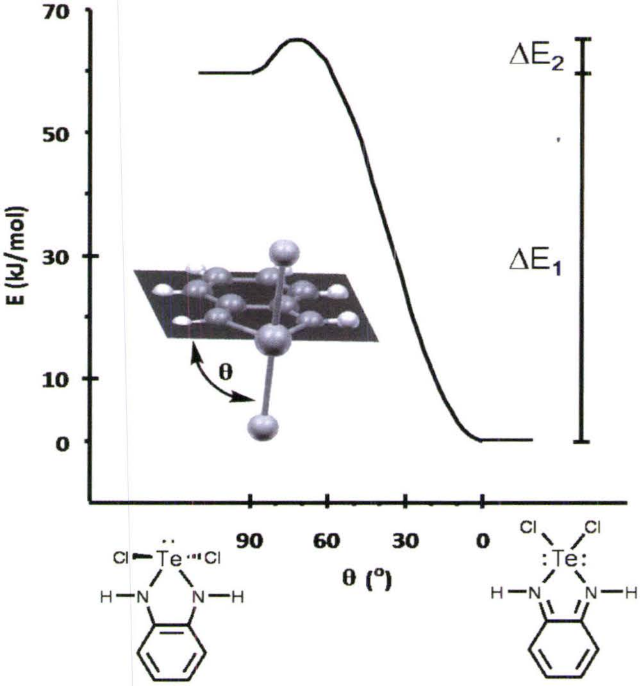

Figure 4.6 Potential energy surface for the isomerisation of $C_6H_4(NH)_2TeCl_2$ (**42**) under C_2 symmetry.

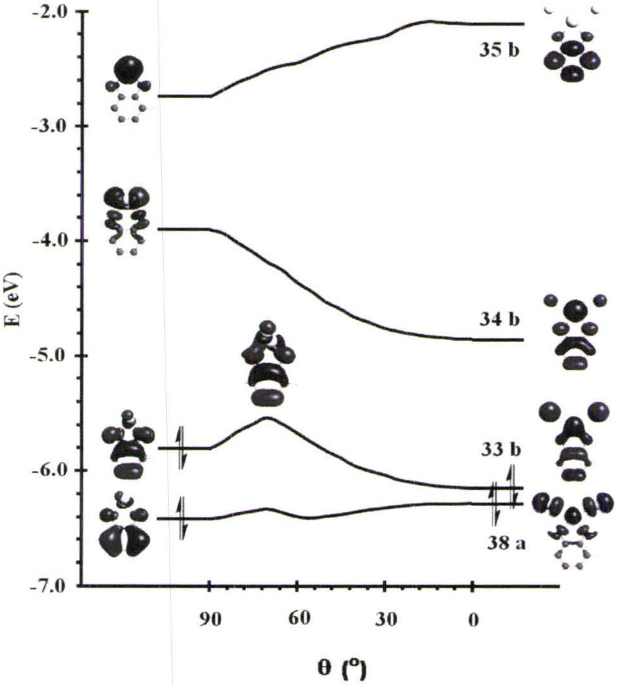

Figure 4.7 Correlation diagram for the isomerisation of $C_6H_4(NH)_2TeCl_2$ (**42**) under C_2 symmetry.

4.3 Summary

The synthesis of benzo-2,1,3-telluradiazoles from $TeCl_4$ and an *ortho*-phenylenediamine, using a base to remove HCl, is a fast and convenient method that should be able to produce a wide variety of benzo-2,1,3-telluradiazoles. The initial product of the reaction was found to be a Te(II) species which can be interpreted as a molecule of benzo-2,1,3-telluradiazole that is N-capped by two protons while the Te centre engage in SBIs with two chloride anions. The reaction mixture of this species and phenylenediamine undergoes a [4+2] cycloaddition reaction that goes to completion above 60 °C.

The calculations discussed both here and in Chapter 3 have successfully explained and predicted the basic supramolecular structures derived from chalcogenadiazoles. Despite the intrinsic limitations, DFT reproduced, with remarkable accuracy, the dimensions related to the SBIs. This does not result from a fortuitous cancellation of errors, but rather from the high degree of covalency in tellurium-centered SBIs which minimizes the relevance of dispersion forces and basis-set superposition errors. In the case of the benzo-derivatives, **38** and **39**, the S-N and Se-N SBIs are not strong enough to overcome the repulsion between hydrogen atoms and no coplanar association can take place. In contrast, the Te-N SBIs are strong enough to form the ribbon polymer.

5 The Effect of Steric Hindrance on the Association of Telluradiazoles through Te–N Secondary Bonding Interactions[216]

5.1 Introduction

Having identified a strong and directional supramolecular synthon, strategies must be devised to exert control over its formation. This is particularly true for the [Te-N]$_2$ supramolecular synthon assembled by association of telluradiazoles as they often form very stable ribbon polymers that have low solubilities.[63,64,150] Such strategies would be necessary for applications involving self-association in solution or in the liquid phase.

The crystal structure of **31**[65] provided an example of how this could be achieved by the placement of substituent groups in appropriate positions on the benzene ring. This concept is tested in this chapter by incorporating a smaller group placed strategically on the heterocycle. A second strategy that could be used is to physically limit the self-association by capping the donor atoms. This was concurrently demonstrated by other research groups who N-alkylated or N-arylated chalcogenadiazole molecules. In these cases, N-capping limits the self-associated 1,2,5-telluradiazoles to dimers,[142,145] but more interestingly, this strategy allowed monomeric,[217] dimeric[143,144] and trimeric[218] 1,2,5-selenadiazole supramolecular aggregates to be isolated. Similar systems, however, have been found to engage in short interactions with the counterion, which competes with self-association.[143-145] In this chapter, the use of N-capping with a Lewis acid is explored as an alternative means to control the self-association of benzo-2,1,3-telluradiazoles.

5.2 Results and Discussion

5.2.1 The Effect of Steric Hindrance from 4,7-Dibromobenzo-2,1,3-telluradiazole on $[Te\text{-}N]_2$

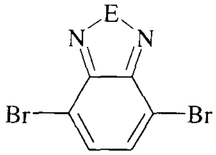

44 E = S
45 E = Se
46 E = Te

Because DFT calculations have successfully predicted the association of **40** into a ribbon chain and have provided excellent SBI distances, an attempt was made to test the ability of the method to deal with greater steric demands. The very large *tert*-butyl substituents in **31** restrict supramolecular association to discrete dimers.[65] Instead of resorting to such voluminous groups, smaller bromine atoms were considered in the target compound **46**, raising the question; what supramolecular structure would be obtained? The first possibility is a ribbon polymer having longer SBIs as in **27**, the second is a coplanar dimer and the third is an alternative helical chain based on the crystallographic structures of some tellurazoles.[47,53] The computational method succeeded in optimizing a coplanar dimer. In the system with three molecules, the calculation predicted an associated dimer with the third molecule appearing to have the tellurium atom oriented towards the nitrogen atom with the bromine-bromine repulsion preventing the formation of the second supramolecular synthon (Figure 5.1). The target compound, **46**, was prepared and crystallized from DMSO. Two crystalline phases were readily identified, separated by hand, and analyzed by X-ray diffraction.

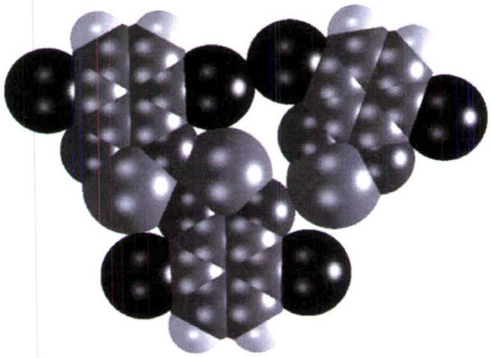

Figure 5.1 Optimized arrangement of a set of three molecules of **46**.

Analysis of the data collected from the diffraction experiment for the first phase indicated that the crystals were twinned. The diffraction data was processed by first classifying the reflections in two different sets and then applying an appropriate rotation matrix to one set to align it with the other. After the final structure was solved, the fraction of the minor component was refined to 44.1%. The asymmetric unit consists of one molecule of **46** which is connected through the $[Te\text{-}N]_2$ supramolecular synthon to the molecule generated by an inversion and unit cell translation along the *b*-axis to form a discrete dimer as was predicted by the computational method. The dimers are arranged in parallel planes that stack with a 3.518 Å spacing along [10-2] (Figure 5.2). The intramolecular Te-N bond distances of **46**, 1.994(8) and 1.982(7) Å, are statistically equal to each other and to those measured in **31**, 2.006(4) and 2.002(3) Å,[65] but slightly shorter than the values calculated for the model $\mathbf{46}_2$, 2.024 and 2.041 Å. In this case, the bond distances also indicate a high degree of double bond localization. The Te-N SBI length, 2.697(8) Å, is shorter than observed in **31**, 2.764(6) Å,[65] but longer than 2.620 Å, which was calculated for the $\mathbf{46}_2$ model.

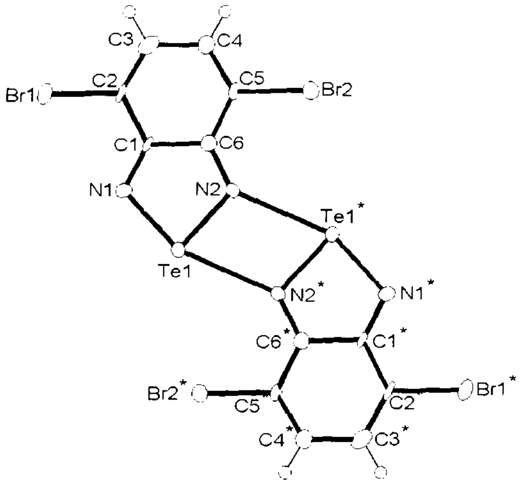

Figure 5.2 ORTEP representation and numbering scheme for the asymmetric unit plus the unit at -x,-y+1,-z in the crystal structure of **46**. Thermal ellipsoids are shown at the 50% probability level.

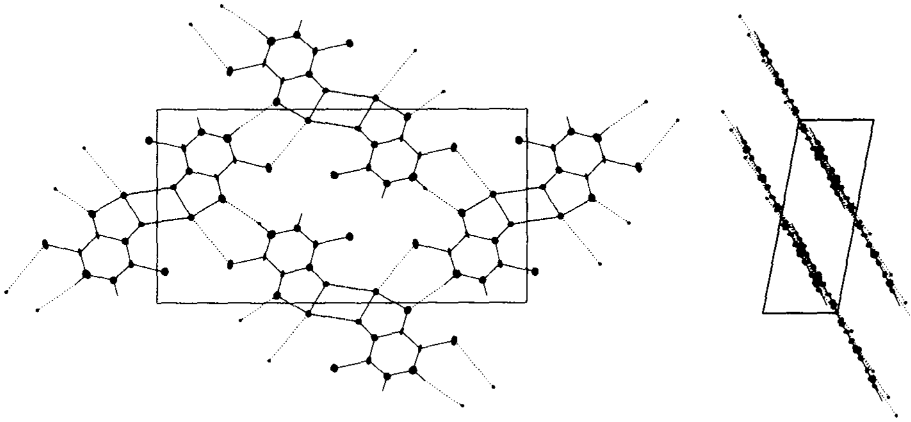

a **b**

Figure 5.3 Two views of the unit cell of **46**. (a) along [100]; (b) along [010]. Thermal ellipsoids are shown at the 50% and 25% probability levels, respectively.

Table 5.1 Crystallographic and refinement data for **46**, **46**·DMSO, **47** and **48**.

Compound	**46**	**46**·DMSO	**47**	**48**
Empirical formula	$C_6H_2Br_2N_2Te$	$C_8H_8Br_2N_2TeSO$	$C_{42}H_{34}B_2N_2Te_1$	$C_{24}H_{19}B_1N_2Te_1$
Crystal system, Space group	Monoclinic, $P2_1/c$	Triclinic, $P\bar{1}$	Monoclinic $P2_1/c$	Monoclinic $P2_1/c$
a [Å]	3.9476(9)	6.905(2)	13.0123(7)	8.0389(6)
b [Å]	19.707(4)	8.431(2)	15.2679(6)	32.245(3)
c [Å]	10.501(2)	11.932(3)	17.828(1)	15.754(1)
α [°]	90.00	100.118(7)	90	90
β [°]	100.755(7)	104.354(7)	106.256(4)	90.755(1)
γ [°]	90.00	109.822(7)	90	90
V [$Å^3$]	802.6(3)	606.8(2)	3400.3(3)	4083.2(6)
Z	4	2	4	8
ρ(calc.) [g. cm^{-3}]	3.224	2.559	1.399	1.542
T [K]	173(2)	173(2)	286(2)	296(2)
μ [mm^{-1}]	13.591	2.559	0.908	1.468
θ range	1.97 – 28.55	1.84 – 36.28	1.63-24.69	1.26-26.47
Limiting indices	$-5 \leq h \leq 5$	$-9 \leq h \leq 11$	$-15 \leq h \leq 15$	$-10 \leq h \leq 10$
	$-25\ k \leq 25$	$-13 \leq k \leq 10$	$-17 \leq k \leq 17$	$-40 \leq k \leq 40$
	$-13 \leq l \leq 13$	$-19 \leq l \leq 17$	$-20 \leq l \leq 17$	$-19 \leq l \leq 18$
Refl. collec./ unique	6913/ 1914	11043/ 4994	41888 / 15197	8396 / 4271
R(int)	0.0639	0.0485	0	0.1341
No. of parameters	102	137	517	506
R_1 / wR_2 ($I>2\sigma(I)$)[a]	0.0432/ 0.0913	0.0506/ 0.1028	0.0393 / 0.0504	0.0710 / 0.1487
R_1 / wR_2 for all data[a]	0.0568/ 0.0954	0.1134/ 0.1242	0.1428 / 0.0712	0.1731 / 0.1836
Goodness-of-fit on F^2	1.040	0.957	0.564	1.014
Larg. diff. peak/ hole [e·$Å^{-3}$]	2.080/ -1.161	2.157/ -2.560	2.813 / -1.465	1.187 / -1.034

[a] $R_1 = \Sigma\ \|\|F_o\|-\|F_c\|\| / \Sigma\|F_o\|$, $wR_2 = \{\Sigma[w(F_o^2-F_c^2)^2] / \Sigma w(F_o^2)^2\}^{½}$

Table 5.2 Selected bond lengths and angles [Å, °] for **46** and **46**·DMSO.

	46	**46**·DMSO
Te1-N1	1.994(8)	2.002(5)
Te1-N2	1.982(7)	2.000(5)
Te2-N3		
Te2-N4		
N1-C1	1.30(1)	1.311(7)
N2-C6	1.31(1)	1.320(7)
N3-C7		
N4-C12		
C1-C6	1.51(1)	1.474(8)
C7-C12		
N1-Te1-N2	85.5(3)	85.1(2)
N3-Te2-N4	-	-

Interestingly, the dimers in the crystal of **46** appear to engage in SBIs with other molecules in the same plane (Figure 5.3a). The Br1 atom is in close proximity to Br2 (3.506(2) Å) and Te1 (3.683(1) Å) in a dimer generated by a screw axis followed by a unit cell translation along the *a*-axis; the two contacts are shorter than the sum of the van der Waals radii (3.70 and 3.91 Å, respectively).[219] All interplane contacts are comparable to the sum of van der Waals radii. A detailed analysis of the in-plane interactions was conducted by optimizing the tetramer model **46-46**$_2$**-46** as observed in the crystal structure (Scheme 5.1). The interaction energy was decomposed as described by eq 5.1, where ΔE_{Reorg} is the energetic cost of the geometrical changes that take place upon interaction, $\Delta E_{Binding}$ is the energy of formation the SBI between the building blocks and ΔE_{BSSE} is the basis set superposition error. The results are summarized in Table 5.3. A similar scheme was previously employed to describe these types of systems[214] but in this case, the zero point energy, which would be a small contribution, was not calculated. Instead, the potentially more significant ΔE_{BSSE} values are included; these are much smaller than the total interaction energies and are naturally dependent on the size of the model.

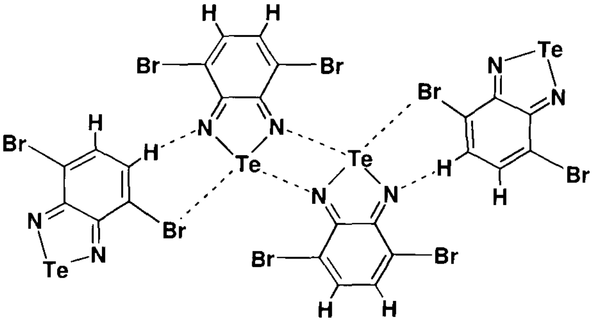

Scheme 5.1 Supramolecular arrangement in the crystal of **46**.

$$\Delta E_{Total} = \Delta E_{Reorg} + \Delta E_{Binding} + \Delta E_{BSSE} \qquad 5.1$$

Table 5.3 Contributions to the energy of interaction (kJ/mol) for the supramolecular structure of **46**.

	[Te-N]$_2$ Synthon		Other SBIs			
	$\Delta E_{Binding}$	ΔE_{Reorg}	$\Delta E_{Binding}$	ΔE_{Reorg}	ΔE_{BSSE}	ΔE_{Total}
46$_2$	-90.91	13.22			5.46	-72.23
46-46$_2$**-46**	-90.31	13.88	-38.97	1.20	15.32	-98.88
46$_2$·DMSO$_2$	-89.76	16.28	-92.86	4.98	12.3	-149.06

Structural optimization of the extended model **46-46**$_2$**-46** did not have a discernable effect on intramolecular distances and angles, but did elongate the Te-N SBI to 2.663 Å. There was a small energetic cost for this but an overall stabilization by the additional SBIs was observed. The Br-Br contact appears as though it could be a halogen bond, with one bromine acting as a donor and the other as an acceptor.[18] Calculations performed on two molecules of **46** associated through the Br-Br interaction provided an optimized Br-Br distance of 3.500 Å and an estimated total association energy of only 0.88 kJ/mol. On the other hand, the Te-Br SBI was optimized at 3.633 Å and a total association energy of 19.66 kJ/mol was calculated. The Te-Br SBI, however, appears to be supplemented by a weak hydrogen bond (C3-H2···N1). The H-bond contribution was estimated to be 8.60 kJ/mol by replacing Br with H as seen in Scheme 5.2.

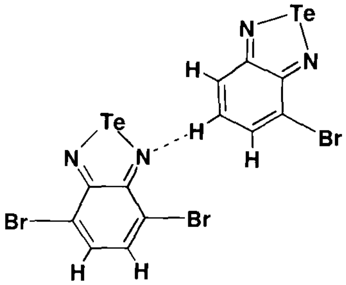

Scheme 5.2 Isolation of H-bond contribution to dimer of **46**.

5.2.2 Heteromolecular Association with a Lewis Base

Single-crystal X-ray diffraction of the second phase obtained by the crystallization of **46** from DMSO revealed a pseudopolymorphic phase consisting of a DMSO solvated dimer. The powder XRD pattern of the bulk sample showed peaks that corresponded only to the Miller indices of the unsolvated phase, suggesting that the pseudopolymorph is a very minor component. The asymmetric unit contained one molecule of **46** and one molecule of DMSO bound by a Te-O SBI. The inversion center generates the other half of the dimeric structure (Figure 5.4). A Te-DMSO SBI (2.82-2.91 Å) has only been observed in the case of 2,2,7,7-tetraiodo-1,3,6,8-tetrahydrobenzo[1,2-*c*;3,4-*c*']ditellurophene.[220]

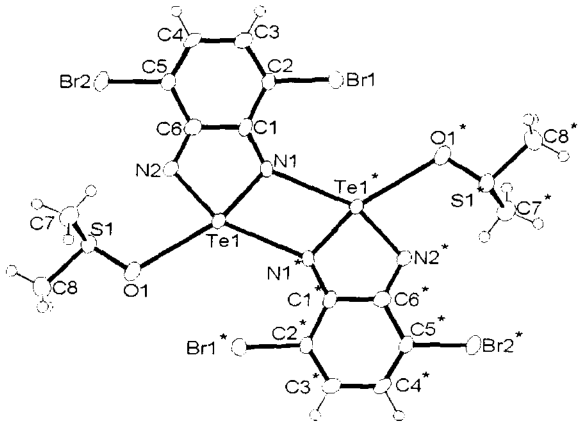

Figure 5.4 ORTEP representation and numbering scheme for the asymmetric unit plus the molecule at -x+1,-y+2,-z in the crystal structure of **46**·DMSO. Thermal ellipsoids are shown at the 50% probability level.

The structure of the solvated dimer was fully optimized using DFT which was also used to evaluate the strengths of the SBIs (Table 5.3). The calculations indicated that the two solvent molecules that are bonded to tellurium provide 87.88 kJ/mol of stabilization compared to the 73.48 kJ/mol that results from the $[Te\text{-}N]_2$ supramolecular synthon. The calculated Te-O SBI distance is 2.737 Å while the experimental value is 2.834(5) Å. Additionally, in the optimized geometry the oxygen atoms appear in the plane of the rings while the crystal structure shows a deviation of 0.240(5) Å. These deviations probably result from crystal packing. The calculation indicates that DMSO solvation results in the lengthening of the Te-N SBI distance to 2.728 Å, which is consistent with the experimental distance, 2.744(4) Å.

5.2.3 The Effects of N-Capping Benzo-2,1,3-telluradiazole with Triphenylborane

The incorporation of the dibromo substituents demonstrated that control over the supramolecular association is possible using steric hindrance. Using a Lewis acid to cap the nitrogen atoms was also envisioned as a viable method for controlling supramolecular aggregation. By modifying the ratio of cap to supramolecular building block, different chain lengths could, in principle, be isolated.

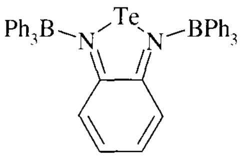

47

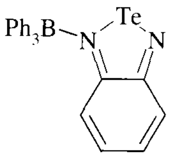

48

Both the 2:1 (**47**) and 1:1 (**48**) triphenylborane (BPh_3) adducts were isolated by using the appropriate stoichiometry of reactants in toluene. The products were isolated in micro-crystalline form and fully characterized. Crystals of **47** suitable for an X-ray crystal structure determination were grown from a 1:1 (v/v) mixture of bromobenzene and acetonitrile while crystals of **48** were grown from toluene. The crystallographic and refinement data are given in Table 5.1 and selected bond lengths and angles are provided in Table 5.4

Table 5.4 Selected bond lengths (Å) and angles (°) for **47** and **48**.

	47	**48**	**48**[a]
Te1-N1	1.996(2)	1.977(8)	1.998(9)
Te1-N2	2.006(2)	2.056(7)	2.048(8)
N1-B1	1.629(3)	1.65(1)	1.62(1)
N2-B2	1.66(3)		
N1-C1	1.336(2)	1.34(1)	1.33(1)
N2-C6	1.338(2)	1.31(1)	1.30(1)
C1-C6	1.450(2)	1.46(1)	
N1-Te1-N2	81.79(2)	82.3(3)	82.5(3)
Te1-N1-B1	116.0(1)	118.1(6)	119.2(6)
Te1-N2-B2	115.1(1)		
N1-B1-C11	100.2(2)	102.1(7)	102.8(8)
N1-B1-C21	108.8(2)	108.6(8)	108.7(8)
N1-B1-C31	108.0(2)	107.9(7)	107.8(8)
N2-B2-C41	101.2(2)		
N2-B2-C51	108.6(2)		
N2-B2-C61	108.8(2)		

[a] Second molecule in asymmetric unit

The asymmetric unit of **47** (Figure 1) contains a molecule of **40** with BPh_3 attached to each nitrogen atom. Although **47** occupies a general position, the structure approximates C_2 symmetry. Two of the phenyl rings hinder access to the chalcogen, preventing further association with a Lewis base. This would be the first example of a $C_2N_2Te^{II}$ ring that does not appear to be associated to another heterocyclic molecule, solvent, anion or donor atom through the tellurium in the solid state. The aromatic ring, however, appears to be involved in a Te-centered interaction. The N-B-C bond angle is significantly smaller for the rings next to the tellurium atom. These rings exhibit short distances from their centroids to Te (3.1188(2) and 3.1311(2) Å). Similar Te-aryl interactions have been examined by Zukerman-Schpector and Haiduc,[34] but in **47** the distances from Te to the centroids of the rings are significantly less than the value reported for the shortest contact of this type (3.482 Å).[221] On closer inspection, the chalcogen is in contact (2.801(2) Å) with an atom of one ring while for the other ring, the shortest distance (2.7925(2) Å) is to the centroid of a C-C bond. All these distances are shorter than the sum of Te and C van der Waals radii (3.76 Å). The Te-N bond lengths of **47** are comparable to those observed in the ribbon polymer of **40** (2.003(7) Å) and dimers of **46** (1.988(8) Å unsolvated, 2.001(5) Å DMSO-solvated).[203] The DFT-optimized geometry of **47** under C_2 symmetry reproduces all the major structural features.

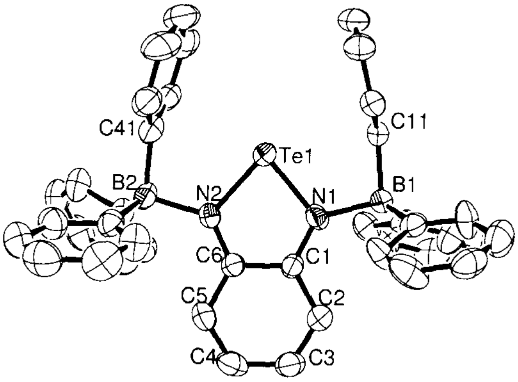

Figure 5.5 ORTEP (50% probability) of the asymmetric unit in the crystal of **47**. Hydrogen atoms and disordered atoms are omitted.

The crystal structure of **48** (Figure 5.6) confirmed the binding of one borane molecule to each heterocycle. Because one of the nitrogen atoms and the chalcogen atom in this 1:1 adduct are capable of forming secondary bonds, a dimer is formed by the [Te-N]$_2$ supramolecular synthon. Although **48**$_2$ is, in principle, centrosymmetric, its placement on a general position duplicates the geometrical parameters. In this case, the Te-N supramolecular contacts (2.591(9) and 2.580(8) Å) are ca. 0.1 Å shorter than those in the dimer of **46** (2.697(8) Å)[8] but almost 0.2 Å longer than in the analogous structure of the *N*-methyl benzotelluradiazolium cation (2.471(3) Å)[145] and almost 0.3 Å longer than in the *N-tert*-butyl telluradiazolium cation (2.301(5) Å).[142] As is observed in the telluradiazolium cations, the Te-N bond opposite to the secondary interaction is significantly longer than the other within each heterocycle. The structure of **48**$_2$ also displays short distances from the heavy atoms to the aromatic rings ($d_{\text{Te-centroid(C-C)}}$ = 2.9157(7), 2.9487(7) Å; $d_{\text{Te-centroid(Ph)}}$ = 3.4108(7), 3.4179(8) Å) with N-B-C angles which are smaller for the phenyl ring that interacts with the Te atom. The DFT-optimized geometry of **48**$_2$ reproduces all the major structural features.

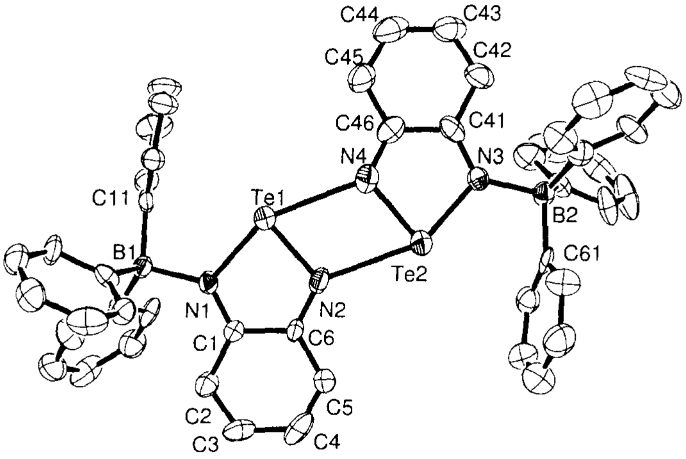

Figure 5.6 ORTEP (50% probability) of the asymmetric unit in the crystal of **48**$_2$. Hydrogen atoms are omitted.

Because the shorter secondary bonding distances suggest that the supramolecular interactions might be stronger in the borane adducts than in the parent heterocycles, the association energies were estimated from the DFT total bonding energies by considering the reaction enthalpies for eqs 5.2 to 5.5; the numbers include contributions from structural relaxation but not BSSE or ZPE corrections, which are very small in closely related systems.[203] The average B-N bond energy from eqs 5.2 and 5.3 (126.2 kJ/mol) is within the range of ab initio binding energies for a number of simple Lewis base-borane adducts (59.8–230.8 kJ/mol).[188,222] The enthalpies from eqs 5.2 and 5.6 indicate that the secondary bonding interactions are indeed stronger in the borane adduct. This enhancement of binding energy was analyzed considering three contributions: (1) the Pauli (steric) repulsive contribution that arises from the interaction of completely occupied orbitals, (2) the electrostatic contribution that results from the local dipole moments, and (3) the interaction of empty and occupied orbitals. The Pauli repulsion and the electrostatic interaction was stabilizing by 57.6 and 25.4 kJ/mol, respectively, while the orbital interaction was destabilizing by 74.5 kJ/mol. The net stabilization of the Te-N intermolecular interactions in $\mathbf{48}_2$ is therefore primarily the result of the charge redistribution.

$\mathbf{40} + BPh_3 \rightarrow \mathbf{48}$ $\Delta H = -125.1$ kJ/mol 5.2

$\mathbf{48} + BPh_3 \rightarrow \mathbf{47}$ $\Delta H = -123.5$ kJ/mol 5.3

$\mathbf{40}_2 + 2\ BPh_3 \rightarrow \mathbf{48}_2$ $\Delta H = -259.8$ kJ/mol 5.4

$\mathbf{40} + \mathbf{40} \rightarrow \mathbf{40}_2$ $\Delta H = -67.5$ kJ/mol 5.5

$\mathbf{48} + \mathbf{48} \rightarrow \mathbf{48}_2$ $\Delta H = -75.9$ kJ/mol 5.6

5.2.4 Solution Behaviour of N-Capped Benzo-2,1,3-telluradiazoles

In addition to serving as examples of supramolecular control, systems isolated with neutral N-caps are neutral analogues of the mono- and di-cations derived by formal N-alkylation of 1,2,5-chalcogenadiazolyl heterocycles that have received increasing attention because of their intriguing structural and chemical properties. In spite of Coulombic repulsion, the monoalkylated selenium[143,144,223] and tellurium[142,145] rings can form dimers that are characteristic of the crystal structures of the parent heterocyles[214] with even shorter secondary-bonding distances. The existence of such aggregates in solution has been proposed as an explanation for the singular redox behaviour of the *N*-methyl benzotelluradiazolium cation, when compared with its lighter congeners, which prevented the observation of the corresponding neutral free radical by EPR.[145]

At room temperature, the ^{1}H NMR spectrum of **47** in solution displays, as expected, two resonances for the protons of the benzotelluradiazole moiety. The corresponding resonances in the spectrum of **48**$_2$ appeared as very broad peaks in d_8-toluene, d_6-benzene and d_2-dichloromethane. Analysis of VT experiments in d_8-toluene (Figure 5.7) confirmed the presence of a dynamic exchange process. While two resonances were clearly defined above 340 K, three resonances were resolved below 250 K, the fourth was obscured by other aromatic resonances. Line shape analysis for the proton exchange in positions 4 and 7 of the heterocycle gave a concentration-independent activation energy of 83 ± 9 kJ/mol. Although the magnitude of this activation barrier is comparable to the supramolecular association energy calculated for **48**, the high-temperature ^{1}H NMR spectrum implies that the dynamic process includes a rapid shift of the BPh_3 moiety between the two nitrogen atoms. This behaviour is also observed in the 1:1 adduct of pyrazine and BPh_3, for which VT experiments gave an activation barrier of 78 ± 8 kJ/mol. DFT calculations provide an estimate of 102.1 kJ/mol for the association of BPh_3 to pyrazine. These observations suggest that the VT ^{1}H NMR spectrum of **48**$_2$ does not reflect the simple dissociation of the dimer and that dissociation of the B-N bond is the most important, if not the only, contribution to the activation barrier.

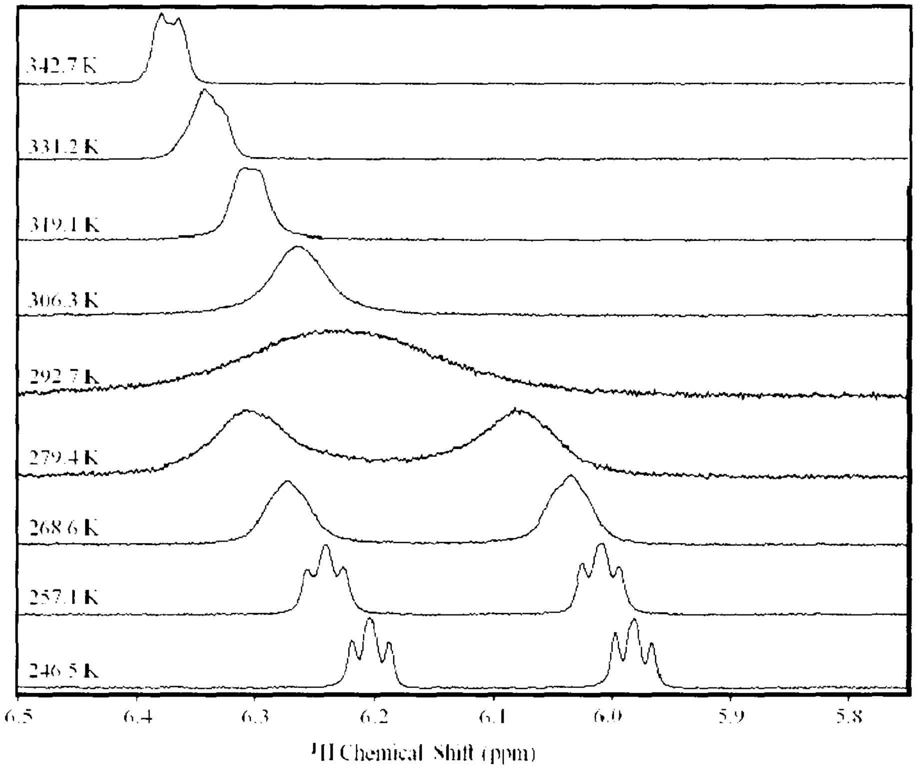

Figure 5.7 Resonances of the ortho (4, 7) protons in the benzo moiety of **48_2** in d_8-toluene solution at different temperatures.

The ^{125}Te resonance shifted to lower frequencies upon attachment of each BPh_3 molecule; from 2401 ppm in **40** to 2203 ppm in **48_2**, and 2188 ppm in **47**. A similar trend was observed for the resonances of the benzo protons when extrapolated to 306.3 K. Atomic charges were calculated in order to examine the influence of the Lewis acid on the electron density as a possible explanation for this trend. Mulliken and Natural Population (NPA) analyses, Hirshfeld and Atoms-In-Molecules (AIM) charges, and the Voronoi Deformation Densities (VDD) were evaluated under the PW91 GGA and the B3LYP hybrid exchange-correlation functionals with the DZ DZP, TZP and TZ2P basis sets and the ZORA relativistic correction. As it is often the case,[224,225] the Mulliken, AIM and NPA charges each varied with the choice of basis set and exchange-correlation functional, precluding a meaningful interpretation. Density-based charges (Hirshfeld and VDD) were less dependent on the basis set and functional; Table 5.5 summarizes these results. While the dimerization of **40** and **48** causes minimal changes to the charges, formation of the B-N bond has a more significant influence. The most significant increases of positive charge are located at the tellurium atom and in the benzo moiety. The positive charge on boron decreases and the phenyl rings acquire a more negative charge; this change is less pronounced, however, on the aromatic ring which is in contact with the chalcogen. Consequently, the observed changes of ^1H and ^{125}Te chemical shifts upon borane coordination are probably due to depletion of π electron density on the benzo ring and the anisotropic shielding of tellurium by the phenyl rings.

Table 5.5 Hirshfeld and VDD (in parentheses) atomic/group charges (au) for **40**, BPh_3 and their adducts calculated using PW91 with the TZP basis set.

	40	**40**$_2$	BPh_3	**48**	**48**$_2$	**47**
Te	0.37 (0.32)	0.36 (0.30)		0.47 (0.39)	0.47 (0.36)	0.58 (0.63)
N	-0.23 (-0.23)	-0.20 (-0.19)		-0.23 (-0.23)		
N_B				-0.08 (-0.08)	-0.09 (-0.09)	-0.09 (-0.10)
N_{SBI}		-0.24 (-0.24)			-0.19 (-0.19)	
C_6H_4	0.09 (0.13)	0.08 (0.14)		0.19 (0.23)	0.19 (0.27)	0.25 (0.28)
B			0.13 (0.09)	0.01 (-0.05)	0.01 (-0.05)	0.01 (0.03)
Ph_a			-0.04 (-0.03)	-0.08 (0.01)	-0.11 (-0.03)	-0.06 (-0.08)
Ph_b			-0.04 (-0.03)	-0.14 (-0.14)	-0.14 (-0.14)	-0.14 (-0.15)
Ph_c			-0.04 (-0.03)	-0.14 (-0.13)	-0.14 (-0.13)	-0.14 (-0.15)

5.3 Summary

The DFT method was able to predict the formation of dimers of **46** and provided a rational interpretation of the organization of the dimers in the crystal in terms of additional Te-Br SBIs. In addition to the structure of the simple dimer, **46** also provided a hitherto unobserved solvated telluradiazole dimer. The formation of SBIs between the tellurium atom and both DMSO and a bromine atom of a neighbouring molecule highlights the electron acceptor abilities of σ^* orbitals and strongly suggests that these molecules will be able to associate with other Lewis bases.

Alternatively, the attachment of a Lewis acid to one of the nitrogen atoms of the telluradiazole ring highlighted the ability of these heterocycles to react with other Lewis acids. It was found that single Lewis acid substitution results in stronger subsequent secondary bonding interactions (assessed from experimental distances and calculated dimerization energies). Variable temperature NMR spectroscopy, however, could not provide direct evidence for the existence of dimers in solution. The structures of **47** and **48**$_2$ suggest further research into the use of N-capping as a means to control the association of chalcogenadiazoles and related heterocycles as well as to introduce functionality to their supramolecular structures.

6 Gas-Phase Molecular and Supramolecular Investigations of 1,2,5-Chalcogenadiazole Heterocycles[226]

6.1 Introduction

The discussion presented in Chapter 3 was based on the electron density constructed from Kohn-Sham molecular orbitals. While the exact physical meaning of Kohn-Sham molecular orbitals (KSMOs) remains a matter of discussion,[227,228] recent studies have suggested that not only do their compositions allow for accurate bonding analyses,[229] but that their orbital energies approximate the vertical ionization potentials (VIPs) reasonably well.[230] Furthermore, the calculated binding energy of the $[Te\text{-}N]_2$ supramolecular synthon suggests that supramolecular aggregates can be observed in the gas phase.

DFT calculations predict that the formation of the strong SBIs will be accompanied by measurable changes in the electronic structure. These changes could, in principle, be measured using ultraviolet photoelectron spectroscopy (UPS) because a decrease of approximately 1 eV is calculated for the first ionization energy of a dimer of **40** when compared with a monomer. This, however, would require that the bulk of the sample exists as dimers in the gas phase because the UPS data is time and species averaged. UPS studies have previously been performed on benzothiadiazole (**38**) and benzoselenadiazole (**39**) and were interpreted with the assistance of semi-empirical[213,231-233] and ab initio[234] calculations. Some of the assignments are ambiguous and there were disagreements in the ordering of the molecular orbitals. While these two systems are not expected to form dimers in the gas phase, an accurate assignment of their ionization bands is necessary in order to properly interpret the UPS data for **40**.

Evidence for the persistence of the $[Te\text{-}N]_2$ supramolecular synthon in the gas phase could also be found with mass spectrometry. Mass spectrometry is much more sensitive to trace amounts of substances and has been used very successfully in identifying supramolecular aggregates in the gas phase, including hydrogen bonded structures, crown ether-cation complexes and transition metal-ligand coordinated structures.[235-239] Ultraviolet laser desorption/ionization time-of-flight mass spectrometry (UV-LDI TOFMS) is, in principle, suitable for probing the supramolecular behaviour of benzo-2,1,3-chalcogenadiazoles in the gas phase because: (1) the sample can be analyzed without introducing a charge beforehand; (2) benzo-2,1,3-chalcogenadiazoles absorb strongly in the UV, thus desorption/ionization can occur without the need of a matrix; (3) the sensitivity and mass separation would facilitate the detection of small amounts of supramolecular aggregates in the gas phase; (4) the sample can be prepared and run under an inert atmosphere; and (5) the plume, where secondary ions are formed, approaches equilibrium conditions allowing the use of thermodynamic criteria to identify ions that may result from supramolecular association

This chapter includes the ultraviolet photoelectron spectra of **38**, **39** and their analogue **40**, and compares them to the results of relativistic DFT calculations with different exchange-correlation functionals in an attempt to clarify the details of their electronic structures and to benchmark the computational method that has previously been employed to rationalize the solid-state structures of these systems.[203] Also included are the gas-phase measurements of benzo-2,1,3-chalcogenadiazoles by UV-LDI TOFMS. The spectra are interpreted in order to rationalize the behaviour of the sample under UV-LDI conditions in an effort to identify gas-phase aggregates that result from the self-association of the heterocycles through the formation of the $[E\text{-}N]_2$ supramolecular synthon.

6.2 The Valence Electronic Structure of Benzo-2,1,3-chalcogenadiazoles Studied by Photoelectron Spectroscopy and Density Functional Theory.

6.2.1 He I Photoelectron Spectra

The photoelectron spectra of the benzo-2,1,3-chalcogenadiazoles **38-40** are displayed in Figure 6.1, the vertical length of each data point corresponds to the experimental variance.[84] The spectrum of **38** is consistent with those recorded previously,[213,232-234] consisting of three groups of overlapping bands between 8 and 10 eV, 10 and 12 eV, as well as between 12 and 14 eV. The spectra of the heavier **39** and **40** display similar patterns that are shifted to lower energies; in the latter, the second set of bands is split into two bands. There are two previous reports of the photoelectron spectrum of **39**[232,234] but none of the spectrum of **40**.

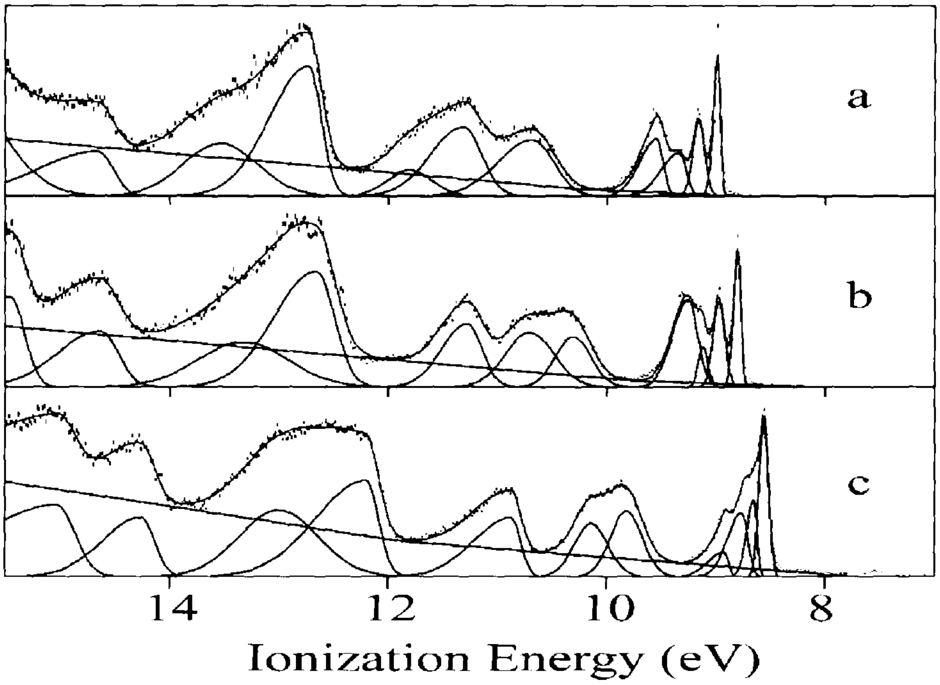

Figure 6.1 Photoelectron spectra of (a) **38**, (b) **39** and (c) **40**.

For the spectrum of **38**, the bands between 10 and 12 eV were modeled with three asymmetric Gaussian envelopes while the bands between 12 and 14 eV required two asymmetric Gaussian envelopes. The measured vertical ionization energy for each model band is given in Table 6.1 and is compared with those determined in previous studies; most values agree within ±0.04 eV but there are several exceptions. The first group of bands corresponds to ionization from the two highest-lying orbitals only, the first of which displays vibrational structure that is fit with a progression of three Gaussians in each spectrum. An earlier report[231] lists the second ionization energy as 9.65 eV, which is 0.11eV above the value observed in this work. Another peak was reported at 12.38 eV but this corresponds to the bottom of a valley between two bands in the present study; the disagreement is possibly the result of a typographical error. Three reports list an

Table 6.1 Experimental VIPs and assignments for **38**, **39** and **40** in eV.

		38				Assignment			
IE[a]	IE[b]	IE[c]	IE[d]	IE[e]	IE[f]	a	b	c	f
8.98	9.00	8.98	9.00	8.95	9.00	a_2 (π)	a_2 (π)	a_2 (π)	a_2 (π)
9.54	9.55	8.95	9.65	9.50	9.56	b_1 (π)	b_1 (π)	b_1 (π)	b_1 (π)
10.68	10.71	9.52	10.71	10.66	10.69	b_2 (σ)	b_2 (σ)	a_1 (σ)	b_2 (σ)
11.31	11.32	10.64	11.27	11.32	11.28	a_1 (σ)	a_2 (π)	a_2 (π)	a_2 (π)
		11.31				a_2 (π)	a_1 (σ)		
11.80				11.7[g]	11.70	b_1 (π)	b_1 (π)	b_2 (σ)	a_1 (σ)
12.73	12.83	11.6[g]	12.38	12.74	12.78	a_1 (σ)	a_1 (σ)		b_1 (π)
						b_2 (σ)	b_2 (σ)		
						a_1 (σ)	a_1 (σ)		

		39	Assignment		
IE[a]	IE[b]	IE[f]	a	b	f
8.80	8.81	8.76	a_2 (π)	a_2 (π)	a_2 (π)
9.26	9.30	9.24	b_1 (π)	b_1 (π)	b_1 (π)
10.30	10.55	10.36	b_2 (σ)	b_2 (σ)	b_2 (σ)
10.70		10.62	a_1 (σ)	a_2 (π)	a_2 (π)
			a_2 (π)	a_1 (σ)	
11.27	11.30	11.25	b_1 (π)	b_1 (π)	a_1 (σ)
12.66	12.85	12.41	b_2 (σ)	a_1 (σ)	b_1 (π)
		12.76	a_1 (σ)	b_2 (σ)	a_1 (σ)
			a_1 (σ)	a_1 (σ)	

40	Assignment
IE[a]	a
8.57	a_2 (π)
8.92	b_1 (π)
9.82	b_2 (σ)
10.14	a_1 (σ)
	a_2 (π)
10.87	b_1 (π)
12.20	a_1 (σ)
	b_2 (σ)
	a_1 (σ)

a) This work, see the end of discussion for justification.
b) Reference [234]
c) Reference [213]
d) Reference [231]
e) Reference [233]
f) Reference [232]
g) shoulder

ionization shoulder at 11.6 eV[213] and 11.7 eV,[232,233] which must correspond to the band fitted at 11.84 eV.

Compared to the spectrum of **38**, the photoelectron spectrum of **39** displays the most conspicuous differences in the second set of peaks. The sharp features of this spectrum correspond, within ±0.08 eV, to the previously reported values (Table 6.1).[232,234] In the first study, however, the feature between 9.8 and 11 eV was attributed to a single ionization; the new determination clearly resolves two bands and corresponds well with the second study. There is also disagreement in the position of the ionization at 12.66 eV but the peak fitting method employed in the present study is more accurate in the characterization of peaks with poorly defined maxima.

6.2.2 Molecular Orbital Compositions

Successful matching of electronic structure calculations with the photoelectron spectrum of a molecule requires agreement in both the values of the ionization energies and the nature of the corresponding molecular orbitals. As a first approximation, assignments of the experimental spectra from the calculated electronic structures can be attempted by application of Koopmans' theorem, bearing in mind that such an approach does not account for correlation or relaxation upon electron removal. One more fundamental issue is that KSMOs are inherently different from those obtained by HF methods. Fortunately, recent investigations have shown that it is possible to correlate the DFT orbital energies with the vertical ionization potentials[230] as long as a correction is introduced to account for a systematic error that is unique to each exchange-correlation functional.[240]

The electronic structures of the benzochalcogenadiazoles were calculated using three GGA and one hybrid exchange-correlation potential: BP86 which has been commonly used with ADF; PW91 which usually provides better structural parameters for heavy main-group systems; SAOP which is usually recommended for TD-DFT calculations and has been recently proposed for the assignment of photoelectron spectra;[230] and the popular B3LYP. Atomic contributions to the molecular orbitals are dependent on the nature of the chalcogen but, for each molecule, the composition of the KSMOs determined with all four methods is essentially identical. The energies and the order of the inner orbitals show small variations between functionals. Figure 6.2 displays the calculated composition of the LUMO and the ten highest occupied orbitals of **40**, which correspond to the electrons that are most easily removed: those in the π manifold and the lone pairs. The C_{2v} symmetry allows the distinction of π- (a_2, b_1) and σ-orbitals (a_1, b_2). The calculated LUMO (b_1) is a π-orbital with four nodal planes and predominantly chalcogen-nitrogen antibonding character. The composition of the HOMO (a_2 symmetry) corresponds to electron density on the C=C bonds in the Lewis structure and has less than 2% chalcogen character in all three cases. The HOMO-1 (b_1) is primarily the chalcogen π lone pair (S: 33%, Se: 48%, Te: 62%). The HOMO-2 (b_2) and HOMO-3 (a_1) are both σ-orbitals that represent the in-phase and out-of-phase combinations of the N lone pairs; the HOMO-3 also contains a significant contribution from the chalcogen σ lone pair (S: 8%, Se: 16% and Te: 23%). The HOMO-4 (a_2) and HOMO-5 (b_1) are π-orbitals with two nodal planes each. There is a small overlap in the HOMO-5 between the chalcogen and nitrogen; the chalcogen contribution to this orbital decreases down the group (S: 18%, Se: 17%, Te: 12%). The HOMO-6 and HOMO-7 are σ-orbitals with symmetries a_1 and b_2, respectively, which swap order in the case of **39**. The a_1 orbital contains chalcogen σ lone pair character (S: 46%, Se: 21% and Te: 19%). The HOMO-8 (a_1) is also part of the sigma framework with chalcogen σ lone pair character (S: 6%, Se: 16% and Te: 13%). The HOMO-9 (HOMO-10 for **38**) is the lowest energy π orbital, it has a b_1 symmetry with one node, and its chalcogen contribution decreases in the heavier molecules (S: 27%, Se: 13% and Te: 6%). Overall, the electronic structures display increasing localization of electron density as the π-overlap between nitrogen and the chalcogen becomes less efficient; indeed the crystal structures of these compounds do show a high degree of bond alternation.[65,203]

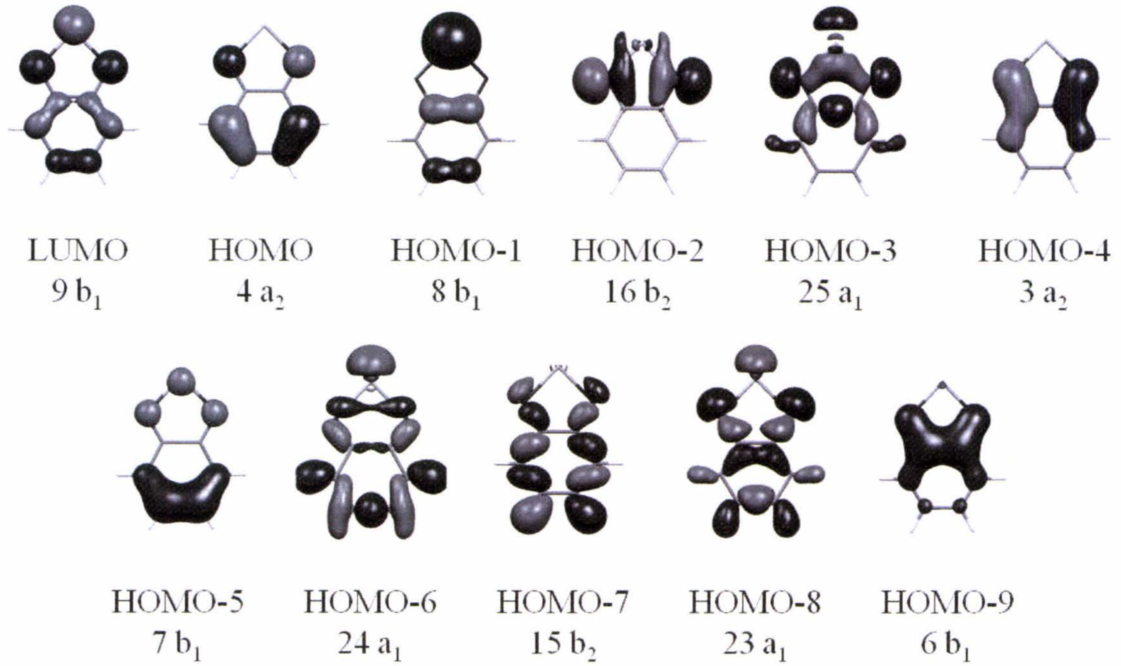

Figure 6.2 LUMO and the ten highest-occupied molecular orbitals of **40**. Isosurfaces are plotted at 0.05 au.

6.2.3 Spectral Assignments

The empirical correction factors that were necessary for the comparison of the Kohn-Sham orbital energies with the measured ionization energies were obtained by averaging the difference between the energy of the HOMO and the first measured ionization band for all three compounds, these corrections are -2.77 eV for PW91, 1.29 eV for SAOP, -2.72 for BP86 and -2.14 for B3LYP, and were used to offset the orbital energies calculated with each functional. The DFT orbital energies corrected in this way are given in Table 6.2. The values obtained from calculations with the gradient-corrected functionals BP86, PW91 and SAOP are close to each other. The maximum differences of BP86 from PW91 are 0.18, 0.01 and 0.02 eV for **38**, **39** and **40**, respectively. The corresponding SAOP differences are 0.18, 0.13, and 0.25 eV; and 0.61, 0.60 and 0.59 eV for B3LYP. The first two ionizations match the corrected energies of the HOMO and the HOMO-1 within 0.1 eV for all functionals with exception of the SAOP HOMO-2 of **40**. Subsequent bands cannot be assigned because individual ionization processes are not resolved.

In order to obtain more reliable assignments than those based on Koopmans' theorem alone, relaxation can be accounted for by calculating the vertical ionization potentials as the energy difference between ground and the ionized states evaluated by removal of one electron from a particular orbital of the molecule in the ground state geometry (eq 6.1). The vertical ionization potentials calculated with PW91 and B3LYP are reported with no further correction in Table 6.2. There are significant differences between the VIPs calculated by these functionals. B3LYP overestimates the ionization

Table 6.2 Koopmans' theorem ionization energies, calculated vertical ionization potentials and corresponding orbital symmetries for **38-40**.

	Benzo-2,1,3-thiadiazole (**38**)					
	Koopmans' Theorem Energies				VIPs	
	PW91	SAOP	BP86	B3LYP	PW91	B3LYP
a_2 (π)	8.97	9.02	8.96	8.96	9.08	9.32
b_1 (π)	9.49	9.45	9.48	9.49	9.53	9.87
b_2 (σ)	10.09	10.27	10.09	10.63	10.80	11.55
a_1 (σ)	10.64	10.65	10.64	11.17	10.84	11.56
a_2 (π)	11.09	11.16	11.08	11.35	11.47	11.92
b_1 (π)	11.73	11.73	11.73	12.05	11.84	12.42
a_1 (σ)	12.18	12.10	12.09	12.64		13.22
b_2 (σ)	12.26	12.18	12.18	12.85		
a_1 (σ)	12.44	12.40	12.26	13.05		

	Benzo-2,1,3-selenadiazole (**39**)					
	Koopmans' Theorem Energies				VIPs	
	PW91	SAOP	BP86	B3LYP	PW91	B3LYP
a_2 (π)	8.79	8.82	8.79	8.79	8.85	9.10
b_1 (π)	9.23	9.15	9.23	9.22	9.32	9.58
b_2 (σ)	9.90	10.02	9.90	10.38	10.34	11.04
a_1 (σ)	10.23	10.17	10.23	10.69	10.51	11.15
a_2 (π)	10.96	10.99	10.96	11.23	11.24	11.70
b_1 (π)	11.37	11.33	11.37	11.66	11.43	11.98
a_1 (σ)	12.18	12.05	12.18	12.62		12.93
b_2 (σ)	12.15	12.04	12.15	12.74		
a_1 (σ)	12.30	12.26	12.31	12.90		

	Benzo-2,1,3-telluradiazole (**40**)					
	Koopmans' Theorem Energies				VIPs	
	PW91	SAOP	BP86	B3LYP	PW91	B3LYP
a_2 (π)	8.59	8.51	8.59	8.59	8.59	8.84
b_1 (π)	8.83	8.61	8.84	8.77	8.86	9.11
b_2 (σ)	9.55	9.53	9.56	9.96	9.74	10.36
a_1 (σ)	9.66	9.50	9.68	10.05	10.02	10.61
a_2 (π)	10.80	10.71	10.80	11.07	10.99	11.45
b_1 (π)	11.00	10.88	11.01	11.27	11.01	11.54
a_1 (σ)	11.89	11.64	11.89	12.33		12.54
b_2 (σ)	11.93	11.71	11.94	12.52		
a_1 (σ)	12.14	11.99	12.15	12.73		

[a] Energies are in eV.

energies by between 0.24 and 0.75 eV when compared with PW91. The VIPs calculated with PW91 agree with the experimental VIPs within 0.10, 0.06 and 0.06 eV for the first two orbitals of **38**, **39** and **40**, respectively. However, this approach alone cannot conclusively assign the next bands.

$$\mathrm{VIP} = E(h\nu) - E(e^-) = E(M^+) - E(M) \qquad 6.1$$

Further insight into the identity of the inner orbitals, from which each of the next ionization bands originate, can be obtained by comparison of the spectra along the series of benzo-2,1,3-chalcogenadiazoles. Because all members of this family should have valence orbitals of similar composition and energy order, the ionization energies should decrease as the atomic number of the chalcogen increases and the trend should be almost linear, as in the cases of the dimethyl chalcogenides ($(CH_3)_2E$, E = S, Se, Te),[241] the pnictabenzenes (P, As, Sb),[242] and the triphenyl derivatives of groups 14[243] and 15[244] elements. Figure 6.3 presents the experimentally determined and calculated ionization potentials as a function of the first ionization potential of the chalcogen atoms.[245] Approximately linear trends are observed for several orbital/ionization energies and can be quantitatively characterized by the slope and the correlation coefficient (Table 6.3). When the relevant molecular orbital has a greater contribution from the chalcogen, the correlation coefficient is better; likewise, when the orbital is mostly localized in the benzene rings the correlation is worse. This analysis is limited to the first six ionizations, for which correlations are clearly defined.

Table 6.3 Slopes (m) and correlation coefficients (R^2) for ionization energies of **38-40** with atomic first ionization energies of S, Se and Te.

PES	Ionization Band	1	2	3	4		5	6
	m	0.3	0.46	0.64	0.86		0.68	0.4
	R^2	1.00	1.00	1.00	1.00		0.98	0.88
Koopmans' Theorem	Orbital	HOMO	HOMO-1	HOMO-2	HOMO-3	HOMO-4	HOMO-5	HOMO-6
PW91	m	0.29	0.5	0.41	0.75	0.22	0.56	0.22
	R^2	1.00	0.99	0.98	1.00	1.00	1.00	0.85
BP86	m	0.28	0.49	0.41	0.74	0.21	0.55	0.16
	R^2	1.00	0.99	0.98	1.00	1.00	1.00	0.57
SAOP	m	0.39	0.65	0.59	0.85	0.34	0.65	0.36
	R^2	0.99	0.99	0.98	1.00	0.99	1.00	0.88
B3LYP	m	0.28	0.55	0.51	0.86	0.22	0.6	0.24
	R^2	1.00	0.99	0.99	1.00	1.00	1.00	0.81
VIP	Ionization	1	2	3	4	5	6	
PW91	m	0.37	0.51	0.81	0.62	0.36	0.64	
	R^2	1.00	0.97	1.00	1.00	1.00	1.00	
B3LYP	m	0.37	0.59	0.90	0.72	0.35	0.67	
	R^2	1.00	0.99	1.00	1.00	1.00	1.00	

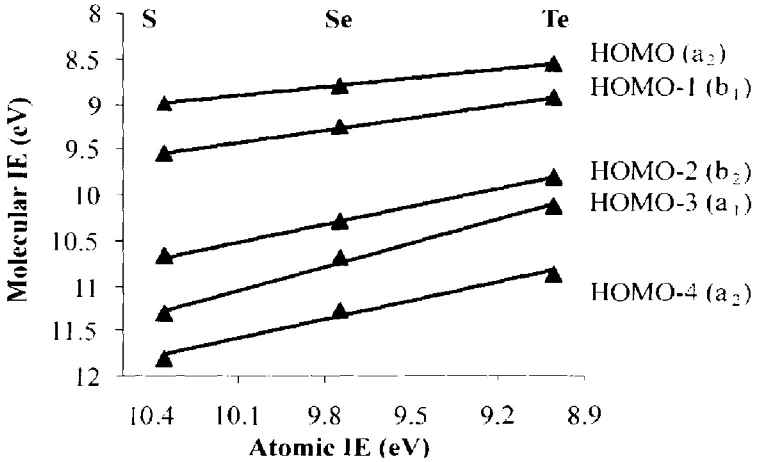

Figure 6.3 Experimental ionization energies of **38-40** correlated to the first ionization potential of the respective chalcogen.

The slopes are also useful to confirm the assignments and, in some instances, they can clarify ambiguous assignments. For example, based only on the orbital energies calculated by BP86, PW91, and SAOP, assignment of the 3rd and 4th ionizations is ambiguous because one of the ionizations from either the HOMO-2 or the HOMO-4 is not visible. The slope magnitudes indicate that it is HOMO-4 that does not have a distinguishable ionization band in the He I spectrum. Assignment of the 3rd and 4th ionizations to HOMO-2 and HOMO-3 agrees with the B3LYP orbital energies within 0.14, 0.08 and 0.14 eV for **38**, **39**, and **40**, respectively. The slope magnitude, however, cannot be used as an absolute criterion to determine the nature of each molecular orbital. In the present case, the HOMO is nodal at the chalcogen and HOMO-1 has primarily chalcogen lone pair character, yet the slopes of their corresponding ionizations only differ by 0.2 at most.

The shapes of the bands, including the vibrational structure, are also indicative of orbital character. The narrow first two bands are consistent with ionization from π-orbitals, for which the corresponding ionized states undergo very small geometric changes. The vibrational structure of the first ionization band (8-10 eV in the case of **2**) contains some information on the nature of the HOMO. The vibrational frequency measured as the distance between maxima in the vibrational progression is $1350 \pm 160\ \mathrm{cm}^{-1}$ (0.02 eV) for all three compounds **38**, **39** and **40**. This value must correspond to an A_1 normal mode in a region characteristic of ν_{CC} and ν_{CN} stretching vibrations within the carbocycle and are consistent with removal of an electron from a wavefunction that has electron density located over the C=C and C=N bonds. The calculated normal mode that best fits these requirements has frequencies of 1342, 1321 and 1318 cm^{-1} in **38, 39,** and **40**, respectively; experimentally, the Raman spectra have bands that closely agree at 1359 for **38**,[246] 1349 for **39**,[246] and 1343 cm^{-1} for **40**.[203] This interpretation of the vibrational structure is consistent with the composition of the HOMO and agrees with the previous report for **38** and **39**.[232]

The combination of VIP energies and slopes within the homologous series leads to the final assignment for ionizations observed below 13 eV that is presented in Table 1. Agreement for PW91 results is within 0.16 eV for all the ionizations in each of the molecules except for the 4th ionization of the S and Se analogues which differs by 0.47 and 0.19 eV, respectively. Interestingly, B3LYP gave larger errors (0.19 - 0.87 eV).

Close spacing of orbitals precludes assignments with this approach above 13 eV for each spectrum.

6.2.4 Reorganization Energy

The solvent-independent changes of energy associated with the structural relaxation upon ionization of each molecule were determined in two steps. The first consisted of fitting the intensities in the vibrational progression to a Poisson distribution (eq 6.2). Here, I is the intensity of the n^{th} vibrational band and S is a distortion parameter. The latter parameter was then applied to eq 6.3, where *h* is Planck's constant and λ the reorganization energy.

$$I_n = \frac{S^n}{n!} e^{-S} \tag{6.2}$$

$$\lambda_v = \sum_k S_k h \upsilon_k \tag{6.3}$$

Overlap of the first and second ionizations was taken into account when modeling the vibrational progression in each spectrum. From the progression frequencies given above, the fitted distortion parameters and the corresponding reorganization energies were: 0.65, 0.11 ± 0.02 eV; 0.80, 0.13 ± 0.02 eV; and 0.60, 0.10 ± 0.02 eV for **38**, **39** and **40**, respectively. These energy values are comparable to those calculated using PW91: 0.08, 0.09 and 0.07 eV for **38**, **39** and **40**.

The small magnitudes of reorganization energy (c.f. 0.180 ± 0.005 eV for 1,10-phenanthroline[247] and 0.059 ± 0.004 eV for pentacene[248]) together with the tendency of these molecules to form extended supramolecular structures[203,214] invite further investigations of the charge transport properties of materials based on chalcogenadiazole heterocycles.

6.3 Identification of Gas-Phase Supramolecular Aggregates of Benzo-2,1,3-chalcogneadiazoles in the Ultraviolet Laser Desorption/Ionization Plume

6.3.1 UV LDI TOF Mass Spectra

The experiment could not be performed under the usual conditions because most common matrices contain acidic protons which would facilitate the hydrolysis of the analytes by adventitious moisture. In the absence of a separate matrix, each sample performed the functions of energy absorption and transfer. Each parent molecule under study is denoted as M throughout this discussion based on these considerations. In each experiment, the laser power was increased until the fluence 'threshold' was reached and the signal was maximized without saturating the detector. Each compound had a characteristic fluence threshold because this parameter is dependent on the sublimation energy of the sample and the efficiency with which the chromophore absorbs UV radiation and converts it to heat. The full set of LDI mass spectra for all the compounds listed in Table 6.4 is provided as electronic supplementary information. All the ions observed under the experimental conditions had $z = 1$. For the samples in which a higher laser power density was required in order to observe a signal, clusters of chalcogen atoms were observed: $[nE]^+$ (E = Se or Te) for n ranging from 2 to 9. Similar chalcogen clusters have been observed under LDI conditions in the mass spectra of elemental Se or Te.[249,250]

All of the spectra contain $[M]^+$ and/or $[M+H]^+$ peaks. A significant amount of the $[M+H]^+$ ion was observed in the spectrum of **41** despite the absence of protons in the sample. It is possible that despite all the precautions taken, the sample contained a trace impurity which acted as a proton source or that residual protons were present in the MALDI chamber. The spectrum of aprotic compound **49**, however, showed no proton containing ions even when this sample was prepared in open atmosphere conditions.

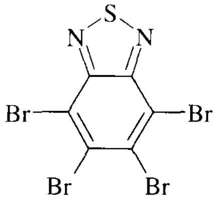

49

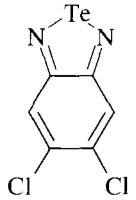

50

Table 6.4 Supramolecular ions in the UV LDI-TOF mass spectra of benzo-2,1,3-chalcogenadiazoles.

Sample	Monoisotopic mass of M	Ions	Abundance
39[a]	184.0		Not observed
40[b]	234.0	$[2M+H]^+$	100
44[a]	291.8		Not observed
46[a]	389.8	$[2M+H]^+$	5
49[a]	447.7		Not observed
50[b]	301.9	$[2M+H]^+$	30
41[a, c]	305.9	$[2M]^+$	40
		$[2M+H]^+$	10

[a] Pressed powder.

[b] Single crystal.

[c] Isotopic distribution of $[2M]^+$ and $[2M+H]^+$ overlap.

Although the composition of most of the ions that reached the detector was determined, the present discussion focuses on ions that correspond to possible supramolecular aggregates. These are listed in Table 6.4 and were identified by the presence of two chalcogen atoms and a mass consistent with 2M or 2M plus a proton. In the case of **41**, the isotopic distribution could only be reproduced by consideration of both $[2M]^+$ and $[2M+H]^+$ in 4:1 proportions (Figure 6.4).

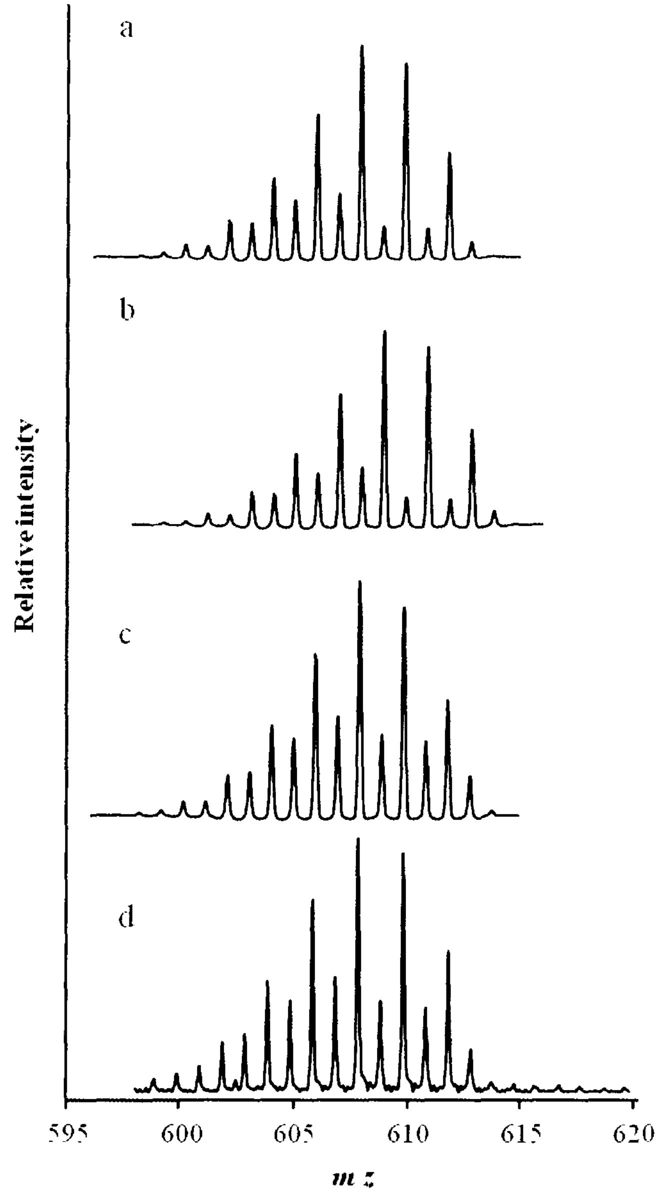

Figure 6.4 Modeled and experimental isotopic distribution of supramolecular aggregates of **41**: (a) $[2M]^+$, (b) $[2M+H]^+$, (c) $[2M]^+ + [2M+H]^+$ (d) experimental.

6.3.2 Structural Identification of Ions

The observed spectrum is a glimpse of the distribution of the ions present upon extraction from the ionization chamber. The laser pulse in a typical experiment is absorbed by the matrix, which is partially ablated and creates a plume which is initially both hot and dense.[251,252] The plume contains predominantly neutral molecules as well as a number of primary ions such as $[M]^+$, $[M+H]^+$, $[M]^-$, and $[M-H]^-$ ions, where M is the matrix molecule.[253, 254] The secondary ions are formed as the plume expands and cools during the period where the plume density is approximately 10% of the solid and the mean free path remains short enough to allow for a high collision rate. At this point the ion-to-neutral (matrix and analyte) ratio is 10^{-4} to 10^{-7} and therefore the relevant reactions occur between an ion and a neutral molecule.[255] The most common reactions that occur are collision charge transfers and collision proton transfers.[256] As the plume further expands and cools, the molecules approach local equilibrium and the chemistry is therefore governed by thermodynamics.[255] It is these molecules in this near-equilibrium plume that are extracted for detection.

$$M^+ + M \rightarrow [2M]^+ \qquad 6.4$$

$$[M+H]^+ + M \rightarrow [2M+H]^+ \qquad 6.5$$

DFT modeling has been performed on model systems in order to help identify the structures that correspond to the ions listed in Table 6.4. Thermodynamic arguments can be used to help identify the geometries of the ions because the conditions in the plume approach near-equilibrium conditions. The basis set, exchange-correlation functions and relativistic correction used for DFT modeling of these systems have been previously employed for 1,2,5-chalcogenadiazole heterocycles and have been shown to reproduce structural parameters and ionization energies (Sections 3.2.3, 4.2.4, 5.2.3 and 6.2).[203,214,257]

6.3.3 DFT modeling of primary ions

In order to model the ions that result from the secondary ionization process in eqs 6.4 and 6.5, the geometries of the primary ions that are involved in these reactions must first be determined. Protonation of the neutral molecule is expected to occur at the nitrogen atom in the gas phase which is consistent with the crystal structures of protonated **39**[195,199] and diprotonated **40**[199] (Section 4.2.3). The calculated gas-phase proton affinities of the unsubstituted heterocycles, **38-40**, are 886.9, 910.3 and 943.2 kJ/mol, respectively. These are of the same order of magnitude as the proton affinities calculated for a series of pyridoindoles, pyridylindoles and pyridylpyridoindoles that were investigated as matrices for UV-MALDI-TOFMS and in all cases an $[M+H]^+$ ion was observed for these heterocycles.[258]

The $[M]^+$ ion results from the single ionization of the neutral molecule. The vertical ionization energies for compounds **38-40** have been discussed in Section 6.2. The electron is removed from a weakly bonding orbital in the π-framework resulting in limited structural distortion. Both the $[M+H]^+$ and the $[M]^+$ ions are capable of reacting with a neutral M to form the $[E\text{-}N]_2$ supramolecular synthon.

6.3.4 DFT Modeling of Supramolecular Aggregates

The $[2M+H]^+$ ions observed in the mass spectra of **40**,**41**, **46** and **50** should be formed by the reaction of M with $[M+H]^+$ (eq 6.5). Because both the primary and the corresponding secondary ion is observed, the resulting molecule is probably held together by interactions that would be reversible in the conditions within the plume such as π-stacking, hydrogen bonds, Te-aryl SBIs or Te-N SBIs. Tellurium-aryl SBIs (Section 3.2.5) and π-stacking[259] could not compete with hydrogen bonding[3] or formation of the $[Te\text{-}N]_2$ supramolecular synthon[214] as they are approximately five times weaker, Four possible supramolecules (Figure 6.5) assembled by Te-N secondary bonds, hydrogen bonds, or combinations of both were optimized. Structure contains a single hydrogen bond, combines a hydrogen bond and a Te-Te SBI, features a hydrogen bond and a Te-N SBI and dimerizes as a result of the formation of the $[Te\text{-}N]_2$ supramolecular synthon. Interestingly, the structure of $\mathbf{39}_2\cdot HI_3\cdot I_2$ features alternating links of the selenium analogues of **51** and **54**.[195] The calculated binding energies between M and $[M+H]^+$ are 75.2, 50.7, 75.3 and 156.2 kJ/mol for **51-54**, respectively.

Of the four investigated geometries, the most stable arrangement is **54**. In this structure the $[Te\text{-}N]_2$ supramolecular synthon is not symmetric, i.e., the Te-N SBI opposite to the protonated nitrogen is shorter than the other. While the long Te-N SBI (d = 2.270 Å) is longer than the average Te-N SBI distance observed in the crystal structure of **40** (2.701(7) Å),[214] the short SBI (d = 2.775 Å) is shorter than that observed in the crystal structures of the N-alkylated 1,2,5-telluradiazolium cations (2.417(3) Å and 2.301(5) Å) [142,145] Considering that the calculated dimerization energy of **40** is 68.8 kJ/mol, the results indicate that protonation of one nitrogen atom stabilizes the $[Te\text{-}N]_2$ supramolecular synthon. The same trend is predicted for the Se analogues, for which the binding energy increases from 26.9 to 98.4 kJ/mol.

Ions of this type, $[2M+H]^+$, were observed in the UV-LDI-TOFMS of some of the pyridoindoles, pyridylindoles and pyridylpyridoindoles mentioned earlier, but no attempt was made to identify the structures of these ions.[258]

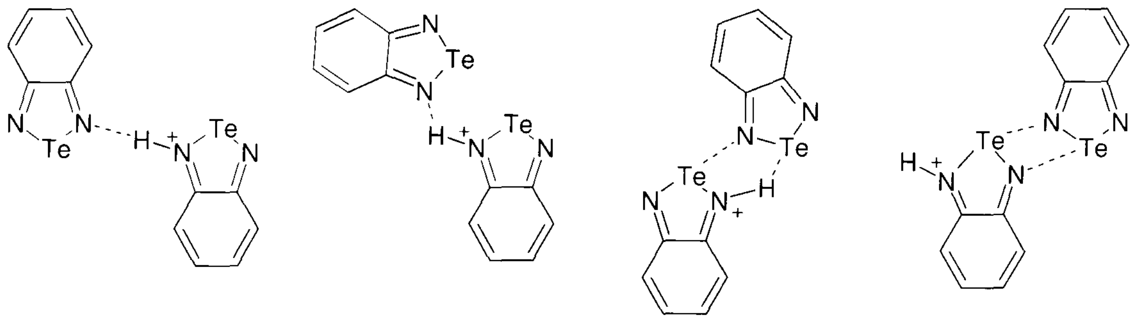

51 **52** **53** **54**

Figure 6.5 Candidates for the identification of the structure of the $[2M+H]^+$ ion in the mass spectra of benzo-2,1,3-telluradiazoles.

The mass spectrum of **41** contains the $[2M]^+$ ion which would arise from the reaction of $[M]^+$ with M (eq 6.4). This reaction would most closely resemble the self-assembly that leads to the formation of the $[Te\text{-}N]_2$ supramolecular synthons found in the crystal structures of the 1,2,5-telluradiazole heterocycles. The interaction energies for the structures shown in Figure 6.6 are calculated from eq 6.4. For **40** the interaction energy is 158.1 kJ/mol and for **41** the interaction energy is 146.1 kJ/mol. The calculated Te-N SBI distances in the $[2M]^+$ ions are 2.484 Å for **40** and 2.503 Å in **41**. Both of these calculated distances are more than 0.2 Å shorter than the solid-state aggregates of the corresponding neutral heterocycles (Sections 4.2.4 and 8.2).[203]

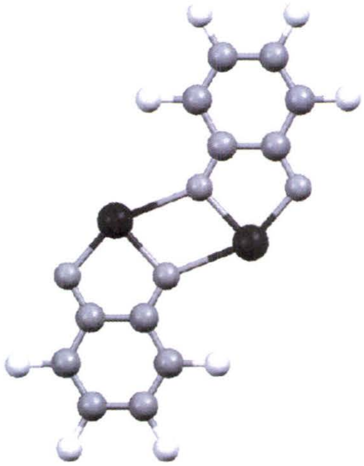

Figure 6.6 DFT modeled structures for $[2M]^+$ ions of **41**.

6.4 Summary

The investigation of the photoelectron spectra of the benzo-2,1,3-chalcogenadiazole homologous series, including the sulphur, selenium and tellurium derivatives, demonstrated that both GGA and hybrid DFT calculations could successfully be used in their interpretation. Although preliminary assignments can be conducted using a single point B3LYP calculation, a more reliable identification of orbitals requires actual calculation of vertical ionization potentials and a study of the correlations of orbital energies with the first ionization potential of the chalcogen atoms.

Mass spectra were acquired from benzo-2,1,3-chalcogenadiazoles under UV-LDI conditions. In all cases either the radical cation or the singly protonated ion of the parent heterocycle was observed. The 1,2,5-telluradiazole heterocycles formed ions of the type $[2M+H]^+$ and $[2M]^+$; DFT calculations suggested that the most stable arrangement occured when the molecules associated to form the $[Te\text{-}N]_2$ supramolecular synthon. The equivalent ions were not observed in the mass spectrum of S and Se analogues; this could be explained by the much smaller energies calculated for the S-N and Se-N SBIs.

7 Parameterization of a Force Field for Te-N Secondary Bonding Interactions and its Application in the Design of Supramolecular Structures Based on Heterocyclic Building Blocks

7.1 Introduction

Investigations into the use of SBIs in supramolecular chemistry must address a fundamental question: what new supramolecular structures (and properties) would be available through the use of SBIs that are not attainable by more conventional approaches such as hydrogen bonding or the coordination of metal ions? In principle, the answer could be provided through a comprehensive research program involving the synthesis and characterization of multiple derivatives. This daunting task can be abbreviated with the use of modern computational methods, not to replace the experiments but to facilitate the process of design and identification of the systems that represent the most interesting synthetic targets.

As evidenced in the preceding chapters, DFT has been a valuable tool for modeling the association of 1,2,5-telluradiazoles in the solid state and gas phase. There are, however, intrinsic limitations to quantum mechanical methods that hamper their application to the design of large supramolecular structures. For example, the contribution of dispersion forces cannot be accurately calculated even though there have been significant advances.[260-262] The most important challenge to overcome in this respect would be the computational expense of modeling large systems. Molecular mechanics is a different approach for molecular modeling which is applicable to a wide range of organic and biological supramolecular systems.[263] The approach relies on evaluating the energetic cost of distorting the internal dimensions of a molecule from the ideal values with simple harmonic or anharmonic functions that constitute a force field. The application of molecular mechanics to heavy main-group systems has been quite limited. One of the reasons for this is that the great variety of oxidation states and coordination geometries available precludes the existence of a universal set of parameters. Force fields must therefore either have a large number of situation-specific atom types,[264-268] or define sets of rules that quickly identify the correct type of structure and parameters.[269,270] The number of parameters available for main-group elements is rather small and those available apply only to strongly covalent bonds between atoms; SBIs are simply neglected within molecular mechanics.

This chapter presents the parameterization of the MMX force field to account for supramolecular SBIs, the results from testing the parameter set against experimentally determined structures, and the application of the method to design new supramolecular structures based on the $[Te\text{-}N]_2$ supramolecular synthon.

7.2 Results and Discussion

7.2.1 Choice of Force Field and Parameterization

The MMX force field,[139] an extension of Allinger's MM2 force field,[264,268] was selected for these investigations because it allows the use of anharmonic potentials which are, in principle, more accurate than harmonic potentials. The force field consists of bond-stretching, bond-angle bending, stretch-bending, torsion, and van der Waals potentials. In this model, the bond-stretching potential energy (eq 7.1) is a function of the interatomic distance (r), the force constant (K_r), and the equilibrium bond distance (r_{eq}). Bending of a bond angle, including the out of plane angle for atoms bonded to three other atoms, (eq 7.2) results in a potential energy contribution that is a function of the angle (θ), a force constant (K_θ), the equilibrium bond angle (θ_{eq}) and the *sextet* angle bending constant (S). The combination of changes in bond distances and angles yields a potential (eq 7.3) with its own force constant (K_{sb}). The torsion of a dihedral angle (φ) is modeled by a periodic function (eq 7.4) where the location of the minimum or minima is defined by D_1, D_2 or D_3 (generally 1, -1 and 1, respectively) and the force constants V1, V2 or V3. The van der Waals potential is calculated according to the Buckingham model (eq 7.5) as a function of the distance (r_{ij}) between a pair of atoms, their van der Waals radii (r_i and r_j), and three universally applied constants A, B and C. The tellurium parameters in the current version of the MMX force field are limited to those necessary for optimizing ditellurides with sp^2 hybridized carbons attached to the tellurium atoms. With the exception of the van der Waals radii, none of the supplied parameters are appropriate for modeling tellurium-nitrogen organic heterocycles, even less, the $[\mathrm{Te\text{-}N}]_2$ supramolecular synthon.

$$E_{bond} = K_r (r - r_{eq})^2 \left[1 - 2(r - r_{eq}) + \frac{7}{3}(r - r_{eq})^2 \right] \quad 7.1$$

$$E_{angle} = E_{out-of-plane} = \frac{K_\theta}{2}(\theta - \theta_{eq})^2 \left[1 + S(\theta - \theta_{eq})^4\right] \quad 7.2$$

$$E_{stretchbend} = K_{sb}(\theta - \theta_{eq})(r - r_{eq}) \quad 7.3$$

$$E_{torsion} = \frac{V_1}{2}(1 + D_1 \cos\varphi) + \frac{V_2}{2}(1 + D_2 \cos 2\varphi) + \frac{V_3}{2}(1 + D_3 \cos 3\varphi) \quad 7.4$$

$$E_{VdW} = Ae^{-\frac{B}{\rho}} - \left(\frac{C}{\rho}\right)^6, \quad \rho = \left(\frac{r_i + r_j}{r_{ij}}\right) \quad 7.5$$

A distinction must be made between internal ("covalent") and external (SBI) parameters in order to define all of the parameters necessary for isolated and associated 1,2,5-telluradiazoles. This was enabled by adopting the numbering scheme shown in Scheme 7.1. The required internal parameters include those for the potentials of the Te1-N1 bond stretch; the N1-Te1-N2 and C=N1-Te1 angle bends, the out-of-plane bends and the torsions within the five-membered ring. The external parameters correspond to the Te1-N3 SBI stretch as well as the bends, out-of-plane bends and torsions relevant to the $[Te\text{-}N]_2$ supramolecular synthon. The number of crystallographically determined structures of 1,2,5-telluradiazole derivatives is too small to reliably parameterize the force field from experimental averages, instead the behaviour of the different components of the force field can be evaluated through more accurate DFT calculations. The optimal parameters were derived by mapping the force fields onto the DFT potential energy surfaces (PESs) as described below; their values are collected in Tables 7.1-7.4.

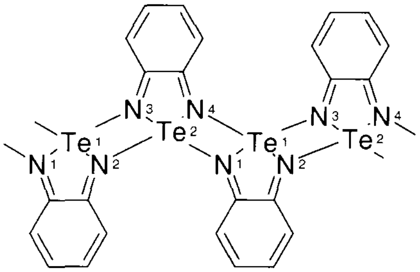

Scheme 7.1 Numbering system used in the definition of molecular mechanics parameters for the $[Te\text{-}N]_2$ supramolecular synthon.

Table 7.1 Optimized MMX bond-stretch parameters as defined by eq **7.1** for 1,2,5-telluradiazole rings.

Bond	r_{eq} (Å)	K_r (kJxmol^{-1}xÅ^{-2})
Te_1-N_1	2.021	1835
Te_1-N_3	2.700	150.5

Table 7.2 Optimized MMX bond angle bend parameters as defined by eq **7.2** for 1,2,5-telluradiazole rings.

Bond Angle	θ_{eq} (deg)	K_θ (kJxmol^{-1}xdeg^{-2})
N$_1$-Te$_1$-N$_2$	83.3	0.0256
Te$_1$-N$_1$-C	110.8	0.0825
C-N$_1$-Te$_2$	141.0	0.0000
N$_1$-Te$_1$-N$_3$	153.3	0.0000
N$_1$-Te$_2$-N$_2$	136.7	0.0000
N$_1$-Te$_1$-N$_4$	70.0	0.1466
Te$_1$-N$_1$-Te$_2$	110.0	0.1466

Table 7.3 Optimized MMX stretch-bend parameters as defined by eq 7.3 for 1,2,5-telluradiazole rings.

Out-of-Plane Angle	K_θ (kJxmol^{-1}xdeg^{-2})
C-N$_1$-Te$_1$-Te$_2$	57.28
N$_1$-Te$_1$-N$_2$-N$_3$	57.28

Table 7.4 Optimized MMX torsion angle parameters as defined by eq 7.4 for 1,2,5-telluradiazole rings.

Dihedral Angle	V1 (kJ/mol)	D$_1$
H-C-C-N$_1$	42	-1
H-C-N$_1$-Te$_1$	42	1
C-C-C-N$_1$	0	1
C-C-N1-Te1	75[a]	-1[a]
C-N$_1$-Te$_1$-N$_2$	84	-1
N$_1$-C-C-N$_2$	84	-1
H-C-N$_1$-Te$_2$	84	-1
C-C-N$_1$-Te$_2$	42[a]	-1[a]
C-N$_i$-Te$_j$-N$_k$	42	c[b]
N$_i$-Te$_j$-N$_k$-Te$_l$	42	c[b]

[a] Values are given for V2 and D2

[b] $\varphi = 0°$, $c = 1$; $\varphi = 180°$; $c = -1$

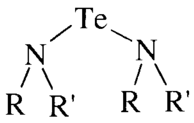

55 R=R'=H
56 R=R'=Me_3Si
57 R=Me_3Si R'=^tBu
58 R=R'=Me

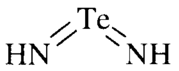

59

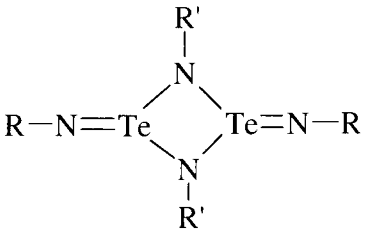

60 $R_{(cis)}$=R'=^tBu
61 $R_{(trans)}$=PPh_2NSiMe_3, R'=^tBu
62 $R_{(trans)}$=PPh_2NSiMe_3, R'=^tOct

Equilibrium bond lengths and angles were taken directly from the optimized geometries. The internal Te_1-N_1 bond stretching and the N_1-Te-N_2 bond angle bending force constants could ideally be obtained from DFT vibrational calculations. Each normal coordinate of these cyclic molecules, however, consists of a combination of correlated displacements of multiple atoms. Instead, the parameters were estimated from the vibrational calculations for acyclic compounds. Because the Te-N bond length in the 1,2,5-telluradiazoles is intermediate between those of the unambiguous single and double Te-N bonds, both the diamino telluride (**55**) and tellurium diimide (**59**) were considered. The geometries of these molecules were optimized assuming C_{2v} symmetry and their force constants were extracted from the calculation of the molecular vibrations. The optimized geometry of **55** was comparable to those of previously calculated structures[271] as well as to those of the monomeric di(bis(trimethylsilyl)amido)-[272] (**56**) and bis(tert-butyl(trimethylsilyl)amido) tellurium[273] (**57**) (see Table 7.5). Compared to the two experimental structures of the diamides, the Te-N bond length and the N-Te-N bond angle of **55** were overestimated by less than 0.05 Å and 3.1°, respectively. The optimized geometry of **59** was comparable with a previously calculated structure[271,274] as well as with the tellurium diimide dimers (**60**,[275] **61**[276] and **62**[65]) (see Table 7.6); there are no known monomeric tellurium diimides. The Te=N bond lengths, when compared with the experimental structures, were overestimated by less than 0.05 Å. The force constants for the heterocycle were obtained by interpolation at the equilibrium values of the bond length and angle from the heterocycle. The C=N$_\mathrm{I}$-Te$_\mathrm{I}$ bending potential was given the same force constant as the C=N-S bend already parameterized for MMX. Force constants for torsion potentials were initially given high, albeit unrealistic, values to enforce the planarity of the heterocycle, as observed in most telluradiazole crystal structures, and then decreased until the torsion angles in the central units of a 32-unit chain of sterically encumbered **27** provided the best match to the experimental crystallographic coordinates.[64] The torsional force constants applied to the telluradiazole ring were of the same order of magnitude as those used in MMX to model torsions in aromatic rings (V1 = 0 kJ/mol, V2 = 30.916 kJ/mol and V3 = 4.184 kJ/mol).[139]

Table 7.5 Comparison of selected calculated and experimental bond lengths (Å) and angles (°) for **55**.

	PW91[a]	HF[274]	MP2[274]	B3LYP[274]	**56**(exp)[272]	**57**(exp)[273]
Te-N	2.075	2.001	2.042	2.029	2.045(2)/ 2.054(2)	2.043(2)/ 2.050(2)
N-H	1.022	0.991	1.002	1.007		
N-Te-N	108.9	104.4	108.4	108.1	105.8(1)	105.7(1)
H-N-Te	110.6	120.8	116.4	119.3		
H-N-H	108.3	114.5	112.2	113.5		

[a] This work

Table 7.6 Comparison of selected calculated and experimental bond lengths (Å) and angles (°) for **59**.

	PW91[a]	B3PW91[271]	**60**(exp)[275]	**61**(exp)[276]	**62**(exp)[65]
Te-N	1.933	1.897	1.900(5)	1.88(1)	1.901(4)
N-H	1.035	1.028			
N-Te-N	119.8	119.8			
H-N-Te	110.0	112.9			

[a] This work

The Te-N SBI stretching force constant was evaluated by fitting the change of potential energy when two molecules of **26** are displaced from the equilibrium position along a path parallel to the SBI axis without any geometry relaxation to eq 7.1. The force constant derived in this manner was split equally between the two Te-N SBIs. Figure 7.1 compares the DFT-calculated potential energy profile for **26** with a purely harmonic function and the MMX anharmonic function calculated for **40**. The parameter was optimized by minimizing the absolute differences in the energy weighted with the inverse of the DFT energy over a region where the DFT-calculated PES did not exceed 25 kJ/mol. It can be seen from this figure that the anharmonic PES follows the DFT-calculated PES closely from 2.4 to 3.2 Å, deviating by a maximum of -4.3 kJ/mol at 3.1 Å, while the harmonic PES has a more limited range, 2.5 to 3.1 Å, before deviating beyond 4.3 kJ/mol.

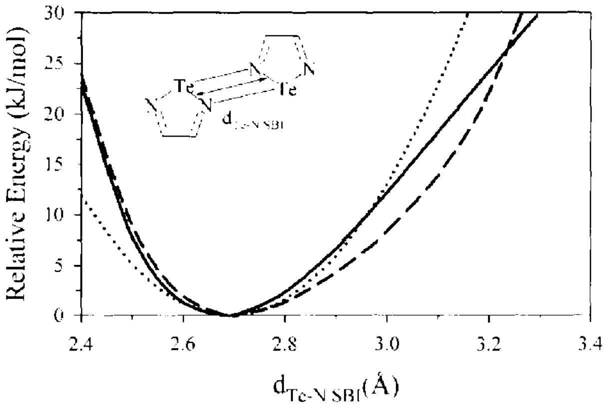

Figure 7.1 Potential energy curves for the in-plane dimerization through two simultaneous antiparallel Te-N SBIs as a function of the intermolecular distance modeled with DFT for **26** (——), a harmonic potential for **40** (· · · ·) and an anharmonic potential (eq 7.1) for **40** (- - -).

In a similar way, the N_1-Te_1-N_4 and N_2-Te_1-N_3 SBI bending force constants were obtained by fitting the DFT potential energy surface to eq 7.2. The DFT PES was calculated by sliding two telluradiazoles along an in-plane path described by the change in the N_1-Te_1-N_3 and N_3-Te_2-N_1 angles while maintaining a parallel arrangement of N_1-Te_1 and N_3-Te_2 bonds and keeping the Te_1-N_3 and Te_2-N_1 SBI distances constant,. The optimal parameter was obtained by minimizing the absolute differences in the energy weighted with the inverse of the DFT energy over a region where the DFT-calculated PES did not exceed 60 kJ/mol. Bending of each angle was assumed to contribute equally (¼) to the total potential thus the force constants are identical. Figure 7.2 compares the DFT calculation with the optimized MMX potential model, where the maximum deviation between 100 and 120° is 6.3 kJ/mol at 120°.

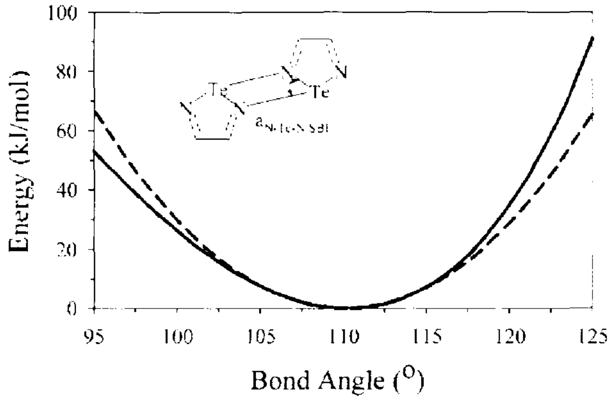

Figure 7.2 Potential energy curves for the in-plane dimerization through two simultaneous antiparallel Te-N SBIs as a function of the intermolecular angle modeled with DFT for **26** (——) and an anharmonic potential (eq 7.2) for **40** (- - -).

7.2.2 Validation of MMX Parameters

In order to verify the reliability of the structural predictions by MMX using the optimized set of force field parameters, the structures of systems for which the crystallographic determination is available were modeled. It is not possible to perform such validation for an isolated molecule of a 1,2,5-telluradiazole because all the hitherto published structures correspond to molecules associated through either Te, N or both and DFT studies have shown that binding at these sites results in measureable structural reorganization.[148,203,214] The crystal structure of **40** consists of supramolecular ribbons;[203] the dimensions of the molecules and the supramolecular synthon have been previously modeled by DFT calculations using oligomers with two to six units.[214] The same approach has been applied with molecular mechanics calculations. Table 7.7 summarizes these results and compares them to the experimental values. The most relevant dimensions are those of the molecules in the middle of the chain as they should most closely mimic the molecules within the crystal. The molecular mechanics parameters reproduce the bond lengths within 3σ of the experimental value and the bond angles within 1.2°.

Table 7.7 Comparison of selected calculated and experimental bond lengths (Å) and angles (°) for **40** and the central units in models of its ribbon polymer.

	40 (Exp)[203]	**40** (DFT)[214]		**40** (MMX)[a]		
Number of units	Avg.	1	6	1	6	20
Te_1-N_1	2.003(7)	2.021	2.054	2.022	2.022	2.022
N_1-C	1.32(1)	1.33	1.32	1.36	1.36	1.36
C-C	1.467(9)	1.482	1.481	1.478	1.478	1.478
Te_1-N_3	2.701(7)		2.690		2.687	2.687
N_1-Te_1-N_2	83.8(3)	88.2	83.1	86.1	86.0	86.0
Te_1-N_1-C	110.7(5)	105.9	110.4	108.9	109.0	109.0
N-$_2$-Te_1-N_3	69.2(2)		69.9		70.0	70.0

[a] This work

In addition to computational expediency, one advantage of modeling supramolecular structures with molecular mechanics, when compared with the most commonly used density functionals, is the ability to approximate the contribution from dispersion forces with a simple van der Waals potential.[277] This should, in principle, provide reasonable models of the stacking of the heterocycles. A model stack of four dimers of **40** was optimized from four different starting points with arbitrary initial spacing of parallel molecules. Each minimization led to the same structure which is displayed in Figure 7.3 along with the actual spacing of ribbon polymers from the crystal structure. The calculated interplanar spacing of 3.72 Å is in excellent agreement with the actual measurements from the crystal structure: 3.67(1) and 3.71(1) Å[203] However, the vertical alignment of molecules on different planes calculated by MMX displays significant differences from the arrangement of ribbons in the crystal structure.

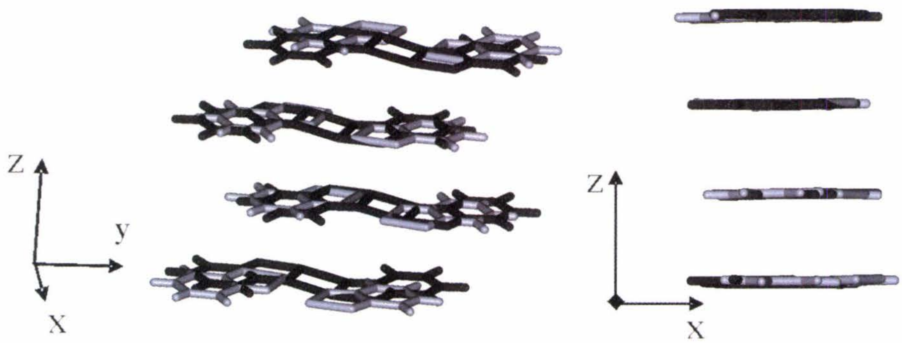

Figure 7.3 Comparison of π-stacking in the experimental crystal structure of **40** (light grey,)[203] with the MMX modeled structure (dark grey). SBIs are omitted for clarity.

The crystal structure of **27**,[64] a twisted ribbon polymer, was useful for the evaluation of the dihedral parameters. The deviation from planarity of the ribbon polymer distorts the geometry of the five-membered heterocycle, causing puckering, while the virtual ring formed by the SBIs remains planar with 0° dihedral angles. Selected structural parameters are summarized in Table 7.8 and show that as the chain grows the intramolecular dimensions deviate from those in the modeled monomer and approach those found in the crystal structure. Although the dihedral angles were difficult to reproduce with accuracy (a 10° deviation was obtained for the N_1-C-C-N_2 dihedral angle), the overall structure was well reproduced. The central pair of molecules in the 32-unit chain had an average deviation of 0.19 Å and a maximum deviation of 0.34 Å from the crystallographically determined positions (Figure 7.4).[203]

Table 7.8 Comparison of selected calculated and experimental bond lengths (Å) and angles (°) for **27**.

	27 (Exp)[64]	**27** (MMX)[a]					
Number of units		1	2	4	8	16	32
Te$_1$-N$_1$	2.023(6)	2.021	2.021	2.021	2.021	2.021	2.022
N$_1$-Te$_1$-N$_2$	84.3(3)	81.9	83.2	86.6	87.2	87.2	87.2
N$_1$-Te$_1$-N$_2$-C	2.5	0.0	0.0	5.6	4.3	4.8	4.9
Te$_1$-N$_1$-C-C[b]	6.6	0.0	0.0	5.0	12.1	13.5	13.6
N$_1$-C-C-N$_2$	9.4	0.0	0.0	6.8	17.5	19.6	19.8
C-C-C-C[c]	16.3	0.0	0.0	5.4	14.1	15.9	16.0
Te$_1$-N$_3$	2.825(8)/ 2.842(8)		2.822	2.866	2.875	2.888	2.890
N$_2$-Te$_1$-N$_3$	70.7(3)/ 71.1(3)		73.2	71.9	70.9	70.4	70.4
N$_2$-Te$_1$-N$_3$-Te$_2$	0.0		0.0	0.3	0.1	0.0	0.2
Te$_1$-N$_3$-Te$_2$-N	0.0		0.0	0.2	0.1	0.0	0.2

[a] Average values from the two central molecules

[b] Within the five-membered ring

[c] Sharing central C with N$_1$-C-C-N$_2$

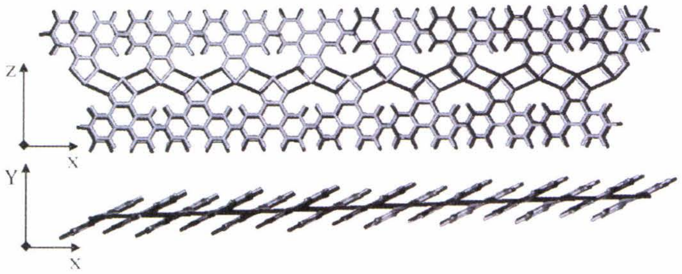

Figure 7.4 Comparison of the experimental crystal structure of **27** (light grey)[64] with MMX modeled structure (dark grey). SBIs are omitted for clarity.

The stability of supramolecular isomers can be compared by the strain energy. While the systems discussed up to this point are symmetrical and can only form one supramolecule, **31** can dimerize to form three different structures (Scheme 7.2). The dimensions and strain energies of the [Te-N]$_2$ supramolecular synthons in the optimized dimers of **31** are provided in Table 7.9 where it can be seen from the strain energy that supramolecular isomer I is the most stable, indeed this is the structure that is observed in the solid state.[65]

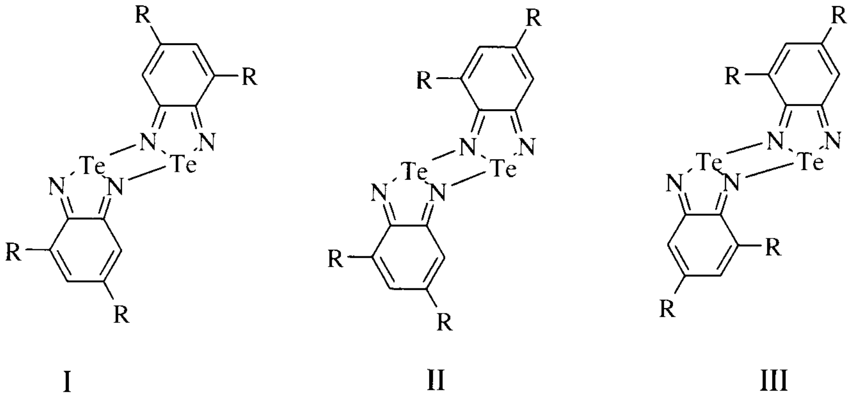

Scheme 7.2 Three possible arrangements for the dimers of **31**.

Table 7.9 Structural and energetic parameters of the $[Te\text{-}N]_2$ supramolecular synthon in dimers of **31**.

	Supramolecular dimer		
$[Te\text{-}N]_2$ parameters	I	II	III
$d_{Te\text{-}N}$ (Å)	2.692	2.716 / 2.898	2.969
$a_{N\text{-}Te\text{-}N}$ (°)	69.9	69.8 / 74.0	74.0
$a_{Te\text{-}N\text{-}Te}$ (°)	110.1	111.5 / 104.8	106.0
strain energy (kJ/mol)	0.0	2.7	11.5

Because the MMX force field treats cyclic and acyclic systems separately, the new parameter set could be adapted to model the structures of acyclic diamino tellurides. Because there is an approximately 15° increase in the N-Te-N angles from the cyclic telluradiazoles to the acyclic tellurium diamides, additional parameters were created for the acyclic N-Te-N bond angle and force constant (100.3°, 0.09058 kJ × mol^{-1} × deg^{-2}). The parameters for the diamino tellurides were evaluated by modeling $((CH_3)_2N)_2Te$[278] (**58**) which forms a ribbon polymer through the $[Te\text{-}N]_2$ supramolecular synthon.

Comparison of the calculated and experimental structures (Table 7.10) reveals that although these parameters were not fully optimized they perform well enough to model the extended structure (see Figure 7.5).

Table 7.10 Comparison of selected calculated and experimental bond lengths (Å) and angles (°) for **58**.

	58 (Exp)[278]	**58** (MMX)		
Number of units	Avg.	1	6	12
Te$_1$-N$_1$	2.050(2)	2.026	2.027	2.027
N-$_1$-Te$_1$-N$_2$	100.4(1)	101.5	105.7	105.7
Te$_1$-N$_3$	2.959(2)		2.850	2.850
N-$_2$-Te$_1$-N$_3$	77.7(1)		70.8	70.8

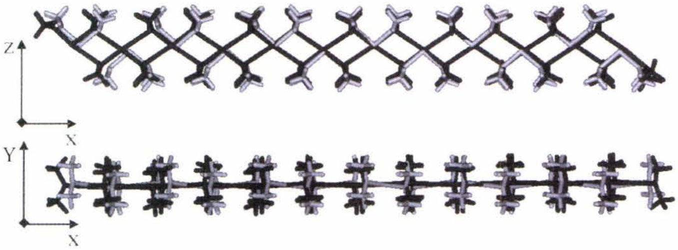

Figure 7.5 Comparison of the crystal structure of **58** (light grey, SBIs are omitted for clarity)[64] with MMX modeled structure(dark grey).

7.2.3 Modeling the Steric Control of Self-Association

There is a remarkable lack of structurally characterized examples of non-associated 1,2,5-telluradiazole rings. Although the reported properties of **41** hint that it could be monomeric, no actual crystallographic data is available in literature.[109] It is desirable to examine a non-associated telluradiazole as a structural and spectroscopic point of reference against which the properties of the supramolecular dimers and polymers could be compared. In addition to capping the N or Te atoms with Lewis acids[148] or bases,[142,203] respectively, such a species could be obtained by placing bulky groups at the 4 and 7 positions of benzo-2,1,3-telluradiazole and which would introduce less change to the electronic structure of the heterocycle. Moderate steric hindrance (Scheme 7.3a) does stabilize the dimers that have been crystallographically characterized.[65,203] It is therefore reasonable to expect that even bulkier groups would lead to monomeric telluradiazoles (Scheme 7.3b).

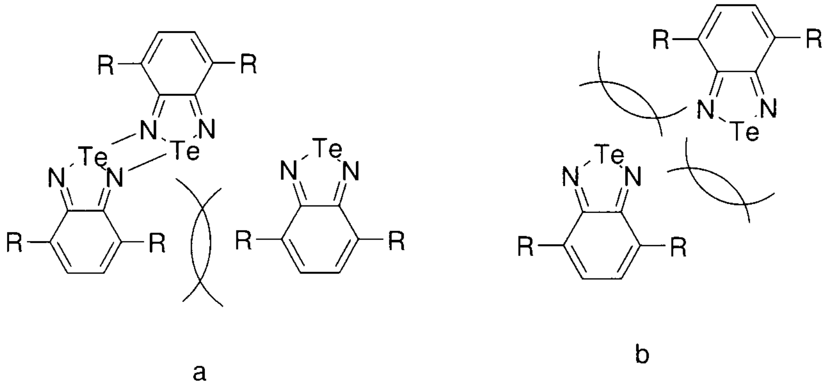

Scheme 7.3 Steric repulsion between 4,7-disubstituted benzo-2,1,3-telluradiazoles.

In order to probe the effect of several bulky substituents, the dimers of benzotelluradiazoles **40**, **46**, and **63** to **77** were modeled using the optimized force field parameters. Although DFT methods are certainly capable of minimizing each of these systems, molecular mechanics is a more efficient screening method. Table 7.11 contains the structural parameters and strain energies of the $[Te\text{-}N]_2$ supramolecular synthons for the each of the supramolecules that were optimized. The calculated SBI distances range from 2.693 to 2.996 Å and the $[Te\text{-}N]_2$ supramolecular synthon strain energies range from less than 0.01 to 17.11 kJ/mol. The cases in which the largest deviations from the equilibrium SBI distance are observed are those of the molecules substituted with the t-butyl (**69**), trimethylsilyl (**70**), cyclohexyl (**72**) and 1-adamantyl (**73**) groups. Molecules with phenyl-based groups (**74**-**77**) do not lead to a significant change in the SBI distances because the aromatic rings can rotate to leave enough room for association. The bond angles in the [Te-N]$_2$ supramolecular synthon range from 102.8° to 110.1° with the most significant deviations observed in the molecules with the t-butyl (**69**), trimethylsilyl (**70**), trityl (**71**) and 1-adamantyl (**73**) substituents. Although the 1-adamantyl group also maximizes the strain energy on the [Te-N]$_2$ supramolecular synthon, the magnitude is smaller than the DFT-calculated interaction energy for a pair of 1,2,5-telluradiazoles,[214] this indicates that even with the bulkiest groups considered here, there will always be a strong drive for dimerization in the solid state.

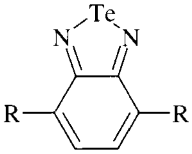

63 R=F
64 R=Cl
46 R=Br

65 R=I
66 R=Me
67 R=Et

68 R=^{i}Pr
69 R=^{t}Bu
70 R=Me$_3$Si

71 R=
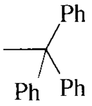

72 R=
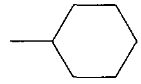

73 R=
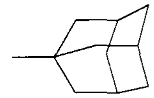

74 R=
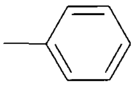

75 R=
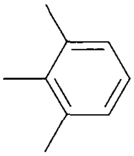

76 R=
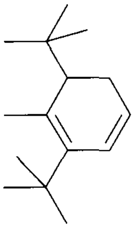

77 R=
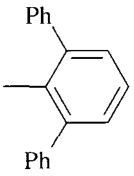

Table 7.11 Comparison of selected bond distances[a], angles[a] and strain energies[a] for the [Te-N]$_2$ supramolecular synthon in the dimers of the telluradiazoles **40**, 46, and **63** to **77**.

Telluradiazole dimer	Te-N SBI (Å)	Te-N strain (kJ/mol)	Te-N-Te SBI (°)	Te-N-Te strain (kJ/mol)	Total strain (kJ/mol)
40$_2$	2.693	0.00	110.1	0.00	0.01
63$_2$	2.689	0.00	109.9	0.00	0.00
64$_2$	2.728	0.05	108.9	0.09	0.46
46$_2$	2.744	0.13	108.3	0.21	1.10
65$_2$	2.758	0.22	107.7	0.38	1.98
66$_2$	2.728	0.06	108.9	0.09	0.48
67$_2$	2.738	0.10	108.7	0.13	0.72
68$_2$	2.770	0.32	108.0	0.30	1.82
69$_2$	2.996	4.04	105.7	1.38	13.58
70$_2$	2.872	1.62	105.8	1.27	8.32
71$_2$	2.749	0.16	105.8	1.35	5.73
72$_2$	2.777	0.38	107.8	0.37	2.23
73$_2$	2.814	0.78	102.8	3.89	17.11
74$_2$	2.713	0.01	109.3	0.04	0.19
75$_2$	2.707	0.00	109.4	0.03	0.12
76$_2$	2.706	0.00	109.6	0.01	0.05
77$_2$	2.710	0.01	109.1	0.04	0.19

[a] The average values are reported for the dimers of **71**, **73**, **76** and **77**.

7.2.4 Modeling Two-Dimensional Arrays

Supramolecular arrays extending beyond one dimension could be constructed from building blocks with more than one telluradiazole ring. There are examples using S-N and Se-N SBIs that are related to this approach.[167] The associations of the bifunctional compounds **78** and **79** were modeled. Compound **78** formed a supramolecular sheet (Figure 7.6) that maximizes the number of Te-N SBIs with only a small strain energy on the [Te-N]$_2$ supramolecular synthon: 0.00-0.05 kJ/mol on each of the N-Te-N SBI angles and 0.00-0.11 kJ/mol on the Te-N SBIs in a 12 unit planar structure. This model was expanded by optimizing the π–stacking. A second layer was initially placed eclipsing the first, optimization resulted in a shift in the centre of mass by 3.9 Å along the molecular

Te-Te axis (Figure 7.7) giving a van der Waals potential of -21.8 kJ/mol. In order to explore other stacking arrangements, the second layer was rotated by 45° and 90° before optimization. Both conditions led to structures with less favourable van der Waals interaction energies (-19.9 kJ/mol and -20.7 kJ/mol, respectively). From the most stable structure, two possible orientations were considered for the third sheet by either reversing (Figure 7.7a) or by repeating the interlayer shift (Figure 7.7b). The predicted space groups and crystallographic parameters for these arrangements are given in Table 7.12. The predicted densities are comparable to those experimentally determined for **40** and **46**, which suggests that the predicted structures are realistic.

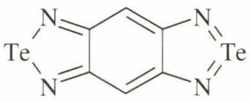

78

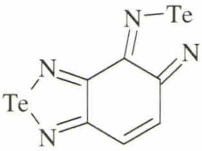

79

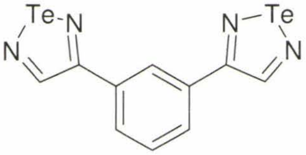

80

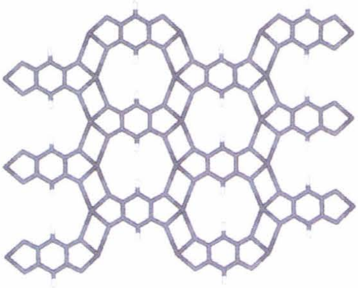

Figure 7.6 Supramolecular sheet formed by association of **78**.

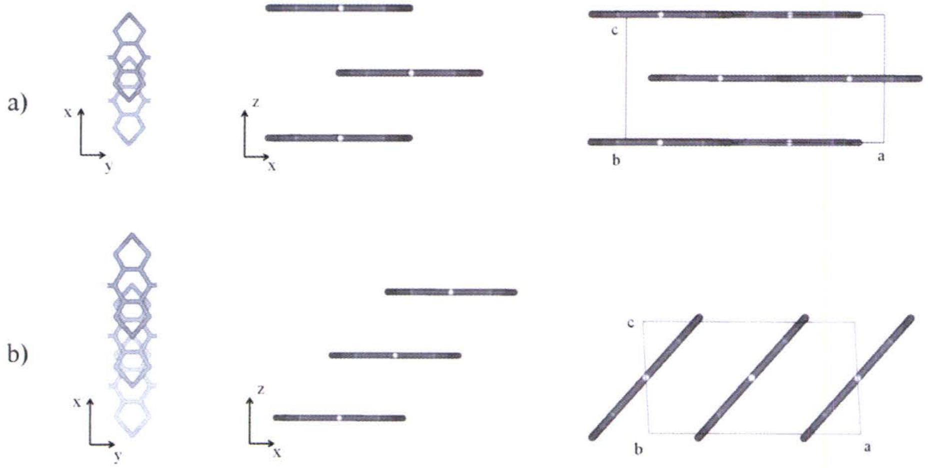

Figure 7.7 Optimized crystal structures of **78**; (a) monoclinic, (b) orthorhombic.

Table 7.12 Predicted crystallographic parameters for the optimized crystal structures of **78**.

Polymorph	a	b
Empirical formula	$C_6H_2N_4Te_2$	$C_6H_2N_4Te_2$
Crystal system	Monoclinic	Orthorhombic
Space group	C2/c (No. 15)	$C222_1$ (No. 20)
a [Å]	10.40	14.68
b [Å]	7.68	7.69
c [Å]	5.51	7.26
β [°]	93.53	90
Z	2	4
ρ(calc.) [g/cm^3]	2.91	3.12

The most stable of the possible 2-D arrangements obtained from compound **79** was a slightly puckered sheet (Figure 7.8) in which each molecule has one tetracoordinated and one tricoordinated Te atom participating, respectively, in two and one $[Te\text{-}N]_2$ supramolecular synthons. Therefore the structure features a combination of the dimer and the ribbon polymer motifs with their SBI axes at 120° with respect to each other. Puckering is caused by the Te-H steric repulsion between neighbouring molecules.

The ribbons consist of two different supramolecular synthons: one that is almost planar (N-Te--N-Te torsion angle 1.8°) and one that is significantly distorted (N-Te--N-Te torsion angle 6.4°). The N-Te--N-Te torsion angle between the tricoordinated Te centers is 2.4°. The distortion to the $[Te-N]_2$ supramolecular synthon also impacts the Te-N SBI distances: 2.749 Å and 2.770-2.810 Å for the two different supramolecular synthons along the ribbons and 2.681 Å in the dimers. Modeling the π-stacking in this case was significantly complicated by the puckering and was not attempted.

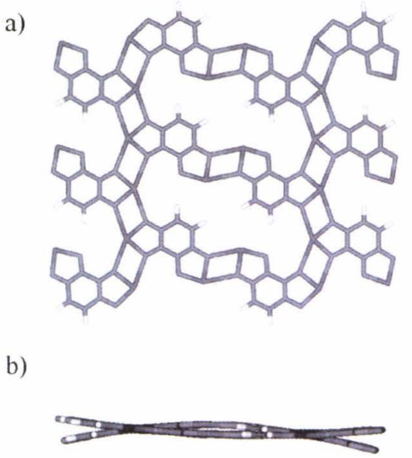

Figure 7.8 The two views of optimized two-dimensional array of **79**.

7.2.5 Modeling Rings and Spirals

In addition to the 2D array described above, building block **79** is capable of assembling two other arrangements: a cyclic hexamer with an optimized inner diameter of approximately 11 Å which can then be stacked (Figure 9), and a spiral with an inner diameter of about 10 Å (Figure 9).

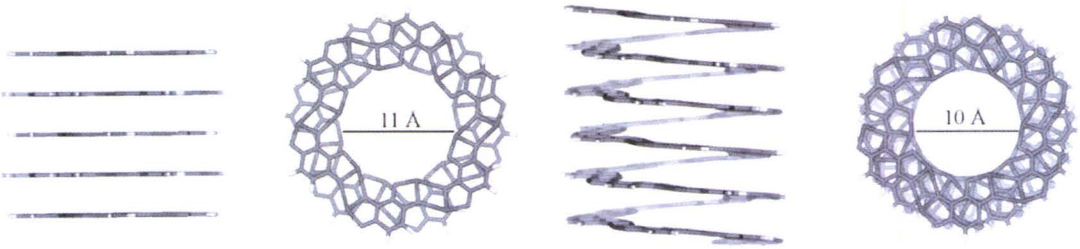

Figure 7.9 Possible supramolecular assemblies of **79**. (a), (b) π-stacks of cyclic hexamers, and (c), (d) spiral chain.

The more flexible molecule **80** should facilitate the formation of similar planar chains, rings and spirals. The calculated strain energy for a chain was 139 kJ/mol, irrespective of the model length. Rings of increasing size displayed a decrease of strain energy from 152 kJ/mol with four molecules to 141 kJ/mol with five, 138 kJ/mol with six, and 139 kJ/mol with both seven and eight molecules. While the four to six-membered rings were essentially planar, the larger rings were highly puckered. The six-membered ring, with a diameter of approximately 20 Å (Figure 7.10) is the most stable because of the approximately 120° bite angle between the two telluradiazoles in **80**. The stabilities of these rings was further tested by removing the two SBIs of one supramolecular synthon for each case. The four- and five-membered rings relaxed to the chain structure but incipient spirals were obtained from the larger rings. While the six-, seven- and eight-membered rings coincided in the diameter of the column, the five-membered ring led to a narrower structure. Larger models of the two spirals were then modeled (Figure 7.11); the strain energy was larger for the narrow spiral (115 kJ/mol) than for the wider structure (108 kJ/mol). Although the bite angle of the building block is likely to determine the preferred size of the column, these results suggest that the diameter of such a structure could be influenced by environmental conditions such as the inclusion of a guest species within the spiral.

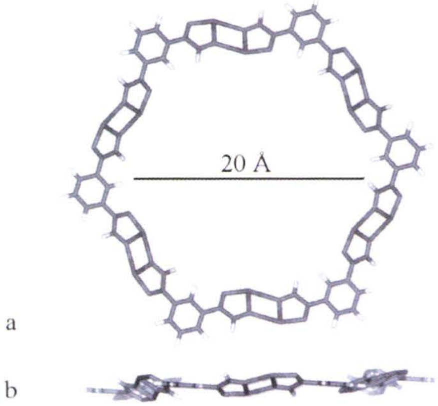

Figure 7.10 The two views of the cyclic hexamer of **80**.

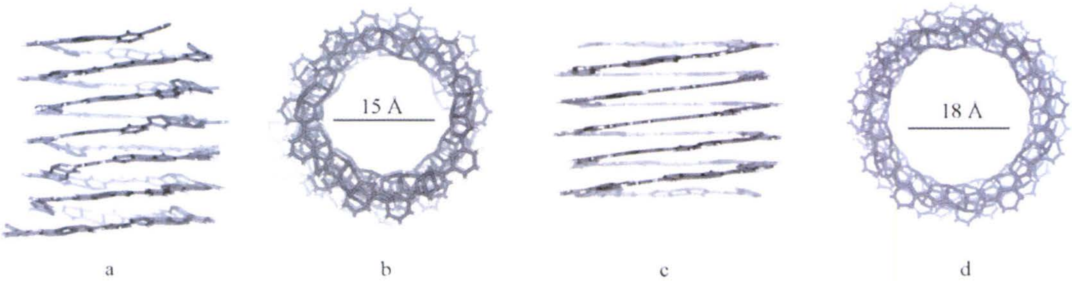

Figure 7.11 Spiral chains assembled by **80**. (a), (b) 5 units per turn, and (c), (d) 6 units per turn.

7.3 Summary

The MMX force field was parameterized to enable molecular mechanics modeling of Te-N intra- and intermolecular bonds in systems containing the 1,2,5-telluradiazole ring. These parameters were able to reproduce many of the intra- and intermolecular structural features in the crystal structures containing these heterocycles.

This set of parameters was used to investigate the assembly of supramolecular structures from hypothetical building blocks.

8 Supramolecular Functional Materials

8.1 Introduction

One of the primary goals of supramolecular chemistry is to achieve control over the properties of a substance through careful design and control of the molecular arrangements. The previous chapters provide an account of the steps taken to identify an efficient SBI supramolecular synthon, synthesize and characterize the corresponding building blocks, and develop the methods to facilitate the design of supramolecular assemblies. It remains to be demonstrated that the $[Te\text{-}N]_2$ supramolecular synthon is indeed useful for the construction of materials that have physical properties that could lead to practical applications.

In very general terms, there are three basic approaches to creating a functional supramolecular material:

1. Use the shape of the structure, rather than the properties of the building blocks, to generate the function. This is exemplified by the vast work carried out in the development of porous "metal-organic" frameworks.[279]

2. Exploit the energy balance between the intermolecular interactions and the entropy to control the transitions between phases, as in the case of liquid crystals.[280]

3. Use mutual perturbations between interacting molecules to manipulate the electronic structure of the material; this has been used, for example, in the design of antiferromagnetic networks.[281-283]

This chapter presents three examples in which materials have been developed by applying these principles.

8.2 The Crystalline Phases of 4,5,6,7-Tetrafluorobenzo-2,1,3-telluradiazole

8.2.1 Thermochromic Solid-Solid Phase Transition of 41

Although it had previously been reported that **41** was prepared by the reaction of $TeCl_4$ with 1,2,3,4-tetrafluoro-5,6-diaminobenzene in boiling *o*-dichlorobenzene, the yield was only 20%.[109] The original report implied that the properties of the compound were not consistent with a self-associated ribbon polymer in the solid state, but no structural data was reported. It was, therefore, of interest to establish the solid-state structure of this compound. Direct application of the method optimized for the synthesis of **40** afforded the compound with an 84% yield.

Recrystallization from saturated pyridine or DMSO solutions produced small red plates, but significant twining and polycrystallinity precluded satisfactory refinement of the X-ray diffraction data. The structure of the material was established when single crystals were grown by slow sublimation under static vacuum at 140 °C. The crystallographic parameters and refinement details for the structures discussed in Section 8.2 are provided in Table 8.1. The refined structure of this phase (α-**41**) has an asymmetric unit which consists of four independent molecules; their internal dimensions, however, are identical within statistical error. Selected average bond lengths and angles are summarized in Table 8.2. Each molecule has pseudo-C_{2v} symmetry with the largest deviation occurring in the Te-N bond lengths. This structure, which is reminiscent of the structure of **40**, consists of ribbon polymers (Figure 8.1). The molecules are connected to each other through the $[\text{Te-N}]_2$ supramolecular synthon which is distorted because of the greater repulsion between fluorine atoms in **41** than between hydrogen atoms in **40**. The distortion causes one of the Te-N SBI distances to be longer (average 2.94(2) Å) than the other (average 2.68(2) Å). In apparent agreement with Alcock's bond description, the shorter Te-N SBI is located opposite the longer Te-N single bond, and vice versa. The distortion of the $[\text{Te-N}]_2$ supramolecular synthon is also reflected in the N-Te--N and Te-N--Te bond angles (64.9(6) and 71.3(6)° in **41** (compared with 68.6(2)-69.7(2)° in **40**[203]) as well as the angles between molecular planes (12.0(4) and 10.8(5)° compared with 2.5(4)° in **40**[203]). The ribbon chains (Figure 8.1) stack along both the *a*-axis and the *b*-axis; both 2D arrays are related by a 74.6° rotation about the *c*-axis. This structure is nearly isostructural with **40** if a monoclinic supercell (11.30 Å, 11.29 Å, 22.82 Å, 96.87°) of α-**41** is considered. The loss of symmetry, when compared with **40**, is the result of the distortion of the ribbon chain in order to accommodate the increased size of the fluorine atoms.

Table 8.1 Crystallographic data for α-**41**, β-**41** and **41**·Py.

Compound	α-**41**	β-**41**	**41**·Py
Empirical formula	$C_6F_4N_2Te$	$C_6F_4N_2Te$	$C_9H_5F_4N_3Te$
Crystal system	Triclinic	Triclinic	Monoclinic
Space group	$P\bar{1}$ (No. 2)	$P\bar{1}$ (No. 2)	$P2_1/c$ (No. 14)
a [Å]	7.972(2)	3.9831(4)	5.423(2)
b [Å]	7.973(2)	7.9969(9)	10.807(4)
c [Å]	22.773(6)	11.521(1)	20.081(7)
α [°]	85.259(5)	89.68(1)	90
β [°]	85.096(5)	89.870(8)	92.644(8)
γ [°]	89.960(5)	90.455(9)	90
V [Å^3]	1437.3(7)	366.96(7)	1175.6(7)
Z	8	2	4
ρ(calc.) [g. cm^{-3}]	2.807	2.749	2.163
T [K]	173(2)	173	173(2)
μ [mm^{-1}]	4.16		2.57
θ range	1.8-24.71		2.14-27.65
Limiting indices	$-9 \leq h \leq 4$		$-6 \leq h \leq 7$
	$-9 \leq k \leq 9$		$-14 \leq k \leq 13$
	$-26 \leq l \leq 26$		$-17 \leq l \leq 26$
Refl. collec./ unique	14339 / 4886		14325 / 2715
R(int.)	0.1443		0.1033
No. of parameters	470		172
No. of restraints	428		0
R_1 / wR_2 (I>2σ(I))[a]	0.0732 / 0.1388		0.0433 / 0.0791
R_1 / wR_2 for all data[a]	0.1512 / 0.1699		0.0844 / 0.0912
Goodness-of-fit on F^2	0.985		0.993
Larg. diff. peak/ hole [e·Å^{-3}]	1.733/-1.534		0.861/ -0.741

[a] $R_1 = \Sigma \, ||F_o|-|F_c|| \, / \, \Sigma|F_o|$, $wR_2 = \{\Sigma[w(F_o^2-F_c^2)^2] \, / \, \Sigma w(F_o^2)^2\}^{½}$

Table 8.2 Selected intramolecular crystallographic bond lengths (Å) and angles (°) for α-**41** and **41**·Py.

	α-**41***	**41**·Py
Te1-N1	2.04(2)	2.004(5)
Te1-N2	2.01(2)	2.020(4)
N1-Te1-N2	85.1(7)	85.2(2)
N1=C1	1.33(3)	1.307(7)
Te1-N1=C1	108.1(1)	109.2(4)
N2=C6	1.32(3)	1.315(7)
Te1-N2=C6	109.5(1)	108.8(4)

* Average values of equivalent bonds and angles in the four molecules in the asymmetric unit.

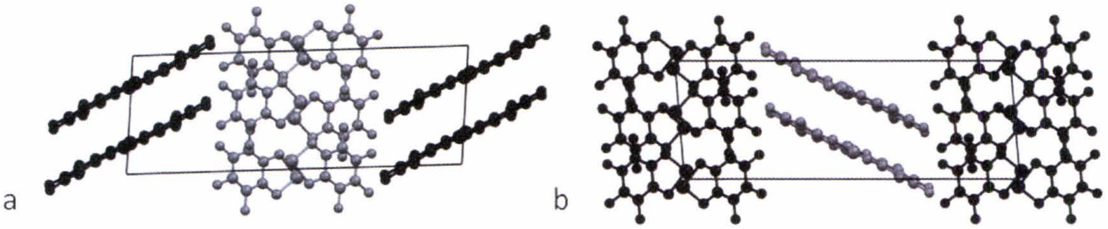

Figure 8.1 Ball and stick representation of two views of the packing in the crystal structure of α-**41**. (a) along [010], (b) along [100]. Stacked layers are distinguished by their shade.

A second phase, β-**41**, was obtained by fast sublimation at 100 °C onto a cold finger under dynamic vacuum (ca. 60 mTorr). This phase is a yellow microcrystalline powder which is clearly different from α-**41**. Attempts to grow single crystals, however, yielded the α-phase. The structural characterization of this solid could, therefore, only be based on powder X-ray diffraction data. The unit cell was identified and the structure was solved by optimizing the position of a rigid model of **41** by minimizing the difference between the calculated the experimental powder patterns of this phase. Although the main features of the structures can be identified, the quality of the data does not permit standard deviations to be obtained. The asymmetric unit consists of a single molecule of

41. The molecules self-associate into ribbon chains through centrosymmetric $[Te\text{-}N]_2$ supramolecular synthons (Figure 8.2a). Unlike the ribbon polymers in **40**, the SBI distances and angles in the $[Te\text{-}N]_2$ supramolecular synthon alternate along the ribbon chain; one having 2.7 Å SBIs and 65° N-Te--N angles and the neighbouring supramolecular synthon having 2.9 Å SBIs and 70° N-Te--N angles. This asymmetry appears to be a different way for the steric repulsion between neighbouring fluorine atoms to be accommodated. The ribbons stack along [100] and the parallel ribbons in this stack shift so that the tellurium atoms are offset between layers; this offset continues in the same direction (Figure 8.2b). These stacked layers are organized with respect to each other by a unit cell transformation along [001]. The arrangement of molecules in β-**41** resembles the arrangement in **27**, where all the ribbon chains run parallel to each other. The stacking of the ribbon chains, however, differs between β-**41** and **27** because the distorted phenanthrene rings, as opposed to the tellurium atoms, direct the stacking and, therefore, force the offset between stacked ribbon chains to be more pronounced.[64]

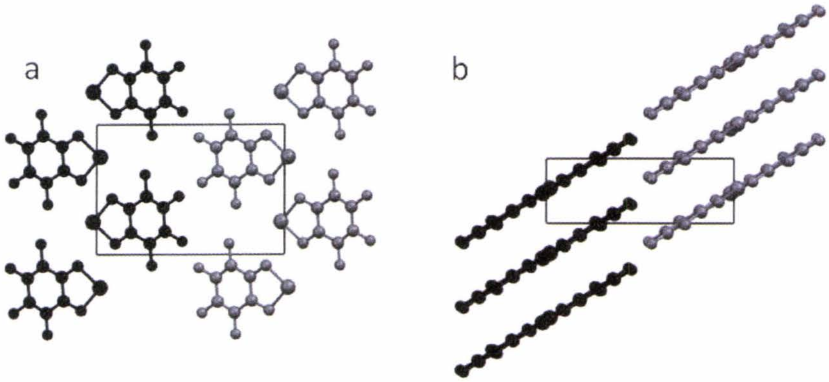

Figure 8.2 Ball and stick representation of two views of the packing in the crystal structure of β-**41**. (a) along [100], (b) along [010]. Stacked layers are distinguished by their shade.

The structures of the polymorphs each have long and short SBIs as well as wide and narrow angles within the $[Te\text{-}N]_2$ supramolecular synthons. In α-**41**, these features are combined within the same supramolecular synthon and result in an acentric distortion. In β-**41**, these features are found to alternate along the ribbon chain in centrosymmetric supramolecular synthons. DFT calculations of model oligomers of these structures show that, even though the association energies are nearly equal (-64.0 kJ/mol for α-**41** and -62.0 kJ/mol for β-**41**), the HOMO-LUMO gap differs because the alternating series of long and short centrosymmetric $[Te\text{-}N]_2$ supramolecular synthons results in a less efficient overlap between the π-orbitals of neighbouring molecules. The molecular HOMO-LUMO gap is 2.2 eV in monomeric **41** and it decreases to 1.4 eV in a hexamer of α-**41** , but only 1.8 eV in a hexamer of β-**41**.

The observed colour differences and the measured diffuse reflectance spectra (Figure 8.3) of these phases are consistent with this interpretation. There are no significant differences in π-stacking between the two phases that could justify the observed changes. Electronic excitation calculations were performed on model oligomers of α-**41** and β-**41**. The model chains were extended until the longest wavelength of absorption with a meaningful oscillator strength ($f > 0.001$ au) was constant within 5 nm, for both systems this condition was attained with a tetramer. For each tetramer, the calculated excitations with the largest oscillator strength or the longest wavelength are given in Table 8.3. There is a calculated red-shift of 63 nm from tetramers of α-**41** to tetramers of β-**41** (Figure 8.3). Although the wavelength of the first transition is overestimated by TD-DFT for both structures, the difference is qualitatively correct when compared with the experimental absorption spectra.

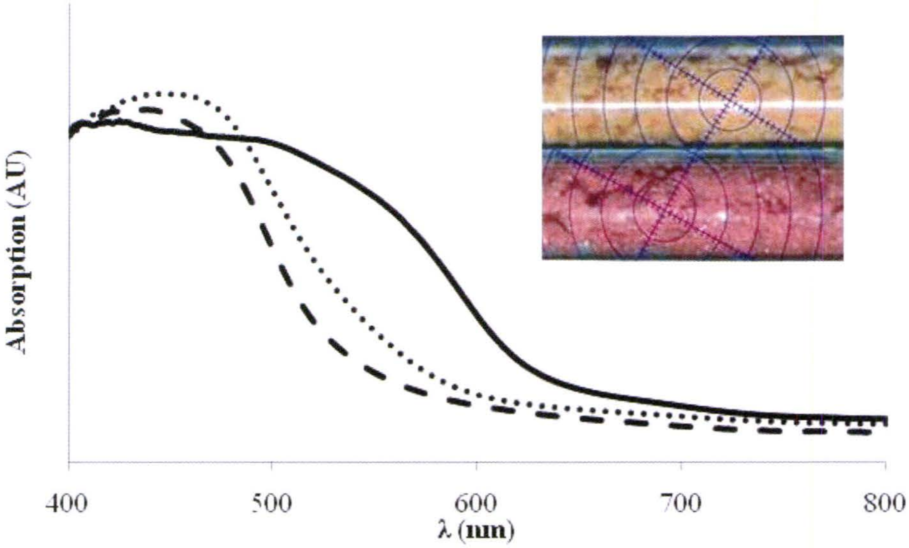

Figure 8.3 Absorption spectra of α-**41** (—) and β-**41** (- - -) and **41**·Py (•••) in the solid state obtained from diffuse reflectance measurements. Inset are images of β-**41** before (yellow) and after (red) heating which induces the phase change to α-**41**.

Table 8.3 Lowest energy and largest oscillator strength transitions between 300 and 800 nm for monomeric **41**, tetramers of α-**41** and β-**41**, and the dimer of **41**·Py including major contributions (>10%).

Species	λ (nm)	f (au)	Contribution (%)	
41	367	0.207	LUMO ← HOMO	(95.7)
	456	0.014	LUMO ← HOMO-1	(92.0)
α-**41**	361	0.185	LUMO+3 ← HOMO-1	(33.8)
			LUMO+3 ← HOMO-4	(19.2)
	710	0.007	LUMO ← HOMO-1	(98.1)
β-**41**	362	0.345	LUMO ← HOMO-1	(84.3)
	647	0.005	LUMO+1 ← HOMO-10	(16.9)
			LUMO+2 ← HOMO-4	(11.5)
			LUMO+2 ← HOMO-2	(11.5)
41$_2$•Py$_2$	360	0.201	LUMO+3 ← HOMO-2	(34.2)
			LUMO+1 ← HOMO	(15.3)
	531	0.050	LUMO ← HOMO-1	(60.0)
			LUMO+1 ← HOMO	(21.8)

Upon heating, β-**41** undergoes a phase change to α-**41** with the consequent colour change. (Figure 8.3 inset). The identities of the phases were confirmed by powder X-ray diffraction. DSC measurements (Figure 8.4) indicate that this is an exothermic monotropic phase change (ΔH = 2.297 kJ/mol) with an onset temperature of 116.0 °C. Starting at 220 °C a second change occurs that corresponds to mass loss in the TGA (Figure 8.5) and is attributed to either decomposition with loss of a volatile product, or sublimation.

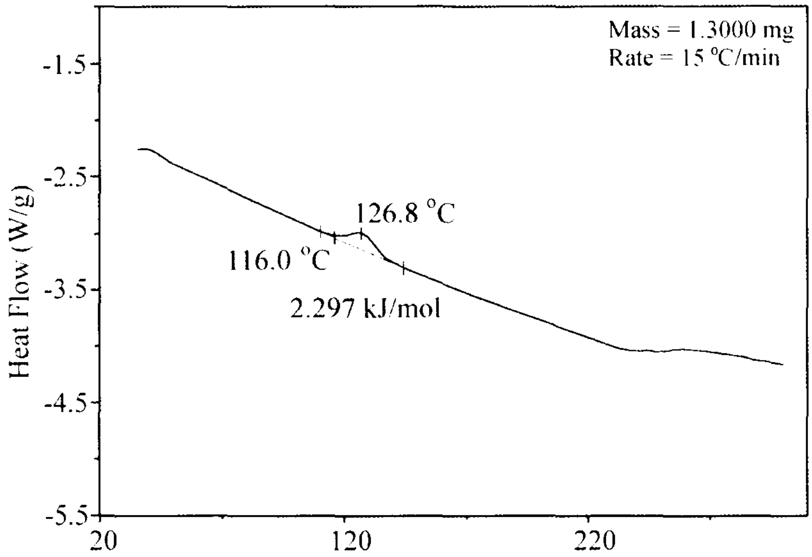

Figure 8.4 DSC curve of β-**41**.

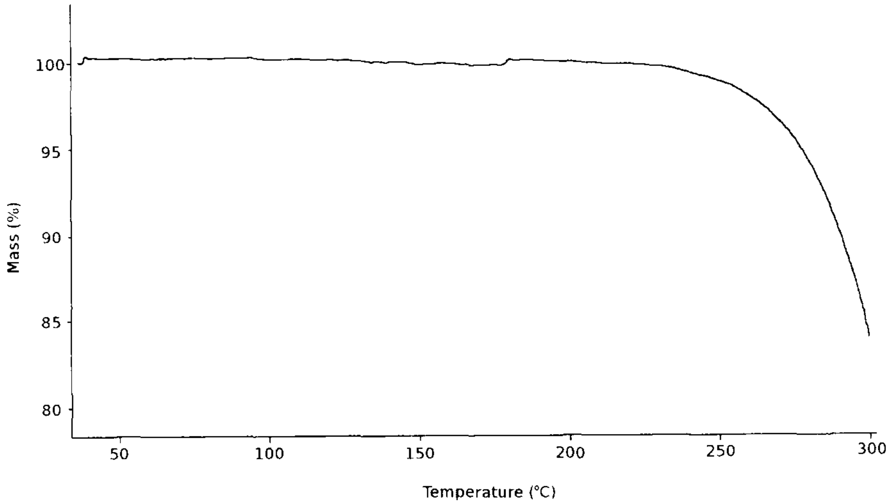

Figure 8.5 TGA curve of β-**41**.

Previous literature reports have related colour changes to the formation of chalcogen-centered SBIs. For example, the colour of organotellurium iodides are significantly different in the solid state when compared to the colour in chlorinated hydrocarbon or cyclohexane solutions.[284] Also, the diazenes RSN=C(R')N=NC(R')=NSR

(Scheme 8.1) appear to have distinct colours that depend on the conformation of the molecule and the length of the intramolecular SBI.[185] In these systems the significant covalent component of the SBIs causes changes in the HOMO-LUMO gap.[185] The thermochromic material **41** would be the first example in which this phenomenon is demonstrated by a phase transition between two crystalline polymorphs.

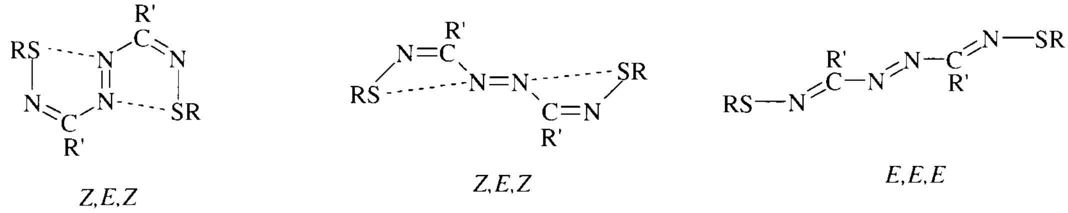

81 **82** **83**

Scheme 8.1 Structurally characterized isomers of RSN=C(R')N=NC(R')=NSR.

8.2.2 The pyridine solvate $41_2{\cdot}Py_2$

While α-**41** readily crystallizes from pyridine at room temperature, at -24 °C yellow crystals of a solvated dimer, **41**$_2$·Py$_2$, have also been isolated. The structure of the material was established by single-crystal X-ray diffraction; selected bond distances and angles are summarized in Table 8.2. The intramolecular distances of **41** in **41**$_2$·Py$_2$ are identical to those in α-**41** within statistical error. The crystal structure consists of centrosymmetric dimers of **41** with each tellurium atom capped by one pyridine molecule (Figure 8.6); this is analogous to the structure of the DMSO solvated dimers of **46**. Because the dimer is constructed by a centrosymmetric [Te-N]$_2$ supramolecular synthon, the asymmetric unit consists of only one molecule of pyridine and one molecule of **41**. The Te-N SBI distances in the [Te-N]$_2$ supramolecular synthon are both 2.767(5) Å which is longer than those observed in the unsolvated dimer of **46** (2.697(8) Å)[203] but almost equal to that of the solvated dimer **46**$_2\cdot$DMSO$_2$ (2.744(4) Å).[203] The Te-N SBI distance between **41** and pyridine is 2.787(5) which is only 0.020 Å longer than the SBIs within the dimer. Pyridine is also associated through short Te-N SBIs (< 80% Σr_{vdW}) to **13** ($d_{\mathrm{Te\text{-}N\ SBI}}$ = 2.426 Å)[43] and **19** ($d_{\mathrm{Te\text{-}N\ SBI}}$ = 2.2677, 2.852 Å).[57] In the present case, the SBI with pyridine tips the thermodynamic balance away from the distorted polymer and sequesters a stable dimer of **41**. The DFT-calculated association energy for the four SBIs in the supramolecule **41**$_2\cdot$Py$_2$, is 169.8 kJ/mol.

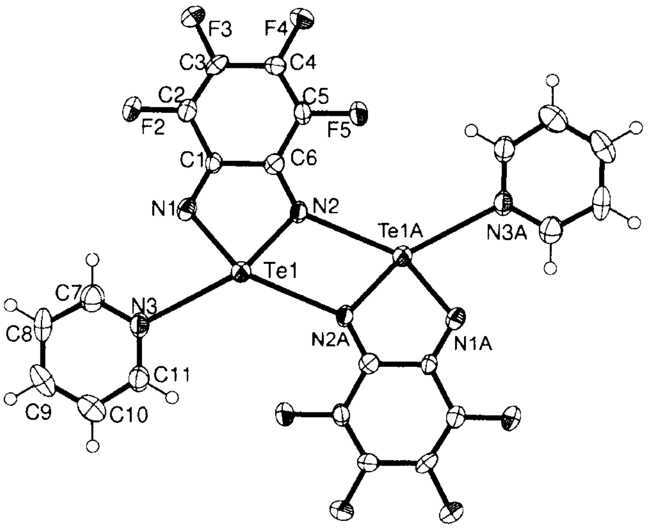

Figure 8.6 ORTEP representations and numbering schemes of the asymmetric unit plus inversion centre of **41**$\cdot$Py. Thermal ellipsoids are shown at the 50% probability level.

The crystals of **41**$_2\cdot$Py$_2$ lose pyridine easily to produce α-**41**. Therefore, the properties of this material provided an interesting comparison with the properties of β-**41**. The visible absorption spectrum was obtained by means of diffuse reflectance measurements for the yellow crystals (Figure 8.3). The calculated excitations with either the largest oscillator strength or the longest wavelength for the DFT-minimized model of

41$_2$·Py$_2$ are given in Table 8.3. The lowest energy transition of **41**$_2$·Py$_2$ is calculated to be red shifted with respect to an optimized monomer of **41**, but blue shifted when compared with α-**41**. The two transitions predominantly involve the HOMO-1, HOMO and LUMO which are π-orbitals that are delocalized over the two benzo-2,1,3-telluradiazole heterocycles. In this system, the mixing of orbitals in the π-framework causes the red shift with respect to the monomer, but the mixing is limited by the pyridine 'caps' which physically restrict the association to a dimer resulting in the blue shift with respect to α-**41**.

8.3 Non-centrosymmetric Lattices Induced by Distortion of the [Te-N]$_2$ Supramolecular Synthon

That the molecules of **41** form supramolecular ribbons in the solid state, in spite of the steric repulsion caused by the fluorine atoms, underscores the strength of the Te-N SBIs. Moreover, the geometric distortions in α-**41** warrant particular consideration because they remove the inversion centre from the [Te-N]$_2$ supramolecular synthon. If this feature propagates through the lattice by virtue of other intermolecular interactions and packing, the result would be a noncentrosymmetric crystal. This condition is not satisfied by α-**41** but it is conceivable that other building blocks might be able to direct the formation of a noncentrosymmetric lattice.

Materials that lack an inversion centre in their crystal structure have received much attention due to their optical properties. The macroscopic response of a substance to an electric field, the polarization (*P*), is described by the power series expansion in the electric field (E) shown in eq 8.1, where the coefficients $\chi^{(n)}$ are the n^th^ order dielectric susceptibilities.

$$P = \chi^{(1)}E + \chi^{(2)}EE + \chi^{(3)}EEE + \ldots \qquad 8.1$$

The nonlinear terms are significant only when the electric field (including the component of an electromagnetic wave) and/or the susceptibilities have a large magnitude. The even order susceptibilities are only non-zero in noncentrosymmetric materials. The nonlinear response defined by $\chi^{(2)}$ has a number of important applications such as frequency conversion[285] and electro-optic modulation.[286] While a number of inorganic crystals, such as β-BaB_2O_4, are by now routinely used in tuneable laser sources, the rational design of nonlinear optical (NLO) materials is still an important goal of supramolecular chemistry.

Hydrogen bonding has frequently been used to engineer acentric crystal lattices.[287,288] Benzoic acids that form acentric ribbon chains tend to crystallize in acentric space groups (11 out of 21 examples). Of these, the ortho-substituted rings show the highest preference for acentric spacial arrangement due to interchain interactions. On the other hand, dimers of benzoic acid tend to crystallize in centric space groups (116 of the 118 examples).[289] The use of noncentrosymmetric supramolecular ribbons to promote a non-centric lattice has been extended to include other types of supramolecular interactions. There are a number of examples which use coordination polymers with acentric bridging ligands to promote acentric lattice formation.[290-292] It is therefore reasonable to propose that the noncentrosymmetric distortion to the $[Te\text{-}N]_2$

supramolecular synthon could be used to build a noncentrosymmetric ribbon polymer which would produce a noncentrosymmetric crystal. This would only be the second example in which main-group SBIs have been used to design a nonlinear optical material. Previously, the [I O-I-O] supramolecular synthon, both alone[26] and in combination with hydrogen bonds,[293] has been used to guide the noncentrosymmetric packing of the crystal structure.

Clearly, as was observed with **46**,[203] too much steric hindrance will result in the dissociation of every other synthon in the crystal, as opposed to the distortion of the $[Te\text{-}N]_2$ supramolecular synthon. Moderate steric hindrance could be introduced by 3,4 or 5,6 disubstituting the 1,2,5-telluradiazole or benzo-2,1,3-telluradiazole heterocycles, respectively.

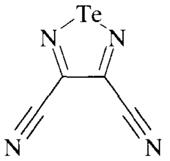

84

8.3.1 Syntheses and Structures of 3,4-Dicyano-1,2,5-telluradiazole (50) and 5,6-Dichlorobenzo-2,1,3-telluradiazole (84)

The telluradiazoles **50** and **84** were synthesized by the reaction of $TeCl_4$ with the appropriate diamine according to the methods described in Chapter 4. Removal of the solvent yielded **84** as a yellow powder and **50** as a purple-red powder. The triethylamine hydrochloride byproduct was removed from **50** by flotation in dichloromethane.

Compound **84** was isolated from this byproduct by extraction with pyridine. Each product was further purified by sublimation.

X-ray diffraction quality crystals of **84** were grown as needles from a saturated pyridine solution at -20 °C. The crystallographic data and final refinement parameters, and selected bond lengths and angles for all the structures in Section 8.3 are collected in Tables 8.4 and 8.5, respectively. The asymmetric unit consists of a single molecule (Figure 8.7). The intramolecular parameters of the five member ring in **84**, which has pseudo C_{2v} symmetry within the standard deviations, are identical to those in **26** within 3σ.[63] The atoms within the five member ring are coplanar and only N4 lies outside the plane of the ring (0.05(1) Å). The ribbon polymers in **84** are assembled along a two-fold screw axis, as opposed to across an inversion center as in **26**, and the $[Te\text{-}N]_2$ supramolecular synthons have a significant non-centrosymmetric distortion (see Table 8.5). The neighbouring heterocycles are not coplanar and have a 4.7(1)° angle between them (c.f. 0° for **26**)[63]. The interplanar distance (Figure 8.8a) between ribbon chains is 3.460(9) Å, this is slightly less than in **26** because the Te atom in one plane is positioned over the space between the two nitrile groups in **85**, whereas in **26** the Te atom is positioned over the five member ring. The ribbon chains arrange themselves in a herringbone-type pattern (Figure 8.8), similar to what is observed in **26**, with an angle of 70.66(7) ° (c.f. 123.14 ° for **26**).[63]

Table 8.4 Crystallographic and refinement parameters for **84**, **50** and **86**.

Compound	**84**	**50**	**86**
Empirical formula	C_4N_4Te	$C_6H_2Cl_2N_2Te$	$C_{13}H_9N_2OTe$
Crystal system,	Orthorhombic	Orthorhombic	Monoclinic
Space group	$P2_12_12_1$	$Pca2_1$	C2
a [Å]	5.983(2)	7.588(2)	10.647(7)
b [Å]	7.781(3)	7.744(2)	7.761(5)
c [Å]	12.932(5)	28.008(6)	14.31(1)
α [°]	90	90	90
β [°]	90	90	96.78(2)
γ [°]	90	90	90
V [$Å^3$]	602.0(4)	1645.9(6)	1174(1)
Z	4	8	4
ρ(calc.) [g. cm^{-3}]	2.556	2.426	1.900
T [K]	173(2)	173(2)	173(2)
μ[mm^{-1}]	4.840	4.192	2.516
θ range	3.06 - 32.03	1.45 - 28.85	2.87 - 23.28
Limiting indices	$-8 \leq h \leq 8$	$-8 \leq h \leq 9$	$-10 \leq h \leq 11$
	$-11 \leq k \leq 8$	$-10 \leq k \leq 10$	$0 \leq k \leq 8$
	$-19 \leq l \leq 18$	$-37 \leq l \leq 37$	$0 \leq l \leq 15$
Refl. collec./ unique	9691 / 2087	12915 / 3931	1164 / 1164
R(int.)	0.0748	0.0870	0
No. of parameters	83	200	155
Twin fraction	0.244	0.360	
Twining	racemic	racemic	180°; [001]
R_1 / wR_2 ($I>2\sigma(I)$)[a]	0.0451 / 0.0835	0.0634 / 0.1561	0.0546 / 0.1100
R_1 / wR_2 for all data[a]	0.0696 / 0.0909	0.1085 / 0.1732	0.0722 / 0.1157
Goodness-of-fit on F^2	0.987	1.058	1.021
Larg. diff. peak/ hole [e·$Å^{-3}$]	2.302 / -1.097	2.738 / -2.178	1.508 / -1.212

[a] $R_1 = \Sigma \,||F_o|-|F_c|| / \Sigma|F_o|$, $wR_2 = \{\Sigma[w(F_o^2-F_c^2)^2] / \Sigma w(F_o^2)^2\}^{1/2}$

Table 8.5 Selected bond lengths (Å) and angles (°) for **84**, **50** and **86**.

	84	**50**[a]	**50**[b]	**86**
Intramolecular[c]				
Te-N1	2.022(6)	2.01(1)	2.04(2)	2.02(1)
Te-N2	2.035(6)	2.02(1)	2.05(2)	2.03(2)
N1=C	1.300(9)	1.33(2)	1.29(2)	1.29(2)
N2=C	1.306(9)	1.36(2)	1.28(2)	1.29(2)
C-C	1.443(8)	1.45(2)	1.46(2)	1.50(2)
N-Te-N	82.5(2)	84.2(6)	84.4(6)	82.8(5)
Te-N1=C (°)	111.1(5)	112(1)	108(1)	112(1)
Te-N2=C (°)	109.9(4)	109(1)	108(1)	111(1)
Intermolecular[c]				
Te--N1 (Å)	2.767(6)	2.513(14)	2.541(14)	2.68(2)
Te--N2 (Å)	2.659(6)	2.89(1)	2.87(1)	2.80(2)
N2-Te--N1 (°)	67.1(2)	72.4(5)	73.2(5)	71.6(6)
N1-Te--N2 (°)	69.6(2)	64.2(5)	65.8(5)	68.8(5)
Te--N1-Te (°)	109.7(2)	104.9(6)	103.3(6)	107.7(7)
Te--N2-Te (°)	113.5(2)	118.2(7)	117.5(6)	111.8(7)

[a] This column refers to atoms in the heterocycle containing Te1

[b] This column refers to atoms in the heterocycle containing Te2

[c] For second molecule in the asymmetric unit of **50** (Te2-C110), these distances and angles refer to the corresponding atoms.

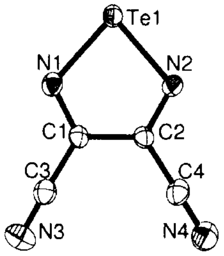

Figure 8.7 ORTEP and numbering scheme for the asymmetric unit in the crystal structure of **84**. Thermal ellipsoids are shown at the 50% probability level.

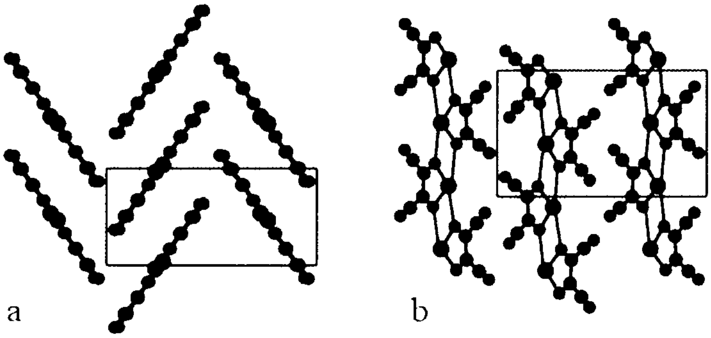

Figure 8.8 Two views of the crystal structure of **84**: (a) along [010]; (b) along [100]. Models presented as ball and stick.

X-ray diffraction quality crystals of **50** were grown as plates by cooling a saturated pyridine solution from 80 °C to room temperature. The asymmetric unit consists of two independent molecules which are displayed in Figure 8.9. The intramolecular parameters of the five member ring in both molecules of the asymmetric unit are the same within the standard deviations. The five-membered rings have pseudo C_{2v} symmetry and have the same intramolecular dimensions, within 3σ, as those observed in **40**.[203] The atoms within each molecule are coplanar and only C19 deviates significantly out of the plane (0.6(2) Å). The ribbon polymers in **50** are assembled by a translation along [010]. The neighbouring heterocycles have a 5.5(3)° angle between them (c.f. 2.5(4)° for **40**).[203] The parallel ribbon planes (Figure 8.10a) are constructed through the combination of a glide plane and a translation giving an interplanar distance of 3.43(3) Å, slightly smaller than observed in **26** or **40**; here the Te atom in one plane is positioned over the five member ring as seen in the crystal structure of **26** and **40**. The ribbon chains arrange themselves in a herringbone pattern (Figure 8.10), similar to that observed in **84** and **26**, with an angle of 128.8(9)°. In both **84** and **50**, it is the combination of the noncentrosymmetric distortion to the supramolecular synthon and the interference with the efficient packing between neighbouring chains that propagates the noncentrosymmetric motif throughout the lattice.

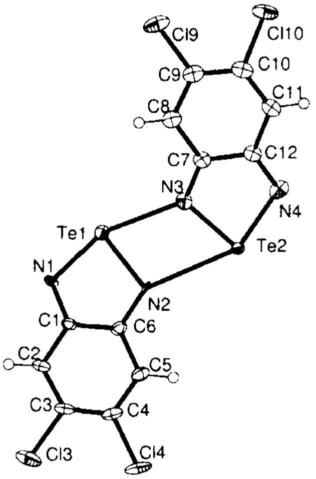

Figure 8.9 ORTEP and numbering scheme for the asymmetric unit in the crystal structure of **50**. Thermal ellipsoids are shown at the 50% probability level.

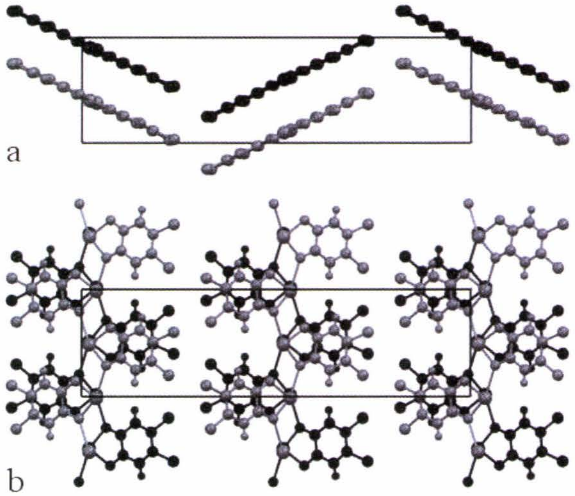

Figure 8.10 Two views of the crystal structure of **50**: (a) along [010]; (b) along [100]. Models presented as ball and stick, different layers are represented in different shades for clarity.

8.3.2 The Second Harmonic Generation of 50 and 84

The NLO activities of crystalline samples of **84** and **50** were examined by measuring the second-harmonic generation (SHG) efficiency at 1064 nm using the Kertz-Perry method. The SHG efficiencies of the samples were measured with respect to KH_2PO_4 (KDP) (d_{eff} = 0.39 pm/V)[294] and were found to be 0.105 and 0.035 for **84** and **50**, respectively. The reflectance spectra of both samples are shown in Figure 8.11. The significant absorption at 520 nm by each sample suggests that the observed NLO response is influenced by resonance enhancement.

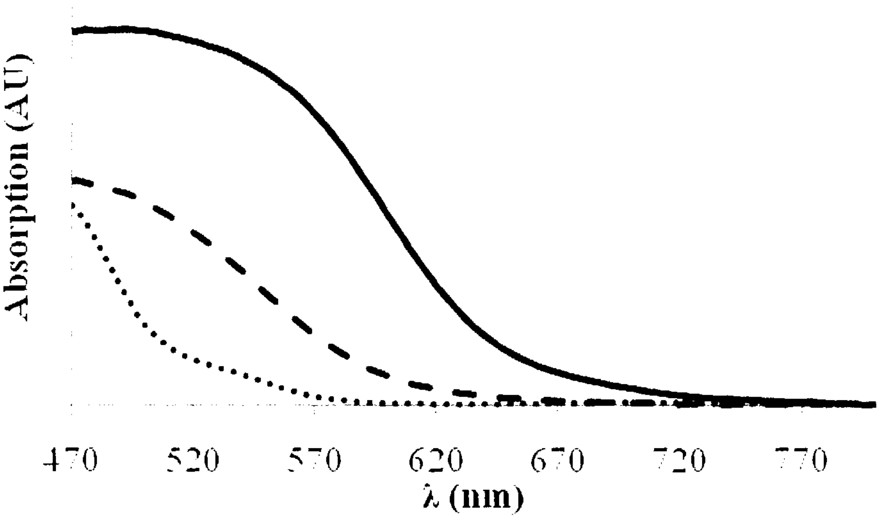

Figure 8.11 Solid-state visible absorption spectra (from diffuse reflectance measurements) of **50** (—), **84** (•••) and **86** (- - -).

DFT and TD-DFT calculations have been performed on **84** and **50**, as well as **26** and **40** for comparison, in order to estimate the static molecular hyperpolarizabilities β and the SHG hyperpolarizabilities at 1064 nm. Table 8.6 gives some of the calculated values that are relevant to the NLO activity, specifically the SHG efficiency. The values are, in most cases, approximately an order of magnitude smaller than the experimental value for *para*-nitroaniline (23 x 10^{-30} esu, HRS in $CHCl_3$),[295] a well studied NLO active push-pull molecule. The TD-DFT results suggest that there is, however, a significant increase of SHG efficiency for **50** when compared to **40**, and **84** when compared to **26**. These increases are due to the greater dipole moments upon introduction of electron withdrawing groups. In both cases this is accompanied by a decrease in HOMO-LUMO gap.

These materials can only be expected to have modest SHG efficiencies because the dipole moments of the heterocycles in the supramolecular ribbons must be nearly antiparallel. The overall second-order activity is a result of packing. The point group of the $P2_12_12_1$ lattice in which **84** crystallizes is non-polar. This results in the mutual cancellation of the molecular dipole moments giving a macroscopic nonlinear response that arises only from the octopolar contributions to the second-order tensor. On the other hand, the point group of the lattice for **50** is polar with an overall unit cell dipole parallel to the *c*-axis. DFT calculations on the asymmetric unit of **50** gave a dipole moment of 1.95 D for the dimer; the component parallel to the *c*-axis for each pair of molecules, however, is only 0.25 D.

Table 8.6 DFT and TD-DFT calculated values pertaining to the NLO activity.

	26	**40**	**84**	**50**	**86**
static $\langle\beta\rangle$ (esu $\times 10^{30}$)	1.60	1.93	2.79	8.08	1.94
SHG_{1064} $\langle\beta\rangle$ (esu $\times 10^{30}$)	1.68	1.88	3.55	15.58	2.99
μ (D)	0.04	0.13	6.99	2.32	3.22
HOMO-LUMO Gap (eV)	3.14	2.45	2.84	2.33	2.23
$\lambda_{\text{lowest energy}}$ (eV)	3.70	2.97	3.47	2.82	2.56

8.3.3 5-Benzoylbenzo-2,1,3-telluradiazole (86)

The two compounds described above do provide proof of principle for the successful formation of a noncentrosymmetric crystalline lattice by distorting the $[Te\text{-}N]_2$ supramolecular synthon. One strategy for achieving greater SHG efficiency would be to append a chromophore with a large NLO response onto the molecular structure. Ideally the chromophore could also impose the steric restrictions that led to the noncentrosymmetric distortions in **84** and **50**. The commercially available diamine **85** gave derivative **86** by following the standard synthetic method (Chapter 4). X-ray diffraction quality crystals of **86** were grown as prisms by slow sublimation under static vacuum (30 mTorr) at 120 °C. The asymmetric unit consists of a single molecule (Figure 8.12). The internal parameters of the five-membered heterocycle, within the standard deviations, are the same as the previously discussed structures. The plane of the benzoyl group is rotated by 51(1)° from the plane of the heterocycle. The molecules are assembled into ribbon chains through $[Te\text{-}N]_2$ supramolecular synthons constructed by a screw axis perpendicular to the *ac* plane (Figure 8.13b). The neighbouring rings within the ribbon chain are coplanar within 3σ (Figure 8.13) and the ribbon chains are stacked with an interplanar spacing of 3.4(1) Å (Figure 8.13a). The noncentrosymmetric distortion to the $[Te\text{-}N]_2$ supramolecular synthons appears to propagate throughout the lattice as a result of the interdigitation of the benzoyl groups between neighbouring ribbon chains (Figure 8.13b)

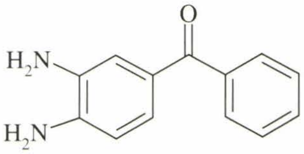

85

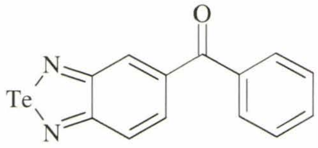

86

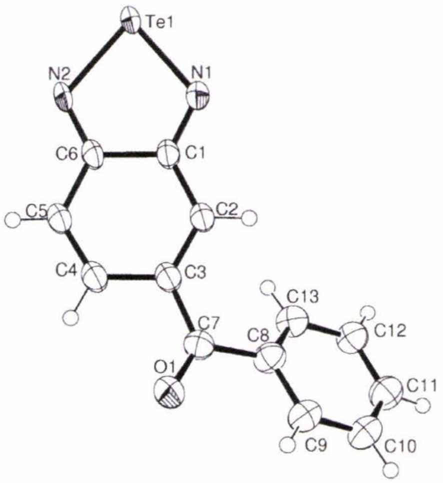

Figure 8.12 ORTEP and numbering scheme for the asymmetric unit in the crystal structure of **86**. Thermal ellipsoids are shown at the 50% probability level.

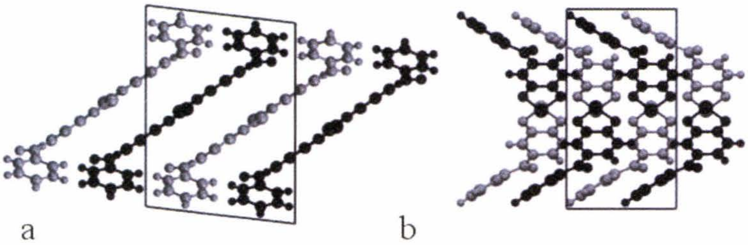

Figure 8.13 Two views of the crystal structure of **86**: (a) along [010]; (b) along [100]. Models presented as ball and stick, different layers are represented in different shades for clarity.

The d_{eff} of the crystalline sample of **86** was 0.076 with respect to KDP; this was intermediate with respect to the values for **84** and **50**. The molecular hyperpolarizability (Table 8.6), as calculated by TD-DFT, does not show an appreciable increase in activity over the unsubstituted molecule **40**. The point group of the lattice is polar with an overall unit cell dipole that is parallel to the *b*-axis. Similar to **50**, the molecules are aligned in an almost anti-parallel fashion, thus, the dipolar contribution parallel to the *b*-axis in the crystal structure of **86** is calculated to only be 1.94 D for each molecule. The reflectance spectrum of **86** is provided in Figure 8.11 and shows a non-zero absorption at 520 nm which again implies a contribution from resonance enhancement.

8.4 Charge Transfer Salts

The colour change, reflectance spectra and DFT calculations pertaining to the phase transition of **41** together suggest that the ribbon polymers formed by the association of 1,2,5-telluradiazoles have some degree of conjugation. It is conceivable that there are molecular orbitals delocalized through the ribbon. These materials should, therefore, have advantageous electron transport properties. Given the magnitude of their band gaps (2.1 to 2.9 eV), these compounds would be poor semiconductors. The generation of charge carriers by removal of electrons from the ribbon, however, might result in the creation of a conduction band. This topic could be conveniently explored through the synthesis of charge transfer salts with electron acceptors such as tetracyanoquinone (TCNQ, **87**).

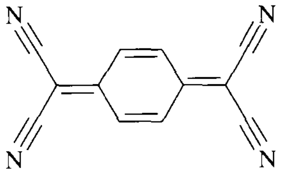

87

In preliminary experiments, each of the three benzo-2,1,3-chalcogenadiazoles (**38-40**) was mixed in a 1:1 molar ratio with **87**. Grinding the solids resulted in colour changes in **39** and **40** that were consistent with the formation of the charge transfer salts.

Crystals of the benzotelluradiazole derivative where grown by subliming the mixture along a temperature gradient starting at 120 °C in a glass tube sealed under vacuum (30 mTorr). This initial crop contained yellow crystals of **87** and dark purple crystals with a metallic luster. Crystallographic analysis (vide infra) established the composition of the dark purple material as $\mathbf{40}_2\cdot\mathbf{87}$. Attempts to sublime 2:1 mixtures yielded similar results, which might be a consequence of a large difference in the vapour pressures of the components. Crystals of the charge transfer salt of **39** could not be obtained by sublimation, instead they were obtained from the molten mixture as well as from acetone or toluene solutions. The crystallographic analysis established a 2:1 stoichiometry for this salt. The red crystals were not stable and a yellow colouration would develop slowly as **39** evaporated from the salt. The present isolation of the TCNQ salt of **39** is in conflict with a previous report which identified the composition of a violet cocrystal as 1:1 using elemental analysis.[296] In contrast to **39** and **40**, all attempts to grow crystals of the charge transfer complex with **38** failed.

8.4.1 Crystal Structures of the Salts

Single crystal X-ray diffraction of the samples revealed that the charge transfer salts of **39** and **40** are isomorphic. The crystallographic data and refinement parameters, and selected bond lengths and angles for both structures described in this section are collected in Tables 8.7 and 8.8, respectively.

Table 8.7 Crystallographic and refinement data for **39$_2$·87** and **40$_2$·87**.

Compound	**39$_2$·87**	**40$_2$·87**
Empirical formula	$C_{12}H_6N_4Se$	$C_{12}H_6N_4Te$
Crystal system,	Triclinic	Triclinic
Space group	$P\bar{1}$	$P\bar{1}$
a [Å]	7.647(1)	7.748(1)
b [Å]	8.165(1)	8.128(1)
c [Å]	9.7421)	9.963(2)
α [°]	69.282(3)	67.073(4)
β [°]	81.927(3)	79.963(4)
γ [°]	78.586(3)	77.745(4)
V [Å3]	556.0(1)	561.8(2)
Z	2	2
ρ(calc.) [g. cm^{-3}]	1.703	1.973
T [K]	173(2)	173(2)
μ [mm^{-1}]	3.356	2.627
θ range	2.24 - 30.51	2.23 - 27.32
Limiting indices	$-10 \leq h \leq 10$	$-9 \leq h \leq 10$
	$-10 \leq k \leq 1$	$-9 \leq k \leq 10$
	$0 \leq l \leq 13$	$-0 \leq l \leq 12$
Refl. collec./ unique	3311 / 2443	2558 / 1618
Twinning axis	[100]	[021]
Twinning Rotation (°)	180	180
Minor component	0.289	0.478
No. of parameters	155	155
R_1 / wR_2 ($I>2\sigma(I)$)^a	0.0383 / 0.0643	0.0544 / 0.0998
R_1 / wR_2 for all data^a	0.0549 / 0.0666	0.0908 / 0.1078
Goodness-of-fit on F^2	0.875	0.824
Larg. diff. peak/ hole [e·Å^{-3}]	0.966 / -0.451	3.158 / -1382

^{a} $R_1 = \Sigma \,||F_o|-|F_c|| \,/\, \Sigma|F_o|$, $wR_2 = \{\Sigma[w(F_o^2-F_c^2)^2] \,/\, \Sigma w(F_o^2)^2\}^{1/2}$

Table 8.8 Selected bond lengths (Å) and angles (°) in **39**$_2$·**87** and **40**$_2$·**87**.

	39$_2$·**87**	**40**$_2$·**87**
Heterocycle		
Intramolecular		
E-N1	1.797(2)	1.998(6)
E-N2	1.799(2)	2.019(6)
N1=C1	1.333(3)	1.330(9)
N1=C6	1.324(3)	1.309(9)
C1-C6	1.454(3)	1.477(9)
N1-E1-N2	93.29(9)	84.1(2)
E1-N1=C1	107.3(2)	111.0(5)
E1-N2=C6	107.6(2)	110.2(5)
Intermolecular		
E1--N2	2.910(2)	2.689(6)
E1--N1	2.949(2)	2.737(6)
N1-E1--N1	74.70(8)	68.4(3)
N2-E1--N2	73.27(8)	69.8(3)
E1--N1-E1	105.30(8)	111.6(3)
E2--N1-E2	106.73(8)	110.2(3)
87		
C=N	1.140(3)	1.138(9)
C=N	1.136(3)	1.15(1)
C-C	1.450(4)	1.42(1)
C-C	1.454(3)	1.44(1)
C=C	1.374(3)	1.40(1)
C-C	1.438(3)	1.43(1)
C-C	1.450(3)	1.45(1)
C=C	1.342(3)	1.34(1)

The asymmetric units consist of a single molecule of benzo-2,1,3-chalcogenadiazole and half a molecule of **87** (Figure 8.14). The annulated heterocycles display a pseudo C_{2v} symmetry and in both cases the bond distances are equal, within 3σ, to those observed in the crystals of the pure compounds. The N-Se-N angle, however, is 1.4° smaller than in **39**.[194]

The largest deviations from the molecular planes are observed for N1 (above) and N2 (below) by 0.026(2) and 0.024(2) Å, respectively, within the molecule of **39** and 0.031(6) and 0.025(6) Å, respectively, within the molecule of **40**. Within the molecule of **87**, N4 is slightly out of the ring plane by 0.097(4) Å in the salt of **39** and 0.030(6) Å in the salt of **40**. Packing in these crystals is illustrated in Figures 8.15 and 8.16. The arrangement consists of ribbon polymers assembled by $[E\text{-}N]_2$ supramolecular synthons and the polymers are flanked by molecules of **87** (Figure 8.15). Within each ribbon there are coplanar pairs of chalcogenadiazoles, neighbouring pairs are separated by 0.486(6) Å in $\mathbf{39}_2\cdot\mathbf{87}$ and 0.288(7) Å in $\mathbf{40}_2\cdot\mathbf{87}$. The SBI distances in the $[E\text{-}N]_2$ supramolecular synthon alternate along the ribbon chain and the longer SBIs are located within the coplanar dimers. The average SBI distance in the tellurium compound (2.713(6) Å) is the same as the average in the structure of **40**. Similarly, in the selenium case the average 2.929(2) is also comparable to distances observed in ribbon polymers of other selenadiazoles.[158,169] It should be noted that the $[E\text{-}N]_2$ supramolecular synthon is not formed in the crystal structure of **39**, instead there are Se-N contacts (3.154(4) Å)[194] that are just below the sum of van der Waals radii (3.36 Å).[297] The ribbon chains in adjacent layers are offset by a translation along [010] (Figure 8.16) and have an interplanar spacing of 3.295(5) Å in $\mathbf{39}_2\cdot\mathbf{87}$ and 3.307(9) Å in $\mathbf{40}_2\cdot\mathbf{87}$. These values are significantly smaller than in the crystal structure of **40** (3.67(1) and 3.71(1) Å).[203] The magnitude of the standard deviations in the dimensions of the TCNQ molecule does not permit comparison with the structures observed in other salts in order to assess the degree of electron transfer.[298]

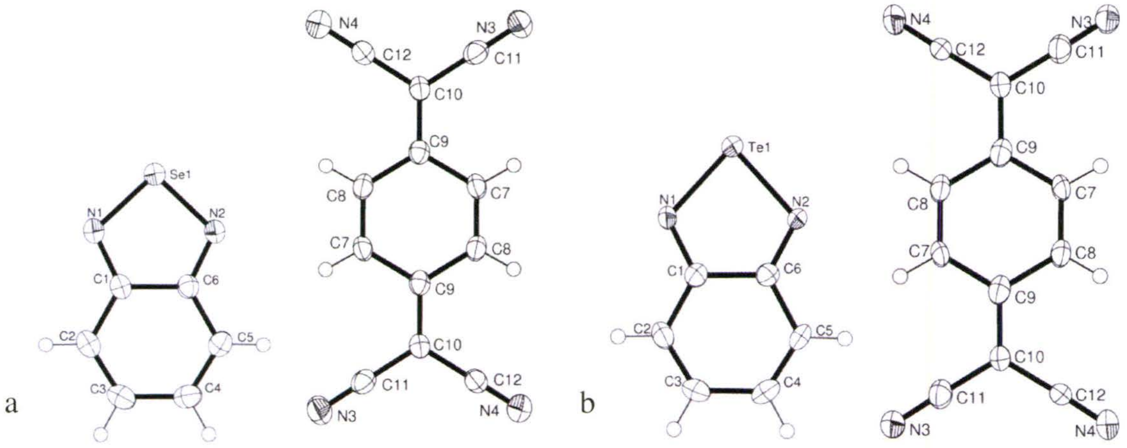

Figure 8.14 ORTEP representations of molecules in the asymmetric units of (a) $\mathbf{39_2 \cdot 87}$ and (b) $\mathbf{40_2 \cdot 87}$. Thermal ellipsoids are shown at the 50% probability level.

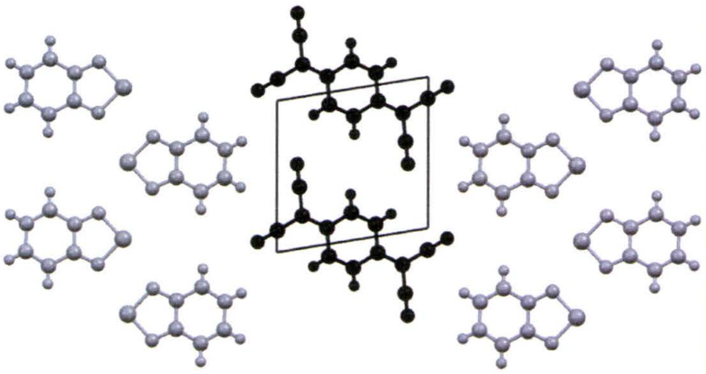

Figure 8.15 Packing in $\mathbf{39_2 \cdot 87}$ and $\mathbf{40_2 \cdot 87}$ ($\mathbf{39_2 \cdot 87}$ shown) along [001]; only one layer shown for clarity.

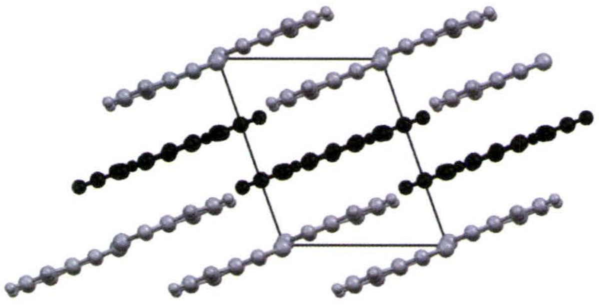

Figure 8.16 Packing in $\mathbf{39_2 \cdot 87}$ and $\mathbf{40_2 \cdot 87}$ ($\mathbf{39_2 \cdot 87}$ shown) along [100].

8.4.2 DFT-optimized Geometries of Neutral and Charged Oligomers of 40

The ionization energies measured by UPS (Section 6.2) suggest that there should be a greater degree of charge transfer in **40_2·87** than in **39_2·87**. Additionally, structural reorganization would pose less of an obstacle for charge transport in **40_2·87**. It can be expected, however, that the supramolecular structure of these systems will have important consequences on the charge carrier properties of these molecules.

To explore the effects of the ribbon chain formation, oligomers (monomer through hexamer) of **40** were modeled using DFT. Similar modeling was attempted for the oligomers of **39** but the calculations were plagued by convergence problems. The optimized structural parameters of the $[Te\text{-}N]_2$ supramolecular synthons are collected in Table 8.9. In the case of **40_n**, increasing the charge decreases the SBI distance, while increasing the length of the chain results in a lengthening of the SBI distance. It has been previously argued that the lengthening of the SBI distance that occurs with an increase in the number of units in the chain is the result of steric hindrance between neighbouring molecules.[203,214] The steric hindrance may account for the apparent lack of change in the average SBI distance in **40_2·87** when compared with **40** despite the charge transfer. This is in stark contrast to the short SBI distances (2.417(3) Å) observed in the N-methylated dimers of **40** for which steric hindrance is not a factor.[145]

Table 8.9 DFT-optimized supramolecular distances and angles in $[Te\text{-}N]_2$ in charged oligomers of **40**.

	Charge	dimer	trimer	tetramer	pentamer	hexamer
Te--N (Å)*	0	2.568	2.636	2.677	2.679	2.681
	1	2.480	2.571	2.622	2.635	2.642
	2	2.419	2.566	2.604	2.624	2.617
N-Te--N (°)*	0	70.20	69.94	69.61	69.58	69.65
	1	69.71	69.39	69.26	69.44	69.36
	2	69.43	69.34	69.25	69.46	69.27

*Average of innermost supramolecular synthon

8.4.3 DFT Calculated Effects of Oligomerisation of 40 on Hole Formation

Estimates of the polymerization energy for the neutral, mono, and dicationic chains of **40** were obtained by building model heterocycle chains of increasing length and plotting the association energy as a function of the chain length according to eqs 8.2-8.4 (Figure 8.17); ZPE corrections were omitted in this case. The slope of each linear plot corresponds to the association energy per molecule of chalcogenadiazole. It can be seen that the association energy increases with the charge. The enhancement of supramolecular synthon strength due to increased charge is not unexpected given the recent experimental observations that N-substituted selenadiazolium[143-145] and telluradiazolium[142,145] cations form discrete dimers held together by very short chalcogen-nitrogen SBIs. For the oligomer of **40**, the difference in energy between the neutral species and the cation corresponds to the first ionization energy and the difference between the cation and dication corresponds to the second ionization energy (Table 8.10). From these values, it can be seen that there is a significant decrease in ionization energy that accompanies chain elongation which would promote charge transfer.

$$n\mathbf{40} \rightarrow \mathbf{40}_n \qquad 8.2$$

$$n\mathbf{40} \rightarrow \mathbf{40}_n^{1+} + 1e^- \qquad 8.3$$

$$n\mathbf{40} \rightarrow \mathbf{40}_n^{2+} + 2e^- \qquad 8.4$$

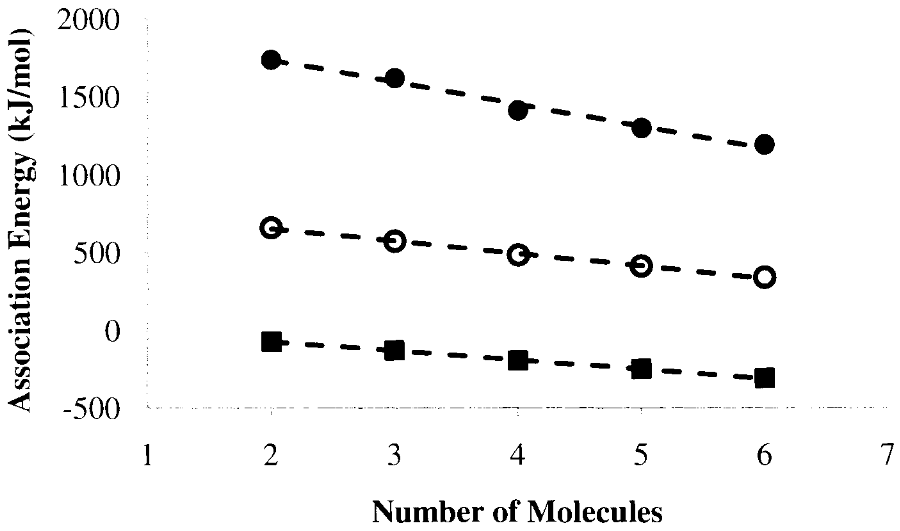

Figure 8.17 Total association energy of model telluradiazole oligomers. (●) **40**$_n$, -60.3 kJ/mol; (○) **40**$_n^+$, -80.7 kJ/mol; (■) **40**$_n^{2+}$,-141.6 kJ/mol.

Table 8.10 DFT calculated first and second adiabatic ionization energies for oligomers of **40**.

	monomer	dimer	trimer	tetramer	pentamer	hexamer
1st IE (eV)	8.50	7.57	7.27	7.00	6.84	6.73
2nd IE (eV)	14.79	11.16	10.83	9.61	9.18	8.83

The charge transfer will lead to conductivity only if it introduces a hole into a band. A closer inspection of the frontier orbitals was performed in order to probe whether the overlap in the ribbon chain is sufficient to form a band. From the UPS study, it was determined that the closely spaced HOMO and HOMO-1 of both **39** and **40** reside in the π-manifold of the ring. As the SBIs form, the HOMO and HOMO-1 in neighbouring molecules are placed in close proximity; orbital overlap then yields a group of closely spaced orbitals in the π-framework. Figure 8.18 shows the energies of the frontier orbitals as a function of the number of molecular units in an oligomer model; the result does suggest that bands would be formed in the solid state. Actual band calculations, however, would be necessary to address this point.

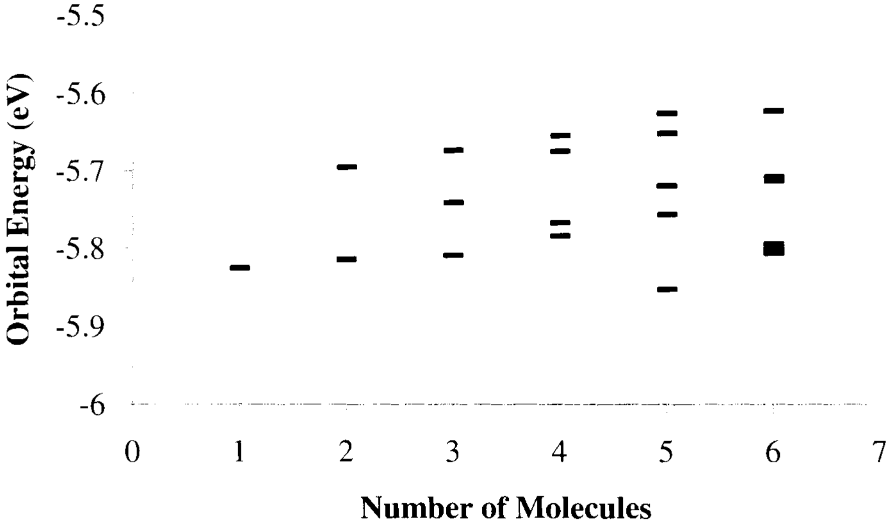

Figure 8.18 Evolution of n highest occupied Kohn-Sham molecular orbitals in $\mathbf{40}_n$.

8.4.4 Summary

This chapter provided three examples of materials that have properties which rely on the supramolecular structure. In the first example, moderate steric hindrance prevented the formation of a planar ribbon polymer of **41**. The $[Te\text{-}N]_2$ supramolecular synthon was, instead, distorted in two different patterns. Each pattern led to a different crystalline polymorph, the polymorphs were related by a thermochromic phase transition. Similarly, the loss of pyridine from the crystal of the solvate $\mathbf{41}_2\cdot Py_2$ resulted in a color change; this example does suggest the possibility of analytical applications.[299,300] In the second example, strategically placed substituents caused an acentric distortion to the supramolecular synthon which propagated throughout the lattice and, thereby, enabled second-order NLO properties in **50**, **84** and **86**. The third example constituted an encouraging step towards using the self-assembled ribbons to create electrical conductors.

These three examples illustrate the application of the $[Te\text{-}N]_2$ supramolecular synthon as a design element for the construction of large structures, and highlights the potential of SBIs in supramolecular chemistry.

9 Conclusions and Outlook

The results of the work described in this thesis constitute a significant step forward in the application of main-group SBIs in supramolecular chemistry. The viability of 1,2,5-telluradiazole heterocycles and their annulated derivatives as supramolecular building blocks was established by a combination of computational modeling (DFT and molecular mechanics), synthetic studies and structural studies. The supramolecular synthon formed by the self-association of these building blocks has ideal features for supramolecular chemistry: strength, directionality and reversibility.[214] The results of DFT calculations show that the strength and directionality of the $[Te-N]_2$ supramolecular synthon originate in complementary covalent and electrostatic interactions between the atoms. An additional contribution from dispersion cannot be evaluated with this DFT method, but it can only provide further stabilization. The Te-N SBI, which is a Lewis acid-base interaction, has an important donor-acceptor character which DFT calculations indicate can be further stabilized by incorporating electron-withdrawing substituents. The binding energies, that were calculated with DFT, for the $[Te-N]_2$ supramolecular synthon are comparable to those of some hydrogen bonds, thus it is expected that, in optimal conditions, supramolecular aggregates of 1,2,5-telluradiazoles would exist in the gas phase. While the photoelectron spectrum of benzo-2,1,3-telluradiazole was consistent with the electronic structure of individual molecules, ions that were detected with mass spectrometry are most likely Te-N SBI-assembled dimers. A general method for the synthesis of 1,2,5-telluradiazoles was developed. The reaction of 1,2-diamines with

$TeCl_4$, followed by addition of a base, allowed the efficient synthesis of a wide variety of derivatives. Structural studies of the products provided an understanding of how steric hindrance can be used to control the self-association and distortion of the $[Te\text{-}N]_2$ supramolecular synthon. This control strategy led to the design of materials that crystallize in noncentrosymmetric lattices as well as crystalline phases that are related by a thermochromic phase change. To facilitate the design of large structures, the main features of the DFT-calculated potential energy surface of the $[Te\text{-}N]_2$ supramolecular synthon were incorporated into the MMX force field. This method has been used to screen a variety of model compounds and it was determined that a number of these would be interesting to study experimentally because of their potential to form interesting supramolecular structures. Both the experimental optical absorption and the DFT calculations suggest that there is significant conjugation throughout the self-assembled telluradiazole ribbon polymers. This feature would be advantageous in conducting materials, provided that a conduction band could be created. To this effect, charge transfer salts were formed by crystallization with an electron acceptor and it was found that the ribbon polymer structure was maintained.

9.1 Significance and Impact

Over the course of these investigations, the nature of this project and the scope of the research have evolved. The topics that have been covered by these investigations necessarily had to be adapted to in response to developments from other research groups. On the other hand, the findings of this project have influenced the research that has been carried out elsewhere. The following is a brief overview of the themes of the publications by other authors that have cited the articles[148,203,214,257] which are the early outcome of this research.

There is a renewed interest in the supramolecular chemistry of main-group element SBIs. Recent theoretical studies have been concerned with SBIs centred on chalcogen atoms as well as other main-group elements.[10,11,19,149,301-309] Additionally, the bonding models that describe the nature of these interactions have been used to explain the bonding in related systems, for example the 1,2,5-chalcogenadiazolium cations[142,218] and the thienylene-2,5-disubstituted-phenylenes,[310] as well as to interpret trends observed in series of molecules that participate in chalcogen-centred SBIs. [10,149,301,305] The results of this work have also been used to examine the importance of both intramolecular and intermolecular chalcogen-centred SBIs as structure determining features in the solid-state structures of several compounds.[90,144,145,198,218,311-317] Furthermore, the emphasis on the structure directing roles of chalcogen-centred SBIs has motivated their use as design elements in the solid state.[198,218,310,313,316,318-321] The estimates of the binding energies in the $[Te\text{-}N]_2$ supramolecular synthon were used to aid in the understanding of the anomalous solution redox behaviour of the benzo-2,1,3-telluradiazolium[145] and benzo-1,2,3-thiatellurazolium[90] cations when compared with their lighter analogues.

9.2 Suggestions for Future Work

9.2.1 Identification of SBI Spectroscopic Signatures

It is conceivable that the supramolecular chemistry of SBIs will evolve to include systems that may not be amenable to characterization by single-crystal X-ray diffraction, such as folding polymers or the spirals modeled in Chapter 7. Moreover, systems of this type could display dynamic behaviour. In order to characterize such supramolecular assemblies, it would be indispensable to identify the spectroscopic signatures that accompany SBI formation. Several options could be considered for the 1,2,5-telluradiazoles. The ^{125}Te nucleus is NMR active (natural abundance = 6.99%, $I = ½$) and its chemical shift is sensitive to subtle changes in the environment of the atom (see Section 5.2.4). These measurements will, however, probably be complicated by factors such as solvation, the magnitude of the HOMO-LUMO gap, and the magnetic susceptibility of the samples. Another method that might be sensitive to the formation of SBIs would be vibrational spectroscopy. Strong SBIs involving Te might have vibrational modes that can be observed by low-energy Raman spectroscopy or far-IR spectroscopy. Preliminary experiments were conducted in these areas within this project, but there is the need for more detailed investigations before any conclusions can be drawn.

9.2.2 Design of New Supramolecular Synthons

The design of a supramolecular synthon requires the consideration of the geometrical features that would maximize the orbital interactions between the atoms involved in the SBIs. Consider, for example, the hypothetical heterocycle **88** which is designed to form a strong dimer as shown in Scheme 9.1. The resulting supramolecular synthon has been previously observed in sulfur compounds.[322] It is also possible that a helical polymer could be formed, similar to those observed in the crystal structures of 1,2-tellurazoles.[47,53]

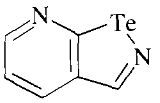

88

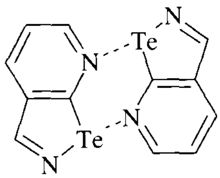

Scheme 9.1 Dimer of **88** constructed with $[Te\text{-}1\text{-}N]_2$.

One route to developing a more efficient tellurium-centred supramolecular synthon is to incorporate additional points of attachment. A supramolecular synthon with four points of attachment would have the same general motif as the solvated dimers of **46** or **41**: a central $[Te\text{-}N]_2$ synthon with two additional [Te N] supramolecular synthons. The geometry of the DMSO or pyridine fragments in these structures are, in principle, already optimal for SBI formation. Using the new molecular mechanics parameters for Te-N SBIs, an appropriate covalent linkage (curved line in Scheme 9.2) between one telluradiazole and one solvent molecule could be identified in order to create the new supramolecular synthon: $[Te\text{-}N\text{-}m\text{-}D]_2$. Two MMX minimized examples, based on $\mathbf{41}_2\cdot Py_2$, are shown in Figure 9.1 where the solvent molecule has been attached by either an acetylene or an imine bridge. A supramolecular synthon such as this will be, in principle, twice as strong as the $[Te\text{-}N]_2$ supramolecular synthon formed between unmodified 1,2,5-telluradiazoles. A supramolecular synthon of this strength would drive the equilibrium towards self-association and facilitate solution and gas-phase studies of self-associated systems. Beyond this, it would be instrumental in the design of supramolecular architectures that rely on the self-association of two subunits rather than the formation of a ribbon polymer. With systems such as **46** or **41**, additional small molecule adducts (e.g. with DMF, urea or thiourea) could be investigated for the purpose of identifying additional new building blocks that will form similar supramolecular synthons.

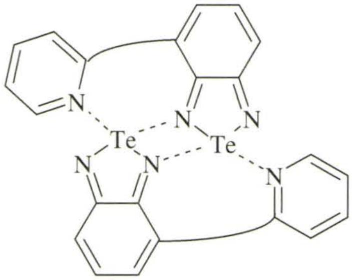

Scheme 9.2 Proposed benzo-2,1,3-telluradiazole with a bridged donor group.

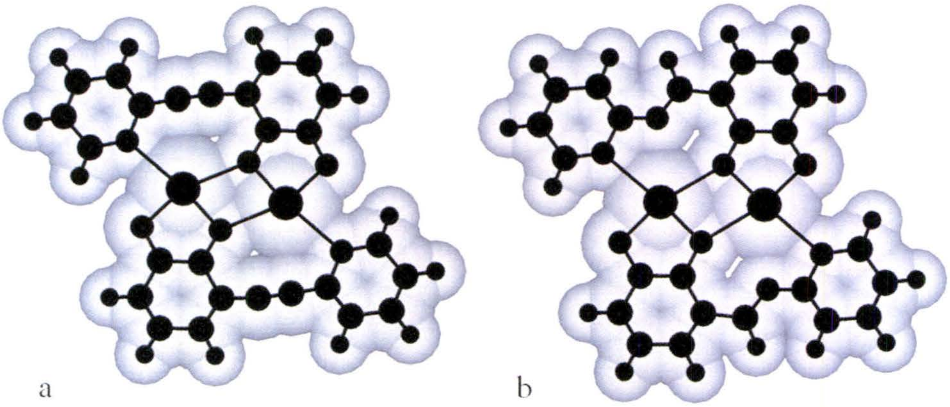

Figure 9.1 MMX minimized [Te-N-5-N]$_2$ supramolecular synthon with (a) an acetylene bridge or (b) an imine bridge.

9.2.3 Conducting Materials

The possibility of conductivity enabled by SBI formation was highlighted in the crystal structures of the **40**$_2$·**87** and **39**$_2$·**87**charge transfer salts. The properties of these materials have not been completely evaluated due to the limitations of the current method of crystal growth. The preparation of these salts with high purity reagents should be pursued in order to obtain samples suitable for conductivity and magnetic moment measurements.

After achieving a preliminary understanding of these systems, a perturbational approach could be used to improve the properties of the material. The conductivity in these systems probably depends on both the overlap in the supramolecular π-framework and the ease of creating charge carriers. 1,2,5-Telluradiazoles with more easily ionized π-frameworks could be obtained from diamines such as 1,2-diaminophenazine which should self-associate with little change to the supramolecular synthon.

In addition to having a filled band into which a hole may be introduced, the ribbon chain of benzo-2,1,3-telluradiazoles is expected, according to DFT calculations, to have a similar virtual band in the π-framework. It is conceivable that the addition of a charge carrier to this band may also result in a potentially conducting material. This concept has been explored by others with the K salts of [1,2,5]selenadiazolo[3,4-c][1,2,5]thiadiazole[323] and benzo-2,1,3-thiadiazole,[324] neither of which formed the $[E\text{-}N]_2$ directed ribbon polymer in the solid state. It is conceivable that the much stronger Te-N SBIs will persist in the solid state structures of the K salt of **40**.

The above modifications assume the conducting band would be formed along ribbon chain. In the case of **27**, the crystal structure contains a distorted ribbon polymer. In this case it is possible that a band would be formed by π-π overlap between the neighbouring phenanthrene rings. Here the $[Te\text{-}N]_2$ supramolecular synthon can be considered to act as a "molecular anvil" that puts pressure on the π-stacked aryl rings and thereby promotes the formation of a band along the periphery of the ribbon chain. Expanding on this idea, charge transfer salts of the spirals formed by **79** or **80** would be interesting because the movement of electrons could occur through the π-stack, along the ribbon, or both; it is worth noting that the internal column diameter in the spiral of **80** is wide enough to accommodate a whole molecule of TCNQ.

9.2.4 Analytical Applications

There are additional properties of the SBIs in these systems that could enable other functions. One example would be in the chemistry of anion receptors.[325-329] The crystal structure of **42** (Section 4.2.3) highlights the ability of these systems to strongly, yet reversibly, associate with anions. Association with an anion, however, will always be in competition with self-association in 1,2,5-telluradiazoles; this can be seen in the crystal structure of *N*-methyl benzo-2,1,3-telluradiazolium triflate. [145] The design of a system such as **89** or **90** removes this competition by removing one strongly Lewis acidic region that could cooperatively interact with the lone pair on the nitrogen atom.

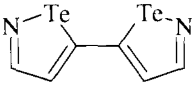

89

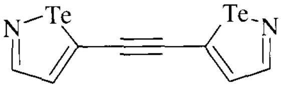

90

These two systems could be considered as prototypes of a catalyst that could promote S_N1 reactions that involve reagents with poor leaving groups such as Cl, or that involve the poorly stabilized carbocations formed at secondary or primary carbons. Supramolecular structure **91** highlights the four SBIs that can be formed which would compensate the energetic cost of carbocation formation. The activity of a catalyst such as this could be further enhanced by using the N-capping strategies discussed in Section 5.2.3 (**92**).

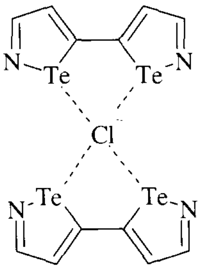

91

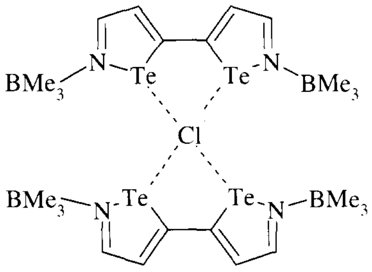

92

The arrangements shown for the supramolecules **91** and **92** are reminiscent of the bonding that is encountered in coordination compounds with multidentate ligands. This leads to idea of designing chelating ligands for monatomic anions (e.g. H^-, F^-, Cl^-, Br^-, I^-, O^{2-}, S^{2-}, Se^{2-}, N^{3-} or P^{3-}). The charge on the cations could be adjusted by using combinations of N-alkylation/arylation and N-borylation (e.g. **93** and **94**) to match the charge of the desired anion, and the bridge length can be adjusted in order to match the size of the anion.

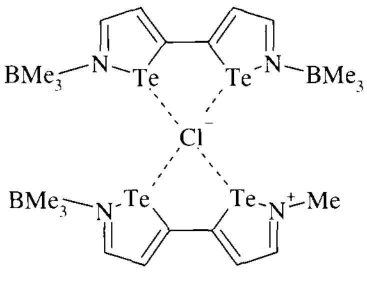

93

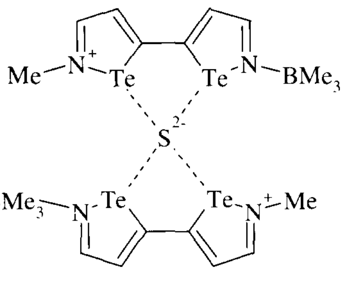

94

9.3 Concluding Remarks

In a recent publication dealing with tubular structures assembled using chalcogen-chalcogen interactions, Gleiter[23] posed the question (Is there) "*A world beyond hydrogen bonds?*" Considering the work described in this thesis, and published by others, the answer is: yes, but this new world requires extensive exploration since there remains much to learn about these interactions. Although the focus of this project has been on the fundamental research that is necessary to have an understanding of chalcogen-centred SBIs, the implications of these results could eventually lead to practical applications.

10 References

(1) Nic, M.; Jirat, J.; Kosata, B.; Jenkins, A. *IUPAC. Compendium of Chemical Terminology, 2nd ed. (the "Gold Book"). Compiled by A. D. McNaught and A.Wilkinson.* ; Blackwell Scientific Publications: Oxford, 1997; Vol. XML on-line corrected version: http://goldbook.iupac.org (accessed Oct 2009).

(2) *Nobel lectures: Physics. 1901-1921*; Elsevier Publishing Company: Amsterdam, 1967.

(3) Steed, J. W.; Atwood, J. L. *Supramolecular Chemistry*; Wiley: New York, 2000.

(4) Israelachvilli, J. N. In *Intermolecular and Surface Forces*; 2nd ed.; Academic: London, 1985, p 83.

(5) Bondi, A. *J. Phys. Chem.* **1964**, *68*, 441.

(6) Pyykko, P. *Chem. Rev.* **1997**, *97*, 597.

(7) Haiduc, I. In *Encyclopedia of Supramolecular Chemistry*; Steed, J., Atwood, J., Eds.; Marcel Dekker, Inc.: New York, 2004, p 1215.

(8) Alcock, N. W. *Adv. Inorg. Chem. Radiochem.* **1972**, *15*, 1.

(9) Mont, W.-W. d.; Salzen, A. M.-v.; Ruthe, F.; Seppälä, E.; Mugesh, G.; Devillanova, F. A.; Lippolis, V.; Kuhn, N. *J. Organomet. Chem.* **2001**, *623*, 14.

(10) Bleiholder, C.; Werz, D. B.; Koppel, H.; Gleiter, R. *J. Am. Chem. Soc.* **2006**, *128*, 2666.

(11) Mohajeri, A.; Pakiari, A. H.; Bagheri, N. *Chem. Phys. Lett.* **2009**, *467*, 393.

(12) Newton, M. G.; King, R. B.; Haiduc, I.; Silvestru, A. *Inorg. Chem.* **1993**, *32*, 3795.

(13) Clark, T.; Hennemann, M.; Murray, J.; Politzer, P. *J. Mol. Model.* **2007**, *13*, 291.

(14) Chen, J.-M.; Santra, B. K.; Liu, C. W. *Inorg. Chem. Commun.* **2004**, *7*, 1103.

(15) Vargas-Baca, I.; Chivers, T. *Phosphorus Sulfur Silicon Relat. El.* **2000**, *164*, 207.

(16) Chivers, T. *A Guide To Chalcogen-nitrogen Chemistry*; World Scientific Publishing: Hackensack, NJ, 2006.

(17) Svensson, P. H.; Kloo, L. *Chem. Rev.* **2003**, *103*, 1649.

(18) Metrangolo, P.; Neukirch, H.; Pilati, T.; Resnati, G. *Acc. Chem. Res.* **2005**, *38*, 386.

(19) Politzer, P.; Murray, J. S.; Lane, P. *Int. J. Quantum Chem.* **2007**, *107*, 3046.

(20) Starbuck, J.; Norman, N. C.; Orpen, A. G. *New J. Chem.* **1999**, *23*, 969.

(21) James, S. C.; Norman, N. C.; Orpen, A. G.; Starbuck, J. *CrystEngComm* **2000**, *2*, 67.

(22) Haiduc, I.; Zukerman-schpector, J. *Phosphorus, Sulfur Silicon Relat. Elem.* **2001**, *171*, 171.

(23) Gleiter, R.; Werz, D. B.; Rausch, B. J. *Chem. Eur. J.* **2003**, *9*, 2676.

(24) Werz, D. B.; Gleiter, R.; Rominger, F. *J. Am. Chem. Soc.* **2002**, *124*, 10638.

(25) Werz, D. B.; Staeb, T. H.; Benisch, C.; Rausch, B. J.; Rominger, F.; Gleiter, R. *Org. Lett.* **2002**, *4*, 339.

(26) Sarma, J. A. R. P.; Allen, F. H.; Hoy, V. J.; Howard, J. A. K.; Thaimattam, R.; Biradha, K.; Desiraju, G. R. *Chem. Commun.* **1997**, 101.

(27) Farina, A.; Stefano Valdo, M.; Maria Teresa, M.; Pierangelo, M.; Giuseppe, R.; Giuseppe, V. *Angew. Chem., Int. Ed.* **1999**, *38*, 2433.

(28) Metrangolo, P.; Carcenac, Y.; Lahtinen, M.; Pilati, T.; Rissanen, K.; Vij, A.; Resnati, G. *Science* **2009**, *323*, 1461.

(29) Desiraju, G. R. *Angew Chem Int Edit* **1995**, *34*, 2311.

(30) Aldaye, F. A.; Palmer, A. L.; Sleiman, H. F. *Science* **2008**, *321*, 1795.

(31) Sijbesma, R. P.; Beijer, F. H.; Brunsveld, L.; Folmer, B. J. B.; Hirschberg, J. H. K. K.; Lange, R. F. M.; Lowe, J. K. L.; Meijer, E. W. *Science* **1997**, *278*, 1601.

(32) Allen, F. H. *Acta. Cryst.* **2002**, *B58*, 380.

(33) Greenwood, N. N.; Earnshaw, A. *Chemistry of the elements*; 2nd ed.; Butterworth-Heinemann: Oxford ; Boston, 1998.

(34) Zukerman-Schpector, J.; Haiduc, I. *CrystEngComm* **2002**, *4*, 178.

(35) Rowland, R. S.; Taylor, R. *J. Phys. Chem.* **1996**, *100*, 7384.

(36) Dance, I. *New J. Chem.* **2003**, *27*, 22.

(37) The structures containing metals and interactions between oppositely charged molecules were discarded.

(38) These SBIs are important structure determining features, but will not be discussed further in this study because they generally occur at much longer relative distances than Te-D interactions where D has a lone pair.

(39) Sweigers, G. F. In *Encyclopedia of Supramolecular Chemistry*; Atwood, J. L., Steed, J. W., Eds.; CRC Press, Taylor & Francis Group: Boca Raton, 2004; Vol. 2, p 1263.

(40) Müller, A.; Reuter, H.; Dillinger, S. *Angew. Chem., Int. Ed. Engl.* **1995**, *34*, 2328.

(41) Simard, M.; Su, D.; Wuest, J. D. *J. Am. Chem. Soc.* **1991**, *113*, 4696.

(42) Sudha, N.; Singh, H. B. *Coord. Chem. Rev.* **1994**, 469.

(43) Munzenberg, J.; Roesky, H. W.; Noltemeyer, M.; Besser, S.; Herbst-Irmer, R. *Z. Naturforsch., B: Chem. Sci.* **1993**, *48*, 199.

(44) Lentz, D.; Szwak, M. *Angew. Chem., Int. Ed.* **2005**, *44*, 5079.

(45) Maartmann-Moe, K.; Songstad, J. *Acta Chem. Scand. A* **1982**, *36*, 829.

(46) Rainville, D.; Clingaro, R. A.; Meyers, E. A. *Cryst. Struct. Commun.* **1980**, *9*, 77.

(47) Munno, G. D.; Lucchesini, F. *Acta Cryst.* **1992**, *C48*, 1437.

(48) Pietikainen, J.; Laitinen, R. S.; Konu, J.; Valkonen, J. *Z. Naturforsch., B: Chem. Sci.* **2001**, *56*, 1369.

(49) Haas, A.; Kasprowski, J.; Pryka, M. *Chem. Ber.* **1992**, *125*, 789.

(50) Klapotke, T. M.; Krumm, B.; Ruiz, J. C. G.; Noth, H.; Schwab, I. *Eur. J. Inorg. Chem.* **2004**, 4764.

(51) Kobayashi, K.; Izawa, H.; Yamaguchi, K.; Horn, E.; Furukawa, N. *Chem. Commun.* **2001**, 1428.

(52) Hinrichs, W.; Mandak, D.; Klar, G. *Cryst. Struct. Commun.* **1982**, *11*, 1781.

(53) Campsteyn, H.; Dupont, L.; Lamotte-Brasseur, J.; Vermeire, M. *J. Heterocycl. Chem.* **1979**, *15*, 745.

(54) Collins, M. J.; Ripmeester, J. A.; Sawyer, J. F. *J. Am. Chem. Soc.* **1988**, *110*, 8583.

(55) Sundberg, M. R.; Uggla, R.; Laitalainen, T.; Bergman, J. *J. Chem. Soc., Dalton Trans.* **1994**, 3279.

(56) Fleischer, H.; Mathiasch, B.; Schollmeyer, D. *Organometallics* **2002**, *21*, 526.

(57) Munzenberg, J.; Roesky, H. W.; Besser, S.; Herbst-Irmer, R.; Sheldrick, G. M. *Inorg. Chem.* **1992**, *31*, 2986.

(58) Fleischer, H.; Schollmeyer, D. *Angew. Chem., Int. Ed.* **2000**, *39*, 3705.

(59) Boese, R.; Dworak, J.; Haas, A.; Pryka, M. *Chem.Ber.* **1995**, *128*, 477.

(60) Subrahmanyan, I.; Aravamudan, G.; Rout, G. C.; Seshasayee, M. *J. Crystallogr. Spectrosc. Res.* **1984**, *14*, 239.

(61) Marsh, R. E. *Acta Crystallogr.* **2005**, *B61*, 359.

(62) Klapotke, T. M.; Krumm, B.; Mayer, P.; Scherr, M. *Z. Naturforsch., B: Chem. Sci.* **2006**, *61*, 528.

(63) Bertini, V.; Dapporto, P.; Lucchesini, F.; Sega, A.; Munno, A. D. *Acta Cryst. C* **1984**, *40*, 653.

(64) Neidlein, R.; Knecht, D.; Gieren, A.; Ruiz-Perez, C. *Z. Naturforsch. B.* **1987**, *42*, 84.

(65) Chivers, T.; Gao, X.; Parvez, M. *Inorg.Chem.* **1996**, *35*, 9.

(66) Klapotke, T. M.; Krumm, B.; Mayer, P.; Piotrowski, H.; Ruscitti, O. P.; Schiller, A. *Inorg. Chem.* **2002**, *41*, 1184.

(67) Fleischer, H.; Schollmeyer, D. *Inorg. Chem.* **2001**, *40*, 324.

(68) Lindqvist, O. *Acta Chem. Scand.* **1967**, *21*, 1473.

(69) Bent, H. A. *Chem. Rev.* **1961**, *61*, 275.

(70) Klapotke, T. M.; Krumm, B.; Mayer, P.; Polborn, K.; Ruscitti, O. P. *J. Fluorine Chem.* **2001**, *112*, 207.

(71) Roesky, H. W.; Butcher, R. J.; Bajpai, S.; Srivastava, P. C. *Phosphorus, Sulfur Silicon Relat. Elem.* **2000**, *161*, 135.

(72) Tian, Z.; Tuck, D. G. *J. Organomet. Chem.* **1993**, *462*, 125.

(73) Yoshida, Y.; Matsuda, K.; Sasaki, H.; Matsumoto, Y.; Matsumoto, S.; Tawara, S.; Takasugi, H. *Bioorg. Med. Chem.* **2000**, *8*, 2317.

(74) Belen'kaya, I. A.; Prokhorchuk, E. A.; Uskova, L. A.; Shulla, T. A.; Sirik, S. A.; Goritskaya, E. F.; Grib, O. K. *Fiz. Akt. Vesh.* **1989**, *21*, 52.

(75) Belen'kaya, I. A.; Umarov, A. A.; Khamidov, M. K.; Kozyr, I. M.; Berezovskaya, E. A.; Shulla, T. A.; Sirik, S. A. *Fiz. Akt. Vesh.* **1990**, *22*, 47.

(76) Wang, G.; Phan, L. T.; Or, Y. S.; Qiu, Y.-L.; Niu, D.; Peng, Y.; Busuyek, M.; Wang, Y.; Nakajima, S.; (Enanta Pharmaceuticals, Inc., USA). Application: WO, 2006, p 67.

(77) Belen'kaya, I. A.; Sirik, S. A.; Yasinskaya, O. G.; Ivanova, V. V.; Krokhina, G. P.; Shashenkova, D. K.; Prokhorchuk, E. A.; Uskova, L. A.; Grib, O. K. *Fiz. Akt. Vesh.* **1992**, *24*, 39.

(78) Kochansky, J. P.; Cohen, C. F.; Lusby, W. R.; Svoboda, J. A.; Feldmesser, J.; Wright, F. C. *J. Agric. Entomol.* **1988**, *5*, 131.

(79) Bazan, G. C.; Liu, B.; (The Regents of the University, USA). Application: WO, 2006, p 64.

(80) Pasquier, C.; Charriere, V.; Braun, H.-J.; (Wella Aktiengesellschaft, Germany). Application: WO, 2002, p 44.

(81) Umbricht, G.; Braun, H.-J.; Oberson, S.; Mueller, C.; (Wella AG, Germany). Application: DE, 2002, p 12.

(82) Ammann, C.; Meier, P.; Merbach, A. E. *J. Magn. Reson.* **1982**, *46*, 319.

(83) Bain, A. D. *Prog. Nucl. Magn. Reson. Spectrosc.* **2003**, *43*, 63.

(84) Lichtenberger, D. L.; Copenhaver, A. S. *J. Electron Spectrosc. Relat. Phenom.* **1990**, *50*, 335.

(85) Håkansson, M. *Inorg. Synth.* **1998**, *32*, 222.

(86) *RLATT*, 1998; Bruker-AXS, Inc., Madison, WI

(87) Bruker 2006; APEX2. Bruker AXS Inc., Madison, WI, USA,

(88) Sparks, R. A. *Gemini*, 1999; Bruker-ACS, Inc., Madison, WI

(89) Sheldrick, G. M. *CELL_NOW*, University of Göttingen

(90) Risto, M.; Assoud, A.; Winter, S. M.; Oilunkaniemi, R.; Laitinen, R. S.; Oakley, R. T. *Inorg. Chem.* **2008**, *47*, 10100.

(91) Sheldrick, G. M. *TWINABS*, 2002; University of Goettingen: Germany

(92) Sheldrick, G. M. *SADABS*, 1996; University of Goettingen: Germany

(93) *X-AREA and X-RED32*, Stoe & Cie GmbH

(94) Sheldrick, G. M. *SHELX97 [Includes SHELXS97, SHELXL97, CIFTAB] - Programs for Crystal Structure Analysis (Release 97-2)*,

(95) Farrugia, L. *J. Appl. Crystallogr.* **1999**, *32*, 837.

(96) Farrugia, L. J. *J. J. Appl. Crystallogr.* **1997**, *30*, 565.

(97) Bruno, I. J.; Cole, J. C.; Edgington, P. R.; Kessler, M. K.; Macrae, C. F.; McCabe, P.; Pearson, J.; Taylor, R. *Acta Crystallogr.* **2002**, *B58*, 389.

(98) Taylor, R.; Macrae, C. F. *Acta Crystallogr.* **2001**, *B57*, 815.

(99) Macrae, C. F.; Edgington, P. R.; McCabe, P.; Pidcock, E.; Shields, G. P.; Taylor, R.; Towler, M.; van de Streek, J. *J. Appl. Crystallogr.* **2006**, *39*, 453.

(100) Zhang, W.; Cozzolino, A. F.; Mahmoudkhani, A. H.; Tulumello, M.; Mansour, S.; Vargas-Baca, I. *J. Phys. Chem. B* **2005**, *109*, 18378.

(101) Armarego, W. L. F.; Chai, C. L. L. *Purification of laboratory chemicals*; Butterworth-Heinemann, 2003.

(102) Dodd, R. E.; Robinson, P. L. *Experimental Inorganic Chemistry*; 2nd ed.; Elsevier Publishing Company: New York, 1957.

(103) Harvey, I. W.; Mcfarlane, M. D.; Moody, D. J.; Smith, D. M. *J Chem Soc Perk T 1* **1988**, 1939.

(104) Pilgram, K.; Zupan, M.; Skiles, R. *J. Heterocycl. Chem.* **1970**, *7*, 629.

(105) Tsubata, Y.; Suzuki, T.; Miyashi, T.; Yamashita, Y. *J.Org.Chem.* **1992**, *57*, 6749.

(106) Bublitz, D. E. *J. Heterocycl. Chem.* **1972**, *9*, 539.

(107) Brown, H. C.; Racherla, U. S. *J. Org. Chem.* **1986**, *51*, 427.

(108) Kiviniemi, S.; Nissinen, M.; Alaviuhkola, T.; Rissanen, K.; Pursiainen, J. *J. Chem. Soc., Perkin Trans. 2* **2001**, 2364.

(109) Kovtonyuk, V. N.; Makarov, A. Y.; Shakirov, M. M.; Zibarev, A. V. *Chem. Commun.* **1996**, 1991.

(110) Bahnasawy, A. A. E.; Ahwany, M. F. E. *Phosphorus, Sulfur Silicon Relat. Elem.* **2007**, *182*, 1937.

(111) Te Velde, G.; Bickelhaupt, F. M.; Baerends, E. J.; Fonseca Guerra, C.; Van Gisbergen, S. J. A.; Snijders, J. G.; Ziegler, T. *J. Comp. Chem.* **2001**, *22*, 931.

(112) Guerra, C. F.; Snijders, J. G.; Velde, G. t.; E J Baerends *Theor. Chem. Acc.* **1998**, *99*, 391.

(113) Baerends, E. J.; Autschbach, J.; Bérces, A.; Bickelhaupt, F. M.; Bo, C.; Boerrigter, P. M.; Cavallo, L.; Chong, D. P.; Deng, L.; Dickson, R. M.; Ellis, D.

E.; Faassen, M. v.; Fan, L.; Fischer, T. H.; Guerra, C. F.; Gisbergen, S. J. A. v.; Götz, A. W.; Groeneveld, J. A.; Gritsenko, O. V.; Grüning, M.; Harris, F. E.; Hoek, P. v. d.; Jacob, C. R.; Jacobsen, H.; Jensen, L.; Kessel, G. v.; Kootstra, F.; Krykunov, M. V.; Lenthe, E. v.; McCormack, D. A.; Michalak, A.; Neugebauer, J.; Nicu, V. P.; Osinga, V. P.; Patchkovskii, S.; Philipsen, P. H. T.; Post, D.; Pye, C. C.; Ravenek, W.; Rodríguez, J. I.; Ros, P.; Schipper, P. R. T.; Schreckenbach, G.; Snijders, J. G.; Solà, M.; Swart, M.; Swerhone, D.; Velde, G. t.; Vernooijs, P.; Versluis, L.; Visscher, L.; Visser, O.; Wang, F.; Wesolowski, T. A.; Wezenbeek, E. M. v.; Wiesenekker, G.; Wolff, S. K.; Woo, T. K.; Yakovlev, A. L.; Ziegler, T. *ADF*, 2008.01; SCM, Theoretical Chemistry, Vrije Universiteit http://www.scm.com

(114) van Gisbergen, S. J. A.; Snijders, J. G.; Baerends, E. J. *Phys. Rev. Lett.* **1997**, *78*, 3097.

(115) van Gisbergen, S. J. A.; Snijders, J. G.; Baerends, E. J. *J. Chem. Phys.* **1998**, *109*, 10644.

(116) Vosko, S. H.; Wilk, L.; Nusair, M. *Can. J. Phys.* **1980**, *58*, 1200.

(117) Becke, A. D. *Phys. Rev. A.* **1988**, *38*, 3098.

(118) Perdew, J. P. *Phys. Rev. B.* **1986**, *33*, 8822.

(119) Perdew, J. P.; Wang, Y. *Phys. Rev. B.* **1992**, *45*, 13244.

(120) van Lenthe, E.; Ehlers, A.; Baerends, E.-J. *J. Chem. Phys.* **1999**, *110*, 8943.

(121) van Lenthe, E.; Baerends, E. J.; Snijders, J. G. *J. Chem. Phys.* **1993**, *99*, 4597.

(122) van Lenthe, E.; Baerends, E. J.; Snijders, J. G. *J. Chem. Phys.* **1994**, *101*, 9783.

(123) van Lenthe, E.; van Leeuwen, R.; Baerends, E. J.; Snijders, J. G. *Int. J. Quant. Chem.* **1996**, *57*, 281.

(124) van Lenthe, E.; Snijders, J. G.; Baerends, E. J. *J. Chem. Phys.* **1996**, *105*, 6505.

(125) Fan, L. Y.; Ziegler, T. *J. Chem. Phys.* **1992**, *96*, 9005.

(126) Fan, L. Y.; Ziegler, T. *J. Phys. Chem.* **1992**, *96*, 6937.

(127) van Gisbergen, S. J. A.; Snijders, J. G.; Baerends, E. J. *Comput. Phys. Commun.* **1999**, *118*, 119.

(128) Rosa, A.; Baerends, E. J.; van Gisbergen, S. J. A.; van Lenthe, E.; Groeneveld, J. A.; Snijders, J. G. *J. Am. Chem. Soc.* **1999**, *121*, 10356.

(129) Gritsenko, O. V.; Schipper, P. R. T.; Baerends, E. J. *Chem Phys Lett* **1999**, *302*, 199.

(130) Gritsenko, O. V.; Schipper, P. R. T.; Baerends, E. J. *Int J Quantum Chem* **2000**, *76*, 407.

(131) Schipper, P. R. T.; Gritsenko, O. V.; van Gisbergen, S. J. A.; Baerends, E. J. *J. Chem. Phys.* **2000**, *112*, 1344.

(132) Lee, C. T.; Yang, W. T.; Parr, R. G. *Phys Rev B* **1988**, *37*, 785.

(133) Stephens, P. J.; Devlin, F. J.; Chabalowski, C. F.; Frisch, M. J. *J Phys Chem-Us* **1994**, *98*, 11623.

(134) Becke, A. D. *J. Chem. Phys.* **1993**, *98*, 5648.

(135) Glendening, E. D.; J, K. B.; Reed, A. E.; Carpenter, J. E.; Bohmann, J. A.; Morales, C. M.; Weinhold, F. *NBO 5.0*, Theoretical Chemistry Institute, University of Wisconsin, Madison http://www.chem.wisc.edu/~nbo5/

(136) Ortiz, J. C.; Bo, C. *Xaim*, Universitat Rovira i Virgili. Tarragona. Spain http://www.quimica.urv.es/XAIM/

(137) Visser, O.; Leyronnas, P.; Zeist, W.-J. v.; Luppi, M. *ADF-GUI*, 2008.01; SCM, Amsterdam, The Netherlands http://www.scm.com

(138) Flükiger, P.; Lüthi, H. P.; Portmann, S.; Weber, J. *MOLEKEL 4.0*,

(139) Gajewski, J. J.; Gilbert, K. E.; McKelvey, J. *Advances in Molecular Modeling*; JAI Press: New York, 1990; Vol. 2.

(140) Gilbert, K. E. *PCModel*, Serena Software; Bloomington, NJ http://www.serenasoft.com/

(141) Reproduced in part with permission from Cozzolino, A. F., Vargas-Baca, I., Mansour, S., Mahmoudkhani, A. H., J. Am. Chem. Soc. 2005, 127, 3184-3190. Copyright 2005 American Chemical Society.

(142) Dutton, J. L.; Ragogna, P. J. *Inorg. Chem.* **2009**, *48*, 1722.

(143) Dutton, J. L.; Sutrisno, A.; Schurko, R. W.; Ragogna, P. J. *Dalton Trans.* **2008**, 3470.

(144) Dutton, J. L.; Tindale, J. J.; Jennings, M. C.; Ragogna, P. J. *Chem. Commun.* **2006**, 2474.

(145) Risto, M.; Reed, R. W.; Robertson, C. M.; Oilunkaniemi, R.; Laitinen, R. S.; Oakley, R. T. *Chem. Commun.* **2008**, 3278

(146) Parr, R. G.; Yang, W. *J. Am. Chem. Soc.* **1984**, *106*, 4049.

(147) Yang, W.; Parr, R. G.; Pucci, R. *J. Chem. Phys.* **1984**, *81*, 2862.

(148) Cozzolino, A. F.; Bain, A. D.; Hanhan, S.; Vargas-Baca, I. *Chem. Commun.* **2009**, 4043.

(149) Murray, J.; Lane, P.; Clark, T.; Politzer, P. *J. Mol. Model.* **2007**, *13*, 1033.

(150) Allen, F. H.; Kennard, O. *Chem. Des. Automat. News* **1993**, *8*, 31.

(151) Allen, F. H.; Davies, J. E.; Galloy, J. J.; Johnson , O.; Kennard, O.; Macrae, C. F.; Mitchell, E. M.; Mitchell, G. F.; Smith, J. M.; Watson, J. *J. Chem. Inf. Comput. Sci.* **1987**, *31*, 187.

(152) Esteban-Calderon, C.; Martinez-Ripoll, M.; Garcia-Blanco, S. *Acta Cryst. C* **1984**, *40*, 80.

(153) Barclay, T. M.; Cordes, A. W.; George, N. A.; Haddon, R. C.; Itkis, M. E.; Mashuta, M. S.; Oakley, R. T.; Patenaude, G. W.; Reed, R. W.; Richardson, J. F.; Zhang, H. *J. Am. Chem. Soc.* **1998**, *120*, 352.

(154) Yamashita, Y.; Eguchi, J.; Suzuki, T.; Kabuto, C.; Miyashi, T.; Tanaka, S. *Angew. Chem. Int. Ed.* **1990**, *29*, 643.

(155) Bagryanskaya, I. Y.; Gatilov, Y. V.; Miller, A. O.; Shakirov, M. M.; Zibarev, A. V. *Heteroat. Chem.* **1994**, *5*, 561.

(156) Klimasenko, N. L.; Chetkina, L. A.; Ginzburg, S. L.; Neigauz, M. G.; Smelyanskaya, E. M. *Zh. Strukt. Khim.* **1973**, *14*, 108.

(157) Kane, J.; Schaeffer, R. *Cryst. Struct. Commun.* **1981**, *10*, 1403.

(158) Gieren, A.; Betz, H.; Hubner, T.; Lamm, V.; Neidlein, R.; Droste, D. *Z. Naturforsch. B.* **1984**, *39*, 485.

(159) Yamashita, Y.; Saito, K.; Suzuki, T.; Kabuto, C.; Mukai, T.; Miyashi, T. *Angew. Chem. Int. Ed.* **1988**, *27*, 434.

(160) Yamashita, Y.; Ono, K.; Tanaka, S.; Imaeda, K.; Inokuchi, H.; Sano, M. *Chem. Commun.* **1993**, 1803.

(161) Yamashita, Y.; Ono, K.; Tomura, M.; Tanaka, S. *Tetrahedron* **1997**, *53*, 10169.

(162) Ono, K.; Tanaka, S.; Yamashita, Y. *Angew. Chem. Int. Ed.* **1994**, *33*, 1977.

(163) Hatta, T.; Kawano, M.; Imaizumi, Y.; Tsuge, A.; Moriguchi, T.; Maeda, H.; Tsuge, O. *Heterocycles* **1997**, *46*, 651.

(164) Fukushima, T.; Okazeri, N.; Miyashi, T.; Suzuki, K.; Yamashita, Y.; Suzuki, T. *Tetrahedron Lett.* **1999**, *40*, 1175.

(165) Richardson, C.; Steel, P. J. *Acta Cryst. C* **2001**, *57*, 197.

(166) Suzuki, T.; Fukushima, T.; Miyashi, T.; Tsuji, T. *Angew. Chem. Int. Ed.* **1997**, *36*, 2495.

(167) Suzuki, T.; Fujii, H.; Yamashita, Y.; Kabuto, C.; Tanaka, S.; Harasawa, M.; Mukai, T.; Miyashi, T. *J. Am. Chem. Soc.* **1992**, *114*, 3034.

(168) Mellini, M.; Merlino, S. *Acta Cryst. B* **1976**, *32*, 1074.

(169) Tian, W.; S.Grivas; K.Olsson *J. Chem. Soc. Perkin Trans. 1* **1993**, 257.

(170) Klimasenko, N. L.; Chetkina, L. A.; Gol'der, G. A. *Zh. Strukt. Khim.* **1973**, *14*, 515.

(171) Hanasaki, Y.; Watanabe, H.; Katsuura, K.; Takayama, H.; Shirakawa, S.; Yamaguchi, K.; Sakai, S.; Ijichi, K.; Fujiwara, M.; Konno, K.; Yokota, T.; Shigeta, S.; Baba, M. *J. Med. Chem.* **1995**, *38*, 2038.

(172) Mikhno, O. A.; Ezhkova, Z. I.; Zhdanov, G. S. *Kristallogr.* **1973**, *18*, 99.

(173) Iwaoka, M.; Tomoda, S. *J. Am. Chem. Soc.* **1996**, *118*, 8077.

(174) Ziegler, T.; Rauk, A. *Inorg. Chem.* **1979**, *18*, 1755.

(175) Ziegler, T.; Rauk, A. *Inorg. Chem.* **1979**, *18*, 1558.

(176) Landrum, G. A.; Hoffmann, R. *Angew. Chem. Int. Ed.* **1998**, *37*, 1887.

(177) Tani, K.; Kato, S.; Kanda, T.; Inagaki, S. *Org. Lett.* **2001**, *3*, 655.

(178) Iwaoka, M.; Komatsu, H.; Katsuda, T.; Tomoda, S. *J. Am. Chem. Soc.* **2004**, *126*, 5309.

(179) Bagus, P. S.; Illas, F. *Phys. Rev. B.* **1990**, *42*, 10852.

(180) Hermann, K.; Bagus, P. S. *Appl. Phys. A* **1987**, *A44*, 63.

(181) Bagus, P. S.; Hermann, K.; Bauschlicher, C. W., Jr. *Ber. Bun.-Ges.* **1984**, *88*, 302.

(182) Bagus, P. S.; Nelin, C. J.; Bauschlicher, C. W., Jr. *J. Vac. Sci. Tech. A* **1984**, *2*, 905.

(183) Hermann, K.; Hass, H. J.; Bagus, P. S. *Z. Phys. D.* **1986**, *3*, 159.

(184) Bauschlicher, C. W., Jr.; Bagus, P. S.; Roos, B. O. *J. Chem. Phys.* **1986**, *85*, 354.

(185) Chivers, T.; Krouse, I.; Parvez, M.; Vargas-Baca, I.; Ziegler, T.; Zoricak, P. *Inorg. Chem.* **1996**, *35*, 5836.

(186) Reed, A. E.; Curtiss, L. A.; Weinhold, F. *Chem. Rev.* **1988**, *88*, 899.

(187) Lu, Y.-X.; Zou, J.-W.; Wang, Y.-H.; Jiang, Y.-J.; Yu, Q.-S. *J. Phys. Chem. A* **2007**, *111*, 10781.

(188) Jonas, V.; Frenking, G.; Reetz, M. T. *J. Am. Chem. Soc.* **1994**, *116*, 8741.

(189) Skancke, A.; Skancke, P. N. *J. Phys. Chem.* **1996**, *100*, 15079.

(190) Popelier, P.; Prentice Hall: Essex, England, 2000, p 144.

(191) Koch, U.; Popelier, P. L. A. *J. Phys. Chem.* **1995**, *99*, 9747.

(192) Suzuki, T.; Tsuji, T.; Okubo, T.; Okada, A.; Obana, Y.; Fukushima, T.; Miyashi, T.; Yamashita, Y. *J. Org. Chem.* **2001**, *66*, 8954.

(193) Luzzati, V. *Acta Cryst.* **1951**, *4*, 193.

(194) Gomes, A. C.; Biswas, G.; Banerjee, A.; Duax, W. L. *Acta Crystallogr., Sect. C: Cryst. Struct. Commun.* **1989**, *45*, 73.

(195) Gieren, A.; Hübner, T.; Lamm, V.; Neidlein, R.; Droste, D. *Z. Anorg. Allg. Chem.* **1985**, *523*, 33.

(196) Neve, J.; Hanocq, M.; Molle, L. *Talanta* **1979**, *26*, 15.

(197) Apblett, A.; Chivers, T.; Richardson, J. F. *Can. J. Chem.* **1986**, *64*, 849.

(198) Zhou, A. J.; Zheng, S. L.; Fang, Y.; Tong, M. L. *Inorg. Chem.* **2005**, *44*, 4457.

(199) Lee, L. M.; Elder, P. J. W.; Cozzolino, A. F.; Yang, Q.; Vargas-Baca, I. *Main Group Chem.*, in press.

(200) Bel'skii, V. K.; Éllert, O. G.; Seifilina, Z. M.; Novotortsev, V. M.; Tsveniashvili, V. S.; Garnovskii, A. D. *Russ. Chem. Bull.* **1984**, *33*, 1748.

(201) Hunter, E. P. L.; Lias, S. G. *J. Phys. Chem. Ref. Data* **1998**, *27*, 413.

(202) Erhardt, S.; Frenking, G. *Chem.--Eur. J.* **2006**, *12*, 4620.

(203) Cozzolino, A. F.; Britten, J. F.; Vargas-Baca, I. *Cryst. Growth Des.* **2006**, *6*, 181.

(204) DFT fluoride affinities where benchmarked against selected fluoride affinities calculated by Christie and Dixon. The unknown 1,2,5-chalcogenadiazole fluoride affinites were obtained by linear interpolation or extrapolation, see supplementary information for further details.

(205) Christe, K. O.; Dixon, D. A.; McLemore, D.; Wilson, W. W.; Sheehy, J. A.; Boatz, J. A. *J. Fluorine Chem.* **2000**, *101*, 151.

(206) Reproduced in part with permission from Cozzolino, A. F.; Britten, J. F.; Vargas-Baca, I. Cryst. Growth Des. 2006, 6, 181-186. Copyright 2006 American Chemical Society.

(207) Reproduced in part with permission from Lee, L. M.; Elder, P. J. W.; Cozzolino, A. F.; Yang, Q.; Vargas-Baca, I. Main Group Chem., in press.

(208) Bertini, V.; Dapporto, P.; De Munno, A. *Synthesis* **1982**, 681.

(209) Badyal, J.; Herr, M.; McWhinnie, W. R.; Hamor, T. A.; Paxton, K. *Phosphorus, Sulfur Silicon Relat. Elem.* **1998**, *141*, 221.

(210) Brownstein, S. K.; Enright, G. D. *Acta Cryst.* **1995**, *C51*, 1579.

(211) Reeske, G.; Cowley, A. H. *Chem. Commun.* **2006**, 4856.

(212) Buss, B.; Krebs, B. *Inorg. Chem.* **1971**, *10*, 2795.

(213) Clark, P. A.; Gleiter, R.; Heilbronner, E. *Tetrahedron* **1973**, *29*, 3085.

(214) Cozzolino, A. F.; Vargas-Baca, I.; Mansour, S.; Mahmoudkhani, A. H. *J. Am. Chem. Soc.* **2005**, *127*, 3184.

(215) Chivers, T.; Schatte, G. *Inorg. Chem.* **2002**, *41*, 1002.

(216) Reproduced in part with permission from Cozzolino, A. F.; Britten, J. F.; Vargas-Baca, I. Cryst. Growth Des.. 2006, 6, 181-186. Copyright 2006 American Chemical Society.

(217) Dutton, J. L.; Tuononen, H. M.; Jennings, M. C.; Ragogna, P. J. *J. Am. Chem. Soc.* **2006**, *128*, 12624.

(218) Berionni, G.; Pegot, B.; Marrot, J.; Goumont, R. *CrystEngComm* **2009**, *11*, 986.

(219) Bondi, A. *J. Phys. Chem.* **1964**, *68*, 441.

(220) Morkved, E. H.; Faccin, G.; Manfrotto, D.; Kjosen, H.; Becker, J. Y.; Shapiro, L.; Ellern, A.; Bernstein, J.; Khodorkovsky, V. *J. Mat. Chem.* **1997**, *7*, 1697.

(221) Lang, E. S.; Strähle, U. A. J. *Z. Anorg. Allg. Chem.* **1997**, *623*, 1968.

(222) Leroy, G.; Sana, M.; Wilante, C. *Theor. Chim. Acta* **1993**, *85*, 155.

(223) Bacon, C. E.; Eisler, D. J.; Melen, R. L.; Rawson, J. M. *Chem. Commun.* **2008**, 4924.

(224) Guerra, C. F.; Handgraaf, J.-W.; Baerends Evert, J.; Bickelhaupt, F. M. *J. Comp. Chem.* **2004**, *25*, 189.

(225) Vargas-Baca, I.; Findlater, M.; Powell, A.; Vasudevan, K. V.; Cowley, A. H. *Dalton Trans.* **2008**, 6421.

(226) Reproduced in part with permission from Cozzolino, A. F.; Gruhn, N. E.; Lichtenberger, D. L.; Vargas-Baca, I. Inorg. Chem. 2008, 47, 6220-6226. Copyright 2008 American Chemical Society.

(227) Hohenberg, P.; Kohn, W. *Phys. Rev.* **1964**, *136*, B864.

(228) Kohn, W.; Sham, L. J. *Phys. Rev.* **1965**, *140*, A1133.

(229) Zhang, G.; Musgrave, C. B. *J. Phys. Chem. A* **2007**, *111*, 1554.

(230) Chong, D. P.; Gritsenko, O. V.; Baerends, E. J. *J. Chem. Phys.* **2002**, *116*, 1760.

(231) Johnstone, R. A. W.; Mellon, F. A. *Journal of the Chemical Society, Faraday Transactions 2* **1973**, *69*, 1155.

(232) Petrachenko, N. E.; Vovna, V. I.; Zibarev, A. V.; Furin, G. G. *Khim. Geterotsikl. Soedin.* **1991**, 563.

(233) Hitchcock, A. P.; Dewitte, R. S.; Vanesbroeck, J. M.; Aebi, P.; French, C. L.; Oakley, R. T.; Westwood, N. P. C. *J. Electron Spectrosc. Relat. Phenom.* **1991**, *57*, 165.

(234) Palmer, M. H.; Kennedy, S. M. F. *Journal of Molecular Structure* **1978**, *43*, 33.

(235) Schubert, U. S.; Eschbaumer, C. *J. Inclusion Phenom. Macrocyclic Chem.* **1999**, *35*, 101.

(236) Schalley, C. A. *Mass Spectrom. Rev.* **2001**, *20*, 253.

(237) Pramanik, B. N.; Bartner, P. L.; Mirza, U. A.; Liu, Y.-H.; Ganguly, A. K. *J. Mass Spectrom.* **1998**, *33*, 911.

(238) Smith, R. D.; Light-Wahl, K. J. *Biol. Mass Spectrom.* **1993**, *22*, 493.

(239) Baytekin, B.; Baytekin, H. T.; Schalley, C. A. *Org. Biomol. Chem.* **2006**, *4*, 2825.

(240) Stowasser, R.; Hoffmann, R. *J. Am. Chem. Soc.* **1999**, *121*, 3414.

(241) Chang, F. C.; Young, V. Y.; Prather, J. W.; Cheng, K. L. *J. Electron Spectrosc. Relat. Phenom.* **1986**, *40*, 363.

(242) Batich, C.; Heilbronner, E.; Hormung, V.; Ashe III, A. J.; Clark, D. T.; Cobley, U. T.; Kilcast, D.; Scanlan, I. *J. Am. Chem. Soc.* **1973**, *95*, 928.

(243) Distefano, G.; Pignataro, S.; Szepes, L.; Borossay, J. *J. Organomet. Chem.* **1976**, *104*, 173.

(244) Distefano, G.; Pignataro, S.; Szepes, L.; Borossay, J. *J. Organomet. Chem.* **1975**, *102*, 313.

(245) *CRC Handbook of Chemistry and Physics, Internet Version*; 87 ed.; Lide, D. R., Ed.; Taylor and Francis: Boca Raton, FL, 2007.

(246) Korobkov, V. S.; Sechkarev, A. V.; Zubanova, L. P.; Dvorovenko, N. I. *Izvestiya Vuz. Fizika* **1968**, *11*, 158.

(247) Amashukeli, X.; Winkler, J. R.; Gray, H. B.; Gruhn, N. E.; Lichtenberger, D. L. *J. Phys. Chem. A* **2002**, *106*, 7593.

(248) Gruhn, N. E.; da Silva, D. A.; Bill, T. G.; Malagoli, M.; Coropceanu, V.; Kahn, A.; Bredas, J. L. *J. Am. Chem. Soc.* **2002**, *124*, 7918.

(249) Hearley, A. K.; Johnson, B. F. G.; McIndoe, J. S.; Tuck, D. G. *Inorg. Chim. Acta* **2002**, *334*, 105.

(250) Alberti, M.; Sedo, O.; Havel, J. *Polyhedron* **2003**, *22*, 2601.

(251) Knochenmuss, R. *J. Mass Spectrom.* **2002**, *37*, 867.

(252) Knochenmuss, R.; Zhigilei, L. V. *The Journal of Physical Chemistry B* **2005**, *109*, 22947.

(253) Knochenmuss, R. *Analyst* **2006**, *131*, 966.

(254) Models have been proposed to explain the primary process and the resulting ions and have been reviewed in detail elsewhere. For examples see Knochenmuss, R., Analyst 2006, 131, 966 or Karas, M.; Glückmann, M.; Schäfer, J., J. Mass Spectrom. 2000, 35, 1

(255) Knochenmuss, R.; Stortelder, A.; Breuker, K.; Zenobi, R. *J. Mass Spectrom.* **2000**, *35*, 1237.

(256) Zenobi, R.; Knochenmuss, R. **1998**, *17*, 337

(257) Cozzolino, A. F.; Gruhn, N. E.; Lichtenberger, D. L.; Vargas-Baca, I. *Inorg. Chem.* **2008**, *47*, 6220.

(258) Nonami, H.; Wu, F.; Thummel, R. P.; Fukuyama, Y.; Yamaoka, H.; Erra-Balsells, R. *Rapid Commun. Mass Spectrom.* **2001**, *15*, 2354.

(259) Tran, F.; Weber, J.; Weso; lstrok; owski, Tomasz A. *Helv. Chim. Acta* **2001**, *84*, 1489.

(260) Antony, J.; Grimme, S. *Physical Chemistry Chemical Physics* **2006**, *8*, 5287.

(261) Grimme, S.; Antony, J.; Schwabe, T.; Muck-Lichtenfeld, C. *Organic & Biomolecular Chemistry* **2007**, *5*, 741.

(262) Wu, Q.; Van Voorhis, T. *J. Chem. Theory Comput.* **2006**, *2*, 765.

(263) Cornell, W. D.; Cieplak, P.; Bayly, C. I.; Gould, I. R.; Merz, K. M.; Ferguson, D. M.; Spellmeyer, D. C.; Fox, T.; Caldwell, J. W.; Kollman, P. A. *J Am Chem Soc* **1995**, *117*, 5179.

(264) Allinger, N. L. *J Am Chem Soc* **1977**, *99*, 8127.

(265) Allinger, N. L.; Allinger, J. A.; Yan, L. Q. *Theochem-J Mol Struc* **1989**, *60*, 363.

(266) Allinger, N. L.; Quinn, M. I.; Chen, K. S.; Thompson, B.; Frierson, M. R. *Journal of Molecular Structure* **1989**, *194*, 1.

(267) Allinger, N. L.; Yuh, Y. H.; Lii, J. H. *J Am Chem Soc* **1989**, *111*, 8551.

(268) Sprague, J. T.; Tai, J. C.; Yuh, Y.; Allinger, N. L. *J Comput Chem* **1987**, *8*, 581.

(269) Mayo, S. L.; Olafson, B. D.; Goddard, W. A. *J Phys Chem-Us* **1990**, *94*, 8897.

(270) Rappe, A. K.; Colwell, K. S.; Casewit, C. J. *Inorg Chem* **1993**, *32*, 3438.

(271) Schatte, G.; Chivers, T.; Tuononen, H. M.; Suontamo, R.; Laitinen, R.; Valkonen, J. *Inorg Chem* **2005**, *44*, 443.

(272) Bjorgvinsson, M.; Roesky, H. W.; Pauer, F.; Stalke, D.; Sheldrick, G. M. *Inorg Chem* **1990**, *29*, 5140.

(273) Bjorgvinsson, M.; Roesky, H. W.; Pauer, F.; Stalke, D.; Sheldrick, G. M. *Eur J Sol State Inor* **1992**, *29*, 759.

(274) Kontopoulos, C.; Sigalas, M. P. *J Mol Struc-Theochem* **1999**, *490*, 125.

(275) Chivers, T.; Gao, X. L.; Parvez, M. *J Chem Soc Chem Comm* **1994**, 2149.

(276) Chivers, T.; Gao, X. L.; Parvez, M. *Journal of the American Chemical Society* **1995**, *117*, 2359.

(277) Important progress has been made towards accounting for the dispersion component with DFT functionals. For examples see: a) Grimme, S.; Antony, J.; Schwabe, T.; Muck-Lichtenfeld, C. Org. Biomol. Chem. 2007, 5, 741-758 and b) Zhao, Y.; Truhlar, D. G. Acc. Chem. Res. 2008, 41, 157-167.

(278) Allan, R. E.; Gornitzka, H.; Karcher, J.; Paver, M. A.; Rennie, M.-A.; Russell, C. A.; Raithby, P. R.; Stalke, D.; Steiner, A.; Wright, D. S. *J. Chem. Soc. Dalton Trans.* **1996**, 1727.

(279) Yaghi, O. M.; O'Keeffe, M.; Ockwig, N. W.; Chae, H. K.; Eddaoudi, M.; Kim, J. *Nature* **2003**, *423*, 705.

(280) Gelbart, W. M.; Barboy, B. *Acc. Chem. Res.* **1980**, *13*, 290.

(281) Nytko, E. A.; Helton, J. S.; Muller, P.; Nocera, D. G. *J. Am. Chem. Soc.* **2008**, *130*, 2922.

(282) Nytko, E. A.; Shores, M. P.; Helton, J. S.; Nocera, D. G. *Inorg. Chem.* **2009**, *48*, 7782.

(283) Shores, M. P.; Nytko, E. A.; Bartlett, B. M.; Nocera, D. G. *J. Am. Chem. Soc.* **2005**, *127*, 13462.

(284) McCullough, J. D.; Knobler, C.; Ziolo, R. F. *Inorg. Chem.* **1985**, *24*, 1814.

(285) Kellner, T.; Heine, F.; Huber, G. *Appl. Phys. B: Lasers Opt.* **1997**, *65*, 789.

(286) Lee, M.; Katz, H. E.; Erben, C.; Gill, D. M.; Gopalan, P.; Heber, J. D.; McGee, D. J. *Science* **2002**, *298*, 1401.

(287) Etter, M. C.; Frankenbach, G. M.; Adsmond, D. A. *Mol. Cryst. Liq. Cryst.* **1990**, *187*, 25.

(288) Kadirvelraj, R.; Umarji, A. M.; Robinson, W. T.; Bhattacharya, S.; Guru Row, T. N. *Chem. Mater.* **1996**, *8*, 2313.

(289) Frankenbach, G. M.; Etter, M. C. *Chem. Mater.* **1992**, *4*, 272.

(290) Hao, Z.-M.; Zhang, X.-M. *Cryst. Growth Des.* **2008**, *8*, 2359.

(291) Huang, X.-F.; Li, Y.-H.; Wu, Q.; Ye, Q.; Xiong, R.-G. *Inorg. Chim. Acta* **2005**, *358*, 2097.

(292) Qu, Z.-R.; Hong, Z.; Yi-Ping, W.; Xi-Sen, W.; Qiong, Y.; Yong-Hua, L.; Ren-Gen, X.; Brendan, F. A.; Zhi-Guo, L.; Zi-Ling, X.; Xiao-Zeng, Y. *Chem.--Eur. J.* **2004**, *10*, 53.

(293) George, S.; Nangia, A.; Lam, C.-K.; Mak, T. C. W.; Nicoud, J.-F. *Chem. Commun.* **2004**, 1202.

(294) Craxton, R.; Jacobs, S.; Rizzo, J.; Boni, R. *IEEE J. Quantum Electron.* **1981**, *17*, 1782.

(295) Clays, K. *Phys. Rev. Lett.* **1991**, *66*, 2980.

(296) Singh, H. B.; McWhinnie, W. R.; Ziolo, R. F.; Jones, C. H. W. *J. Chem. Soc., Dalton Trans.* **1984**, 1267.

(297) Bondi, A. *J. Phys. Chem.* **1964**, *68*, 441.

(298) Umland, T. C.; Allie, S.; Cuhlmann, T.; Coppens, P. *J. Phys. Chem.* **1988**, 92, 6457.

(299) Anslyn, E. V. *J. Org. Chem.* **2007**, *72*, 687.

(300) Iki, N. *J. Inclusion Phenom. Macrocyclic Chem.* **2009**, *64*, 1.

(301) Bleiholder, C.; Gleiter, R.; Werz, D. B.; Koppel, H. *Inorg. Chem.* **2007**, *46*, 2249.

(302) Clark, T.; Murray, J. S.; Lane, P.; Politzer, P. *J. Mol. Model.* **2008**, *14*, 689.

(303) Murray, J. S.; Concha, M. C.; Lane, P.; Hobza, P.; Politzer, P. *J. Mol. Model.* **2008**, *14*, 699.

(304) Murray, J. S.; Lane, P.; Politzer, P. *Int. J. Quantum Chem.* **2007**, *107*, 2286.

(305) Murray, J. S.; Lane, P.; Politzer, P. *Int. J. Quantum Chem.* **2008**, *108*, 2770.

(306) Nakanishi, W.; Hayashi, S.; Narahara, K. *J. Phys. Chem. A* **2008**, *112*, 13593.

(307) Nakanishi, W.; Hayashi, S.; Narahara, K. *J. Phys. Chem. A* **2009**, *113*, 10050.

(308) Politzer, P.; Murray, J. S.; Concha, M. C. *J. Mol. Model.* **2008**, *14*, 659.

(309) Wang, W.; Ji, B.; Zhang, Y. *J. Phys. Chem. A* **2009**, *113*, 8132.

(310) Lois, S.; Flores, J. C.; Lere-Porte, J. P.; Serein-Spirau, F.; Moreau, J. J. E.; Miqueu, K.; Sotiropoulos, J. M.; Baylere, P.; Tillard, M.; Belin, C. *Eur. J. Org. Chem.* **2007**, 4019.

(311) Al-Rubaie, A. Z.; Al-Masoudi, W. A.; Al-Jadaan, S. A. N.; Jalbout, A. F.; Hameed, A. J. *Heteroat. Chem.* **2008**, *19*, 307.

(312) Beer, L.; Brusso, J. L.; Haddon, R. C.; Itkis, M. E.; Kleinke, H.; Leitch, A. A.; Oakley, R. T.; Reed, R. W.; Richardson, J. F.; Secco, R. A.; Yu, X. Y. *J. Am. Chem. Soc.* **2005**, *127*, 18159.

(313) Chauhan, A. K. S.; Anamika; Kumar, A.; Srivastava, R. C.; Butcher, R. J.; Duthie, A. *J. Organomet. Chem.* **2006**, *691*, 5887.

(314) Pang, H.; Vilela, F.; Skabara, P. J.; McDouall, J. J. W.; Crouch, D. J.; Anthopoulos, T. D.; Bradley, D. D. C.; De Leeuw, D. M.; Horton, P. N.; Hursthouse, M. B. *Adv. Mater.* **2007**, *19*, 4438.

(315) Robertson, C. M.; Leitch, A. A.; Cvrkalj, K.; Reed, R. W.; Myles, D. J. T.; Dube, P. A.; Oakley, R. T. *J. Am. Chem. Soc.* **2008**, *130*, 8414.

(316) Wang, Y. F.; Parkin, S. R.; Gierschner, J.; Watson, M. D. *Org. Lett.* **2008**, *10*, 3307.

(317) Yu, M.; Zhang, K.; Qian, K. D.; Zhang, L. X.; Liu, Y. Z. *Acta Cryst.* **2007**, *E63*, O2551.

(318) Hayashi, S.; Yamane, K.; Nakanishi, W. *Bioinorg. Chem. Appl.* **2009**, *2009*, doi:10.1155/2009/347359.

(319) Milios, C. J.; Ioannou, P. V.; Raptopoulou, C. P.; Papaefstathiou, G. S. *Polyhedron* **2009**, *28*, 3199.

(320) Rethore, C.; Madalan, A.; Fourmigue, M.; Canadell, E.; Lopes, E. B.; Almeida, M.; Clerac, R.; Avarvari, N. *New J. Chem.* **2007**, *31*, 1468.

(321) Yamane, K.; Hayashi, S.; Nakanishi, W.; Sasamori, T.; Tokitoh, N. *Polyhedron* **2008**, *27*, 2478.

(322) Ichikawa, S.; Kimura, S.; Mori, H.; Yoshida, G.; Tajima, H. *Inorg. Chem.* **2006**, *45*, 7575.

(323) Bagryanskaya, I. Y.; Gatilov, Y. V.; Gritsan, N. P.; Ikorskii, V. N.; Irtegova, I. G.; Lonchakov, A. V.; Lork, E.; Mews, R.; Ovcharenko, V. I.; Semenov, N. A.; Vasilieva, N. V.; Zibarev, A. V. *Eur. J. Inorg. Chem.* **2007**, 4751.

(324) Konchenko, S. N. *Mendeleev Commun.* **2009**, *19*, 9.

(325) Gale, P. A. *Coord. Chem. Rev.* **2000**, *199*, 181.

(326) Gale, P. A. *Coord. Chem. Rev.* **2001**, *213*, 79.

(327) Gale, P. A. *Coord. Chem. Rev.* **2003**, *240*, 191.

(328) Gale, P. A.; Quesada, R. *Coord. Chem. Rev.* **2006**, *250*, 3219.

(329) Sessler, J.; Gale, P.; Cho, W.-S. *Anion Receptor Chemistry*, 2006.